U.PORTO

FACULDADE DE CIÊNCIAS
UNIVERSIDADE DO PORTO

U.PORTO

Dosimetric Effects of Clinical Setup Mismatch in Volumetric Modulated Arc Therapy as Assessed by Monte Carlo Methods

Ricardo José Pires Magalhães
Dissertação de Mestrado apresentada à
Faculdade de Ciências da Universidade do Porto em
Física Médica
2018

Dosimetric Effects of Clinical Setup Mismatch in Volumetric Modulated Arc Therapy as Assessed by Monte Carlo Methods

Ricardo José Pires Magalhães
Mestrado em Física Médica
Departamento de Física e Astronomia
2018

Orientador
Carla Carmelo Rosa, Professora Auxiliar, Faculdade de Ciências da Universidade do Porto

Coorientador
Joana Lencart, Especialista em Física Médica, Instituto Português de Oncologia do Porto de Francisco Gentil
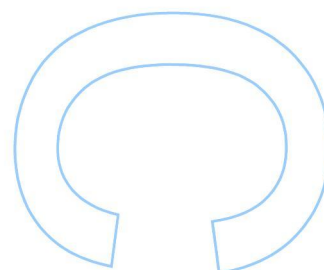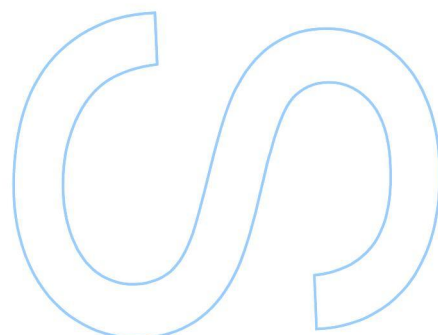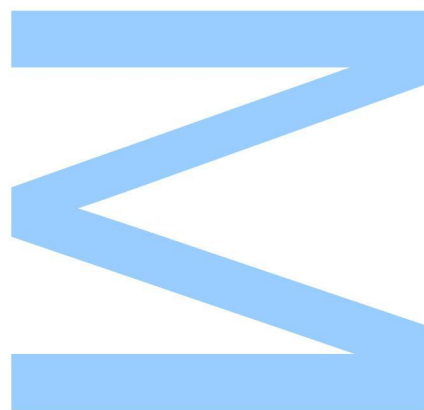
U.PORTO

FC FACULDADE DE CIÊNCIAS
UNIVERSIDADE DO PORTO
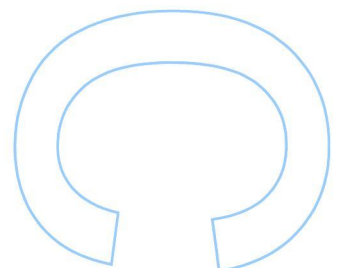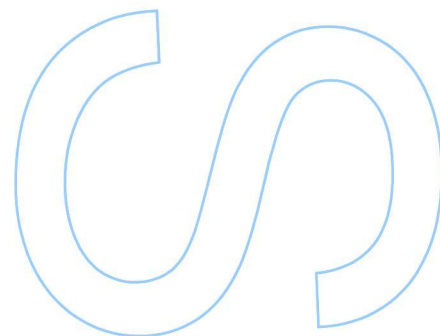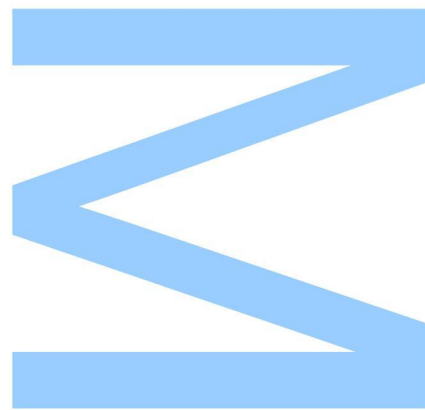
Todas as correções determinadas pelo júri, e só essas, foram efetuadas.

O Presidente do Júri,

Porto, _____/_____/_____

Acknowledgements

Resumo

Atualmente a radioterapia é uma das principais modalidades usadas no tratamento do cancro, sendo que diversas técnicas têm vindo a ser desenvolvidas nesta área de forma de aumentar a precisão no fornecimento de dose e, simultaneamente, minorar a probabilidade de efeitos secundários para o paciente. A radioterapia de intensidade modulada (IMRT) e a terapia em arco volumétrico (VMAT) aparecem com particular relevância neste contexto, visto permitirem reduzir o tempo de tratamento assim como melhorar a conformação da distribuição de dose ao volume alvo.

Um dos aspectos mais críticos no processo de radioterapia é o posicionamento do paciente na mesa de tratamento, pois um desvio na sua localização poderá levar a uma redução da dose fornecida ao volume alvo e a um incremento da dose recebida pelos tecidos saudáveis, aumentando a probabilidade de complicações para o indivíduo. Assim existe o interesse em avaliar os efeitos dosimétricos no paciente resultantes de desvios do seu posicionamento.

O cálculo da distribuição de dose no interior do corpo humano é um processo complexo, sendo que actualmente o método de Monte Carlo é considerado a abordagem mais apropriada a este problema. Neste contexto, o PRIMO surge como um programa para aplicação dessa metodologia ao cálculo da dose fornecida a um volume, também incluindo uma interface gráfica que facilita o seu uso na prática clínica. Assim sendo, o trabalho desenvolvido teve como principal objectivo avaliar os efeitos dosimétricos decorrentes de desvios no posicionamento na técnica de VMAT, através da utilização do método de Monte Carlo.

Com este propósito foram realizadas várias tarefas, nomeadamente a validação de um espaço de fase para o acelerador linear TrueBeam™ instalado no IPOPFG relativo à energia de fotões de 6MV com filtro aplanador, a validação do modelo do MLC fornecido pelo PRIMO, o estudo dos mecanismos de simulação aplicados no PRIMO para a simulação de planos de IMRT e VMAT e a análise dos efeitos dosimétricos, em VMAT, resultantes de vários desvios no posicionamento de modo a estabelecer as condições críticas para a localização do paciente na mesa do TrueBeam™ em operação no IPOPFG.

Por fim, foi desenvolvido um protocolo de adaptação do plano de tratamento a eventuais desvios no posicionamento, tendo por base a informação recolhida durante o trabalho realizado.

Abstract

Currently radiotherapy is one of the main modalities used in the treatment of cancer. Several techniques have been developed in this area as a way to increase the precision in the dose delivery and, simultaneously, to diminish the probability of side effects for the patient. Intensity modulated radiotherapy (IMRT) and volumetric arc therapy (VMAT) appear with particular relevance in this context, because they can reduce the treatment time as well as improve the conformation of the dose distribution to the target volume.

One of the most critical aspects associated to the radiotherapy process is the patient positioning on the treatment couch, since a deviation in their location may lead to a reduction of the dose delivered to the target volume and to an increase of the dose received by the healthy tissues, augmenting the probability of complications for the individual. Consequently, the interest on evaluating the dosimetric effects in the patient resulting from deviations of their positioning surges.

The calculation of the dose distribution inside the human body is a complex process, being the Monte Carlo method currently considered the most appropriate approach to such problem. In this context, PRIMO appears as a program for the application of that methodology to the calculation of the dose delivered to a volume, also including a graphical interface that facilitates its use in the clinical practice. As a result, the main objective of the work done was to evaluate the dosimetric effects resulting from positioning deviations in the VMAT technique through the application of the Monte Carlo method.

With this purpose several tasks were performed, namely the validation of a phase space for the TrueBeam^{TM} linear accelerator installed in IPOPFG relative to 6MV photon energy with a flattening filter, the validation of the MLC model provided by PRIMO, the study of the simulation mechanisms applied in PRIMO for the simulation of IMRT and VMAT plans, and the analysis of the dosimetric effects, in VMAT, resulting from various positioning shifts with the view to establish the critical conditions of the patient location on the treatment couch of the TrueBeam^{TM} operating at IPOPFG.

Finally, a protocol to adapt the treatment plan to eventual positioning mismatches was developed, based on the information collected during the work performed.

Keywords

External Beam Radiotherapy; External Radiotherapy; Radiotherapy; Adaptive Radiotherapy; Varian; TrueBeam; VMAT; IMRT; Setup; Positioning; Dosimetry; Monte Carlo; Simulation; PRIMO; PENELOPE

Index

List of Tables

List of Graphs

List of Figures

List of Abbreviations

3DCRT Three-Dimensional Conformal Radiation Therapy

AAA Analytical Anisotropic Algorithm

AAPM American Association of Physicists in Medicine

BEV Beam's Eye View

CBCT Cone Beam Computed Tomography

CPE Charged Particle Equilibrium

CT Computed Tomography

CTV Clinical Target Volume

DICOM Digital Imaging and Communications in Medicine

DTA Distance To Agreement

DLG Dosimetric Leaf Gap

DVH Dose-Volume Histogram

eV Electron Volt

FF Flattening Filter

FFF Flatenning Filter Free

FWHM Full Width at Half Maximum

GTV Gross Tumour Volume

IAEA International Atomic Energy Agency

ICRU International Commission on Radiation Units and Measurements

IMRT Intensity Modulated Radiation Therapy

IGRT Image-Guided Radiotherapy

ITV Internal Target Volume

IPOPFG Instituto Português de Oncologia de Francisco Gentil

KERMA Kinetic energy released in matter

LASER Light Amplification by Stimulated Emission of Radiation

LCG Linear Congruential Generator

LINAC Linear Accelerator

MATLAB Matrix Laboratory

MC Monte Carlo

MLC Multileaf Collimator

MeV Mega-Electron Volt

MOSFET Metal-Oxide-Semiconductor Field-Effect Transistor

MU Monitor Unit

MV Megavolt

PDD Percentage Depth Dose

PDF Probability Density Function

PTV Planning Target Volume

OAR Organ at Risk

QA Quality Assurance

QUANTEC Quantitative Analysis of Normal Tissue Effects in the Clinic

RNG Random Number Generator

RT External Beam Radiotherapy

SRS Stereotactic Radiosurgery

SRT Stereotactic Radiotherapy

SSD Source-Surface Distance

TCP Tumour Control Probability

TPS Treatment Planning System

VMAT Volumetric Modulated Arc Therapy

Z Atomic Number

1.) Introduction

1.1.) Motivation

In External Beam Radiotherapy (RT) the idea of modulating the radiation field through the motion of a collimating system developed into the Intensity Modulated Radiation Therapy (IMRT) concept. IMRT allows to achieve a practical clinical gain by the creation of complex dose distribution patterns, at the price of great complexity. Volumetric Modulated Arc Therapy (VMAT) is a generalization of the IMRT technique, which introduces the dynamic rotation of the gantry during the treatment.

The patient position is one of the most critical steps during the RT process. A mismatch in the clinical setup can produce undesirable effects from the dosimetric point of view. In principle, the effect of the positioning uncertainty cannot be predictable as it depends on several factors, such as the patient's anatomy, the anatomical region to treat, the radiation beam energy, and the RT technique.

The increase of the technological complexity in VMAT requires patient dedicated Quality Assurance (QA) programs in order to ensure safety to the patient and treatment effectiveness. The pre-treatment patient-specific QA becomes more important as the treatment complexity increases. A general approach is to make use of QA dedicated phantoms and to recalculate the dose distribution substituting the patient with the phantom. Delivering the planned VMAT radiation beam on the phantom allows a comparison between the dose distribution calculated by the Treatment Planning System (TPS) and the measurement. The most common tool to assess the equivalence between the TPS calculated and the measured (2D/3D) dose distribution is the gamma index.

The delivery of the VMAT radiation beam on the phantom requires that the positioning tools, at the treatment unit, are perfectly calibrated and allow the phantom to be placed with the minimum operator uncertainty. In principle, the positioning of patient and phantom can follow the same process. If a mismatch in the positioning instruments occurs, the QA can provide unexpected false results.

In Medical Physics, several dosimetric problems have been addressed by means of the Monte Carlo (MC) simulation method. The MC approach is considered the gold standard method for radiation transport simulation. In some cases it is the only one to perform accurate absorbed dose calculations, since it provides the most detailed and complete description of the radiation fields and the particle transport in matter.

The MC method can be a powerful tool to evaluate dose distributions in undesirable, but possible, conditions, such as patient and/or phantom positioning mismatch. Several codes are available for MC simulations in the field of RT, some of which are GEANT4, EGSnrc/BEAMnrc, PENELOPE, FLUKA, and MCNP. Recently, a new MC code named PRIMO that makes use of the PENELOPE features was developed.

The PRIMO simulation software has a user-friendly approach, which is a suitable and competitive characteristic for the clinical activity. Among the different linear accelerator (LINAC) models provided in the PRIMO release, Varian FakeBeam is an available model of the Varian TrueBeam^{TM} unit. TrueBeam^{TM} has very peculiar features such as the absence of the flattening filter (FFF – Flattening Filter Free), respiratory gating, and a real-time tracking system. This particular LINAC can be used for a wide range of RT applications, including stereotactic and VMAT techniques.

A version of PRIMO is installed at Instituto Português de Oncologia do Porto de Francisco Gentil (IPOPFG) and previous experience on radiation beam modeling of a TrueBeam^{TM} unit has been developed (Master's Degree thesis on implementation of VMAT MC simulation in the clinical activity). As a result, adequate conditions were established for the realization of this thesis.

1.2.) Thesis Outline

This thesis is divided into seven chapters. In chapter one the framework of the work is introduced. Then, chapter two includes the theoretical and experimental background associated with radiation therapy and Monte Carlo simulations. Chapter three represents the objectives of the work performed. Flowingly, in chapter four the materials and methods used are mentioned. Afterwards, chapter five includes all the results obtained and their discussion. Next, chapter six contains the protocol developed for the adaption of the treatment plan. In chapter seven the conclusions of this work are withdrawn and finally chapter eight encompasses the bibliography used.

2.) Theoretical and Experimental Background

Cancer is one of the main life-threatening diseases worldwide and it is expected a rise in this public health problem due to multiple reasons, such as the increase of the Human life expectancy, the continuous growth of the population, and the obesity upsurge (Global Burden of Disease Cancer Collaboration, 2017; Jung, K. *et al*, 2017).

Some oncological therapies currently used are surgery, chemotherapy, radiation therapy (radiotherapy), immunotherapy, hormone therapy, and targeted therapy. Frequently, cancer's therapeutic approach involves a combination of local therapy, like surgery and/or radiotherapy, and systemic therapy, such as chemotherapy and/or hormone therapy (Liu, K. *et al*, 2017; Silverman, P., 2012).

Radiotherapy consists in the use of ionizing radiation to damage the tumorous cells' DNA, leading to the shrinkage and possibly to the control of solid tumours. Commonly, this area is further divided in external beam radiotherapy and brachytherapy. In this thesis the focus will be on external beam radiotherapy, where an ionizing radiation source, placed at some distance from the individual, produces a beam of high energy photons, neutrons or charged particles. The beam is then directed to a specific region of the patient's body in order to deliver a therapeutic amount of radiation, usually referred as radiation dose or simply dose, to a target volume (Salvajoli, J. V. *et al*, 2008; Silver, J., 2006; Voutilainen, A. 2016).

2.1.) Radiobiological Background

Ionizing radiation can damage the cells' DNA directly (direct action) or interact with water molecules and produce free radicals that react with this biological entity, a process known as indirect action. A single strand break, as well as spatially distant multiple single strand breaks, is likely to be repaired by the cell. On the other hand, when two opposite or very close breaks occur there is a high probability of a double strand break, which is considered to be the main reason for radiation induced cell death (Baskar, R. *et al*, 2014; Voutilainen, A. 2016). Ionizing radiation causes similar harm in normal and tumorous cells, however experimental results show that healthy cells can repair the DNA damage faster than cancerous cells. This factor combined with other effects, like reoxygenation of neoplastic cells and reassortment of cells during the cell cycle, leads to an increased sensitivity of the cancerous cells to radiation when the dose is delivered in small fractions over longer periods of time, instead of a

large fraction once. Nevertheless, there is a possibility of further complications for the patient because, for example, the healthy cells may not undergo apoptosis when they are not able to repair all the damage done to the DNA strand or after performing wrong corrections in that molecule (Baskar, R. *et al*, 2014; Voyant, C. *et al*, 2014).

2.2.) Radiation Physics

In this section, the physics associated with the interaction of electrons and photons with matter will be addressed. These are the two types of radiation that a linear accelerator can produce and, consequently, the only ones used at Instituto Português de Oncologia do Porto de Francisco Gentil (IPOPFG) for external radiotherapy treatments. Also, the basic quantities and units associated with radiation dosimetry will be briefly described.

2.2.1.) Interaction of Electrons with Matter

Since electrons have an electric charge, they experience Coulomb interactions with nuclei and atomic electrons during their passage through matter, therefore these particles are defined as directly ionizing radiation. In each interaction event there are several possible energy losses and angular changes that an electron can undergo (Mozumder, A. *et al*, 2003). Any momentum change of an incident particle is defined as a collision and it can be classified as (Autran, J. *et al* 2015; Podgorsak, E. B., 2016; Vidyasagar; P. B. *et al*, 2017; Zhang, S.-L., 2012):

➤ Elastic collision: the kinetic energy of the involved particles after and before the encounter is equal and the incident particle is just deflected from its original path; for energies above ~100 eV elastic collisions with atomic electrons can be neglected;

➤ Inelastic collision: kinetic energy is transferred to the struck particle (nucleus or atomic electron), as a result the involved particles do not have the same kinetic energy after and before the encounter, albeit the total energy is conserved in the process.

The major interaction processes of electrons with matter are excitation, ionization, and inelastic scattering by nuclei, which is known as bremsstrahlung (Sharma, S. 2008).

An incident electron can excite an atomic electron to a higher energy orbital when there is an inelastic collision between the two particles (figure 1.A) and, if the energy provided to the orbital electron is high enough, it may result in the ejection of

the struck electron, leading to the ionization of the atom. The energy of the emitted electron depends on its binding energy as well as on the incident electron's energy. When the ejected electron leaves the atom a vacancy in the electronic band structure is created, which must be filled for the atom to reach its lowest energy state (except when the ejection occurs at the outer shell - figure 1.B and 1.C). If the expelled electron is from an inner shell of the atom, the filling of the vacancy left behind, by the transition of another electron located in a higher energy orbital, originates a release of energy equal to the binding energy difference between the two orbital levels involved (Hornyak, G.L. *et al*, 2008; Knapp, F.F.R. *et al* 2016; Leroy, C. 2016). This energy can be emitted via a photon (radiative emission – characteristic x-rays) or be absorbed by a bound electron of a higher shell, causing its ejection (this released electron is called Auger electron). The probability of non-radiative transitions, with consequent emission of Auger electrons, is higher for low atomic number materials (Splinter, R. 2016).
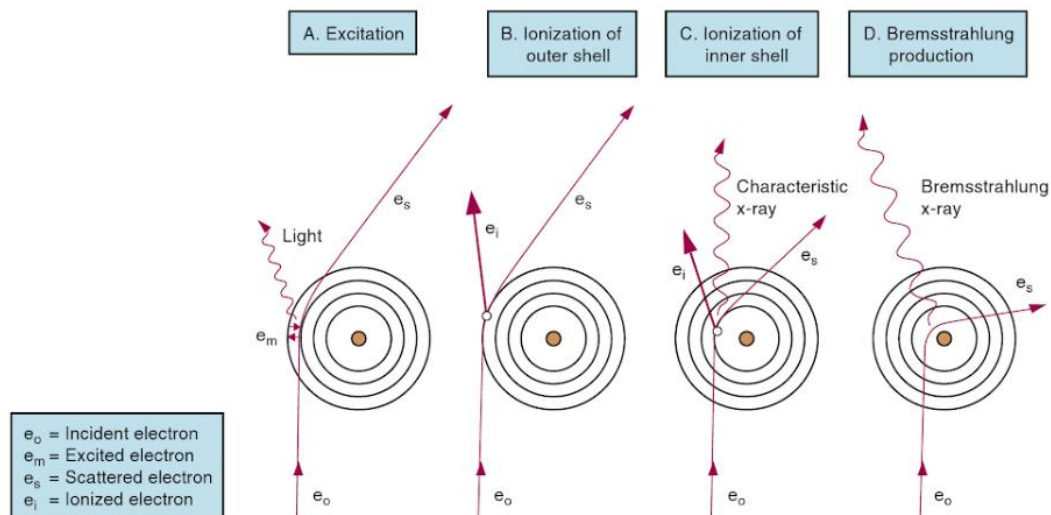
Figure 1 - Interactions of electrons with matter: **(A)** excitation, **(B, C)** ionization, **(D)** bremsstrahlung (adapted from Gunderson, L. L. *et al* 2015).

Another important interaction of electrons with matter is bremsstrahlung (braking radiation – figure 1.D). This process is characterized by the electromagnetic radiation emitted per charged particles when they decelerate in a medium, due to the inelastic interaction with nuclei of absorber atoms within matter. Bremsstrahlung is the dominant mode through which the moderate to high energy electrons lose energy in high atomic number materials (Bushong, S. C., 2017; Halperin, E. C. *et al*, 2013; Podgorsak, E. B., 2016). For the energies used in external radiotherapy, in the order of MeVs, this interaction produces a continuous x-ray emission spectrum, for the reason that there are no transitions between quantized energy levels involved in the process

as opposed to characteristic x-rays, where there exists a well-defined transition that leads to a discrete x-ray emission spectrum (Halperin, E. C. *et al*, 2013).
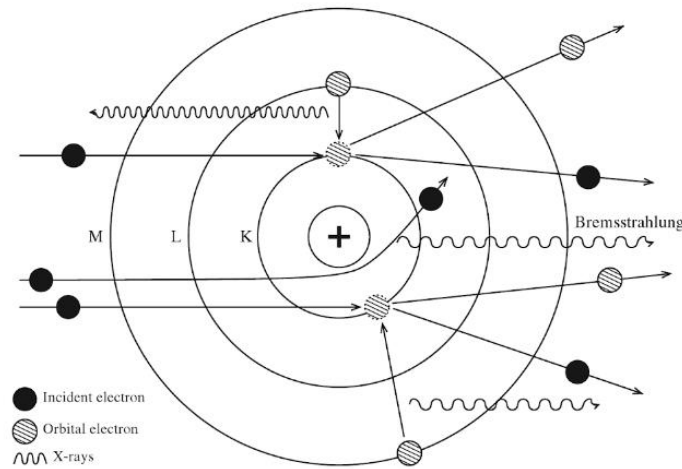
Figure 2 - Bremsstrahlung and generation of characteristic x-rays (adapted from Ahmed, S. N., 2015).

Nevertheless, the bremsstrahlung continuous emission spectrum frequently includes single strong peaks, because the bombarding electrons can expel electrons from the inner atomic shells of the struck particle. As a result, the filling of these vacancies by other electrons located in the higher energy orbitals, as discussed before, produces characteristic x-rays or Auger electrons (Johnston J. *et al*, 2015).
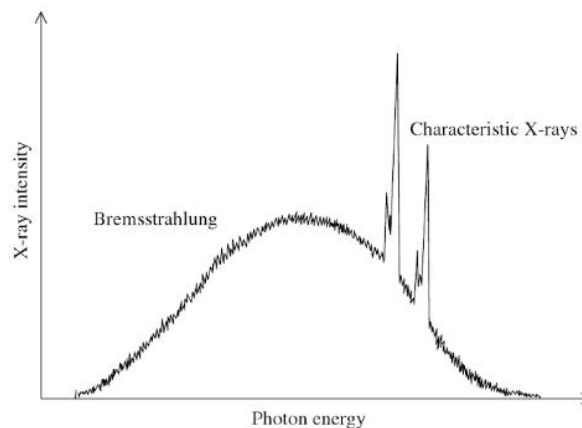
Figure 3 - Typical bremsstrahlung spectrum for an x-ray tube (adapted from Ahmed, S. N., 2015).

There are other types of elastic interactions of electrons with matter, such as Møller scattering and Bhabha scattering, but for the energy range used in radiotherapy this processes can be neglected (Podgorsak, E. B., 2016).

2.2.2.) Interaction of Photons with Matter

Photons are quanta of electromagnetic field, which interact with matter in a different way than electrons due to their charge neutrality, being classified as indirectly

ionizing radiation because they deposit energy in an absorbing medium through a two-step process (Krems, R. V., 2018; Nikjoo, H. *et al*, 2012; Podgorsak, E. B., 2016):

➤ First step: energy transfer from the photon to an energetic charged particle with low weight (electron or positron) that is released in the medium;

➤ Second step: deposition of energy in the medium by the released low weight charged particle.

In radiotherapy treatments, photon beams are directed towards the patient's body. As they pass through the individual, there are three possible outcomes for each photon (Nikjoo, H. *et al*, 2012). It can:

➤ Pass through the patient without interacting;

➤ Interact with the patient and be completely absorbed, depositing its total energy in the medium;

➤ Interact with the patient, deposit part of its energy in the medium, and experience scattering or deflection from its original direction.

There are various interactions that each photon can undergo: it may interact with an atom as a whole, with the nucleus of an atom, or with an orbital electron of the atom. Therefore, different photons in a given beam passing through a certain medium do not necessarily interact in an identical way with matter as they travel. The occurrence probability associated to a particular interaction is generally expressed in terms of an interaction cross section, which depends on the photon's energy as well as on the density and atomic number of the absorber material (Dössel, O. *et al*, 2010; Key, T., 2013; Podgorsak, E. B., 2016). The cross section for a given interaction can be defined as the area of the target (atomic nucleus or subatomic particle) perpendicular to the direction of the incident photon beam; the event occurs whenever a particle hits this area (Brahme, A. *et al*, 2014; Podgorsak, E. B., 2016).

The three main interactions of photons with matter, for the energy range used in radiotherapy, are: the photoelectric effect, the Compton effect, and the pair production. They are dominant at different energies and for different absorber atomic number values, as it is possible to see in figure 4 (Podgorsak, E. B., 2016).
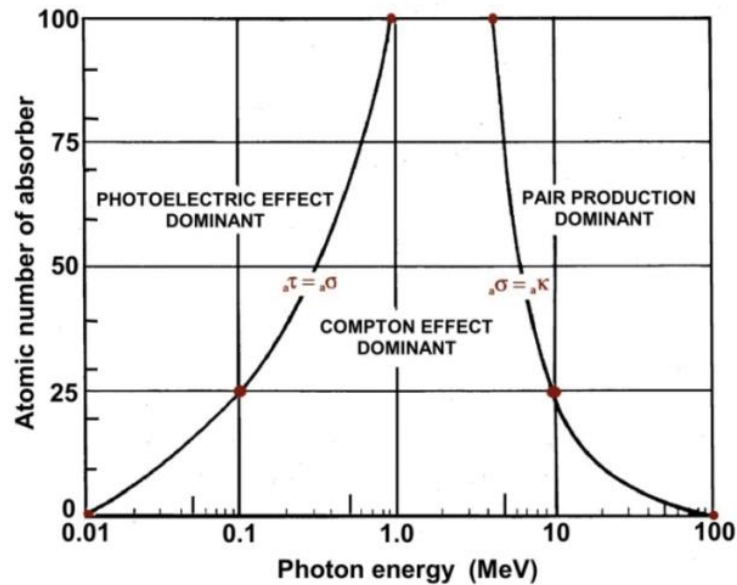
Figure 4 - Regions of relative predominance for the three major interactions of photons with an absorber medium. The left curve is the region where the cross sections for the photoelectric effect and Compton effect are equal ($_a\tau = {_a}\sigma$). The right curve is the region where the Compton cross section is identical to the pair production cross section ($_a\sigma = {_a}\kappa$) (adapted from Sun, Y. *et al*, 2017).

These processes (figure 4) are classified as inelastic because the involved particles do not have the same kinetic energy before and after the event (Biersack, H.-J. *et al*, 2007). Additionally, there are two elastic interactions of photons with matter relevant to medical physics (not shown in figure 4), namely Thomson scattering and Rayleigh scattering (Cremer, J. T. 2012). The latter is considered elastic, even though the atom as a whole absorbs the transferred momentum, for the reason that the recoil energy is very small and, therefore, the scattered photon has essentially the same energy as the original photon (Podgorsak, E. B., 2016). These two processes occur mainly for low energy photons and they do not originate a considerable energy deposition in the medium. Since external beam radiotherapy relies on the energy transfer to a precise location of the patients' body, these elastic interactions will not be detailed in this thesis (Barazzuol, L. *et al*, 2012; Podgorsak, E. B., 2016; Turner, J. E., 2007).

As it is possible to see from figure 4, the photoelectric effect is dominant for photons in the energy range of 0.01 MeV to ~0.1 MeV and its prevalence upsurges with the increase of the absorber's atomic number (Z) (Chin, L. S. *et al*, 2015). During this process an incident photon is completely absorbed by the medium and an electron from a shell of the struck atom is ejected (known as "photoelectron"). The considerations of conservation of energy and momentum indicate that this interaction can only occur on a tightly bound (shell with a higher binding energy) electron, rather than with a "free electron" (shell with a lower binding energy), so that the atom can pick

up the difference of momentum and energy between the photon and the photoelectron
(Chin, L. S. *et al*, 2015; Brahme, A. *et al*, 2014; Yang, F. *et al*, 2010).
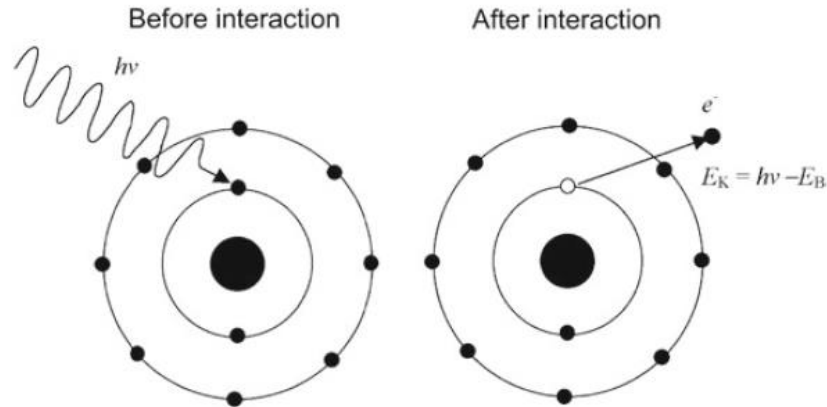
Figure 5 - Schematic diagram of the photoelectric effect: $h\upsilon$ is the energy of the incident photon, E_B is the shell binding
energy and E_K is the kinetic energy of the ejected electron (adapted from Podgorsak, E. B., 2016).

From figure 5, it is possible to conclude that the energy of the incident photon
must be superior to the electron's binding energy for the photoelectron to be ejected.
As a result, the energy of the emitted particle is equal to the incident photon energy
minus the binding energy of the ejected orbital electron. In this interaction the atom is
left in an ionized state (Saha, G. B., 2013). Sometimes the photon energy is not high
enough to emit an orbital electron, but it is sufficient to raise it to a higher energy
orbital, leaving the atom in an excited state (Müller, M., 2007). When an ionization of an
atom occurs, the filling of the vacancy left behind is similar to the process described in
section 2.2.1.), also occurring the emission of an Auger electron or a characteristic x-
ray photon (Klockenkämper, R. *et al*, 2014).

An important last note about this interaction is that the angular distribution of the
ejected electrons is determined by the incident photon energy. At low photon energies
the photoelectrons tend to be ejected at ~90° relatively to the incident photon direction
and, as the photon energy increases, the emission angle starts to decrease.
Consequently the orientation of the electron emission progressively changes towards
the same direction as that of the incident photon (Green, D., 2014; Podgorsak, E. B.,
2016).

A different interaction starts dominating over the photoelectric effect when the
energy of the incident photon increases (figure 4). In this process, called Compton
effect, or scattering, the photon interacts with a free or loosely bound orbital electron,
so that it is possible to consider it stationary for the fact that its binding energy is
insignificant in comparison to the photon's energy. Two particles result from this
interaction: a scattered photon with lower energy than the incident photon, and an

electron known as Compton electron, which is ejected from the atom with a certain kinetic energy (Bushong, S. C., 2017; Kharisov, B. I. *et al*, 2013; McParland, B. J., 2010). The Compton effect may also occur between a photon and a nucleus, however this specific process can be neglected in the area of medical physics and radiation dosimetry (Podgorsak, E. B., 2016).
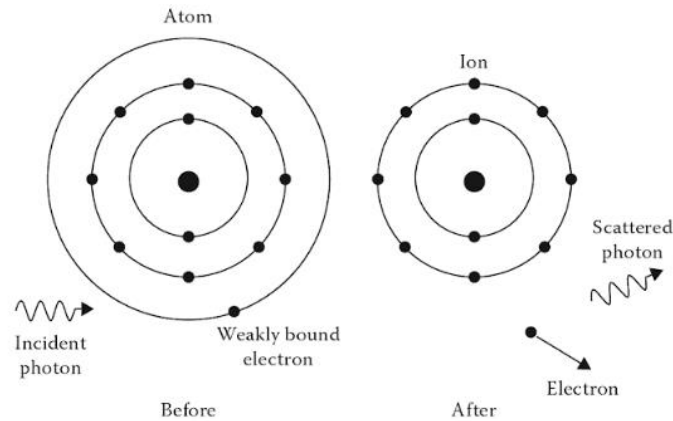
Figure 6 - Schematic diagram of the Compton effect by a loosely bound electron (adapted from Kharisov, B. I. *et al*, 2013).

From the analysis of figure 4, it is possible to view that the pair production processes begin to dominate over the Compton effect as the incident photon energy is further increased and the atomic number of the absorber rises (dependence $\sim Z^2$). When the incident photon energy, $h\upsilon$, surpasses $\sim 1.02 MeV$, i.e. twice the electron's rest mass ($m_e c^2$), the production of an electron-positron pair in combination with the complete absorption of the incident photon becomes energetically viable (Leroy, C., 2012; Pawlicki, T. *et al*, 2016). Three quantities must be conserved for the occurrence of this interaction: energy, charge, and momentum. If the photon's energy verifies the condition stated before ($h\upsilon > 1.02 MeV$), energy and charge can be conserved even if pair production befalls in free space. However, the conservation of its linear momentum implies that this phenomenon can only occur in the Coulomb field of another particle (collision partner). When the collision partner is an atomic nucleus, an appropriate portion of the momentum carried by the incident photon is taken up by that structure (figure 7(a)) (Henley, E. M., 2007; Podgorsak, E. B., 2016; Thornton, S. T. *et al*, 2013). Otherwise, if $h\upsilon > 4m_e c^2$, an orbital electron can receive the exceeding linear momentum. The recoil energy of this atomic electron might be substantial and the process is known as triplet production (pair production in the Coulomb field of the electron). When such event occurs, three particles leave the site of interaction (figure 7(b)) (Andreo, P. *et al* 2017; Pawlicki, T. *et al*, 2016).
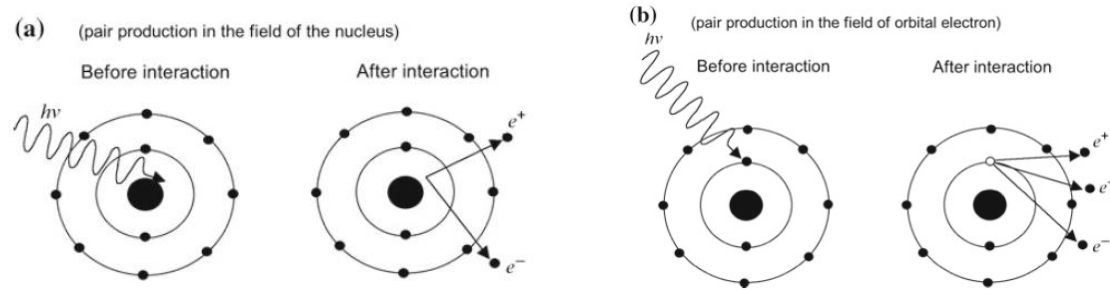
Figure 7 - Schematic representation of pair production: **(a)** nuclear pair production in the Coulomb field of the atomic nucleus; **(b)** electron pair production (triplet production) in the Coulomb field of an orbital electron (adapted from Podgorsak, E. B., 2016).

The positron resulting from this interaction moves through an absorbing medium and, therefore, experiences kinetic energy losses by collisional and radiative processes via Coulomb interactions with orbital electrons and nuclei of the absorber (Podgorsak, E. B., 2016). When the energy of this particle becomes sufficiently low, it experiences a process of annihilation with an orbital electron of the absorber, yielding two photons that approximately move in opposite directions (~180º) (Herrmann, K. *et al*, 2016; Niederhuber, J. E. *et al*, 2013; Podgorsak, E. B., 2016):

Another possible interaction between an energetic photon (8-16 MeV) and an absorber nucleus is the photonuclear reaction (also called photodisintegration), in which the atomic nucleus absorbs a photon. The most probable outcome of such process is the emission of a single neutron. This process does not play a role in overall photon attenuation studies, but it is important in shielding calculations whenever the energy of the photons exceeds the photonuclear reaction threshold (Chang, D. *et al*, 2014; Johnson, T. E., 2017; Podgorsak, E. B., 2016).

2.2.2.1.) Photon Attenuation Coefficients

The interaction mechanisms described before do not occur singly, but rather they combine to produce a global attenuation of the photon beam as it passes through matter. Attenuation can be interpreted as the removal of photons from the original photon beam and it is governed by the inverse-square law, along with absorption and scattering events. This weakening of the beam is frequently expressed in terms of an attenuation coefficient, which describes the interaction probability of the photons in a material. Generally, the macroscopic attenuation coefficient is given by the sum of the attenuation coefficients for all the possible interactions that a photon, with a given energy, can have with an absorber medium (Ahmed, S. N., 2015; Bushberg, J. T. *et al*,

2011; Huda, W; 2010; Podgorsak, E. B., 2016; Singh, H. *et al*, 2016; Vosper, M. *et al*, 2011).

2.2.3.) Basic Quantities and Units in Radiation Dosimetry

In radiotherapy, the prescribed dose must be delivered accurately and safely to the target site in order to reach the treatment goal and, simultaneously, minimize the probability of complications in normal tissues (Lee, E. K. *et al*, 2017). Therefore, the precise measurement of the deposited energy is fundamental for the medical use of radiation (van der Merwe, D. *et al*, 2017). In such context, dosimetry appears as the measurement, calculation, and assessment of the dose delivered to a given volume (Adlienė, R. *et al*, 2017; Meghzifene, A., *et al*, 2010; Tweedy, J. T., 2013).

This area can be divided into two categories, namely absolute dosimetry and relative dosimetry. Absolute dosimetry consists in a direct measure of the absorbed dose, or another dose related quantity, at a certain point by a dosimeter (section 2.5.1.)) under standard conditions, not needing a calibration of the measurement device in a known radiation field. On the other hand, relative dosimetry involves dosimeters that require a calibration of their response to ionizing radiation, in a well-defined radiation field, before the radiation induced signal can be used to obtain dosimetric information (Podgorsak, E. B., 2005; Podgorsak, E. B., 2016; Watanabe, Y., 2014).

There are numerous quantities that were introduced with the objective of quantifying radiation. In this thesis, only the most important will be addressed, according to the International Commission on Radiation Units and Measurements (ICRU) report No.85.

2.2.3.1.) Particle Number and Radiant Energy

The particle number, N, is the number of particles that are emitted, transferred or received. SI Unit: dimensionless.

The radiant energy, R, is the energy (excluding rest energy) of the particles that are emitted, transferred or received. SI Unit: J.

2.2.3.2.) Flux and Energy Flux

The flux, $\dot{N}$, is the increase of the particle number (dN) per time interval (dt), thus:

$$\dot{N} = \frac{dN}{dt} \qquad (1)$$

SI Unit: s^{-1}.

The energy flux, $\dot{R}$, is the increase of radiant energy (dR) per time interval dt, thus:

$$\dot{R} = \frac{dR}{dt} \qquad (2)$$

SI Unit: W.

2.2.3.3.) Fluence and Energy Fluence

The fluence, Φ, *is the number of particles (dN) incident on a sphere of cross-sectional area da, thus*

$$\Phi = \frac{dN}{da} \qquad (3)$$

SI Unit: m^{-2}.

The energy fluence, Ψ, *is the radiant energy (dR) incident on a sphere of cross-sectional area da, thus*

$$\Psi = \frac{dR}{da} \qquad (4)$$

SI Unit: J m^{-2}

2.2.3.4.) Fluence Rate and Energy-Fluence Rate

The fluence rate, $\dot{\Phi}$, is the fluence increase ($d\Phi$) per time interval dt, thus:

$$\dot{\Phi} = \frac{d\Phi}{dt} \qquad (5)$$

SI Unit: m^{-2} s^{-1}

The energy-fluence rate, $\dot{\Psi}$, is the increase of the energy fluence $d\Phi$ in the time interval dt, thus:

$$\dot{\Psi} = \frac{d\Psi}{dt} \qquad (6)$$

SI Unit: W m^{-2}.

2.2.3.5.) KERMA

According to Podgorsak, E. B., 2016, KERMA is an acronym for "Kinetic energy released in matter" and it is only defined for indirectly ionizing radiation. ICRU report No. 85 describes this quantity as: *the quotient of dE_{tr} by dm, where dE_{tr} is the mean sum of the initial kinetic energies of all the charged particles liberated in a mass dm of a material by the uncharged particles incident on dm, thus*

$$K = \frac{dE_{tr}}{dm} \tag{7}$$

SI Unit: J Kg^{-1} = Gy.

The released charged particles can lose kinetic energy through inelastic collisions with atomic electrons (ionization and excitation) or by radiative processes involving atomic nuclei. Therefore KERMA can be decomposed in two quantities, the collision KERMA, K_{col}, which does not take into account the radiative losses of the liberated charged particles, and the radiation KERMA, K_{rad}, that only considers the energy emitted through radiative processes, thus (Khan, F. M. *et al*, 2014; Nilson, B. N., 2015):

$$K = K_{col} + K_{rad} \tag{8}$$

For low atomic number materials (e.g., air, water, soft tissue), charged particles lose the major part of their kinetic energy via collision interactions and only a small fraction through emission of radiation. K_{rad} increases with increasing particle energy, however for absorbed dose (2.2.3.6.)) calculations the radiative losses are not considered because the emitted radiation can exit from the volume of interest. As a result, only the collision KERMA is used as an estimate of the absorbed dose, in conditions of charged particle equilibrium (CPE) (2.2.3.6.1.)) (Khan, F. M. *et al*, 2014; Yukihara, E. G. *et al*, 2010).

2.2.3.6.) Absorbed Dose

The absorbed dose, D, *is the mean energy imparted by ionizing radiation $d\bar{\varepsilon}$ to matter of mass dm, thus*

$$D = \frac{d\bar{\varepsilon}}{dm} \tag{9}$$

SI Unit: J Kg^{-1} = Gy.

This quantity is defined for all types of ionizing radiation (i.e., directly and indirectly ionizing radiation), all materials, and all energies, whereas KERMA is only defined for indirectly ionizing radiation (Khan, F. M. *et al*, 2014). As discussed in section 2.2.3.5.1.), the absorbed dose can be estimated by the collisional KERMA in conditions of CPE.

A relevant quantity related to the absorbed dose is the equivalent dose, defined as the absorbed dose multiplied by a radiation weighting factor (SI Unit: Sievert (Sv)). This measure considers the biological effectiveness of radiation, i.e. the effectiveness of a given type of radiation in causing damage to tissues and organs, and it depends on the radiation type and energy (Hoskin, P. *et al*, 2011; Symonds, R. P. *et al*, 2012). Another pertinent quantity associated with absorbed dose is the effective dose, which

is defined as the tissue-weighted sum of the equivalent doses associated with all the tissues and organs exposed to ionizing radiation (SI unit: Sievert (Sv)). In this case, the weighting factor is called tissue weighting factor and it assesses the risk of stochastic effects that may result from an irradiation of that particular tissue. Therefore, the effective dose evaluates the stochastic health risk to the whole body resulting from a given radiation dose (Allen, B. *et al*, 2012; Hoskin, P. *et al*, 2011).

2.2.3.6.1.) Charged Particle Equilibrium (CPE)

Charged particle equilibrium (CPE), or electronic equilibrium, is said to exist in a volume if each charged particle of a given type, direction, and energy exiting from that volume is replaced by a particle of equal type, direction, and energy entering the same volume (Attix, F. H., 2008). When CPE conditions are fulfilled it is valid to assume that the collision KERMA is equal to the absorbed dose (2.2.3.6.)) (Sibtain, A. *et al*, 2012).

In the buildup region the CPE requirements are not verified, consequently the deposited energy cannot be inferred from the energy transfer to matter in this location. From figure 8(a), it is possible to see that immediately beneath the patient's surface the absorbed dose (D) is much smaller than the collision KERMA (K_{col}). However, D increases quickly with depth (z) until CPE is achieved at z_{max} (depth of maximum absorbed dose) and both quantities become comparable (Andreo, P. *et* al, 2017; Attix, F. H., 2008; Das, I. J., 2017; Nilson, B. N., 2015).

The difference between absorbed dose and collision KERMA, observed in the buildup region, occurs due to the relative long range of the energetic secondary charged particles (electrons and positrons). When these particles are released by interactions of photons with matter they travel through matter, depositing their energy in the medium at a given distance from the location where they were initially freed (Ghom, A. G., 2016).

Considering a more realistic case (figure 8(b)), beyond z_{max} both dose and collision KERMA decrease due to the photon attenuation in the medium, resulting in a transient rather than a true CPE. In this situation, the energy entering the volume is slightly larger than the energy leaving that same volume and the absorbed dose is proportional, but not equal, to the collision KERMA (Andreo, P. *et* al, 2017; Attix, F. H., 2008; Das, I. J., 2017; Nilson, B. N., 2015).
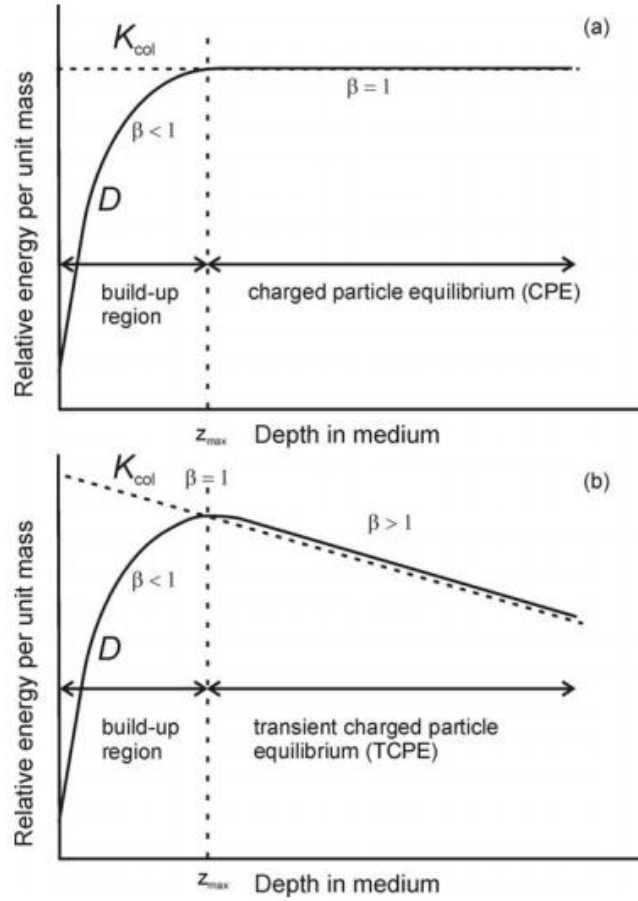
Figure 8 - Variation of the collision KERMA, K_{col}, and absorbed dose, D, with depth in a medium, irradiated by a high-energy photon beam: **(a)** CPE; **(b)** Transient CPE. $\beta = \frac{D}{K_{col}}$ (adapted from Podgorsak, E. B., 2005).

2.2.3.7.) Exposure (*X*)

Exposure, X, is defined as: *the quotient of dq by dm, where dq is the absolute value of the mean total charge of the ions of one sign produced when all the electrons and positrons liberated or created by photons incident on a mass dm of dry air are completely stopped in dry air, thus:*

$$X = \frac{dq}{dm}$$

(10)

SI Unit: C kg^{-1}.

Summing up, this quantity is only defined for photons and it characterizes the capability of photons to ionize the air.

An alternative unit to this measure is the roentgen (R) and it is defined as the amount of photon radiation needed to produce a charge of 2.54x10^{-4} C per kilogram of dry air (under standard conditions for pressure and temperature) (Haynes, K. *et al*, 2013).

2.3.) The Linear Accelerator

The key equipment in external beam radiotherapy is the linear accelerator (LINAC), figures 11 and 12, because it is the source of the ionizing radiation beams used for patient treatment (Healy, B. J. *et al*, 2016).

The primary source of radiation in the LINAC is the electron gun. This component of the accelerator has a heated tungsten filament which, through thermionic emission, emits electrons that will form the LINAC beam (Bhattacharjee *et al*, 2012; Chin, L. S., 2012; Symonds, R. P. *et al*, 2012). After the emission, the electrons are accelerated in a waveguide by means of electromagnetic waves in the microwave range, which are generated via a magnetron or a klystron (Cherry, P. *et al*, 2009; Hanna, S., 2012; Hoppe, R. *et al*, 2010; Symonds, R. P. *et al*, 2012). For LINACs that produce electron beams of 6MV or higher, the necessary accelerating waveguide length is too long to sit in line with the target and so it becomes useful to bend the electron beam through the use of bending magnets. The most commonly used bending systems are named according to the angle that electrons are turned, namely: the 90º bending, 270º bending, and the slalom system (also called 112.5º bending) in which the electrons take a zigzag path (Cherry, P. *et al*, 2009; Khan, F. M., 2012; Kuppusamy, T., 2017).

The electrons that exit the bending magnets system can be used directly for treatment on the body's surface, or they can collide with a target, producing high energy x-rays through bremsstrahlung that can be used to treat deeper areas within the patient (Rahbar, R. *et al*, 2013; Snider, J. W. *et al*, 2016). The resulting beam passes through a primary collimator, where it is collimated. This component is a conical opening machined in a block of a shielding material and it defines the maximum circular field (Cherry, P. *et al*, 2009; Podgorsak, E. B., 2005).

In the clinical energy range (4MV – 25MV) the angular distribution of the bremsstrahlung photons is preferentially in the direction of the incident electrons that exit from the bending magnets system, creating a forward peaked (bell-shaped) transverse dose profile (figure 11). Therefore, in order to provide a flat (uniform) dose distribution at a defined depth, a flattening filter (FF) is introduced in the beam path (Joiner, M. C. *et al*, 2009; Xiao, Y *et al*, 2015; Yan, Y. *et al*, 2016). This component has a conical shape in order to flatten the forward peaked bremsstrahlung spectrum of MV photons. The type of FF used depends on the beam energy produced by the LINAC (Podgorsak, E. B., 2005; Sharma, S. D., 2011; Xiao, Y *et al*, 2015).

Below the flattening filter there are dual, sealed, and independent, ionization chambers. These chambers are sealed in order to give a constant reading at a

constant dose rate, independently of the temperature and pressure in the bunker. Therefore, they can terminate the irradiation when the planned number of monitor units (MUs) is debited. The advantage of having a dual system is that if the primary chamber fails during the treatment, the secondary dose monitoring system can terminate the irradiation when the selected MUs are surpassed by a set limit, providing additional safety for the patient by preventing an excessive output of radiation (Cherry, P. *et al*, 2009; Washington, C. M. *et al*, 2015).

Afterwards, the collimated beam is truncated by the secondary collimators, also known as jaws. These consist of two pairs of adjustable blocks, made of a high Z material (e.g., tungsten or lead) and perpendicular between them. The jaws restrict the radiation emerging from the LINAC's head to specific square or rectangular fields, ranging from 1x1 cm^2 to 40x40 cm^2 at the isocenter of the accelerator (Cherry, P. *et al*, 2009; Podgorsak, E. B., 2012; Sikora, M. P., 2011). The isocenter is the point where the rotation axes of the treatment couch, the gantry, and the collimator intersect (Khan, F. M. *et al*, 2014; Voutilainen, A. 2016). Most modern models of LINACs have an additional system for beam collimation called the multileaf collimator (MLC), figure 9. This component is made up by several thin leaves of a high atomic number material (typically tungsten), allowing the dynamic design of practically any field shape for patient irradiation (Goh, G. *et al*, 2015; Jeraj, M. *et al*, 2004; Salles A. A. F. *et al*, 2011). The MLC is divided into two carriages, also called bank A and bank B, each of which with half of the total number of MLC leaves (figure 10) (Hughes, J. L., 2013). Nowadays, the MLCs used in the clinical practice may have 40 till 160 leaves. These leaves can have different widths, ranging from some millimeters until 1 cm. Every leaf is computer controlled, allowing field conformations with accuracy better than 1mm (Best, L. *et al*, 2013; Chin, L. S. *et al*, 2015; Jeraj, M. *et al*, 2004; Klüter, S. *et al*, 2009; Orlandini, L. C. *et al*, 2015).
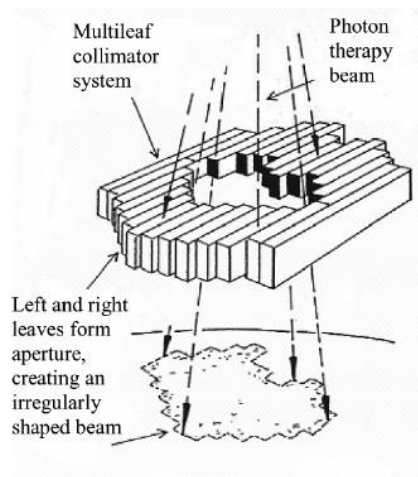
Figure 9 - The working principle of the MLC (adapted from Romeijn, H. E. *et al*, 2005).
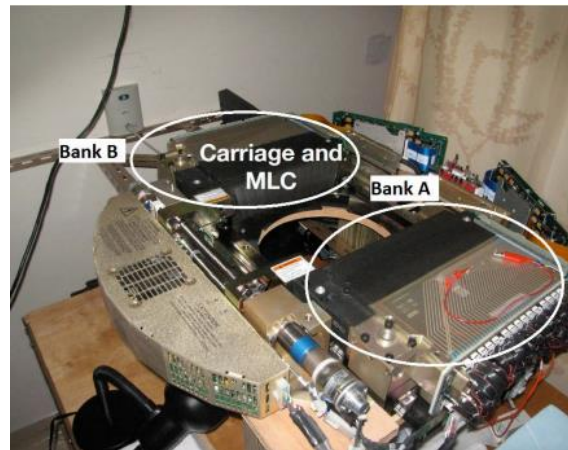
Figure 10 - The two banks of a Varian MLC (adapted from Hughes, J. L., 2013).
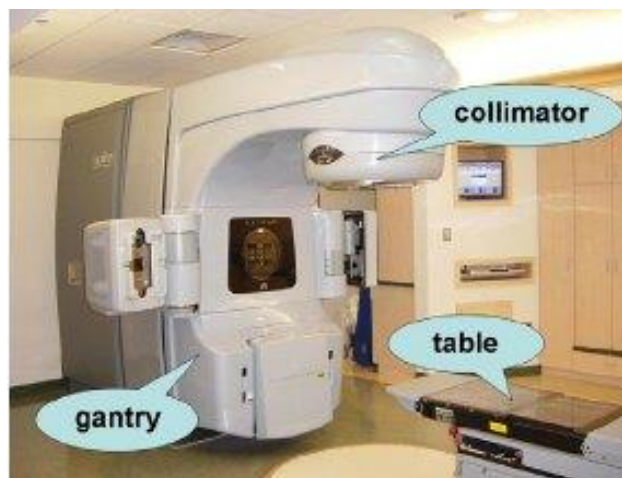
Figure 11 - General structure of a LINAC (adapted from Hamza-Lup, F. G., *et al*, 2014).
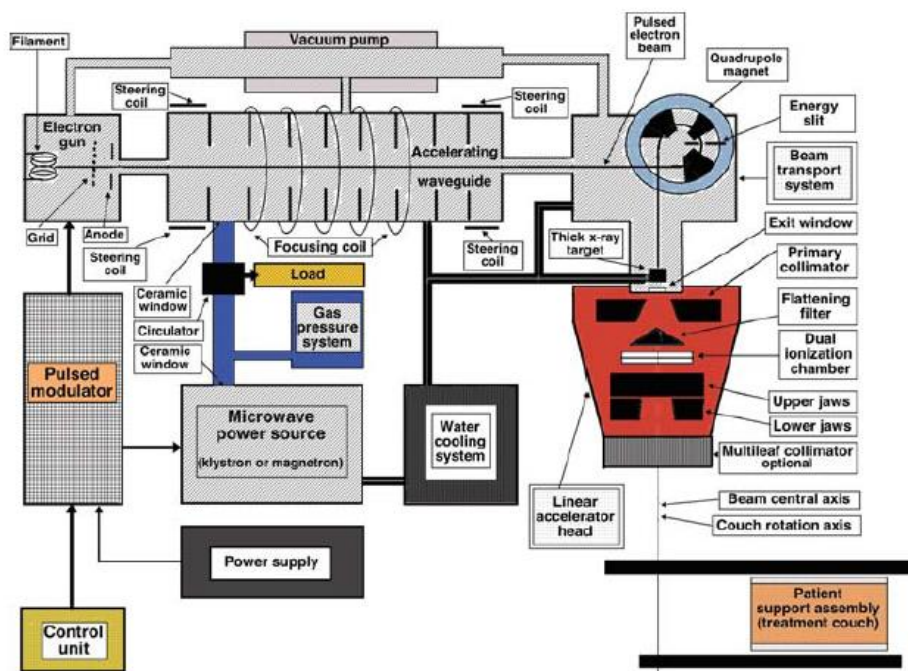
Figure 12 - Schematic block diagram of a LINAC (adapted from Podgorsak, E. B., 2010).

2.4.) The Flattening Filter Free Mode

The advent of advanced radiotherapy techniques, such as stereotactic radiosurgery/radiotherapy (SRS/SRT) where inhomogeneous dose distributions are delivered to the patient, and intensity-modulated radiotherapy (IMRT) (section 2.6.3.2.)) that consists in creating varying fluence patterns across the beam, stimulated a growing interest about operating standard LINACs through a flattening filter free (FFF) mode. In this approach the flattening filter is removed from the photon beam path and, as a result, the treatment beam has a non-uniform (bell-shaped) transverse dose profile exhibiting the highest intensity on its central axis (figure 13) (Cox, J. D. *et al*, 2010; Sharma, S. D., 2011; Xiao, Y. *et al*, 2015). Various Monte Carlo and experimental studies about the dosimetric aspects and the radiation protection problems associated with FFF photon beams, which were created by mechanically removing the flattening filter from LINACs of various makers and models, have been described in the past (Cashmore, J., 2008; Dalaryd, M. *et al*, 2010; Sharma, S. D., 2011). Hrbacek *et al*, (2011) published the measured dosimetric properties of unflattened photon beams produced by a Varian TrueBeam™ LINAC (Varian Medical Systems, Palo Alto, CA), which is capable of generating both flattened and unflattened clinical photon beams. An important aspect to refer is that when the flattening filter is removed in the TrueBeam™, and in other recent LINAC models, a replacement filter of brass or copper is placed to absorb the contaminating electrons (Dalaryd, M., 2015).

The flattening filter of a standard LINAC acts as a photon attenuator and therefore as a beam hardener, hence FFF beams have distinct properties in comparison to flattened photon beams, such as a characteristic transverse profile, higher dose rate, a different photon energy spectrum, and particular head-scatter properties (Mohammed, M. *et al*, 2017; Xiao, Y. *et al*, 2015).

When FFF beams are used the out-of-field doses, which are unwanted and hard to model in the treatment planning system (TPS), can be significantly decreased, mainly due to the reduced head scatter and electron contamination. Therefore, FFF beams lead to a reduction of the peripheral doses during the treatment (Gaya, A. *et al*, 2015; Jaumot, M. *et al*, 2013; Howell, R. M. *et al*, 2010).

From figure 14, it is possible to verify that the central peak in the transverse profile of a FFF beam becomes more pronounced as the field size and energy increase. Nevertheless, the absolute value of that peak exhibits a weak dependence on those two parameters (Shende, R. *et al*, 2016).

The shape of the transverse profile in a FFF beam only changes slightly with depth owing to a considerable reduced off-axis softening effect, which is verified due to

the absence of the preferential absorption of photons in the central axis of the beam caused by the flattening filter. As a result the depth-dose property remains almost constant throughout the field, even for large field sizes (Davidson, S. E. *et al*, 2016; Sharma, S. D., 2011; Xiao, Y. *et al*, 2015). The removal of the flattening filter provides the ability to perform treatments with a higher dose rate, becoming possible to increase this parameter by a factor of 2 to 4. This means that a FFF LINAC can normally be operated at a dose rate higher than 10 Gy/min, under the usual operating conditions used for a LINAC with flattening filter (Gaya, A. *et al*, 2015; Sharma, S. D., 2011).
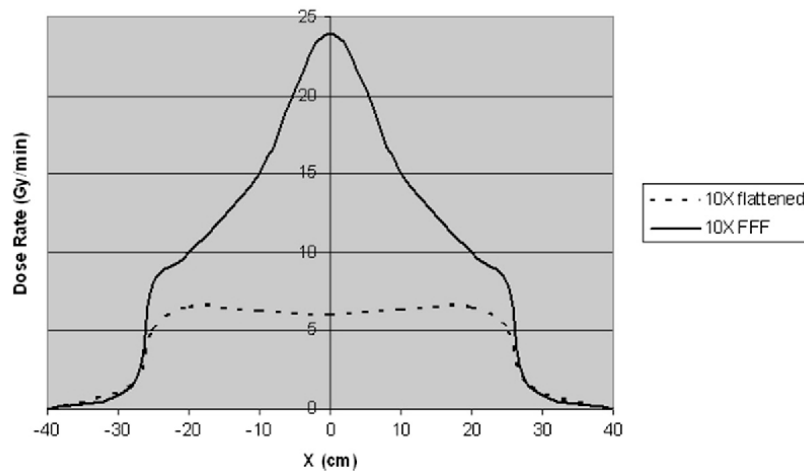
Figure 13 - Transverse beam profile of a 10 MV flattened (dashed line) and unflattened (solid line) photon beam (adapted from Prendergast, B. M. *et al*, 2013)
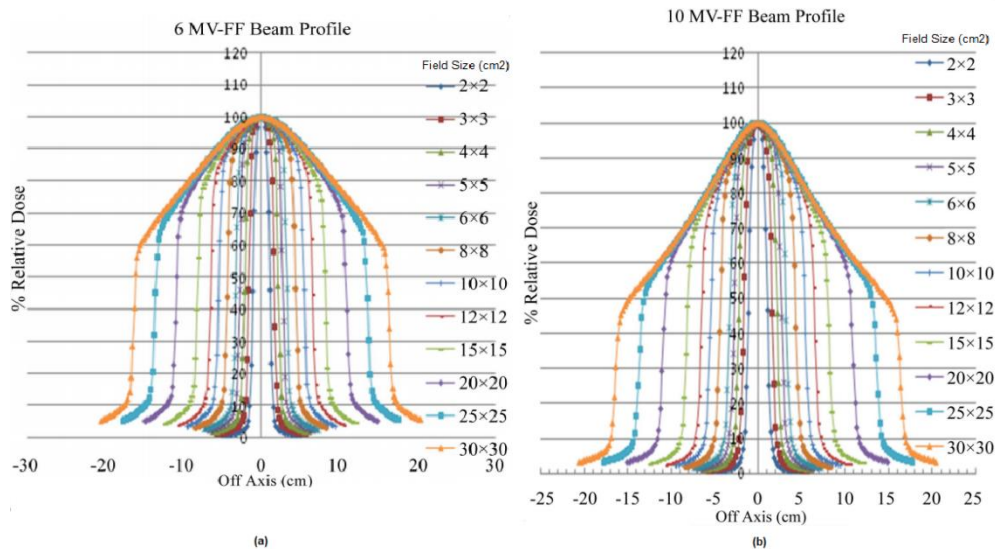
Figure 14 - Transverse profiles for : **(a)** 6MV FFF; **(b)** 10MV FFF photon beams; at SSD = 100 cm considering various field sizes (adapted from Shende, R. *et al*, 2016).

There is a lack of controlled clinical studies addressing the radiobiological consequences of FFF beams in the human body. Nevertheless, the biological effects of

these beams on cell lines were reported by various authors, such as Karan, T. *et al*, 2013; King, R. B. *et al* 2013; Nakano, H. *et al*, 2018, and it was concluded that, at the instantaneous dose-rates investigated, no change in cell response was observed with the removal of the flattening filter.

2.5.) General Aspects of LINAC Calibration

Dosimetry is a critical process for the adequate calibration of a LINAC, because it involves the acquisition of the depth dose curves and beam profiles for each irradiation field, energy and rate, type of radiation, and beam modifier accessory; as well as the implementation of a precise correlation between the absorbed dose at a given depth and the number of monitor units (MUs) associated with that dose, under reference conditions. However, in order to acquire a dosimetric database for a specific LINAC, it is required a meticulous and precise experimental work (Levitt, S. H., 2012; Podgorsak, E. B., 2016; Godley, A. *et al*, 2016).

2.5.1.) Dosimeters

Ionizing radiation is detected through the interaction of radiation with a radiosensitive device. This instrument shall have certain characteristics, such as: perform reproducible, accurate and precise measurements, exhibit dependence on dose or dose rate, and demonstrate linearity, energy response, directional dependence, as well as good spatial resolution, in order to be suitable as a dose meter (dosimeter) for ionizing radiation (Beddar, S., 2016; Izewska, J. *et al*, 2012).

There are various detectors, based on different materials and geometries, that can be used in external beam radiotherapy, such as ionization chambers, radiochromic films, solid state detectors (e.g., Thermoluminescent Dosimeter), and electronic devices (e.g., MOSFETs) (Khan, F. M., 2012; Mijnheer, B., 2017).

2.5.2.) Phantoms

The calibration of a LINAC is performed through measurements in phantoms. These are objects constituted by tissue-equivalent materials that simulate the radiation absorption and scattering properties of the patient's tissues, or known geometries. There are different physical phantoms that can be used, such as geometric phantoms, like the water tank (figure 15), or anthropomorphic phantoms, for example RANDO (figure 16). Besides the physical models, there are also computational phantoms (figure 17) that are used for studies involving computation, e.g. Monte Carlo radiation

transport simulation (section 2.7.1.)) (Cherry, P. *et al*, 2009; DeWerd, L. A. *et al*, 2013; Seco, J. *et al*, 2016).

In comparison to the physical methods, the computational approach has some advantages, namely in terms of efficiency, versatility, accuracy, and safety. For some particular situations, such as internally distributed radiation sources, these computation techniques are the only possible option to estimate the dose delivered to the patient (DeWerd, L. A. *et al*, 2013; Seco, J. *et al*, 2016).

2.5.3.) Characteristic Dosimetric Curves

The calibration and quality assurance of a clinical LINAC is based on the acquisition of several dosimetric curves. The measurement and acquisition of this data is commonly performed through the use of a water phantom, which consists in a tank made up of acrylic walls, full of water, and with controlled height and leveling of the dosimeter (Amestoy, W., 2015; Dieterich, S. *et al*, 2015).
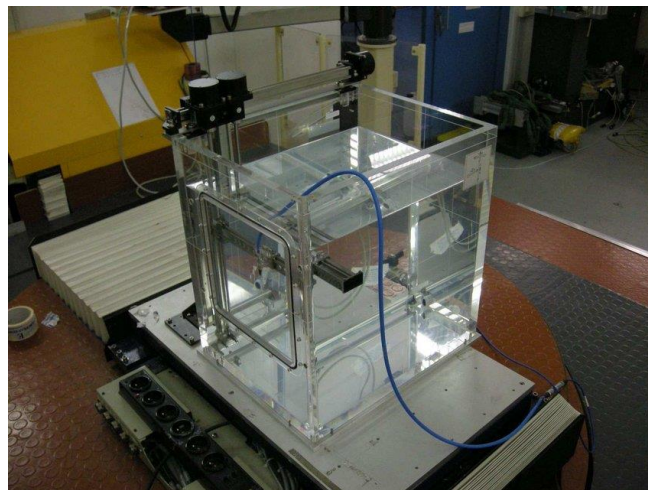
Figure 15 - Example of a water tank phantom (adapted from Prezado, Y., *et al*, 2010).

Figure 16 - (a) Front view of RANDO phantom; **(b)** CT scan of the RANDO phantom (adapted from Puchalska M. *et al*, 2014).

Figure 17 - Computational male and female phantoms (adapted from Xu, G. X, 2014).

2.5.3.1.) Percentage Depth Dose (PDD)

The percentage depth dose (PDD) is a curve defined by the quotient, expressed as a percentage, of the absorbed dose along the beam central axis at a given depth, D_d, to the absorbed dose in the central axis of the beam at a reference depth, D_{d0}, thus (Khan, F. M. *et al*, 2014):

$$PDD = \frac{D_d}{D_{d0}} \times 100\% \tag{11}$$
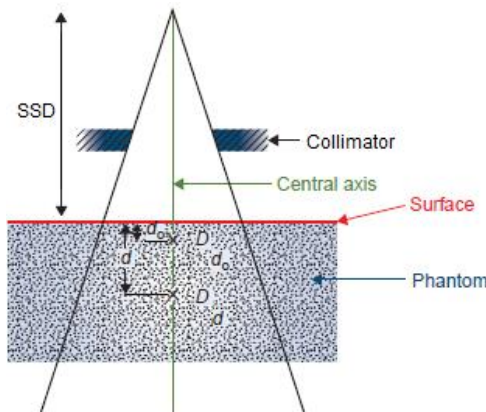
Figure 18 - Percentage depth dose definition (adapted from Khan, F. M, 2014).

The PDD depends on various factors, such as the irradiated material, the size of irradiation field, the beam energy, and the source to surface distance (SSD) (Yarbro, C. *et al*, 2010).

In the following figure, some typical PDDs for electrons and photons are represented:
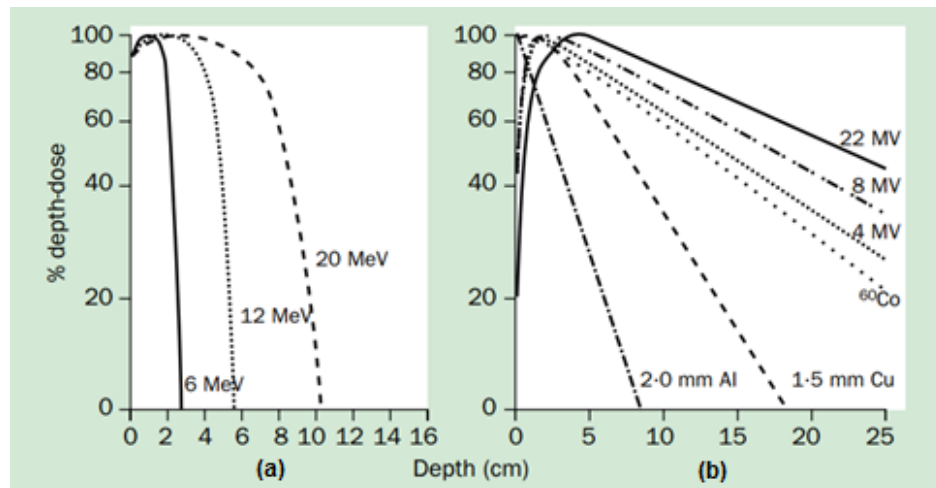
Figure 19 - Percentage depth doses for: **(a)** electron beams ranging from 6–20 MeV for a field size of 10x10 cm^2; **(b)** megavoltage x-ray beams ranging from 1·17–1·33 MeV (60Co) to 22 MV (adapted from Dicker, A. P., 2003, SSD not mentioned in the article, as well as the field size for photons).

For both curves, at zero depth the PDD value represents the dose deposited on the surface/skin of the patient, or phantom (Yadav, G. *et al*, 2009). The region between the surface and the depth of dose maximum, characterized by a progressive increase of the dose with increasing depth, is known as the buildup region. From the comparison of figures 19(a) and 19(b) it is possible to conclude that this region is significantly larger for photons. This occurs due to the relative long range of the energetic secondary charged particles, freed by interactions of photons with matter, which will travel through matter, depositing their energy in the medium at a certain distance from their initial location (Beyzadeoglu, M. *et al*, 2010; Marcu, L. *et al*, 2012; Tavernier, S., 2010).

Beyond the buildup region it is possible to see in figure 19 that the PDD increases with increasing beam energy for photons and electrons. Such correlation occurs because particles with higher energy have greater penetrating power than the ones with lower energy. In this region it is also verifiable that, for the two types of radiation, the PDD decreases with increasing depth in matter, however electrons exhibit a steeper reduction (figure 19(a)) than photons (figure 19(b)) (Levitt, S. H. *et al*, 2012; Maqbool, M., 2017).

2.5.3.2.) Transverse Beam Profile

Dose distributions along the beam central axis only give a portion of the information necessary for an accurate description of the energy deposited in the patient, or phantom. The remaining information, which is fundamental to determine the dose distributions in two or three dimensions, is obtained by combining the central axis information with off-axis dose profiles. This off-axis data is acquired by measuring

various beam profiles perpendicularly to the beam central axis at a certain depth in a phantom (e.g., depth of maximum dose, 5 cm, 10 cm, 20, and 30 cm) (Flores, F. J. H., 2015; Khan, F. M., 2012; Sharma, S. D., 2011; Xhafa, B. *et al*, 2014). The measured dose distribution depends on two components of the LINAC, namely (Kuppusamy, T., 2017):

- ➢ Collimator: influences the beam edges;
- ➢ Flattening filter: controls the beam center.

Therefore, there is a dose variation from the beam axis to its off-axis region because these regions are influenced by different structures of the LINAC. This discrepancy is described through the off-axis ratio (OAR) (Levitt, S. H. *et al*, 2012).

The OAR is defined by the ratio, expressed as a percentage, of the dose at a point away from the beam central axis at a given depth, D_o, to the dose at the point on the central axis of the beam at the same depth, D_a, thus (Levitt, S. H. *et al*, 2012):

$$OAR = \frac{D_o}{D_a} \times 100\% \qquad (12)$$

The graph that illustrates the OAR as function of the distance from the central axis is called the transverse beam profile (figure 20) and it is usually divided in three zones (Flores, F. J. H., 2015; Kuppusamy, T., 2017; Mayles, P. *et* al, 2007; Podgorsak, E. B., 2006):

- ➢ The central dose region, which represents the central portion of the profile, ranging from the central axis to about 1cm to 1.5cm from the geometric field edges of the beam, and contains 100%-80% of the dose at the central axis of the beam;

- ➢ The penumbra region, which is the zone near to the geometric field edges where the dose changes quickly, that is influenced by the field defining collimators, the size of the radiation source, and the lateral electronic disequilibrium. This region contains 80%-20% of the dose at the central axis of the beam;

- ➢ The umbra region, which is the region outside of the radiation field, away from the field edges. The dose in this zone is minimal and it is the outcome of the radiation transmitted through the collimator and the head shielding. This region contains < 20% of the dose at the central axis of the beam.

At shallow depths the flattened beam profile contains horns, which are created by the conical shaped flattening filter, however these disappear at higher depths (figure 20) (Kuppusamy, T., 2017).
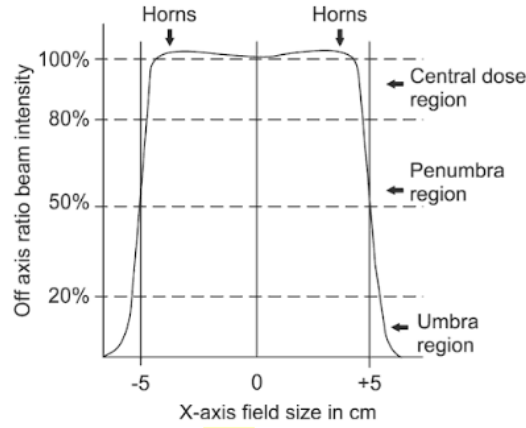
Figure 20 - Flattened 6MV beam profile for a 5x5 cm^2 field (adapted from Kuppusamy, T., 2017).

The characteristics of the transverse beam profile are often checked and characterized by parameters that evaluate its uniformity, namely symmetry and flatness (Kuppusamy, T., 2017).

2.5.3.3.) Symmetry

For the symmetry (S) evaluation the measured beam profile at a given depth, usually the depth of dose maximum, is divided at the central axis, forming two halves. These two sections are then compared for any pair of points. The maximum ratio of the dose at two points symmetric with respect to the central axis of the beam, i.e. $D(x, y)$ and $D(-x, -y)$, is used to calculate S , thus (Beyzadeoglu, M. *et al*, 2010; Kuppusamy, T., 2017; Pathak, P, *et al*, 2015):

$$S = \frac{D(x,y)}{D(-x,-y)} \times 100\% \qquad (13)$$

According to the AAPM Task Group 142, the beam profile should have a maximum disagreement of 2% among two points at the same distance from the beam central axis (Klein, E .E. *et al*, 2009; Kuppusamy, T., 2017).

An alternative approach, for the symmetry assessment, consists in the calculation of the areas below the transverse beam profile ranging from the central axis to the point where the dose is 50% of the central axis dose, to the left, A_L, and to the right, A_R, of the beam central axis (Beyzadeoglu, M. *et al*, 2012; Birgani, M. J. T. *et al*, 2013):

$$S = \frac{A_L - A_R}{A_L + A_R} \times 100\% \qquad (14)$$

2.5.3.4.) Flatness

The flatness (F) evaluates the dose fluctuation, relative to the central axis, over the central 80% of the field size. The value of this parameter represents the maximum percentage variation of the dose across the central 80% of the beam width, thus (Khan, F. M. *et al*, 2014; Kuppusamy, T., 2017; Rodriguez, M. *et al*, 2009):

$$F = \frac{M-m}{M+m} \times 100\%$$ (15)

Where M and m are the maximum and minimum dose values, respectively, existing in the central 80% of the transverse beam profile (Khan, F. M. *et al*, 2014; Kuppusamy, T., 2017).

The quality control procedures in clinical LINACs usually require a flatness lower than 3%, for measurements at 10cm depth, 100cm SSD, and for the largest field (normally 40 x 40cm^2) (Podgorsak, E. B., 2005).

2.6.) External Beam Radiotherapy

2.6.1.) Definition of Volumes

External radiotherapy is a local treatment modality, consequently for each specific patient it is fundamental to define with precision the body regions to be treated and to protect (Burnet, N. G. *et al*, 2004). In the treatment planning process there are various volumes that must be delineated by the physician and/or the dosimetrist, because the absorbed dose cannot be prescribed, recorded, and reported without specification of target volumes and volumes of healthy tissues at risk (ICRU report No.83). In this work, the definitions of ICRU report No.83 for these volumes will be considered, thus:

➢ Gross Tumour Volume (GTV): the GTV is the macroscopic extent and the site of the tumor;

➢ Clinical Target Volume (CTV): the CTV the volume of tissue that encompasses the GTV plus a clinical margin that accounts for a subclinical malignant disease with a certain probability of manifestation, considered pertinent for therapy*;*

➢ Internal Target Volume (ITV): the ITV is the volume of tissue that contains the CTV plus an internal margin that accounts for the physiologic movement and variations in size, shape, and position of the CTV;

➢ Planning Target Volume (PTV): the PTV is the volume of tissue that includes the ITV plus a setup margin that accounts for uncertainties in the patient positioning in all treatment sessions;

> Organs at Risk (OARs): the OARs are the structures that if irradiated could experience significant morbidity, consequently these can influence the treatment planning and/or the prescribed absorbed dose.

2.6.2.) General Treatment Techniques

The selection of the radiotherapy treatment technique for a given patient is determined by the depth and size of the target volume, the anatomic site to irradiate, and the proximity of critical anatomical structures. Some fundamental technique parameters are: the number of beams; the beam energy; the beam weight (the relative quantity of dose delivered by each beam); the shape of the field; the irradiation geometry; and the application of bolus, wedges, compensators, or other devices. The common practice is that photons are often used in a combination of two or more fields, i.e. parallel opposed, wedged pair, three fields, four fields, box or arc; and electrons are used as single *en face* fields, possibly combined with other electron fields in order to cover a larger area.

As the number of fields increases, there are some important comments: the high-dose region becomes more conformal to the target and the peripheral dose diminishes, however the volume of tissue covered by those doses is larger (Dieterich, S. *et al*, 2015; Gunderson, L. L. *et al*, 2015; Khan, F. M., 2014). Nowadays, in radiotherapy it is possible to use from a single field, in a unidirectional treatment, up to various hundreds/thousands of fields, as in dynamic arc treatments (Gunderson, L. L. *et al*, 2015).

2.6.3.) Advanced Treatment Techniques

In the next section, some advanced radiotherapy techniques performed at IPOPFG will be described. These techniques have been extensively recognized as the best therapeutic approach for numerous clinical cases due to their capacity to offer quality conformal dose distributions, and to improve the sparing of the neighboring healthy tissues, as compared to conventional techniques. Consequently, these approaches allow a reduction of the complications in the normal tissues and an escalation of the dose in the target volume (Al-Mamgani, A. *et al*, 2009; Seco, J. *et al*, 2016).

In order to deliver a conformal dose distribution, advanced radiotherapy techniques require a complex treatment planning process and an intricate beam delivery system, which frequently involves an MLC with daedal leaf motion sequences

(Seco, J. *et al*, 2016). Consequently, as the radiotherapy treatment techniques get more advanced/complicated, the quality assurance (QA) programs become more important due to the increase in the probability and severity of the consequences associated with errors (Hoskin, P., 2012).

2.6.3.1.) Three-Dimensional Conformal Radiation Therapy (3DCRT)

The three-dimensional conformal radiation therapy (3DCRT) is a technique that employs multiple beams. Each radiation field has a uniform intensity and is conformed to a treatment area defined by the PTV contour, as seen by an observer positioned in the location of the radiation source (perspective known as the Beam's Eye View (BEV)). The field conformation is frequently performed by the MLC, or via custom blocks made of a metal with high density. This technique enables the safe use of higher radiation levels in the treatment of the patient, leading to an improvement in cell death and tumors shrinkage. As a result, 3DCRT provides better cure, or palliation, rates when compared to the general techniques (Berbeco, R. I., 2017; Esquivias, G. B. *et al*, 2015; Melman, A. *et al*, 2011; Selby, K., 2018; Silberman, H. *et al*¸ 2009).

2.6.3.2.) Intensity Modulated Radiation Therapy (IMRT)

Intensity modulated radiation therapy (IMRT) represents an evolution of the 3DCRT in terms of attainable plan quality, for the reason that each irradiation field in IMRT has a variable intensity, besides being conformed to the target. Therefore, this is a very precise technique that allows the delivery of high radiation doses to the target volume, as well as the reduction of the energy deposited in the neighboring healthy tissues (Chiu, A. G. *et al*, 2011; Mundt, A. *et al*, 2005; Pardee, A. B. *et al*, 2009).

In IMRT the radiation beam is modulated by the computer controlled MLC leaves. The modulation can be interpreted as the division of each beam in small and geometrical subfields, called beamlets. Every individual segment has a given weight, i.e. intensity level, which represents the contribution of that specific beamlet for the total dose delivered to the patient during its irradiation (Beri, S. *et al*, 2010; Taylor, A. *et al*, 2004; Zhang, G. *et al*, 2005). The weight and dimensions of the beamlets are calculated by the TPS algorithm, which also determines the motion of the MLC leaves required to achieve the desired dose distribution (Bortfeld, T. *et al*, 2006; Levitt, S. H. *et al*, 2012).

IMRT can be carried out through two different techniques, namely step-and-shoot and sliding window. In both approaches the prescribed dose is delivered to the patient from a discrete number of gantry angles. However, in sliding window the beam is kept on while the MLC leaves slide across the exit window of the gantry at different rates, creating a continuous fluence pattern. On the other hand, in step-and-shoot the MLC leaves are stepped in a set of discrete conformations and the beam is only turned on when the leaves are motionless at each location, therefore a fluence pattern with a discrete number of levels, equal to the number of steps performed, is obtained (Fuente, T. D. L. *et al*, 2013; Halperin, E. C. *et al*, 2013; Khan, M. I., 2015; Lafond, C. *et al*, 2010).

IMRT requires a more complicated treatment planning process than 3DCRT due to the modulation of the radiation beams by the MLC. In both techniques the radiation oncologist delineates the volumes to treat and to protect, and prescribes the dose to the target volume. However 3DCRT involves a forward planning process, as opposed to IMRT where a different treatment planning method, known as inverse planning, is frequently employed (Gunderson, L. L., 2015; Kuppusamy, T., 2017; Levitt, S. H. *et al*, 2012).

The fundamental difference between these two planning processes is that in the forward planning the dosimetrist must select and optimize the number of radiation beams to use, the gantry angles that each beam will be delivered from, the use of wedges, and the MLC configuration for each specific beam, in order to achieve an adequate dose distribution (Chin, L. S. *et al*, 2015; Gunderson, L. L. *et al*, 2015). On the other hand, in the inverse planning process the dosimetrist gives target doses and importance factors for each structure and, subsequently, an optimization algorithm is run to determine the treatment plan best suited to the imposed conditions (Gunderson, L. L. *et al*, 2011; Washington, C. M. *et al*, 2015.).

2.6.3.3.) Volumetric Modulated Arc Therapy (VMAT)

Volumetric modulated arc therapy (VMAT) is an advanced radiotherapy technique first introduced in 2007 and implemented clinically in 2008, by the marketing of RapidArc® (Varian), Elekta VMAT, and SmartArc (Philips). In VMAT, a LINAC equipped with an MLC delivers a precisely shaped three-dimensional dose distribution by executing a rotation of the gantry around the patient, while continuously irradiating the individual. This ability to irradiate a given volume through continuous rotation of the radiation source is commonly called arc therapy (Olsson, H., 2017; Teoh, M. *et al*, 2011; Unkelbach, J. *et al*, 2015). Nowadays it is possible to treat the whole target

volume, from a full 360° beam angle, in one or two arcs, though complex cases may need more (Teoh, M. *et al*, 2011).

The three-dimensional modulation of the radiation in VMAT is achieved by performing simultaneous and quick adjustments of three factors, namely: gantry rotation speed; treatment aperture shape, which is defined by the MLC orientation as well as the movement of the MLC leaves; and dose rate. As a result, the creation of VMAT treatment plans for the clinical practice requires a more complex TPS (Esquivias, G. B. *et al*, 2015; Teoh, M. *et al*, 2011; Unkelbach, J. *et al*, 2015).

One of the main advantages associated with VMAT is the reduced treatment time, because, as opposed to IMRT approaches during which the equipment has to rotate various times around the patient or make repeated starts and stops to treat the tumor from different angles, this technique can deliver the dose to the target volume in a continuous rotation of the gantry, maintaining the beam on during the whole process. Consequently, a full VMAT treatment session usually takes less than two minutes to perform, minimizing the probability of patient movement during the irradiation, reducing some discomfort that the patient may have throughout the process, increasing the number of patients treated by the LINAC, and delivering a more conformal dose to the target in a smaller time interval, which can increase the tumour control probability (TCP). VMAT also provides a high dose conformity to the target and a significant sparing of the neighboring healthy tissues (Cox, J. D. *et* al, 2010; Deng, Z. *et al*, 2017; French, S. B. *et al*, 2017; Masi, L. *et al*, 2010; Sood, S. *et al*, 2017; Teoh, M. *et al*, 2011).

As the treatment complexity increases, the pre-treatment patient-specific quality assurance (QA) becomes more important. Therefore, due to the totally dynamic implementation and to the different method of operating the LINAC in VMAT, a precise dose delivery must be guaranteed by patient specific QA programs in order to ensure safety to the patient and treatment effectiveness. The QA programs must contain both machine general and specific performance checks, as well as verification of treatment plans by measurements of delivered dose distributions (Masi, L. *et al*, 2010; Natali, M, *et al*, 2012; Schreibmann, E. *et al*, 2009).

Generally, the treatment plan created for the patient is calculated and delivered in QA dedicated phantoms. Then, the dose distribution measured in the phantom is compared with the one planned by the TPS (Elith, C. A. *et al*, 2014; Ozyigit, G. *et al*, 2017). The evaluation of the equivalence between the TPS calculated and the measured (2D/3D) dose distribution is commonly performed by the gamma index (section 2.7.3.)) (Podesta, M., 2014).

2.6.4.) Patient Positioning in External Beam Radiotherapy

The radiotherapy process requires precision and accuracy in all stages. With the introduction of advanced radiotherapy techniques, which allow the delivery of highly conformal dose distributions, it is possible to accurately deliver the prescribed dose to the target volume with improved sparing of organs at risk. To achieve this goal, accurate and reproducible patient positioning is fundamental due to the reduced safety margins typically employed in this type of treatment plans (Walter, F. *et al*, 2016; Abdallah, Y. M. *et al*, 2011). Therefore, the positioning tools associated with the treatment unit must be precisely calibrated to allow the setup of the patient in the treatment couch with the minimum possible operator uncertainty. This lack of accuracy typically exists due to various factors, such as the strcuture and motion of the anatomy, the beam geometry, and the setup of the patient (Frøseth, T. C. *et al*, 2015; Hwang, U. *et al*, 2016).

The first step associated with the patient positioning process consists in acquiring a planning computed tomography (CT) and making tattoos on the skin of the individual, using the LASERs present in the CT room. In order to position the patient in the LINAC's couch, these tattoos will be aligned with the LASERs existing in the treatment room. The light field can also be used in this process (Cherry, P. *et al*, 2009; Lyatskaya, Y. *et al*, 2006; Njeh, C. F. *et al*, 2012; Skrzyński, W., 2004). There are also various advanced imaging devices that allow a more accurate patient setup, such as for example electronic portal imaging device (EPID), kilovoltage (kV) radiography/fluoroscopy, kV computed tomography (CT), cone beam CT, megavoltage CT, and magnetic resonance imaging (MRI). However, these techniques may imply an increase of the dose received by the patient and/or in the occupation time of the LINAC. Therefore, the LASERs continue to be the main instrument used to position the patient in the treatment couch. As a result, they must be precisely aligned with the LINAC's isocenter to avoid unexpected false results from the QA and to minimize the patient positioning uncertainty (Goyal, S. *et al*, 2014; Hwang, U. *et al*, 2016; Lecchi, M. *et al*, 2008; Poirier, Y., 2014).

There are some positioning techniques available in radiotherapy that can monitor the setup of the patient during the treatment course, such as image guided radiotherapy (IGRT) and real-time position management (RPM) (Shi, C. *et al*, 2007). IGRT consists in acquiring information about the size, shape, and position of the target and neighboring tissues, through images obtained at the pre-treatment and treatment delivery stage. This data is then compared against reference imaging, and corrections

in the patient's position are performed, if necessary (Chen, G. T. Y. *et* al, 2009; Goyal, S. *et al*, 2014; Gupta, T.; National Cancer Action Team, 2012; Podgorsak, E. B., 2005).

RPM allows the match between the tumour position and the patient's respiratory cycle and is particularly useful in lung, breast, and upper abdominal cases. Essentially, the system measures the patient's respiratory cycle and the consequent range of movement, displaying them as a waveform. The gating thresholds are then established when the tumor is in the wanted phase of the measured respiratory cycle. These thresholds control when the gating system turns the beam on and off (Goharian, M. *et al*, 2010; Sung, K., *et al* 2014; Tsunashima, Y., 2012).

2.6.4.1.) Positioning Mismatch

A downward trend in radiotherapy accident rates has been indicated by various reports (Bissonnette, J. P. *et al*, 2010 and Clark, B.G. *et al*, 2010), nevertheless severe incidents with harmful effects for the patient, including death, have been reported and received public attention (Yan, G. *et al*, 2013). Clinical setup mismatches, defined as the difference between the actual and the planned position of the patient in the treatment couch, are one of the main causes of accidents in radiotherapy. These deviations lead to imprecise dose deliveries that can result in significant underdoses to the target volume, which contribute to tumor recurrence and treatment failure, as well as in overdoses to the healthy tissues, therefore increasing the probability of complications for the patient (van Dyk, J. V. *et al*, 2014; Yan, G. *et al*, 2013).

Clinical setup deviations can been classified into systematic and random. The systematic contributions are similar between different treatment fractions, consequently they can be anticipated and accounted for. These shifts are caused by various factors, such as changes in the position of the patient's internal organs, modifications in the tumour shape and size, alterations in the target's position relative to the skin tattoos, or the acquisition of the planning CT scan on a different couch than the one existing in the treatment room. The random errors, unlike the systematic inaccuracies, vary between different treatment fractions, as a result they cannot be predicted or compensated beforehand. These random deviations can be caused by several aspects, for example day-to-day variations in the patient's setup during the course of the irradiation, uncertainties associated with the treatment and positioning equipment, or different patient positioning methodologies between the treatment fractions (Pehlivan, B. *et al*, 2008; The Royal College of Radiologists, *et al*, 2008; Suzuki, J. *et al*, 2012).

There are three correction procedures usually employed for the minimization of these setup errors, namely online correction, real-time correction, and offline correction

(Suzuki, J. *et al*, 2012). In the online strategy, which is performed with the patient lying on the couch before or during the irradiation, an image of the setup is acquired and compared to a reference image. Subsequently, the difference between both is quantified and, based on that information, an operator can perform adjustments to the patient's position. The online correction has the advantage to reduce both systematic and random errors, however it implies the delivery of an additional dose to the patient, a higher level of integration between software and hardware, and fast processing speed. This approach also increases the treatment time, because during the error quantification process the patient is on the treatment couch, but the LINAC is not performing the plan (Mansson, S., 2004; Maqbool, M., 2017; Pawlicki, T. *et al*, 2010; Timmerman, R. D. *et al*, 2009).

The real-time correction process is similar to the online method, however in this strategy the positioning adjustments are performed automatically, i.e. without the intervention of an operator, as the radiation is being delivered. These corrections are based on data provided by a real-time tracking system, or thru images obtained throughout the treatment course. This procedure guarantees a faster rectification of the positioning mismatches during the treatment fraction, but it implies a higher dependence and reliability on the automation systems when compared to the online technique (Dieterich, S. *et al*, 2015; Hoppe, R. *et al*, 2010; The Royal College of Radiologists, *et al*, 2008).

In the offline approach an image of the setup is acquired during each of the first fractions of the treatment, e.g. 2-5 fractions. This information is subsequently used to determine the average positioning mismatch of the patient, which will be employed in the correction of the setup in the following treatment fractions. The offline strategy corrects the mean systematic error of the patient's positioning, but it does not compensate for the daily variations (random errors) associated with the setup. The main advantages of this method are the reduction of the imaging dose and the modest workload, which provides a more efficient approach for routine treatments in a busy department by decreasing the time required for image acquisition and analysis. However, besides not correcting for the random errors, this process requires a reproducible and accurate initial patient setup in order to be properly performed (Brock, K. K., 2013; Kusters, J. *et al*, 2009; Li, X. A., 2011; Mansson, S., 2004; Suzuki, J. *et al*, 2012).

2.6.4.2.) Adaptive Radiation Therapy

If a given positioning mismatch or a certain anatomic and/or physiologic change of the individual occurs in a fraction of the radiotherapy treatment, the planned dose distribution is going to be modified in a specific way. Therefore, even if that particular deviation is corrected in the following irradiation sessions, the application of the same plan during the remaining treatment will not compensate for the dose difference received by the various volumes, due to that clinical setup mismatch (Lim-Reinders, S. *et al*, 2017; Thörnqvist, S. *et al*, 2016).

Adaptive radiation therapy appears in this context as a way to adapt a particular treatment plan to patient-specific variations not considered in the initial planning (Lim-Reinders, S. *et al*, 2017; Thörnqvist, S. *et al*, 2016; Yan, D., 2010). This approach consists in evaluating the treatment dose, describing the patient-specific variations, and then including the planned dose distribution for the volumes of interest and the variation characteristics in the treatment control through an adaptive planning optimization, in order to generate a new plan best suited for the radiotherapeutic goal (Böck, M. *et al*, 2017; Yan, D., 2010).

This adaption can be performed offline, where, after the daily treatment fraction, a new plan is created by the adjustment of the dose distribution to the anatomic changes identified on sets of cone-beam CTs (CBCTs), or regular CTs, acquired in irradiation fractions or separate imaging sessions. The generated plan is then performed in the following treatment session(s) (Foroudi, F., 2009; Ghilezan, M. *et al*, 2013; Yang, C. *et al*, 2014). An online adaptive radiotherapy approach is also possible, consisting in the creation a new treatment plan based on deviations observed in images of the patient acquired just before the irradiation. This plan is then applied for that specific treatment fraction. Offline and online adaptive radiotherapy techniques have similar advantages and disadvantages to the offline and online patient position correction procedures, respectively (section 2.6.4.1.) (Foroudi, F., 2009; Lim-Reinders, S. *et al*, 2017; Yang, C. *et al*, 2014). Another strategy used in adaptive radiation therapy is the real-time adaption, which is performed by intertwining the imaging process and the treatment session (Hoppe, R. et al, 2010). This technique consists in adapting the beam during the treatment delivery, i.e. in a real-time replanning, to account for the intrafraction motion of the patient. The real-time approach is a complex method of adaption, demanding more imaging; quicker decisions; and more confidence on the system for guidance, plan modifications, and dose delivery to moving targets (Hoppe, R. et al, 2010; Mijnheer, B., 2017; Timmerman, R. D. *et al*, 2009).
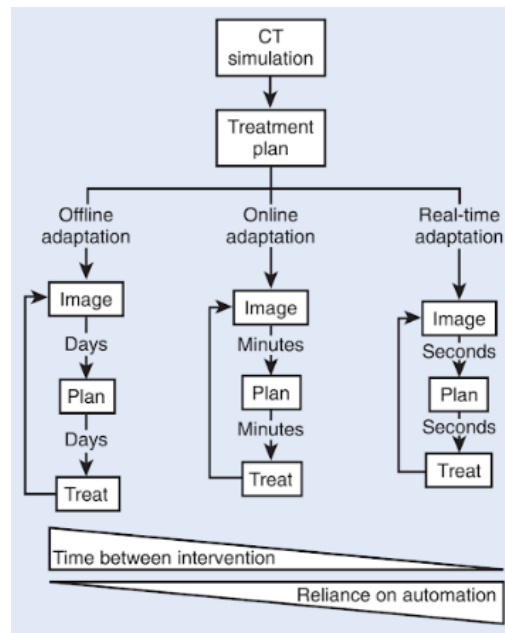
Figure 21 - The various adaption methods for radiotherapy and the required time and automation associated (Hoppe, R. et al, 2010).

2.7.) Computer Simulations in External Beam Radiotherapy

In radiotherapy the patient cannot be used as the subject of experiments and, in most situations, it is not possible to measure the exact dose delivered to a specific organ because the dosimeter would have to be in contact with that structure. Therefore, computer simulations are particularly useful in radiotherapy because they allow the prediction of the dose distribution delivered to the patient, as well as the assurance that the individual will receive the planned dose distribution, without the need to irradiate real patients. An important point to keep in mind is that these calculated dose distributions are estimates, consequently the actual dose distribution delivered to the patient can differ from the calculated one in a greater or smaller quantity, depending on the accuracy of the calculation (Paganetti, H., 2012; Rath, A. K. *et al*, 2016; Seco, J. *et al*, 2016).

Nowadays, there are various computational algorithms that simulate the radiation transport in matter through different methodologies, such as correction-based methods, model-based methods, and Monte Carlo methods (Seco, J. *et al*, 2016). Currently, the Monte Carlo approach is widely accepted as the gold standard technique to perform dose calculations in radiotherapy (Esposito, A. *et al*, 2018).

2.7.1.) The Monte Carlo Method

The Monte Carlo method is a statistical technique applied in various distinct areas, ranging from finance to medicine, and capable of simulating complex problems that include several random processes with known, or assumed, probability density functions. These random processes are simulated through the use of random numbers, or, more precisely, pseudorandom numbers (Haghighat, A., 2014; Rometsch, M, 2008). A general perspective of the Monte Carlo method as described by Seco, J. *et al*, 2016 is: *the Monte Carlo method provides a numerical solution to a problem that can be described as a temporal evolution[1] of objects[2] interacting with other objects based upon object–object interaction relationships[3]. (…) the rules of interaction are processed randomly and repeatedly, until numerical results converge usefully to estimated means, moments, and their variances.*

In radiotherapy, the Monte Carlo method is used to simulate the trajectories of millions of individual particles traversing a target and, consequently, to estimate the total dose deposited in the medium by random sampling the interactions of particles and their transport within matter (Ziegenheim, P. *et al*, 2015). Throughout the years, extensive benchmarks with different geometries have been performed in order to assess the accuracy of the dose calculations obtained with this technique (Ojala, J. J. *et al*, 2014). From various studies, the general conclusion is that the Monte Carlo method is the most accurate technique for calculation of the dose distribution delivered within the patient (Jabbari, K., 2011; Paganetti, H., 2014; Seco, J. *et al*, 2016). However, the high processing time required is a major drawback of this approach. Nevertheless, recent advances in computational techniques and methods have made it practical for specific clinical applications, namely for treatment plan verification in complex or dubious cases, even though the required time still makes it unfeasible for the TPS engine used in the clinic (Chetty, I. J. *et al*, 2007; Lin, H. *et al*, 2016; Seco, J. *et al*, 2016).

2.7.1.1.) Simulating Radiation Transport

When electrons, photons, positrons, or other types of particles pass through a medium they lose energy, are deflected, and possibly produce secondary particles in the course of subsequent individual collisions (Salvat-Pujol, F., 2014). The transport of

---

[1] translation/reflection/mutation
[2] "quantum particles" : photons, electrons, neutrons, protons, charged nuclei, atoms, and molecules; in the case of medical physics
[3] cross sections

particles within matter is governed by a set of differential cross sections, which determine the probability density functions (PDFs) of the random variables associated with the radiation penetration in matter, such as distance travelled between successive interactions, type of interaction, angular deflection, and energy loss. A detailed quantitative knowledge of these interaction probabilities allows the simulation of the radiation transport through matter (Geant4 Collaboration, 2017; Li, Y. G. *et al*, 2011; Salvat, F., 2015; Salvat-Pujol, F., 2014).

The interaction of radiation during its passage in a medium is analytically modeled by the Boltzmann transport equation, however the solution of this equation is hard in simple geometries and impossible in complex ones. Nevertheless the Monte-Carlo sampling techniques can be employed to simulate an ensemble of particle trajectories, based on the relevant interaction cross sections, and thus easily and efficiently solve the problem of radiation transport through matter (Chao, A., 2013; Salvat-Pujol, F., 2014).

In the Monte Carlo simulations involving radiation transport within a medium, the history of a particle is interpreted as a random sequence of "free flights", each one ending with an interaction that can modify its energy, original direction, and possibly originate secondary particles (Omer, M. O. M. E., 2014). The usual steps performed by the Monte Carlo simulation method are (Kajaria, A. *et al*, 2013; Salvat, F., 2015.; Seco, J. *et al*, 2016; Seegenschmied, M. H. *et al*, 2008; Ziegler, J. F., 2012):

1) Each individual particle is created at an initial position, with a certain energy and a given direction of flight;

2) The distance of the "free flight" to the next collision event is sampled from a PDF, which depends on the mean free path of that particular particle in that specific medium. The particle moves the sampled distance along a straight line, in the determined direction of flight, to the location where the next interaction with the medium occurs;

3) The type of interaction is selected from the point probabilities associated with the cross sections of the interaction mechanisms considered;

4) At the interaction location the selected interaction is simulated:

    a. If absorption occurs, the particle tracking is terminated;

    b. Else, the energy loss as well as the change in direction of the particle are sampled, and the eventual secondary particles are generated;

5) If the energy of the particle is still higher than an established energy threshold or if the particle still is inside the medium, the process starts over at step 2), otherwise:

6) The particle tracking stops if it leaves the medium or if its energy becomes lower than a given energy limit.

The secondary particles produced during this process are simulated in a similar way and the simulation of these particles in conjunction with the primary one, which originated them, is often known as a particle history, or "shower" (Seco, J. *et al*, 2016; Zilles, A., 2017). The simulation process described from steps 1) to 6) is called the analogue Monte Carlo method (Bird, G. A., 2009; Kim, S., 2006).

In Monte Carlo, the sampling depends on an easily computed random number generator (RNG) that should be able to generate many millions of random numbers. However, most generators compute pseudorandom numbers, which copy the behavior of true random numbers, but are produced in a deterministic and foreseeable form. This occurs because it is difficult to generate true random numbers with the actual computational resources. The RNG should also pass various statistical tests of randomness, for example if the order of numbers generated is repeated after a period, that period must be long (Lötdstedt, P., online publication; Srinivasan, A. *et al*, 2003; Swenson, C., 2008). One RNG frequently used is the linear congruential generator (LCG), whose formula is:

$$X_{n+1} = (aX_n + c) \bmod m \qquad (16)$$

where a is the multiplier, c is the increment, m is the modulus and X_0 is the seed (Brandt, S., 2014).

2.7.1.1.1.) Variance Reduction

The Monte Carlo method numerically estimates the tracks of the particles within matter, hence there is always some statistical uncertainty associated with this process due to the randomness involved. This imprecision can be minimized by increasing the number of simulated histories, which will also increase the calculation time, or by using variance reduction techniques, which in turn can decrease the simulation time (Mukhopadhyay, N. D. *et al*, 2012; Su, L. *et al*, 2014).

The computational efficiency associated with the Monte Carlo simulation method, ε, is often defined as:

$$\varepsilon = \frac{1}{\sigma^2 T} \qquad (17)$$

where σ is the variance on the quantity of interest and T is the computing time necessary to obtain a variance of σ^2 (Seco, J. *et al*, 2016). From equation (17) it is possible to conclude that for the same variance, a faster simulation has a higher efficiency than a slower one, or, from a different point of view, for the same simulation time a lower variance represents a higher efficiency. Consequently, in order to increase the simulation efficiency it is necessary to decrease the computing time needed to obtain a sufficiently small variance on the quantity of interest, which is frequently done using variance reduction techniques (Louvin, H., 2017; Lux, I. *et al*, 2017; Seco, J. *et al*, 2016).

Some of the common variance reduction techniques are: splitting-roulette, forced interaction, and particle splitting (Mohammed, M. *et al*, 2016).

Particle splitting consists in dividing (splitting) an individual particle, for example a bremsstrahlung photon, into similar particles in the same state that are tracked individually, leading to an increase of the sample size. Therefore if the initial particle has a weight w_0, each particle produced by the splitting will have a statistical weight $w = \frac{w_0}{S}$, where S is the number of identical particles created by the splitting, also known has splitting factor (Haghighat, A., 2014; Ragheb, M., 2013; Seco, J. *et al*, 2016). This process is commonly defined as simple splitting, however other types of splitting can be used, such as rotational splitting (Brualla, L. *et al*, 2010). The rotational splitting method is similar to the simple splitting technique, but it can only be used when the radiation beam and geometry of interest are cylindrically symmetric, which is true for the upper part (i.e., above the jaws) of most LINACs. In rotational splitting, each particle copy is rotated about the central beam axis through a constant azimuthal angle, providing the ability to perform a faster calculation of each particle shower and a reduction of the statistical noise, as demonstrated by Brualla, L. *et al*, 2010 (Bush, *et al*, 2007).

Russian roulette is a technique that can be seen as the opposite of particle splitting. Its objective is to "kill" particles that probably will not contribute to the detector reading, therefore saving computing time (Vassiliev, O. N., 2016). Just like particle splitting, this method can be applied at an interaction point, when secondary particles are produced, or when a particle goes into a volume of interest. In russian roulette, a survival probability $p \ll 1$ must be assigned to each kind of particle and then a random number, γ, is sampled from an uniform distribution in the interval [0, 1]. If $\gamma > p$ the particle is "killed" and its simulation stops, else the particle is allowed to survive at its weight is increased by $\frac{1}{p}$ (Seco, J. *et al*, 2016; Vassiliev, O. N., 2016).

Splitting-roulette is another method that can be employed to reduce the variance, and, as the name indicates, it is a combination of particle splitting and Russian roulette techniques. This method increases the dose calculation efficiency through the application of the Russian roulette to electrons, and the particle splitting to photons that they originate (Brualla, L. *et al*, 2018; Rodriguez, M. *et al*, 2012)

Occasionally, a high variance results from an extremely low photon interaction probability within the medium, in such case the forced interaction variance reduction technique can be useful. This method artificially increases the probability of photons' interaction with matter, diminishing the particles that do not interact, and consequently decreasing the computing time. However, to keep the simulation unbiased, the weight assigned to each particle needs to be suitably modified, since among each pair of "real" events there will be a certain amount of forced interactions (Kling, A. *et al*, 2001; Seco, J. *et al*, 2016; Vassiliev, O. N., 2016).

2.7.1.2.) Dose Scoring Geometries

The computational calculation of the dose delivered to a given geometry is based on voxels. The term voxel refers to a "volumetric pixel", i.e. a 3D pixel, and in dose distribution calculations it defines a given element in a regular grid that segments the simulation volume (figure 22) (Seco, J. *et al*, 2016; Wrenninge, M., 2012).
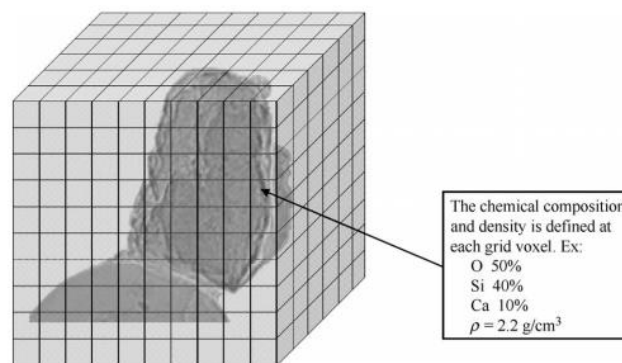
Figure 22 - 3D grid of cubic voxels used to segment a given geometry (adapted from Bottigli, U. *et al*, 2004).

After the segmentation of the volume of interest, the dose calculation method scores the dose deposited in each geometrical voxel by all the contributing particles (e.g., photons, electrons, etc.), taking into account the specific composition and characteristics of each 3D pixel. This information is acquired through the CT performed by the patient/phantom during the treatment planning process (Dössel, O. *et al*, 2010; Seco, J. *et al*, 2016).

Different types of scoring geometries can be employed for three-dimensional (3D) dose calculations, being the cubic or parallelepiped voxels the most commonly used (Seco, J. *et al*, 2016).

2.7.2.) Monte Carlo Codes

Throughout the years several general purpose MC codes have been developed for radiation transport simulation in the field of radiotherapy, such as PENELOPE, EGSnrc, MCNP, and GEANT4 (Stathakis, S. *et al*, 2016). A general purpose MC code should consider all the characteristics of the electron and photon transport in a given medium and be capable to produce precise results in a heterogeneous phantom, such as those used in medicine (Botta, F., 2011; Jabbari, K., 2011). PENELOPE and EGSnrc can simulate the transport of different energies of electrons, positrons, and photons, which are the particles more commonly produced by LINACs. Other codes, such as GEANT4 and MCNP can simulate additional types of particles, such as protons, neutrons, and heavy ions, which may be important to study the radiological protection of the patient in the treatment room or to investigate external radiotherapy techniques not involving LINACs, e.g. proton therapy. Nevertheless, neutrons are produced in a LINAC operating at higher energies (above 10MeV) and no reports were found about the production of other types of particles in a conventional LINAC, therefore these less frequent particles will not be considered in this thesis (Beigi, M. *et al*, 2016; Naseri, A. *et al*, 2015; Sadoughi, H. *et al*, 2013; Seco, J. *et al*, 2016).

2.7.2.1.) PRIMO

PRIMO is a software designed for Monte Carlo simulations in the area of external radiotherapy, not requiring extensive programing or computing knowledge from the user and providing simulation geometries for most of the commercially available Varian LINACs. This program can simulate the radiation transport through the entire LINAC head and binned in slab phantoms, created within the software, or imported CTs (Brualla, L. *et al*, 2016; Brualla, L. *et al*, 2018; Miras, H. *et al*, 2017).

Two simulation engines are provided by PRIMO: one based on the general–purpose Monte Carlo code PENELOPE 2011 combined with the program penEasy (a modified version of release 2012-06-01) and with penEasyLinac; and the Dose Planning Method (DPM) (version 1.1), which is a fast Monte Carlo algorithm for the simulation of electron–photon showers in external radiotherapy. These simulation engines are associated with a graphical user interface (GLASS - Graphical Layer for

the Automation of the Simulation System) that encompasses all the codes in a single user-friendly environment, making PRIMO simple and intuitive to use, unlike other codes available for the Monte Carlo simulation of the radiation transport in matter (Brualla, L. *et al*, 2018; Castillo, M. L. R., 2015; Hermida-López, M. *et al*, 2018). A schematic diagram of the simulation engine based on the PENELOPE 2011 code provided by the software is represented below:
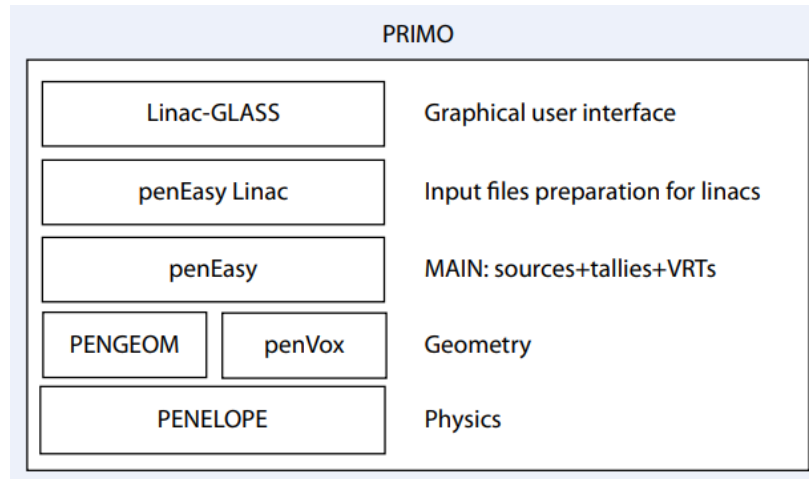
Figure 23 - Schematic diagram representing the layered structure of the simulation engine based on PENELOPE 2011 provided by PRIMO (adapted from Rodriguez, M. *et al*, 2013).

At the start of a new PRIMO project the user must define the ID and the name of the project, select the LINAC model, and choose the type of radiation to use (either photons or electrons). The information about the modeling of the components present in the LINAC head is already included in the software and it is not possible to modify it, or add new structures (Brualla, L. *et al*, 2016). Afterwards, the graphical interface of simulation is presented, being divided in 3 segments, namely s1, s2, and s3. In s1 the user can specify several parameters in order to create a new phase space file, which is tallied in a plane located at the downstream end of the LINAC upper part. This phase space contains the complete information about all the particles in the mentioned plane, namely the particle type, energy, position in Cartesian coordinates (x, y, z), statistical weight, direction cosines (u, v, w), and some additional variables (Brualla, L. *et al*, 2018; Cortés-Giraldo, M. A. *et al*, 2012). The parameters that can be adjusted in s1 are related to the primary beam, these are: energy, full width at half maximum (FWHM) of the energy distribution, FWHM relative to the focal spot, and divergence. PRIMO suggests a set of initial values for the various parameters when a nominal beam energy is selected, however the user can regulate them in order to improve the match between the simulated and the measured results (Brualla, L. *et al*, 2018; Castillo, M. L. R., 2015). In this section, it is also possible to select various variance reduction techniques, such as forced interaction in the target and splitting above the jaws (simple

splitting, rotational splitting, or splitting-roulette) (Brualla, L. *et al*, 2018). Besides simulating/creating a new phase space file, PRIMO allows the user to import or link a previously simulated phase space file in the IAEAPHSP format to the s1 segment (Brualla, L. *et al*, 2018).

In s2 it is possible to select the parameters of the treatment fields, such as number, size, presence or absence of MLC, and type of MLC. The user can also choose the type of electron applicator (electron mode) as well as the angles of the gantry, the collimator, and the couch. The position of the MLC leaves can be imported from a text file (Brualla, L. *et al*, 2018). A new version of PRIMO, released on 1st February, 2018 and used throughout this work, allows the simulation of treatment plans designed for advanced radiotherapy techniques, namely IMRT and VMAT. The user cannot manually create these complex plans on PRIMO, nevertheless they can be generated in the TPS, generally through an inverse planning process, and subsequently imported at this segment. Other new feature introduced in this version of the software is the use of control points, which can be interpreted as the way to discretize the continuous adjustment of the various parameters, performed by the LINAC, during IMRT or VMAT techniques. Each one of these points contains information about the gantry angle, the shape and angle of the MLC, the jaws position, and its weight. Nevertheless, the parameters of the control points are not editable in the graphical user interface (Brualla, L. *et al*, 2018; Goraf, A. *et al*, 2012; Jia, X. *et al*, 2015; Seco, J. *et al*, 2016). At the end of this segment a new phase space is generated, which is tallied in a plane located at the downstream end of the patient-independent portion of the machine (Brualla, L. *et al*, 2018).

The simulation of the interactions between the particles previously simulated and the phantom, or the patient, is performed in segment s3. The default simulation structure is a water phantom of dimensions 40.5cmx40.5cmx40cm, (x, y, z), with a bin size of 0.5cm. However, it is possible to create a slab phantom with various materials provided by PRIMO or import a computed tomography (CT) of a patient or a phantom. Here, the patient/phantom model is always defined by a 3D matrix. In this segment, the user can also adjust the SSD and the isocenter location (Brualla, L. *et al*, 2016; Brualla, L. *et al*, 2018; Castillo, M. L. R., 2015).

For plans involving two or more radiation fields, it is not possible to tally a phase space at s2 for the reason that the angles of the gantry, collimator, and table angles are not saved in that file. As a result, for these cases the user must simulate segments s2 and s3 in conjunction (Brualla, L. *et al*, 2018).

The yield of the s3 segment is a dose distribution in the patient, or phantom, described by percentage depth doses (PDDs), transverse and diagonal profiles, and dose-volume histograms (DVHs). These curves can be analyzed with a tool provided by PRIMO that employs the gamma index (section 2.7.3.). Therefore, it is possible to use the software to compare and evaluate the differences between dose distributions (Brualla, L. *et al*, 2018; Rodriguez, M. *et al*, 2013).

2.7.3.) The Gamma Index

In order to validate a simulation, or perform pre-treatment patient-specific QA, a meaningful comparison between simulated and measured (reference) dose distributions is needed. One evaluation method commonly used is the gamma index, which is currently provided by PRIMO (Li, H. *et al*, 2011; Sarkar, B. *et al*, 2015).

This tool uses the dose difference (DD) and the distance-to-agreement (DTA) parameters to compare two dose distributions (Osorio, E. M. V. *et al*, 2011). The DD is adequate to compare dose regions with low gradient, however in areas of high dose gradient a small spatial deviation between calculated and measured values leads to a large dose difference between the two distributions. As a result, considerable dose differences in steep dose gradient regions may be relatively inconsequential in the final result (Low, D. A. *et al*, 1998; Sarkar, B. *et al*, 2015). Therefore, the DTA concept was introduced to compare these high gradient regions (Chen, M. *et al*, 2009). According to Low, D. A. *et al*, 1998, the DTA is: *… the distance between a measured data point and the nearest point in the calculated dose distribution that exhibits the same dose*. The DD and DTA complement each other when assessing the dose distribution calculation quality, even though they are insufficient in the evaluation when used individually (Chen, M. *et al*, 2009; Low, D. A. *et al*, 1998). Based on these parameters, Low, D. A. *et al*, 1998, introduced the gamma index concept through the combination of the DD and the DTA in a single measure normalized by two acceptance criteria (Chen, M. *et al*, 2009; Schreiner, L. J., 2013). These acceptance criteria express an ellipsoid in a space composed of dose and spatial coordinates, which is defined as (Low, D. A. *et al*, 1998):

$$\Gamma(r_m, r_c) = \sqrt{\frac{r^2(r_m, r_c)}{\Delta d^2} + \frac{\delta^2(r_m, r_c)}{\Delta D^2}} = 1 \qquad (18)$$

where $r(r_m, r_c) = |r_c - r_m|$ is the spatial distance between the measured and calculated dose points, $\delta(r_m, r_c) = D(r_c) - D(r_m)$ is the dose difference between those same points, ΔD is the DD criterion, and Δd is the DTA criterion (Low, D. A. *et al*, 1998). Then, the pass-fail criterion becomes (Low, D. A. *et al*, 1998):

➢ $\gamma(r_m) \leq 1$: the point passes the criteria;

➢ $\gamma(r_m) > 1$: the point fails the criteria.

Consequently, the gamma index allows the determination of the regions where the dose distributions coincide and where they differ, on a point-by-point basis, as well as the quantification of those differences (Pulliam, K. B. *et al*, 2014).

2.8.) Quantitative Analysis of Normal Tissue Effects in the Clinic (QUANTEC)

The Quantitative analysis of normal tissue effects in the clinic (QUANTEC), is a tool resulting from intensive efforts in the radiotherapy community (Lee, T. *et al*, 2013). This initiative contains reviews and summaries about normal tissue toxicity datasets and recommended dose–volume treatment planning guidelines. These allow the clinician to perform a reasonable, but not necessarily accurate, classification of the toxicity risk for a certain tissue.

In the clinical practice, the QUANTEC guidelines for the treatment planning should have some important properties, such as easy to comprehend, simple to implement, and closely associated with the clinical case of interest (Bentzen, S. M. *et al*, 2012; Deasy, J. O. *et al*, 2010; Lee, T. *et al*, 2013; Moiseenko, V. *et al*, 2012).

3.) Objectives

The main objective of this thesis was the investigation, based on the Monte Carlo method for radiation transport simulation, of the dosimetric effects arising from clinical setup mismatches in the VMAT technique

To accomplish this goal various steps were executed. The first objective was the validation of a TrueBeam^{TM} phase space for the photon energy of 6MV with flattening filter. Followingly, the second task consisted in the validation of the HD 120^{TM} MLC model provided by PRIMO and installed in the TrueBeam^{TM} LINAC currently operating at IPOPFG.

With the necessary validations performed, the next goal was to assess the VMAT and IMRT simulation mechanisms used in the new version of the PRIMO software. This was accomplished by measuring and simulating two treatment plans, involving these dynamic treatment techniques, in phantoms and subsequently comparing the measured results against the calculations performed by the TPS and by PRIMO.

After this study, the following step involved the measurement and simulation of two clinical setups, with and without a positioning mismatch, for an abdominal VMAT plan and subsequent evaluation of the obtained results. Subsequently, additional mismatches were simulated for the same plan, in order to investigate the dosimetric effects resulting from those shifts, establish the critical positioning conditions for this specific case, and evaluate the need to consider an adaptive radiotherapy approach.

Bearing in mind this analysis, a protocol for an offline adaptive radiotherapy approach was developed for the TrueBeam^{TM} unit in use at IPOPFG.

4.) Materials and Methods

4.1.) Equipment

4.1.1.) Varian TrueBeam^{TM} Linear Accelerator

Varian TrueBeam^{TM} (Varian Medical Systems, Palo Alto, CA) is a leading edge LINAC currently in use at IPOPFG. The TrueBeam^{TM} system has the capability to dynamically synchronize imaging, patient positioning, motion management, and treatment delivery. This fully-integrated platform allows the realization of several advanced radiotherapy techniques, such as VMAT (RapidArc^{TM}), IMRT, IGRT, and radiosurgery. It is also possible to operate this LINAC in a FFF mode, defined by Varian as a high intensity mode (section 2.4.)), at the photon energies of 6MV or 10MV (Benedict, S. H. *et* al, 2016; Tang, G. *et al*, 2011; Varian Medical Systems, 2010).

The TrueBeam unit installed at IPOPFG is equipped with a High Definition 120 Multileaf Collimator (HD 120™ MLC), which has 32 pairs of leaves with 2.5mm width in the center and 28 pairs of leaves with 5mm width in the periphery. The maximum static field size for this MLC is 40cm x 22cm (Varian Medical Systems, 2016).

4.1.2.) Phantoms

Three types of phantoms were considered in this work, namely a solid water phantom (PTW RW3 Slab Phantom); a pediatric anthropomorphic phantom with 26 numbered slices of 2.5cm thickness each (ATOM 5 year old, Supertech®); and a water tank.

4.1.3.) Ionization Chambers

An ionization chamber is a detector with a gas-filled cavity that gathers the charges created by ionization of the gas molecules within the hollow, through the application of a potential difference (Knoll, G. F., 2010; Podgorsak, E. B., 2005; Symonds, R. P. *et al*, 2012). Two types of ionization chambers were used in this work, namely the semiflex ionization chamber (PTW Semiflex Ionization Chamber 31010) and the Farmer ionization chamber (PTW Farmer® T30013).

4.1.3.1.) Semiflex Ionization Chamber

The PTW semiflex ionization chamber 31010 has a sensitive volume of $0.125cm^3$ and an inner diameter of 5.5mm. This ionization chamber is mainly projected for 3D dosimetry in motorized water phantoms, having a useful energy range, for photons, from 140kV to 50MV (Abdelaal, A. M. *et al*, 2017; PTW, 2014). The Semiflex ionization chamber was used to acquire the PDDs and transverse profiles, in a water tank, for the different field sizes of the 6MV photon beam, with flattening filter, produced by the TrueBeam[TM] unit installed at IPOPFG.

4.1.3.2.) Farmer Ionization Chamber

The Farmer ionization chamber is a detector frequently used for absolute dosimetry of photon and electron beams in external radiotherapy. PTW Farmer[®] T30013 has a sensitive volume of $0.6cm^3$ and a useful energy range, for photons, from 30kV to 50MV (Followill, D. S. *et al*, 2003; Podgorsak, E. B., 2005; PTW, 2016). In this work, the Farmer chamber was used to perform absolute dose measurements for the different field sizes of the 6MV photon beam, with flattening filter, generated by the TrueBeam[TM] LINAC operating at IPOPFG.

4.1.4.) Radiochromic Film

The Gafchromic[TM] EBT3 self-developing film was employed in this thesis to evaluate the dose distributions delivered to the pediatric anthropomorphic phantom. This specific type of film is composed by an active substrate layer with a thickness of 28μm, which is positioned in the middle of two matte-polyester layers, both with 125μm thickness. The EBT3 is particularly appropriate for high energy photons, having an optimum dose range from 0.2Gy to 10Gy, which is indicated by Gafchromic[TM] as the most appropriate measurement interval of this film for techniques like IMRT and VMAT. Nevertheless, the dynamic dose range for this type of dosimeter ranges from 0.1Gy to 20Gy (Rossi, E., 2017; Vadrucci, M. *et al*, 2015).

4.1.5.) Scanner

An Expression 10000XL scanner (Seiko Epson Corporation, Nagano, Japan) was used to digitalize the irradiated radiochromic films.

4.1.6.) Workstation

All the simulations were performed on a workstation existing at the Center for Applied Photonics (CAP) of Institute for Systems and Computer Engineering, Technology and Science (INESC TEC). This unit has an Intel(R) Core(R) i7-3770 CPU @ 3.40GHz with 32.0GB of RAM and 8 CPU cores available.

4.2.) Softwares and Files

4.2.1.) PRIMO

As already mentioned in section 2.7.2.1.), PRIMO is a software that allows the Monte Carlo simulation of radiation transport in matter. This work was performed with the PRIMO versions 0.3.1.1600 and 0.3.1.1626.

4.2.2.) Treatment Planning System (TPS)

The treatment planning system (TPS) used was Eclipse™ by Varian. For the dose distribution calculations, the analytical anisotropic algorithm (AAA) and the Acuros XB were the algorithms of the TPS employed.

4.2.3.) VeriSoft®

VeriSoft®, by PTW, is a program that provides various dose comparison tools, such as 2D/3D gamma index analysis, allowing the user to perform from simple visual evaluations to meticulous quantitative comparisons between two dose distributions. It also offers visualization options, like multiple dose display options, 2D/3D graphs, zoom functions, and slice sliders, which help the analysis of the measured and calculated data (PTW, 2009). In this work, the version 6.2 of VeriSoft® was used to perform the comparison between the measured and calculated dose distributions through the gamma index analysis.

4.2.4) DoseLab

DoseLab, by Mobius Medical Systems, is a program used for quality assurance of LINACs. According to Mobius Medical Systems, this software comprises tools for AAPM TG-40 / TG-142 routine machine QA, IMRT / VMAT / SBRT QA, log file-based machine QA, as well as radiochromic film analysis.

In this thesis, the DoseLab version 6.4 was mainly used to convert the optical density of the digitalized films to absorbed dose using 24h calibration curves.

4.2.5.) MATLAB®

MATLAB® (matrix laboratory) was developed by MathWorks®. It is a multi-paradigm numerical computing environment as well as fouth-generation programming language, which expresses matrix and array mathematics directly. MATLAB® allows the operator to handle of matrices, perform plots of functions and data, implement algorithms, generate graphical interfaces for the user, and interact with programs written in different languages (The MathWorks, 2006; Underwood, C., 2016). For this work the versions R2016a and R2018a of MATLAB® were used to convert the dose text file exported by PRIMO, as well as the images of the digitalized films, to the DICOM format.

4.2.6.) DICOM files

DICOM stands for Digital Imaging and Communications in Medicine and it is an international standard used to transfer, save, acquire, print, process, and exhibit medical information. This file format is also used by the TPS as a way of communication with the LINAC unit and the Record and Verify system (IAEA, 2013; Pianykh, O. S., 2012; Varma, D. R., 2012).

Different types of DICOM files, exported by the TPS, were used in this work, namely (Jia, X. *et al*, 2015):

> ➢ RP."clinical case name".dcm – contains the information about the treatment plan created for a given patient or phantom in the TPS. It defines geometric and dosimetric parameters related to the treatment plan, such as the field size, the planned dose, the number of beams and their angles, the collimator shapes and angles, the presence or not of a beam modifier, the number of control points as well as their sequence, and the weight of each specific field;

> ➢ RS."clinical case name".dcm – includes the delineated anatomical structures, of a patient or an anthropomorphic phantom, in which the generation of the treatment plan, defined in the corresponding RP file, is based;

> ➢ RD."clinical case name".dcm – represents the dose distribution calculated by the TPS algorithm for the different structures of the patient, or phantom, concercing the treatment plan defined in the correspondent RP file.

4.2.7.) ImageJ

ImageJ is a Java-based image processing and analysis program with an open architecture, which can be extendend through new plugins and recordable macros (Ferreira, T. *et al*, 2011; Kainz, P. *et al*, 2015; Rueden, C. T. *et al*, 2017). For this work, the version 1.51j8 of ImageJ was used to visualize and compare images in the DICOM and TIFF formats.

4.2.8.) Other Software packages

Other software packages used in this work were Microsoft Word 2010 and Microsoft Excel 2010, both by Microsoft Corporation, USA.

4.3.) Methodology

4.3.1.) Basic Dosimetry

At the start of this thesis IPOPFG had two validated phase spaces concerning the TrueBeam^{TM} unit installed at the institution. These files are for the photon beam energies of 6MV and 10MV, both without flattening filter. Thus, the first step of this work consisted in the validation of a new phase space that was created by the combination 30 individual files, provided by Varian, for the 6X beam energy (6X indicates the presence of the flattening filter in the 6MV photon beam path). To accomplish such goal a comparison between the measured and the simulated basic dosimetry curves is needed.

These curves, namely percentage depth dose (PDD) and transverse profiles, were acquired in a setup based on a water tank phantom (~200L capacity) during the commissioning of the TrueBeam^{TM} unit. The dose distribution measurements for the 6X beam energy were performed with a semiflex ionization chamber (PTW Semiflex Ionization Chamber 31010) for various field sizes, considering an SSD of 100cm. On the other hand, a Farmer ionization chamber (PTW Farmer$^{®}$ 30013) was used for the absolute dose measurements, in similar conditions.

4.3.2.) Phase Space Validation

The basic steps for a PRIMO simulation are described in section 2.7.2.1.). Taking that information into account, three different PRIMO-based methods for the generation of a valid phase space concerning the 6X beams produced by the

TrueBeam^{TM} were analyzed, but only one was considered viable for the realization of this work.

The first approach consisted in using an experimentally based geometry of the TrueBeam^{TM} LINAC, known as FakeBeam, which was created and made available by the PRIMO developers. This process used that particular model to produce a phase space tallied at the downstream end of the LINAC upper part, through an s1 simulation in PRIMO (Rodriguez, M. *et al*, 2015). The obtained phase space depends on the number of histories simulated, as well as on several adjustable parameters of the primary beam, namely the energy, the FWHM relative to the energy distribution, the FWHM of the focal spot size, and the beam divergence. The values of the parameters used in the first simulation were the ones recommended by PRIMO after the selection of the nominal energy (6MV). The desired phase space can then be obtained by performing a cyclic tuning of the various possible primary beam parameters after each s1 simulation, until an adequate match between the calculated and measured data is reached. This is the ideal validation procedure since it provides all the statistics associated with the phase space, but it is very time consuming. Therefore this method was tested, but not applied in the validation process due to the timeline conditioning.

A different approach based on the use of free phase space files provided by the International Atomic Energy Agency (IAEA) was considered, due to the fact that PRIMO allows the user to import or link an external phase space to the segment s1, as mentioned in section 2.7.2.1.). However, in practice it was not possible to perform the importation these files to the software because PRIMO is based on the PENELOPE 2011 and DPM codes, therefore it can only track photons, electrons, and positrons; and since the phase spaces were created by the code GEANT4, which is able to deal and produce information in the phase space for additional types of particles, these files were not compatible with PRIMO. In the work carried out by Oliveira, J. E. N., 2017, an in-house code was created to remove those undesired particles that prevent the importation of the phase spaces to PRIMO. After this process, the phase spaces were successfully imported to the s1 simulation segment of PRIMO. Still, it was not possible to perform the simulation of the following segment (s2) due to an unknown error.

Since these two approaches were not viable for the execution of this work, a third method, based on a set of phase spaces provided by Varian, was analyzed and considered the most appropriate technique for the phase space generation and validation within the timeframe. This process consisted in downloading from the Varian website 30 TrueBeam^{TM} phase space files, out of 50 available, for the 6X beam energy, which were collected at the downstream end of the LINAC upper part (s1). Each one of

these files has a size of approximately 1GB and they were all combined through the import tool provided by PRIMO for the segment s1, resulting in a single phase space with about 30GB size. The characteristics of the obtained phase space for the segment s1 are described in table 1:

Energy	6X
Stored position Z	26.7cm
Number of histories	2.79×10^{10}
Mean energy	6.18MeV
Energy sigma (σ)	0.053MeV
Energy FWHM[4]	0.125MeV
Sigma X	0.6866mm
Sigma Y	0.7615mm
Beam divergence	1mrad

Table 1 - Parameters of the generated phase space for the segment s1.

The number of histories simulated, 2.79×10^{10}, was large enough to overcome the benchmarks of similar studies (Belosi, M. F. *et al*, 2014; Mohammed, M. *et al*, 2017). After obtaining the phase space a new simulation project was created in order to evaluate the parameters of the generated file. This process consisted in selecting the LINAC model Varian Clinac 2100, as recommended by the user's manual of PRIMO, and linking the TrueBeam[TM] phase space file to the project. The subsequent step was the establishment of the reference conditions used at IPOPFG for the basic dosimetry process, namely field size of $10 \times 10 \text{cm}^2$, SSD equal to 100cm, and a water tank phantom with dimensions of 60cmx40.2cmx40.2cm (x, y, z) (different dimensions from those of the water tank used in the measurements). This phantom had a bin size of 0.2cm.

The segments s2 and s3 were then simulated and, subsequently, the PDD as well as the transverse profiles at various depths (namely 1.5cm, 5.0cm, 10.0cm, 20.0cm, and 30.0cm) calculated by PRIMO where compared against the measured data through the gamma index evaluation tool provided by the software.

Afterwards, the same phase space file was used for a set of additional simulations in identical conditions, but considering different field sizes, namely $2 \times 2 \text{cm}^2$, $3 \times 3 \text{cm}^2$, $4 \times 4 \text{cm}^2$, $6 \times 6 \text{cm}^2$, $8 \times 8 \text{cm}^2$, $15 \times 15 \text{cm}^2$, $20 \times 20 \text{cm}^2$, $30 \times 30 \text{cm}^2$, and $40 \times 40 \text{cm}^2$. For each case, the comparison between the simulated and measured PDDs and transverse profiles, at the same depths, was also based on the gamma index assessment tool provided by PRIMO.

---

[4] $FWHM = 2 * \sqrt{2 * \ln(2)} * \sigma$

With all the field sizes analyzed for the phase space of interest, the file was considered a valid model of the 6X beams produced by the TrueBeam[TM] unit operating at IPOPFG and used in all the subsequent PRIMO simulations performed during this work.

4.3.3.) Dose Calibration in PRIMO

When a simulation is performed in PRIMO the output comes in $\frac{(eV/g)}{\#History}$, consequently a unit conversion must be applied to quantify the calculated dose. The PRIMO versions used allow a convertion from eV/g to Gy through a three step process:

1) The dose in the central axis must be measured in reference conditions (SSD=100cm, field size=10x10cm^2, depth=10cm) in a water tank phantom, using an adequate dosimeter (e.g., ionization chamber), and for a known number of MUs. Different LINACs installed at different institutions can be calibrated differently in terms of dose/MU. Currently at IPOPFG, the output of all treatment machines, for the 6X beam energy, is adjusted until a value of 0.66cGy/MU is achieved under the stated measurement conditions;

2) A PRIMO simulation must be performed in the reference conditions mentioned in step 1 and the value, in eV/g, of the voxel in the central axis at the same depth (10cm) has to be annotated;

3) The dose, D, in Gy, for a single fraction of a given treatment plan is given by the following expression:

$$D = \frac{D_{exp}^{ref}}{MU^{ref}} \frac{D_{MC}}{D_{MC}^{ref}} MU \qquad (19)$$

where D_{exp}^{ref} is the dose (in Gy) measured in reference conditions, MU^{ref} are the monitor units used to obtain the measured dose, D_{MC} is the simulated dose (in eV/g per history) for the treatment plan, D_{MC}^{ref} is the dose (in eV/g per history) estimated by a Monte Carlo simulation in reference conditions, and MU are the monitor units of the plan.

Through the application of this equation, the software converts eV/g to Gy. PRIMO also allows the user to select the number of treatment fractions to consider in the unit conversion process.

4.3.4.) MLC Validation

As mentioned in section 4.1.1.), the TrueBeam^TM unit installed at IPOPFG is equipped with a HD 120™ MLC and a model of that specific MLC is provided by PRIMO.

This LINAC component is a crucial part of any modulated radiotherapy technique, since it allows the modulation of the radiation beam during the treatment. Consequently, it is necessary to verify if the MLC model available in PRIMO adequately simulates the behavior of MLC existing in the TrueBeam^TM unit, in order to have and adequate level of confidence in the results obtained for the 6X beam energy.

The validation procedure of this structure consisted in comparing the measured and simulated dosimetric leaf gap (DLG), as well as the radiation transmission associated with both banks of the MLC. For all the simulations performed in this process, the conditions considered were 6X beam energy, field size of 10x10cm^2, SSD equal to 95cm, and a solid water phantom with the dimensions of 30cmx30cmx12cm (x, y, z).

The transmission between the two banks of the MLC is a value that needs to be measured and inserted in Eclipse^TM for each specific treatment unit. In the validation process, this parameter was determined through the realization of three simulations, one with the bank A completely closed and the bank B fully open, another representing the inverse situation, and a final simulation with both banks completely open. Subsequently, the dose in the central axis at 5cm depth in the phantom was determined for all the situations and the obtained values were compared against the measurements, which were acquired during the routine quality control procedures of the TrueBeam^TM unit.

The DLG models the transmission through the rounded leaf ends of the MLC, i.e. the round-leaf-end effect (figure 24) and it is also measured in the periodic quality control actions of the LINAC (Kim, J., *et al*¸2018; Yao, W. *et al*, 2015).

Eclipse^TM does not automatically consider the effect of the rounded MLC leaves in the dose calculations, therefore the DLG of each treatment unit must be measured by the team of medical physicists and manually input in the system. For the validation of the HD 120^TM MLC model provided by PRIMO, the DLG was calculated taking into account the transmission previously determined and by performing various simulations involving static gaps of different sizes defined by the MLC, namely 2mm, 4mm, 6mm, 10mm, 14mm, 16mm, and 20mm, which moved at a constant velocity along the radiation field. Subsequently, the dose in the central voxel at 5cm depth in the phantom was determined for all the cases.

This information was then used to run a test generally performed in IPOPFG for the determination of the DLG. Afterwards, the value obtained was compared against the DLG currently used for the TrueBeam[TM] LINAC installed at the hospital.
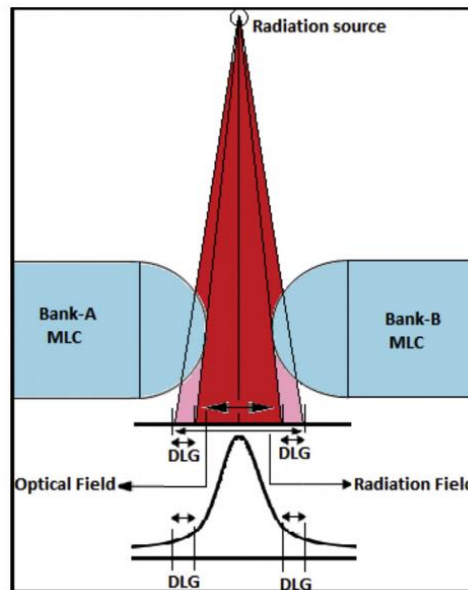
Figure 24 - Representation of the roud-leaf-end effect (adapted from Shende, R. *et al*, 2017).

4.3.5.) Simulation of an IMRT plan

With all the required validations performed, the next step executed was the PRIMO simulation of an IMRT plan. This plan consisted in a dynamic gap of 1cm shaped by the HD 120[TM] MLC (figure 25), which moved from one end to the opposite end of a 10x10cm^2 field defined by the secondary collimators.

In this process, the validated phase space, for the 6X beam energy, was linked to the PRIMO project, the phantom was generated in the software, and the treatment plan created with Eclipse[TM] was imported to the project. The phantom used in this case was a solid water phantom with dimensions of 30cmx30cmx12cm (x, y, z) and it was established an SSD equal to 95cm. In the first simulation only 3 control points were considered, as these were the ones defined in the DICOM RP file exported by the TPS for this specific plan. After the simulation completion, a tool provided by PRIMO was used to compare the obtained dose distribution against the one calculated by the AAA algorithm of the TPS.

After this step, a different simulation was performed for the same conditions stated before, but with the addition of 18 control points to the ones exported by the TPS, making a total of 21 control points (figure 26). These control points were inserted in the .ppj file (project file) that is generated after the creation of a new PRIMO project.

Subsequently, the PRIMO evaluation tool was used to compare the same TPS dose distribution against the result of this second simulation.

The TrueBeam[TM] unit installed at IPOPFG was used to perform the same plan under conditions equal to those simulated. In this irradiation, the dose was measured with an EBT3 film placed at 5cm depth in a solid water phantom (PTW RW3 Slab Phantom). Afterwards, the dose distribution calculations and the film were compared in VeriSoft[®].

Subsequently, a similar process involving the simulation and measurement of the same treatment plan was executed. However, in this approach an SSD of 100cm was considered and the dose was measured with the electronic portal image device (EPID) existing in the TrueBeam[TM.]
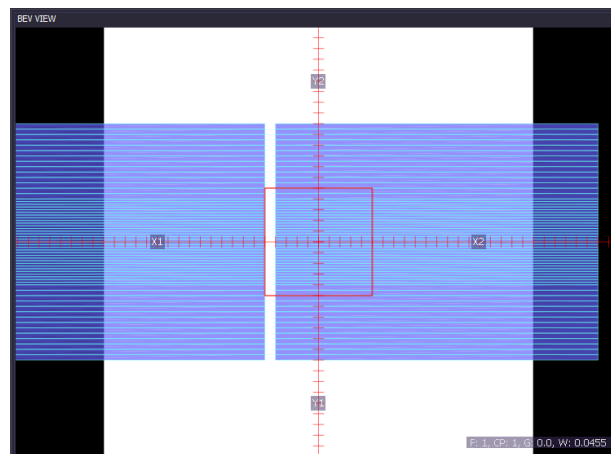
Figure 25 - The 1cm gap defined by the HD 120[TM] MLC.

Figure 26 - (a) Control points of the plan as exported by the TPS; **(b)** Control points after the edition of the project file.

4.3.6.) Simulation of a Brain VMAT Treatment Plan

The next step performed was the PRIMO simulation of a VMAT treatment plan for the brain created in Eclipse[TM]. The dose distribution was calculated and measured in a pediatric anthropomorphic phantom, called RUPERT (figure 27), which has an isocenter in the head region identified with CT markers (figure 29). No clinical setup mismatch was considered for this study.

Figure 27 - The RUPERT phantom used.

Similarly to the previous simulations, the first step consisted in linking the validated TrueBeam[TM] phase space, for the 6X beam energy, to the s1 segment. Subsequently, the partial CT of the phantom's head region, which was already performed and available at the institution, was imported to PRIMO. Afterwards, the delineated structures of the phantom, for this plan, were also uploaded to the software through a DICOM RS file exported by the TPS. Then, the DICOM RP file was imported to the project, but in this case no modification in any of the 354 control points was performed. Finally, the PRIMO simulation was run.

After the simulation completion, the same plan was executed on RUPERT using the TrueBeam[TM] unit installed at IPOPFG. In order to measure the delivered dose, two custom cut Gafchromic[TM] EBT3 films were placed between different slices of the phantom. They were positioned at 3.5cm and at 6.25cm from the phantom's isocenter in the caudal (inferior/-) direction. Relatively to the isocenter defined by the plan, the first film previously mentioned was at 1.5cm from that location in the cranial (superior/+) direction, and the second one was at 1.25cm from the same point in the caudal direction. These were the positions used to measure the delivered dose because the plan's isocenter was located inside a slice of RUPERT. Therefore, as the

radiochromic films can only be positioned between different slices of the phantom, it was not possible to measure the dose distribution in the plane of the isocenter. As a result, it was decided to place the films between the slices closer to that location in order to assess the dose distribution as near as possible to the isocenter.

An important aspect to notice about the coordinate system is that, although the x axis is considered the same between the TPS and PRIMO, the y and z axis are exchanged, i.e. the y axis in Eclipse[TM] is considered the z axis by PRIMO and the y axis in PRIMO is interpreted by the TPS as the z axis (figure 28).
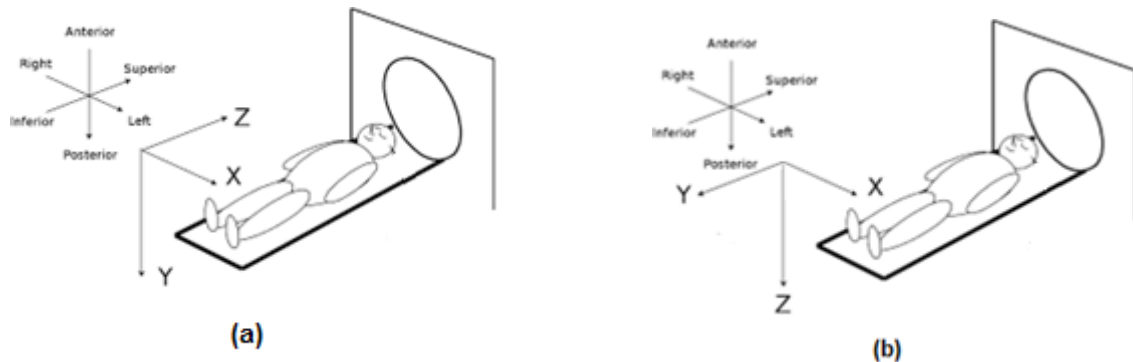
Figure 28 - (a) coordinate system defined in the TPS (Eclipse[TM]); **(b)** coordinate system defined in PRIMO.

Another relevant point to note is that the x and y axis directions in the TPS are identical to the orientations associated with the analogous axis (x and z, respectively) in PRIMO, however the z axis direction defined by Eclipse[TM] is opposite to the orientation of the corresponding axis (y) in PRIMO. To simplify the reading, all the axis and orientations mentioned throughout this thesis are relative to the TPS coordinate system.

After the irradiation of the film it is necessary to wait 24h, since this is the time period used to calibrate the films at the institution. Therefore, after a day the irradiated films are digitalized in the scanner. A non-irradiated film from the same batch is also digitalized, working as the background value when the conversion from optical density to absorbed dose of the irradiated film is performed in DoseLab. The measured and calculated results (by the AAA algorithm of the TPS and by PRIMO) where compared in VeriSoft[t®].

Since VeriSoft[®] can assess the dose distribution in planes, but not in structures, a different tool capable of evaluating the dose delivered to the various volumes was needed. This problem was solved by using the dose evaluation option provided by PRIMO, which allows a comparison based on the gamma index between the PRIMO simulation and a DICOM RD file, such as the one that the TPS exports, or another PRIMO simulation, for all the structures of interest defined by the DICOM RS file.
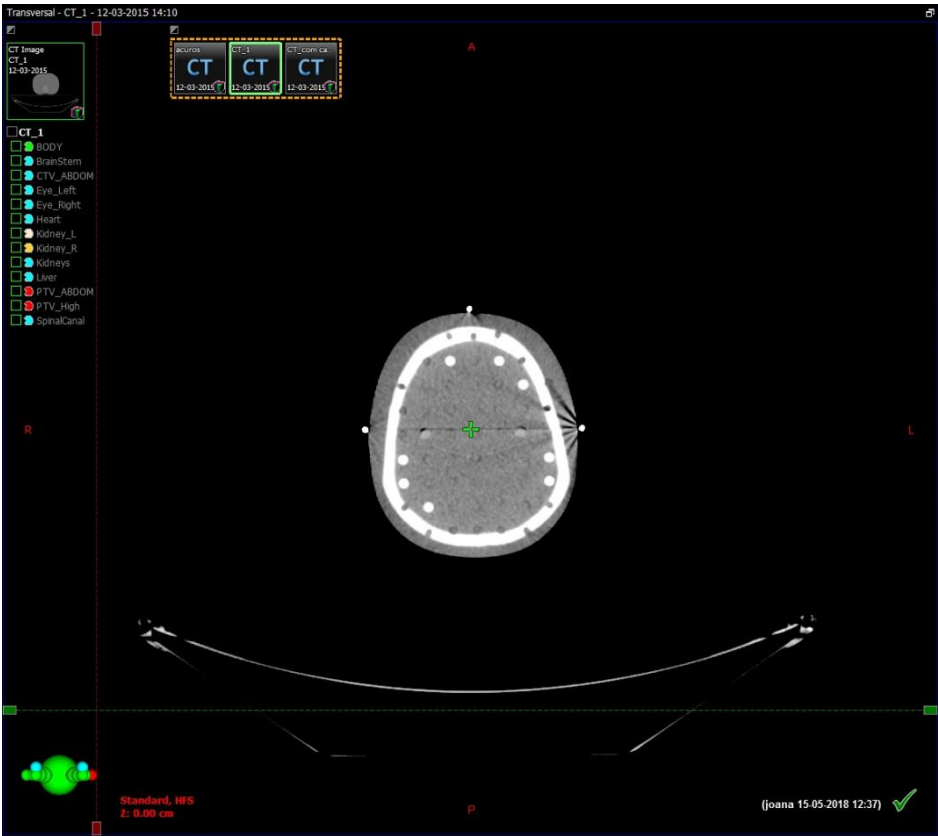
Figure 29 - CT illustrating the isocenter markers placed in the RUPERT phantom.

Figure 30 - The brain VMAT plan after its import to PRIMO.

4.3.7.) Simulation of an Abdominal VMAT Treatment Plan

After the comparison and analysis of the results obtained from the study involving the brain, a new abdominal VMAT plan for the RUPERT phantom was created in the TPS and simulated using PRIMO. The choice of the abdominal region is justified by the proximity of OARs to the PTV, such as the kidneys. Consequently a set of simulations, representing different positioning mismatches in the three axes, was performed as a way to assess the dosimetric effects resulting from clinical setup mismatches in a VMAT treatment plan with Monte Carlo methods.

The first simulation executed in PRIMO did not have any positioning mismatch, but the subsequent was simulated with the isocenter of the plan shifted +0.5cm in the x axis. A relevant point to notice about this software is that the PENELOPE/penEasy engine only allows a maximum of 10^8 voxels in an s3 simulation, therefore the RUPERT whole body CT provided by IPOPFG had to be "cut" so that the desired simulations could be executed. Nevertheless, the process of linking and importing the different required files to the PRIMO projects followed the same steps performed for the previous treatment plan, section 4.3.6.).

Figure 31 - The simulated abdominal VMAT plan without positioning mismatch.

After the completion of the simulations, the same measurement procedure performed for the brain plan was executed, but in this study four EBT3 films were used for each case (with and without positioning mismatch) instead of two. The plan's isocenter is located at 40cm from the CT markers placed on RUPERT in the caudal direction, being approximately situated at the center of the phantom's slice number 18. Consequently, in both situations the four films were placed at a distance of -3.75cm, -1.25cm, +1.25cm, and +3.75cm from the plan's isocenter relatively to the z axis, due to the same reason previously stated for their positioning in the brain VMAT treatment plan (section 4.3.6.)). After a similar scanning and conversion process of the irradiated films from optical density to absorbed dose, the results obtained with the measurements, TPS (AAA and Acuros XB algorithms), and PRIMO were compared in VeriSoft[t®].

The comparison tool provided by PRIMO, already mentioned and applied in section 4.3.6.), was also used for this study as a way assess the dose delivered to the different structures of interest defined by the DICOM RS file.

With this analysis performed, the next step consisted in assessing the dosimetric effects resulting from additional phantom positioning shifts, namely: -0.5cm x, -0.4cm x, -0.3cm x, -0.2cm x, -0.1cm x, +0.1cm x, +0.2cm x, +0.3cm x, +0.4cm x, -0.5cm y, -0.4cm y, -0.3cm y, -0.2cm y, -0.1cm y, +0.1cm y, +0.2cm y, +0.3cm y, +0.4cm y, +0.5cm y, -0.8cm z, -0.7cm z, -0.6cm z, -0.5cm z, -0.4cm z, -0.3cm z, -0.2cm z, -0.1cm z, +0.1cm z, +0.2cm z, +0.3cm z, +0.4cm z, +0.5cm z, +0.6cm z, +0.7cm z, and +0.8cm z.

The results obtained from all the simulations executed for this abdominal plan were then compared using Microsoft Excel 2010, considering a single treatment fraction as well as a typical treatment of 25 fractions. The acquired information was also analyzed based on the recommendations provided by the QUANTEC initiative.

5.) Results and Discussion

5.1.) Validation of the Phase Space

5.1.1.) Phase Space File

As mentioned in section 4.3.2.), the 30GB TrueBeam^{TM} phase space created in PRIMO for validation was based on the junction of 30 individual files, downloaded from the Varian website, for the 6X beam energy.

PRIMO provides different options for the analysis of a phase space, as represented in figures 32, 33, and 34.
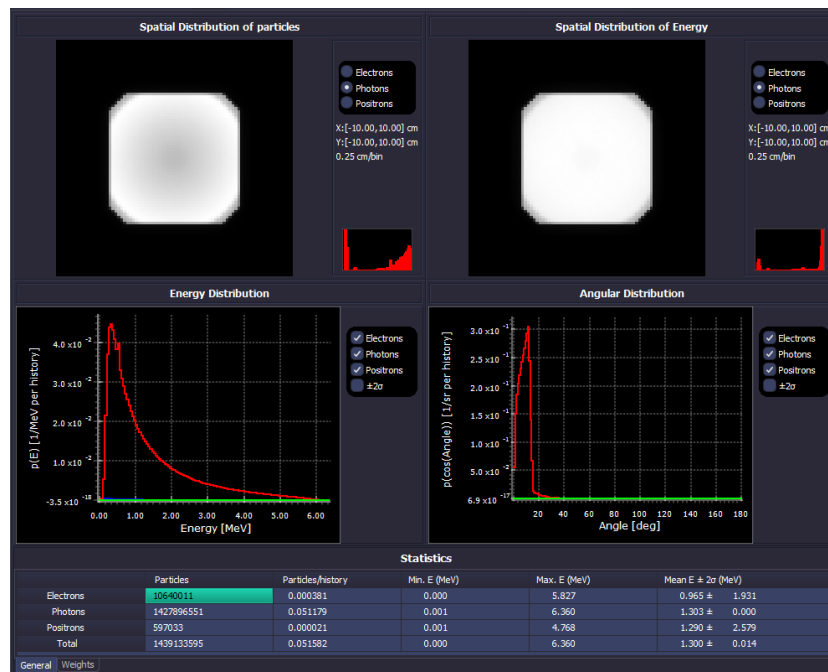
Figure 32 - Analysis of the generated phase space for the segment s1 (electrons are represented by the blue curve, photons are represented by the red curve, and positrons are represented by the green curve).
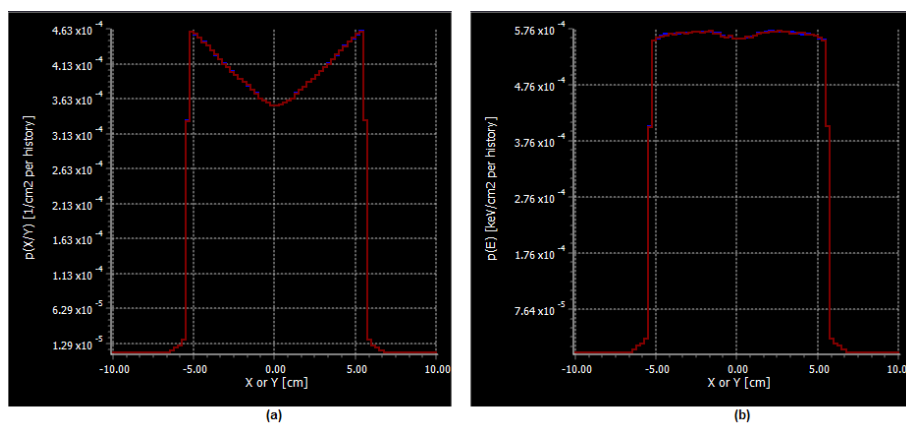
Figure 33 - Profiles of the spatial distribution of **(a)** photons and **(b)** photons energy, in the generated phase space.
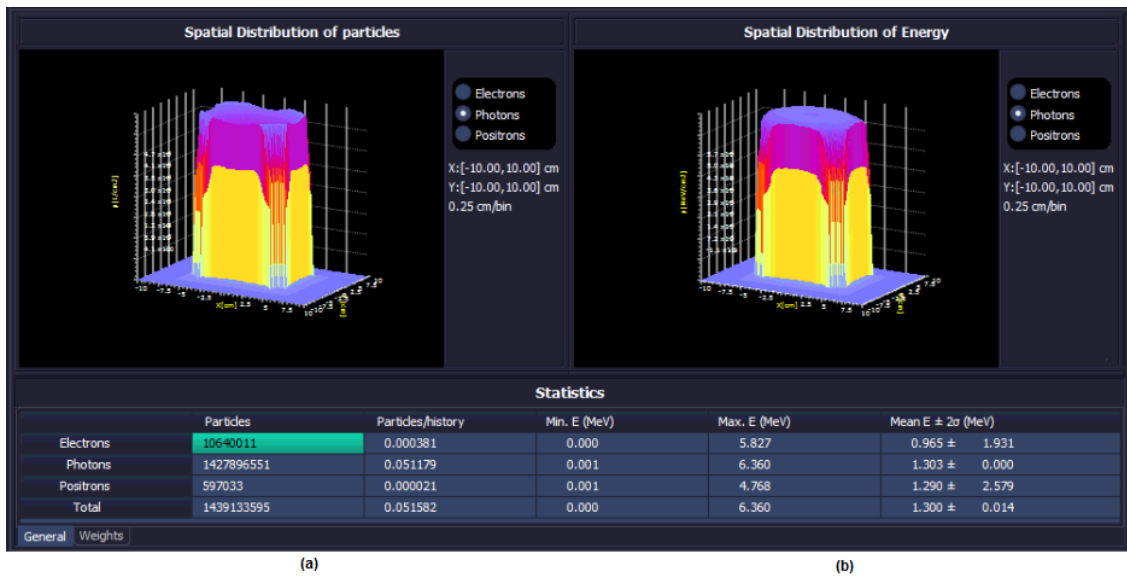
Figure 34 - Surfaces representing **(a)** spatial distribution of photons and **(b)** spatial distribution of photons energy, in the phase space created.

5.1.2.) Measured PDDs and Transverse Profiles

The measured data, namely PDDs and transverse profiles, used for the validation of the phase space was provided by IPOPFG. These curves, represented in appendix A.1.), were acquired during the commissioning of the TrueBeam^TM unit currently installed at the institution.

5.1.3.) Calculated PDDs and Transverse Profiles

The PDDs and transverse profiles obtained with PRIMO and used for the validation of the TrueBeam^TM phase space are represented in appendix A.2.).

5.1.3.) Comparison between Measured and Calculated Data

After the completion of all simulations, the validation of the phase space file was performed by comparing the measured and the simulated PDDs and transverse profiles at different depths for the various field sizes considered. Flowingly, a graphical comparison between the different curves is shown (graphs 1 to 16) and then the results obtained with the PRIMO comparison tool, which employs the gamma index, are presented (table 2).
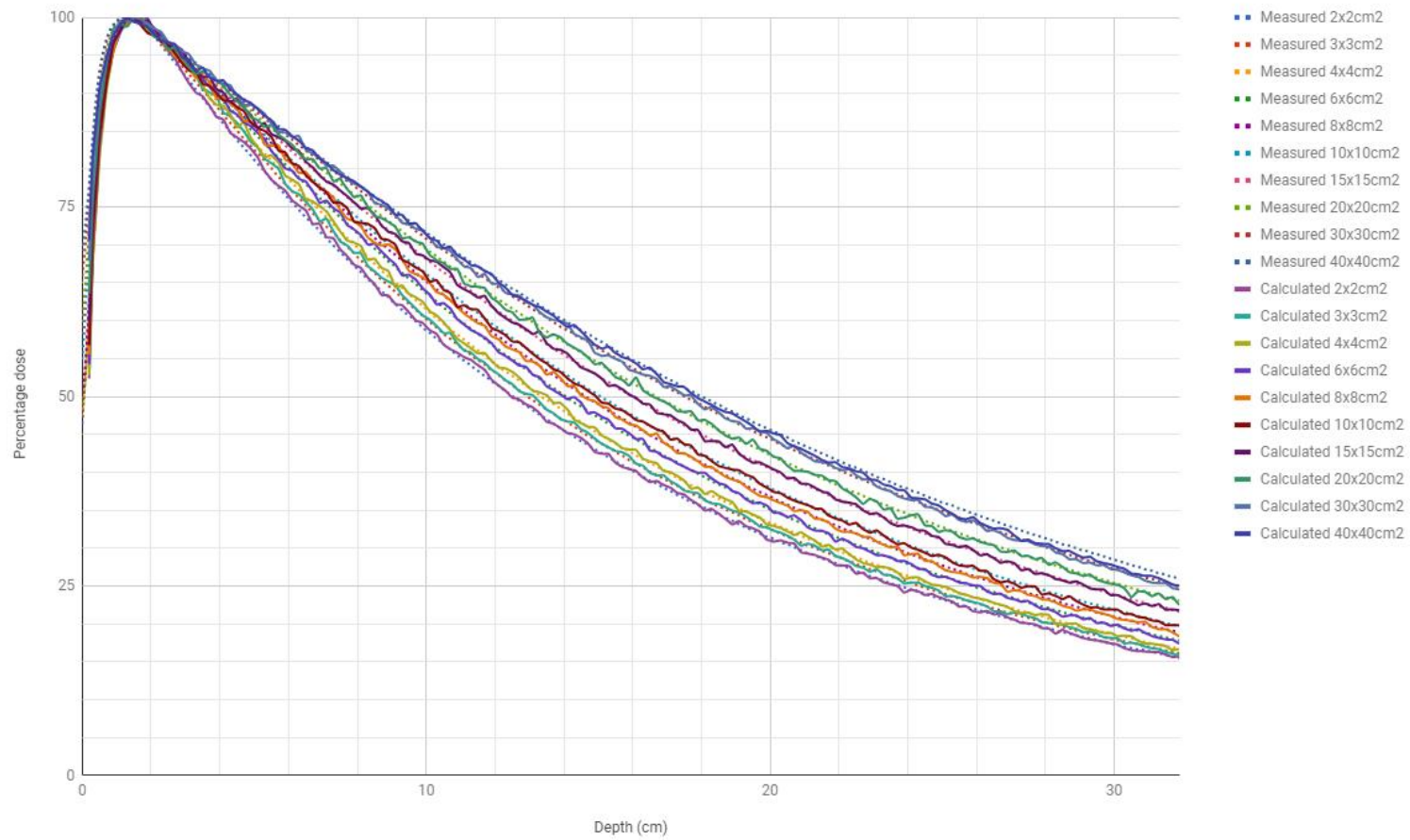
Graph 1 - Comparison between the measured and the calculated PDDs.

Graph 1 shows that the buildup region, although having a small dependence on the field size, is about 1.4cm long for all the analyzed curves. It is also verifiable a direct relation between the field size and the PDD after the buildup region, i.e. if one increases the other will also increase. Such correlation is caused by the contribution of the scattering effect to the central axis of the beam, which becomes more significant with increasing field size (Khan, F. M., 2014; Podgorsak, E. B., 2016).
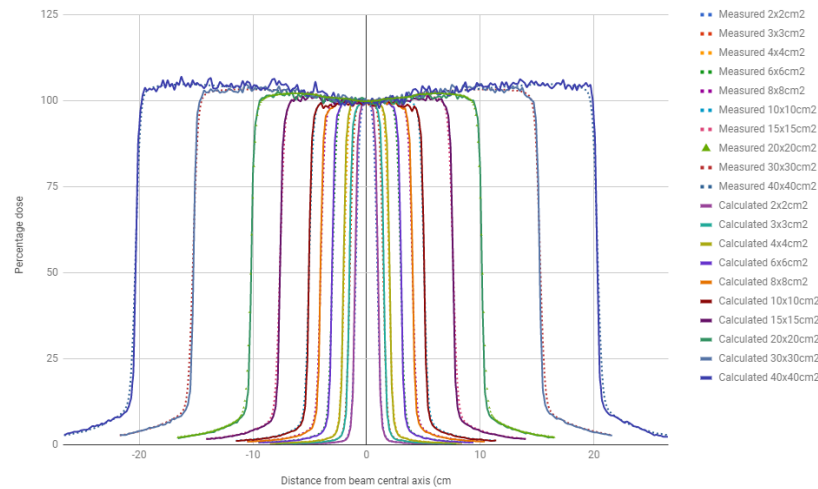
Graph 2 - Comparison between the measured and the calculated transverse profiles at 1.5cm depth.
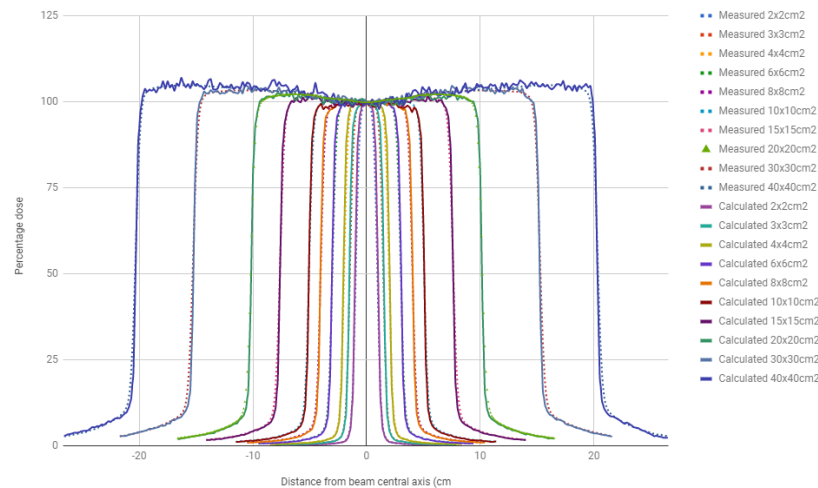
Graph 3 - Comparison between the measured and the calculated transverse profiles at 5.0cm depth.
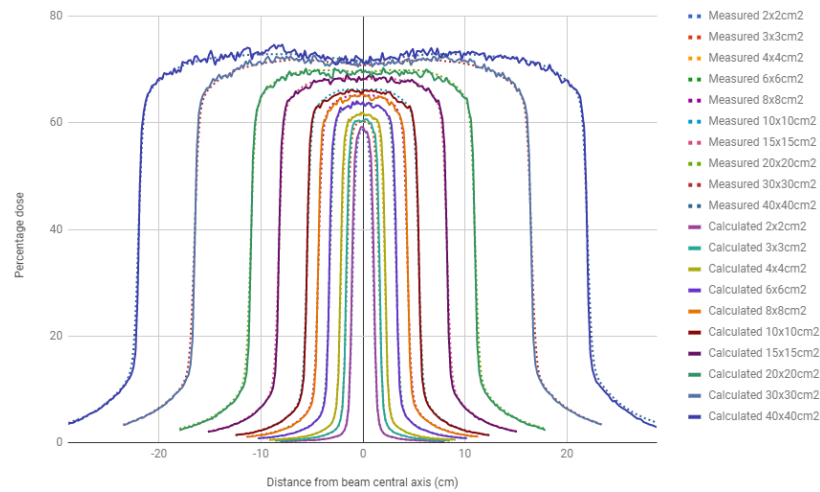
Graph 4 - Comparison between the measured and the calculated transverse profiles at 10.0cm depth.
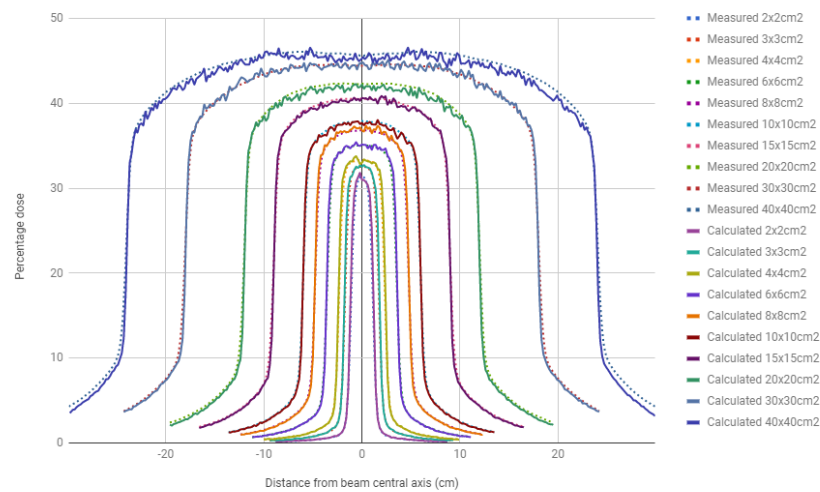
Graph 5 - Comparison between the measured and the calculated transverse profiles at 20.0cm depth.
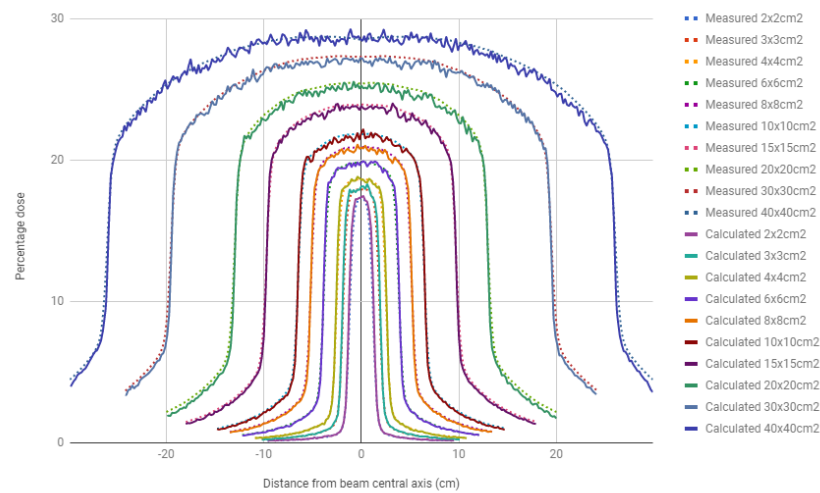
Graph 6 - Comparison between the measured and the calculated transverse profiles at 30.0cm depth.

From graphs 2 to 6 it is possible to conclude that for all field sizes the dose decreases with increasing depth. This occurs because photons are scattered and absorbed, by different interaction mechanisms (section 2.2.2.)), as they move through matter. Therefore, these quanta of electromagnetic field are gradually removed from the original beam, i.e. the photon beam is progressively attenuated, as the distance traveled in the medium increases, leading to a consequent reduction of the dose delivered to matter at greater depths.
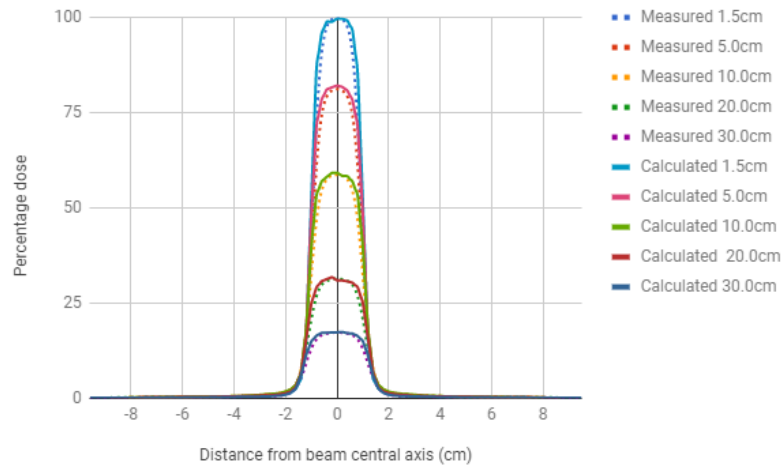
Graph 7 - Comparison between the measured and the calculated transverse profiles at each considered depth for a 2x2cm^2 field size.
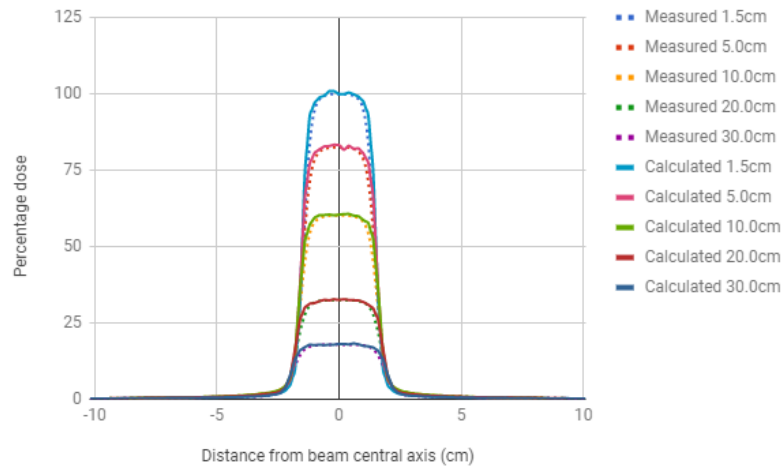
Graph 8 - Comparison between the measured and the calculated transverse profiles at each considered depth for a 3x3cm^2 field size.
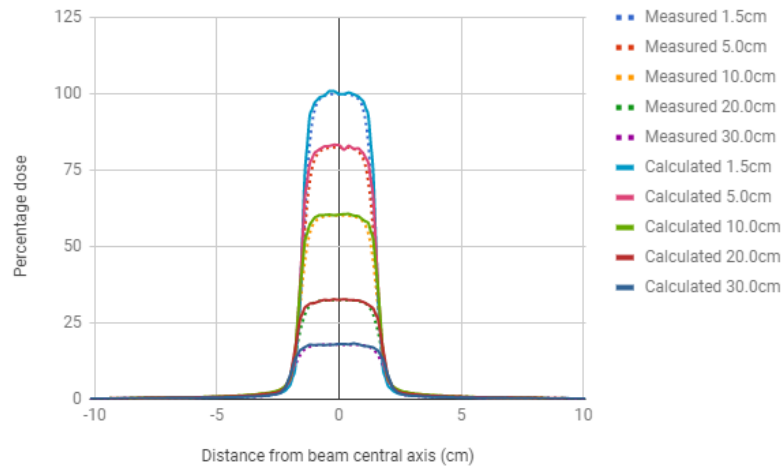
Graph 9 - Comparison between the measured and the calculated transverse profiles at each considered depth for a
4x4cm^2 field size.
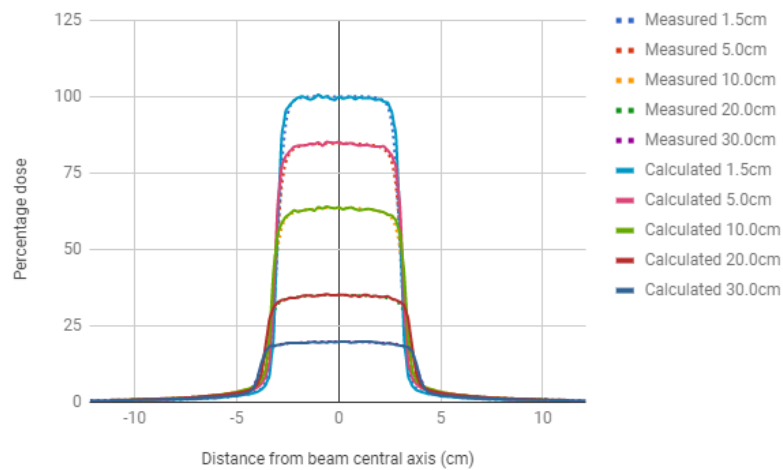
Graph 10 - Comparison between the measured and the calculated transverse profiles at each considered depth for a
6x6cm^2 field size.
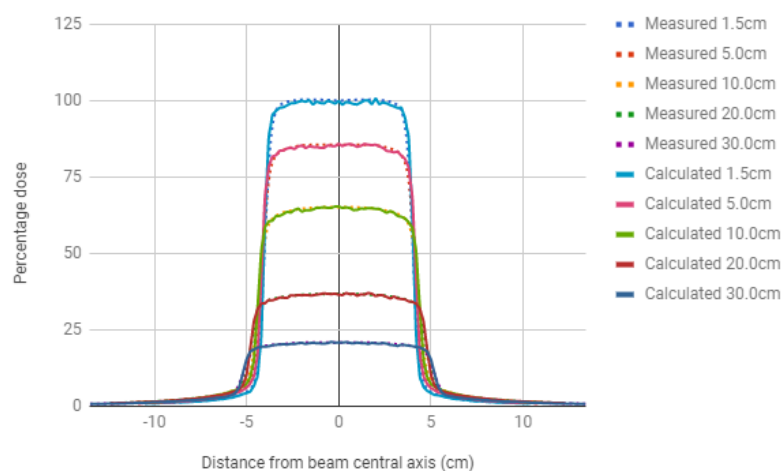
Graph 11 - Comparison between the measured and the calculated transverse profiles at each considered depth for a
8x8cm^2 field size.
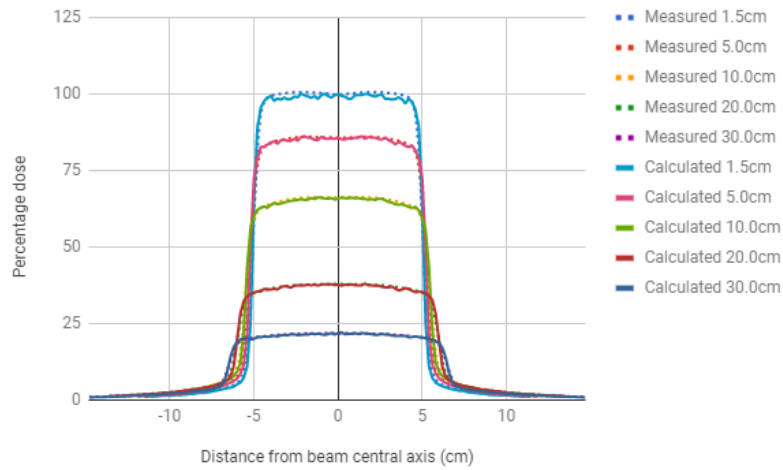
Graph 12 - Comparison between the measured and the calculated transverse profiles at each considered depth for a 10x10cm^2 field size.
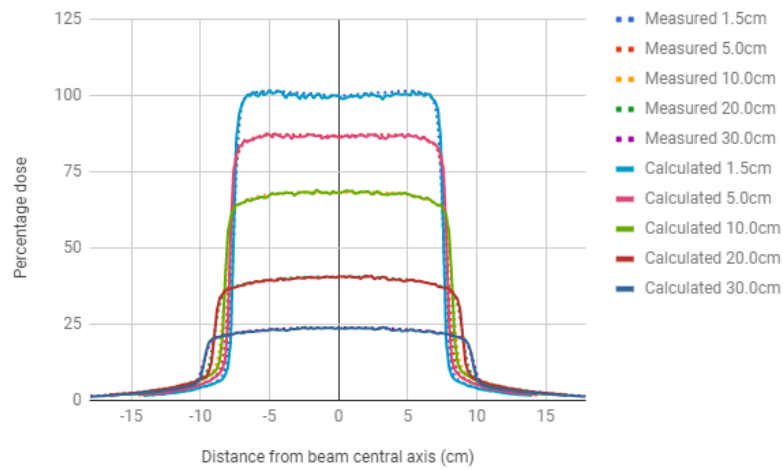
Graph 13 - Comparison between the measured and the calculated transverse profiles at each considered depth for a 15x15cm^2 field size.
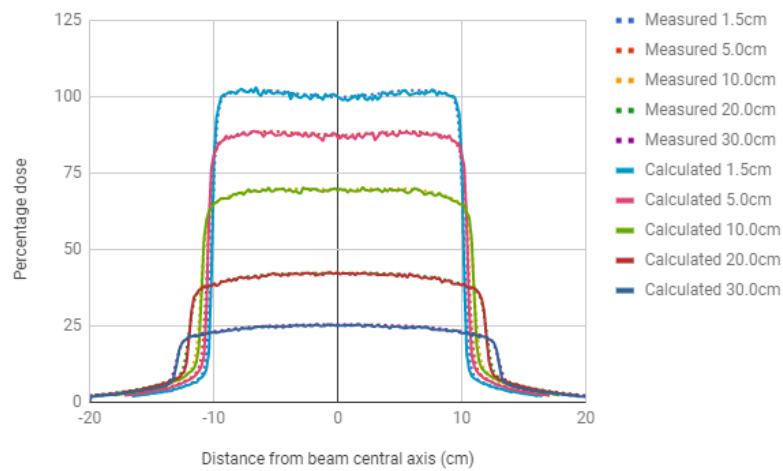
Graph 14 - Comparison between the measured and the calculated transverse profiles at each considered depth for a 20x20cm^2 field size.
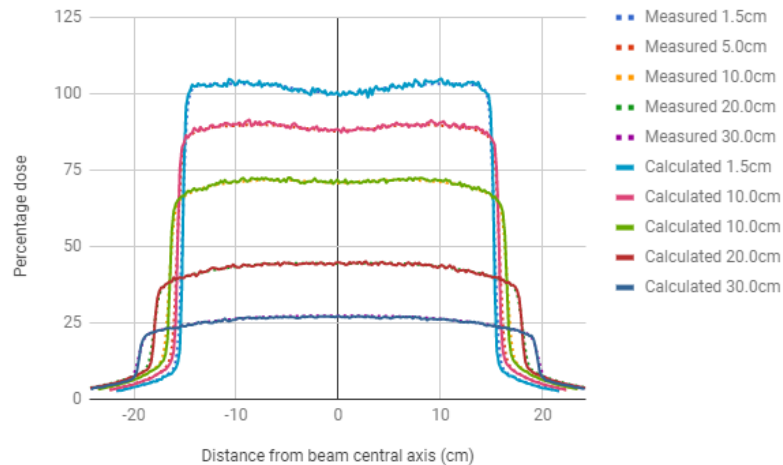
Graph 15 - Comparison between the measured and the calculated transverse profiles at each considered depth for a
30x30cm^2 field size.
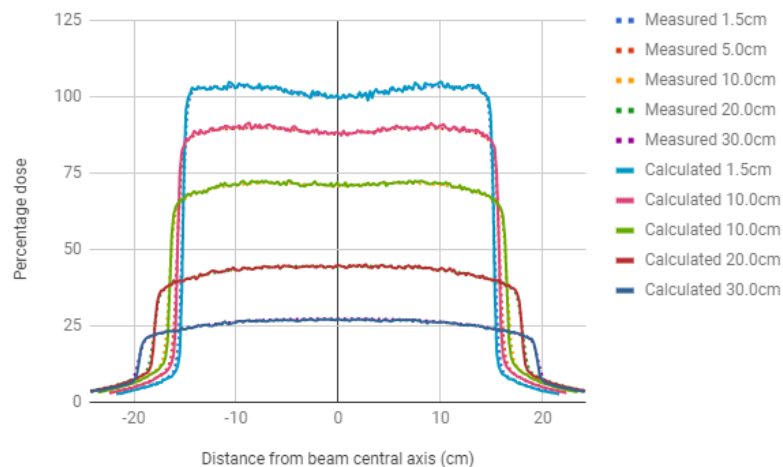
Graph 16 - Comparison between the measured and the calculated transverse profiles at each considered depth for a
40x40cm^2 field size.

The obtained results indicate that the tranverse beam profile gets wider as depth increases. Such relationship exists due to the beam divergence (Khan, F. M., 2014; Mayles, P. *et* al, 2007; Podgorsak, E. B., 2005). The dose, on the other hand, decreases with increasing depth as explained in the previous paragraph.

It is also possible to see that the "horns", produced by the flattening filter, start to appear more clearly at larger beam widths. This is verified because the filter has higher thickness on the axis than off-axis. Nevertheless, these "horns" become less pronounced as depth increases due to an in-scatter/out-scatter imbalance at the edge of the beam, and because the radiation on the beam central axis is more penetrating (i.e. harder), when compared to the off-axis regions (Khan, F. M., 2014; Mayles, P. *et* al, 2007; Podgorsak, E. B., 2016).

In the gamma analysis performed the criteria employed were 2% dose difference and 2mm distance with a 95% tolerance level for the passing rate. These were the parameters applied because various authors used them in the validation of phase space files for Monte Carlo dose calculations, namely Akunzi, J. *et al*, 2016; Belosi, M. F. *et al*, 2014; Esposito, A. *et al*, 2018; Faught, A. M. *et al*, 2017; Sottiaux, A. *et al*, 2016; and Teke, T. *et al*, 2015.

The passing rates obtained in the gamma analysis of the various curves are presented next:

Field size	PDD	Transverse Profile Depth				
		1.5cm	5cm	10cm	20cm	30cm
2x2cm^2	100.00%	96.67%	98.70%	98.77%	97.73%	98.44%
3x3cm^2	99.38%	97.50%	96.34%	98.84%	99.47%	98.53%
4x4cm^2	99.69%	96.47%	98.86%	96.74%	99.50%	99.08%
6x6cm^2	99.69%	99.47%	98.47%	97.57%	100.00%	99.18%
8x8cm^2	99.69%	100.00%	99.08%	99.12%	99.19%	100.00%
10x10cm^2	99.06%	99.57%	99.16%	99.60%	99.26%	100.00%
15x15cm^2	99.06%	98.94%	97.93%	99.34%	100.00%	100.00%
20x20cm^2	100.00%	99.40%	97.97%	100.00%	100.00%	100.00%
30x30cm^2	99.69%	99.08%	99.55%	99.57%	99.59%	100.00%
40x40cm^2	99.69%	97.93%	99.64%	98.79%	98.33%	98.66%

Table 2 - Passing rates obtained in the gamma analysis between simulated and measured PDDs and transverse profiles at the considered depths.

From table 2, it is possible to note that smaller fields generally have lower percentage of points passing the acceptance criteria. Such reduction occurs because it is more difficult to perform accurate measurements in this type of fields, due to the fact that there is a loss of lateral charged particle equilibrium on the beam axis, between other effects - a detailed approach on this topic can be found on TRS 483 by IAEA.

Nevertheless, for all the curves analyzed more than 95% of the points pass the acceptance criteria. With these results, the phase space was considered a valid model of the 6X beams produced by the TrueBeam[TM] LINAC currently installed at IPOPFG, and subsequently used for all the simulations performed in this work.

Figure 35 - (a) Gamma analysis performed on PRIMO for the PDD of a 10x10cm^2 field; **(b)** Gamma analysis performed on PRIMO for the transverse profile of a 10x10cm^2 field at 1.5cm depth.

5.2.) Validation of the MLC

In this step, the phase space previously analyzed was used to validate the HD 120[TM] MLC model provided by PRIMO for the 6X beam energy of the TrueBeam[TM] unit, in order to have an adequate confidence level associated with the simulated results. During this process, two parameters were evaluated, namely the DLG and the transmission between the leaves of the MLC (section 4.3.4.)).

The results obtained from the simulations performed for the validation of the MLC are shown below:

6X MLC Transmission Simulations	
SSD=95cm; Depth=5cm; Field size=10x10cm^2	Reading (Gy)
Open reading (Gy)	1.725
Mt1=Closed MLC [Bank A]	0.012
Mt2=Closed MLC [Bank B]	0.012

Table 3 - Simulated transmission readings.

Transmission factor	
Open Reading	1.725Gy
Mt[5]	0.012Gy
MLC Transmission Factor[6]	0.007

Table 4 - Determination of the transmission factor for the HD 120[TM] MLC.

6X DLG			
SSD=95cm; Depth=5cm; Field size=10x10cm^2			
Gap (mm)	Reading (Gy)	Scaled Mt (Gy)[7]	M (Gy)[8]
2	0.080	0.012	0.068
4	0.110	0.012	0.098
6	0.140	0.011	0.129
10	0.174	0.011	0.163
14	0.189	0.011	0.178
16	0.217	0.010	0.207
20	0.302	0.010	0.292

Table 5 - Values used for the calculation of the DLG.

The transmission through the MLC banks, i.e. 0.012Gy, obtained for the HD 120[TM] MLC model provided by PRIMO is equal to the value measured in the TrueBeam[TM] unit operating at IPOPFG.

---

[5] $Mt = \frac{Mt1+Mt2}{2}$

[6] MLC Transmission Factor $= \frac{Mt}{Open\ Reading}$

[7] Scaled Mt $= Mt \times [1 - \left(\frac{Gap}{120mm}\right)]$

[8] M = Reading – Scaled Mt

With all the simulations performed, the DLG can be determined by plotting M as function of the gap and subsequently fitting a linear regression line to the obtained graph.
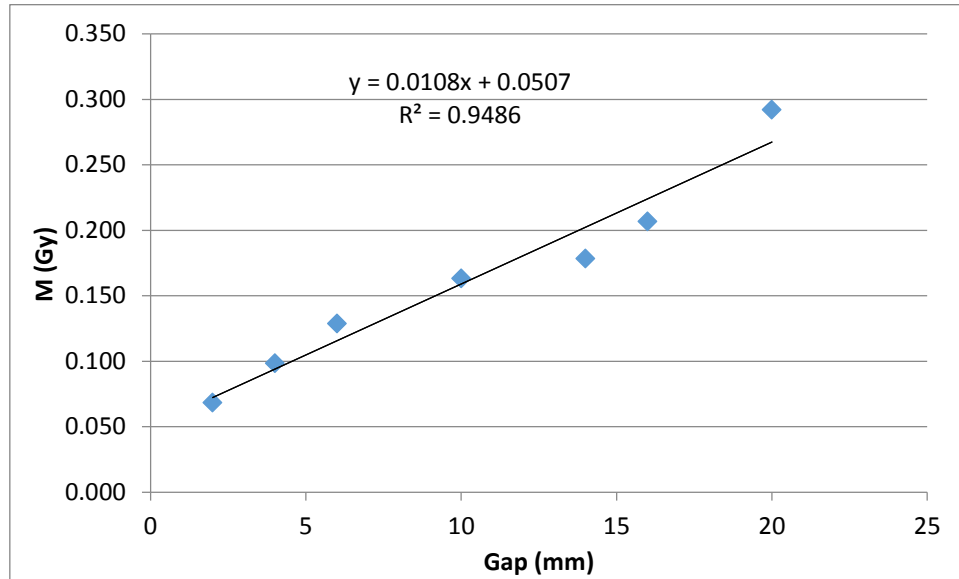
Graph 17 - Plot of dose as function of MLC leaf gap.

The intersection point between the linear regression line and the x axis (M = 0Gy) represents the DLG. Therefore, from graph 17 it is possible to conclude that $\text{DLG} = \frac{0.0507}{0.0108} = 4.6944\ mm$. Nevertheless, it is important to notice that the R^2 metric has a value of 0.9486, which can be caused by the statistical uncertainty inherently associated with the Monte Carlo method.

The factory value indicated for the DLG was about 3mm, however an optimal value of 4.7mm was established at the institution for the 6X beams produced by the TrueBeam[TM] unit. Consequently, it is verified a difference of 0.12% between the simulated and the real DLG. This discrepancy is lower than the one obtained, and recommended, in studies addressing the DLG characterization, which is about 1.31% (Mullins, J. *et al*, 2016; Shende, R. *et al*, 2017).

As a result, the HD 120[TM] MLC geometry provided by PRIMO was considered a valid model of the HD 120[TM] MLC installed in the TrueBeam[TM] treatment unit operating at IPOPFG, for the 6X beam energy.

5.3.) IMRT Plan with a Dynamic Gap

With the necessary validations performed, a study about the simulation mechanism of modulated techniques used by PRIMO was needed because, in the

previous versions of the software, it was not possible to import and simulate treatment plans involving these types of techniques.

The first studied case addressed IMRT for the reason that this approach involves less degrees of freedom during the irradiation process, therefore it is usually easier to perform than a VMAT treatment plan.

5.3.1.) First Approach

As a first approach, a relatively simple IMRT plan was chosen (section 4.3.5.)) and simulated without performing any modifications to the control points. The dose distribution obtained from this simulation is represented in figure 36.

For IMRT, a gamma index having 3% dose difference and 3mm distance-to-agreement as passing criteria, with a 90% tolerance level for the passing rate, has been frequently recommended and routinely used in the clinic, although different criteria can be employed (Dumitrache, M. *et al*, 2016; Ezzell, G. A. *et al*, 2009; Kim, J. *et al*, 2017; Ohira, S. *et al*, 2017; Stojadinovic, S. *et al*, 2015). Nevertheless, these were the parameters used for the evaluation of this particular case.

The gamma analysis between simulated and TPS (AAA algorithm) dose distributions indicates that they are not similar at all (figure 36(b)). The PRIMO simulation resulted in a focusing of the dose at both edges of the $10x10cm^2$ field, whilst the TPS calculation indicates a homogeneous dose distribution over the same field size.

The reason for this discrepancy is that PRIMO calculates the dose delivery to the phantom based merely on the information of the control points, which is provided by the DICOM RP file. Consequently, the software does not simulate the phantom irradiation in the spatial interval existing between those points. On the other hand, the TPS calculates the dose distribution not only based on the control points, which are automatically defined in Eclipse^{TM} according to what is required by the LINAC for the execution of the plan, but also considering the fact that the machine does not stop the irradiation between two adjoining points (in the sliding window technique, obviously), continuously moving from one control point to the next through the regulation of the different adjustable parameters.

Therefore it is possible to conclude that the simulation of a plan involving dynamic movement is a complex problem, which PRIMO still cannot handle properly. This subject matter was approached in the following work (section 5.3.2.)) by the manipulation of the control points defined by the DICOM RP file, after its import to PRIMO.
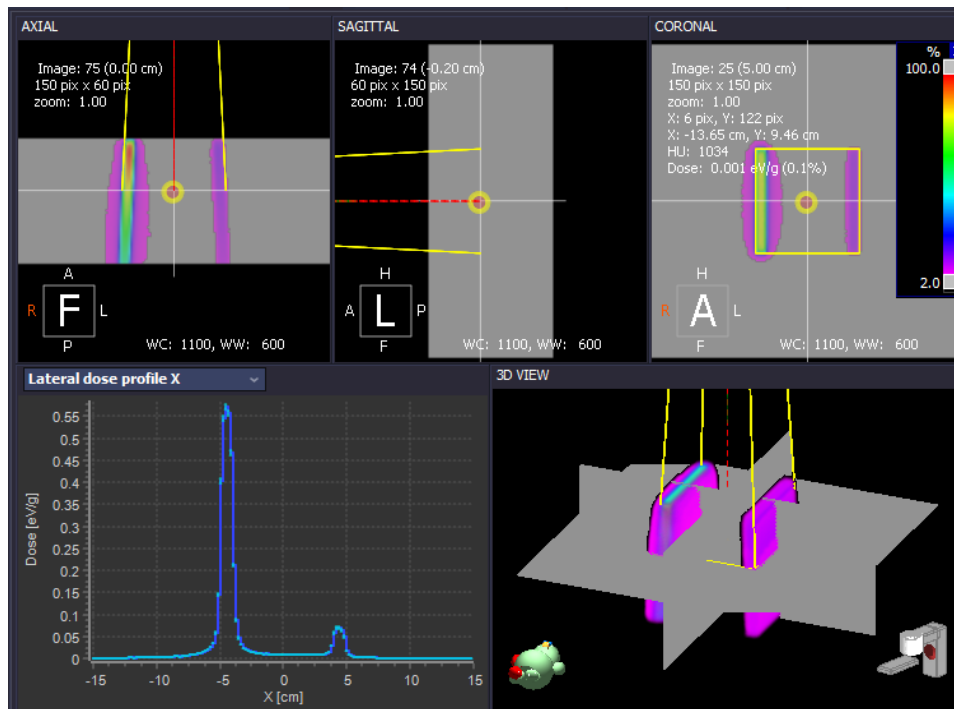
(a)
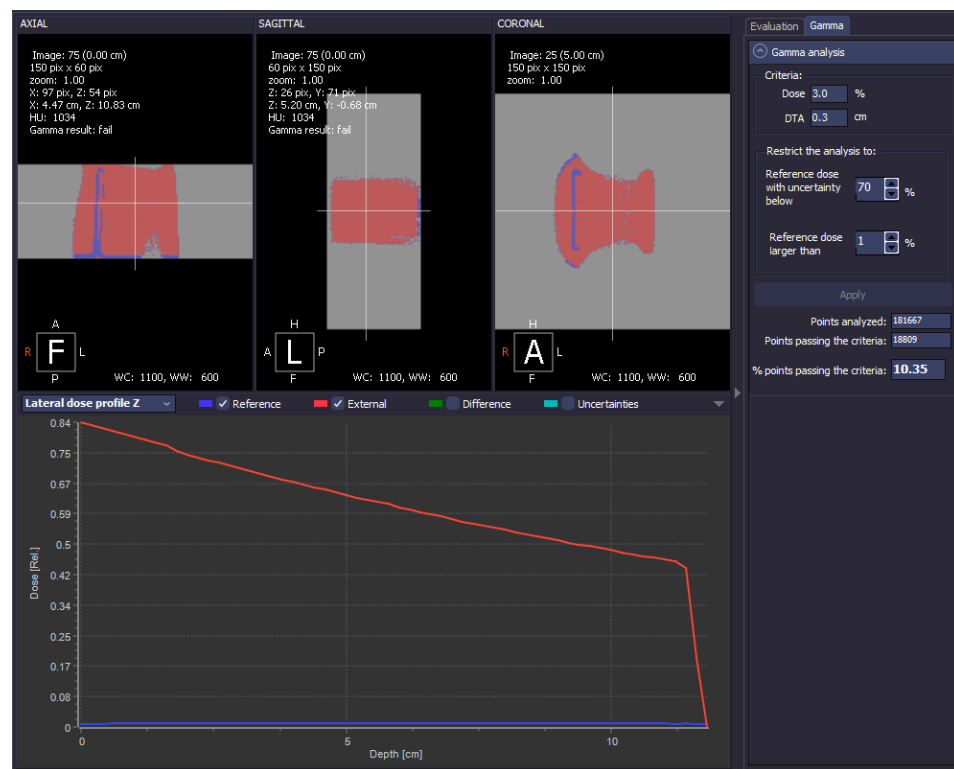
(b)

Figure 36 - (a) Dose distribution calculated by PRIMO. At the top of the image the dose profiles taken along the axial, sagittal, and coronal directions of the orthogonal planes relative to point selected in the views, which is the isocenter in this case, are represented. Below it is illustrated the dose profile on the x axis at the isocenter plane (left) and a 3D view of the calculated dose distribution (right); **(b)** Gamma analysis between the PRIMO and TPS dose calculations performed on PRIMO. The voxels that pass the criteria are represented in blue and those that fail the criteria are indicated in red. The curves below represent the comparison of the transverse dose profile on the z axis between the PRIMO (blue) and the RP file (red) dose distributions at the isocenter.

5.3.2.) Second Approach

After analyzing the results obtained from the previous case, a different approach was performed in order to obtain a dose distribution more similar to the TPS calculation. The ideal solution would have been the exportation of the plan from the TPS with additional control points, however it was not possible to perform such task on Eclipse™. As a result, a second simulation was executed after editing the .ppj of the project, which is a text file generated when a new PRIMO project is created that includes all the data about the plan imported to the software.

Since PRIMO only simulates the irradiation in each control point as if each individual point is a static configuration of the setup, this approach consisted in inserting an adequate number of control points in the .ppj file as a way to mimic the continuous movement of the MLC. Therefore each control point defined by the DICOM RP file, and respective weight, was divided in multiple and equally spaced "sub"control points with equal weight (figure 26) in order to simulate the constant velocity of the 1cm gap. The obtained results are shown in figure 37.

From this image, it is visible that the simulated dose distribution is more similar to the TPS calculation comparatively to previous approach, being verified a significant increase in the percentage of points passing the same gamma criteria. Consequently, it is possible to conclude that the addition of control points approximates the simulation conditions to the real behavior of the MLC, which is a continuous motion from one control point to the next.

Afterwards, a radiochromic film was placed at a depth of 5cm in a solid water phantom and, subsequently, irradiated under the same conditions simulated for this plan.

However, the gamma analysis tool provided by PRIMO does not allow the comparison between measured and calculated dose distributions (by TPS or PRIMO), because it can only import a PRIMO calculation or a DICOM RD file. Therefore a different program had to be considered for this assessment. VeriSoft® was the software used for such task, but it only imports images in the DICOM format, consequently both the PRIMO dose calculation and the digitalized image of the radiochromic film had to be converted to this format. The conversion of the PRIMO result was performed using a MatLab® tool available at IPOPFG, which converts the dose text file exported by PRIMO to a 3D DICOM file that represents the calculated dose distribution in the different axes of the considered phantom, or patient. On the other hand, the digitalized images of the radiochromic films are saved as TIFF (Tagged Image File Format) with a

resolution equal to 72 dpi (dots per inch), therefore a MatLab® function was created for
the conversion of those images from TIFF to DICOM with an adequate pixel spacing.
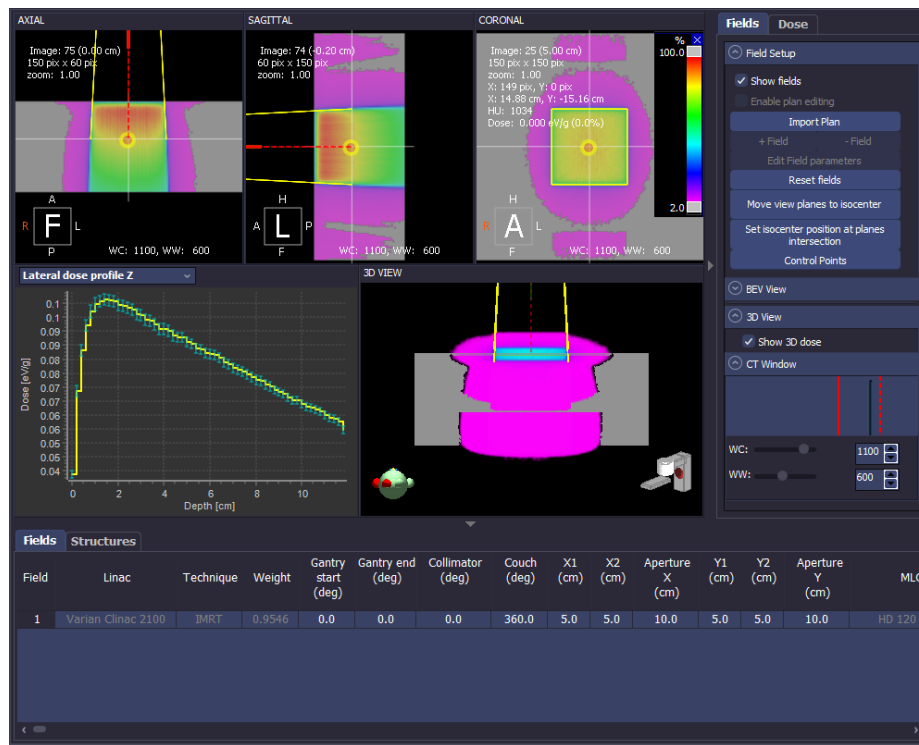
(a)
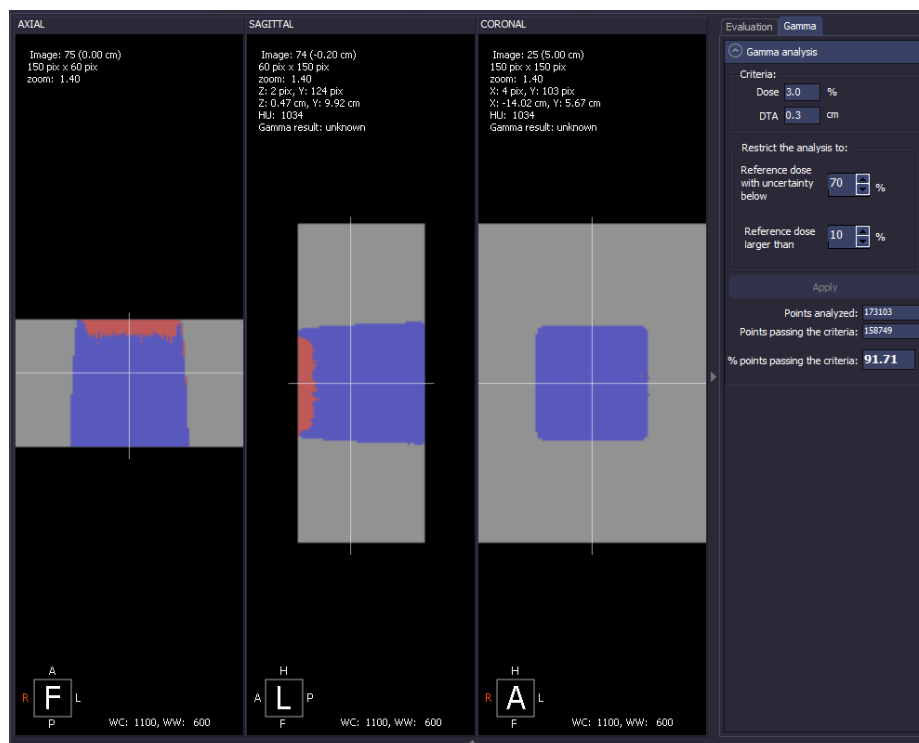
(b)

Figure 37 - (a) Dose distribution obtained after the addition of control points to the .ppj file; **(b)** Gamma analysis
between the PRIMO and TPS calculation, performed on PRIMO.

After the conversion of all the data to the DICOM format, the measured dose distribution was compared against both calculations (PRIMO and AAA algorithm). The results obtained in this process are represented next:

Compared Images	Passing rate
TPS + PRIMO	100.0%
Film + TPS	88.8%
Film + PRIMO	83.8%

Table 6 - Passing rates obtained in the gamma analysis performed between the film and the calculated dose distributions for the IMRT plan.

Table 6 indicates that for the evaluation considering the PRIMO simulation and the AAA calculation all the points pass the gamma criteria. However when those dose distributions are compared against the film, the passing rates fall below the 90% tolerance level established for this study. In figure 38, a representation of the comparison between the TPS and the film is illustrated:
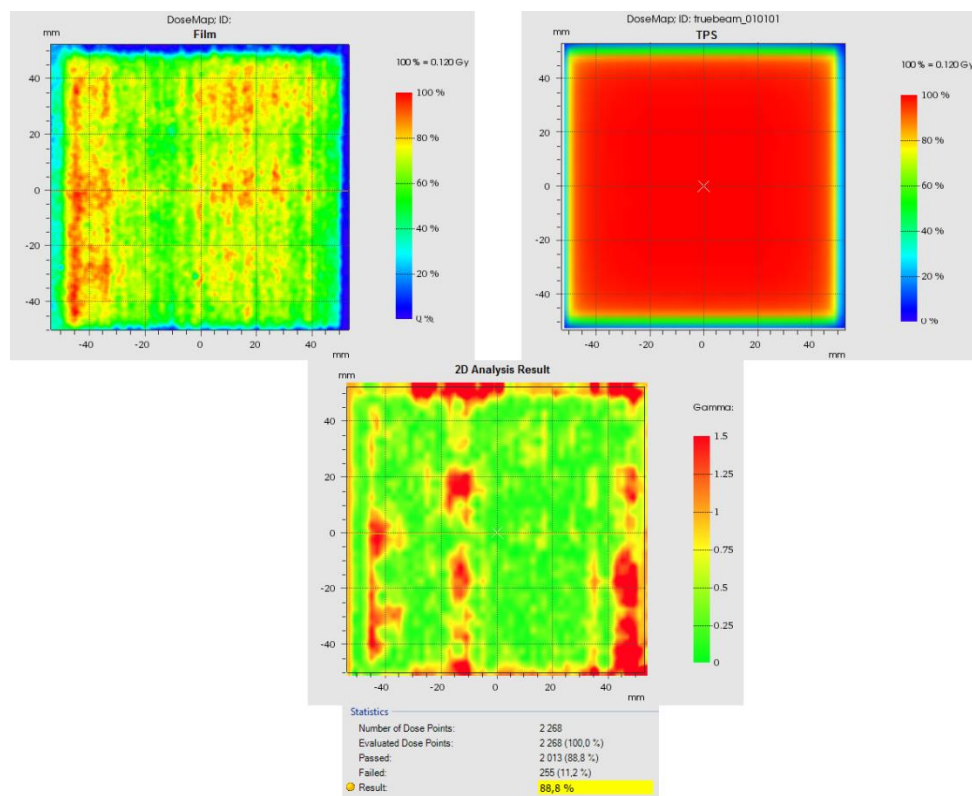
Figure 38 - 2D gamma analysis performed between the film and the TPS calculation.

The film shows a fluctuation of the dose values along the 10x10cm^2 field rather than a homogeneous dose distribution, as calculated by Eclipse^{TM} and PRIMO. From figure 38 it is possible to verify that the maximum dose measured by the dosimeter was 0.120Gy, which is a value located near the lower detection limit indicated for the Gafchromic^{TM} EBT3 film (section 4.1.4.)) and out of the recommended measurement

range for IMRT specified for the dosimeter. Therefore, the reason behind this effect is probably the fact that the film received doses out of its dynamic/optimal range.

In order to measure and assess the dose distribution delivered by the TrueBeam[TM] for this particular siuation a different tactic was employed. The new approach consisted in simulating the same plan under identical conditions, but with an SSD of 100cm. The PRIMO dose distribution and the AAA calculation for this new case were then compared in VeriSoft[®] against an image acquired with the EPID of the TrueBeam[TM]. The resulting passing rates are indicated in the following table:

Compared Images	Passing rate
TPS + PRIMO	100.00%
Portal + TPS	100.00%
Portal + PRIMO	99.50%

Table 7 - Passing rates obtained in the gamma analysis performed between the portal image and the calculated dose distributions for the IMRT plan.

Table 7 indicates that all the comparisons performed pass the gamma analysis with more than 99% of the points passing the acceptance criteria.
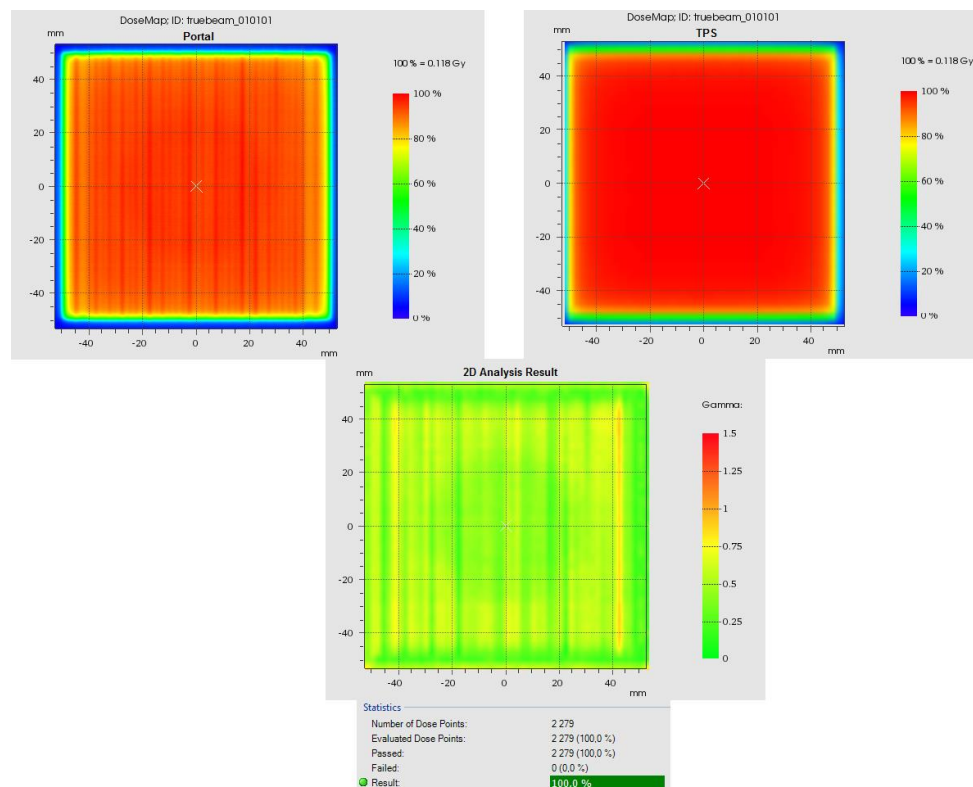
Figure 39 - 2D gamma analysis performed between the portal image and the TPS calculation.

It should be taken into account that the flat panel of the EPID is composed by materials that are non-water-equivalent and PRIMO does not provide a model of that device (Han, B. *et al*, 2017). Therefore, for more complex plans there may not be as

good agreement between calculated dose distributions and portal measurement, as the one obtained in this case.

Nevertheless, from the study performed about IMRT it is possible to draw two conclusions. The first is associated to the EPID of the TrueBeam™, having been verified that it can be an adequate tool to measure doses lower than the dynamic dose range of the EBT3 film. The second conclusion is that as the number of control points is increased, the dose delivery conditions simulated by PRIMO become more similar to the real radiation delivery environment. Therefore, in order to simulate the actual behavior of the LINAC in PRIMO, an infinite number of control points would have to be added between each control point specified by the DICOM RP file, but practically it is not possible to perform this task yet. This problem was addressed in more detail, for the previous version of PRIMO, in the master's degree thesis by Oliveira, J. on the theme "Clinical implementation of Monte Carlo simulations of a Varian TrueBeam unit".

5.4.) Brain VMAT Plan on RUPERT

After the study of the IMRT simulation mechanism employed by PRIMO, an investigation on how this software simulates the VMAT technique was performed. A typical VMAT plan exported by Eclipse™ has 177 control points per complete arc, which means that there is a control point for about 2º of gantry rotation angle (Lin, M.-H. *et al*, 2013). In this case, the brain plan imported to PRIMO is composed by 2 full arcs, leading to a total of 354 control points (figure 40 – control point number zero is also considered). Therefore it is expected a simulated dose distribution similar to the real situation, even without the addition of control points to the .ppj file.

The versions of PRIMO used throughout this thesis provide a new feature, already applied in the IMRT study, which allows the user to perform a comparison based on the gamma index between a PRIMO simulation and a DICOM RD file, or between two PRIMO simulations. With this evaluation method it is possible to assess the dose delivered to the different structures defined by the DICOM RS file. Such tool was applied in this work as a way to compare the dose distributions calculated by the TPS (AAA algorithm) and by PRIMO for the PTV, right eye, left eye, spinal canal, and brainstem.

The gamma criteria recommended by several scientific reports for the VMAT QA procedure, such as Heilemann, G. *et al*, 2013; Kim, J. *et al*, 2014; Kim, J. *et al*, 2017; Laub, W. *et al*, 2013, is 2% dose difference and 2mm distance-to-agreement (DTA) with a 90% tolerance level for the passing rate. The results obtained from the application of these criteria are shown in table 8.

Figure 40 - Number of control points associated with the brain VMAT plan simulated in PRIMO.
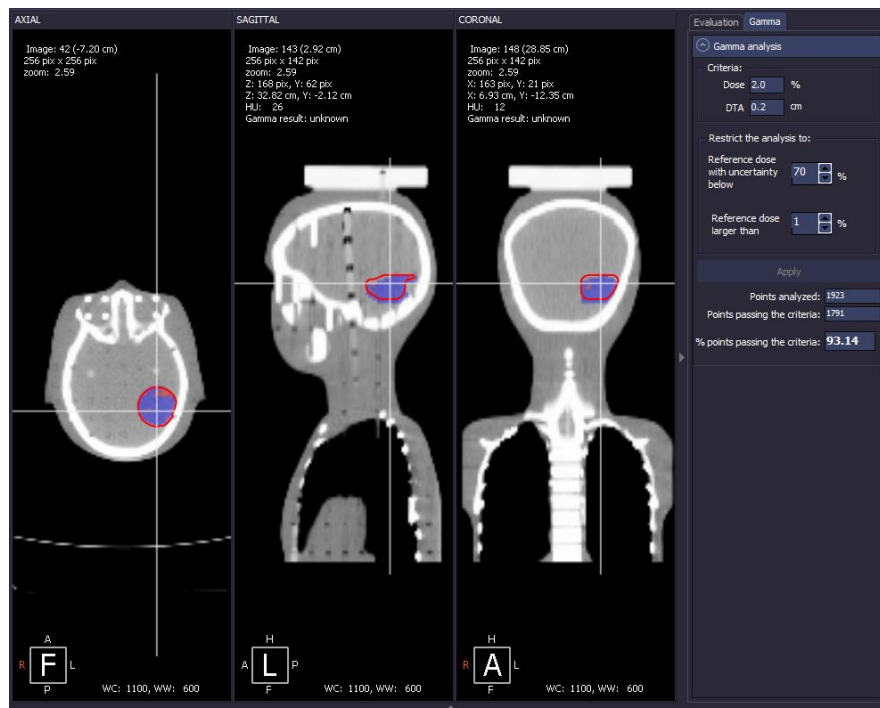
Figure 41 - Example of a gamma analysis for the PTV performed in PRIMO. The grey axes intersection represents the
isocenter

Structure	Passing rate
PTV	93.14%
Right Eye	100.00%
Left Eye	99.68%
Spinal Canal	99.83%
Brainstem	99.03%

Table 8 - Gamma analysis results for the structures of interest.

All the comparisons performed demonstrate a passing rate above 90%, this is an indication that number of control points defined by the DICOM RP file can be adequate for the simulation of VMAT treatment plans in PRIMO, nevertheless a comparison involving measurements is required.

Therefore, the dose distribution was measured in two planes of RUPERT by placing radiochromic films between different slices of that phantom (section 4.3.6.)). Afterwards, the 2D gamma index analysis tool provided by VeriSoft® was used for the comparison of the calculated and measured dose distributions, however before this assessment the same conversion process of the PRIMO simulation and the measurements to the DICOM format performed in the IMRT study was executed.

.For this evaluation, the gamma criteria previously stated as the recommendation for VMAT QA procedures was applied.

An important effect that needs to be taken into account in this comparison is the fact that PRIMO does not only simulate the dose distribution inside the body, but also calculates the energy deposited outside of that volume. These doses are originated due to the scattering of radiation by different structures, such as the body, the treatment couch, or the head of the gantry, and they were not included in the TPS calculation or in the measurement (figure 42).

Consequently, all the information outside of the body structure was removed in the conversion of the PRIMO dose text file to DICOM in order to improve the 2D gamma analysis results (figure 43).
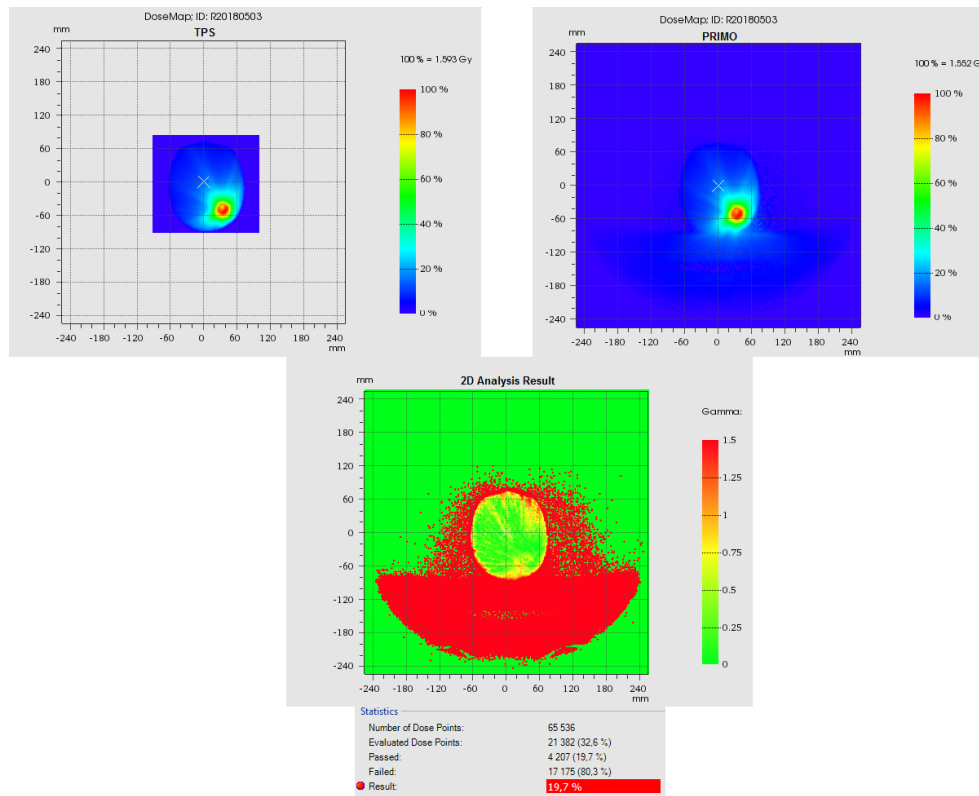
Figure 42 - Effect of the out of the body doses on the 2D gamma comparison performed in VeriSoft® between the AAA calculation and the PRIMO simulation.
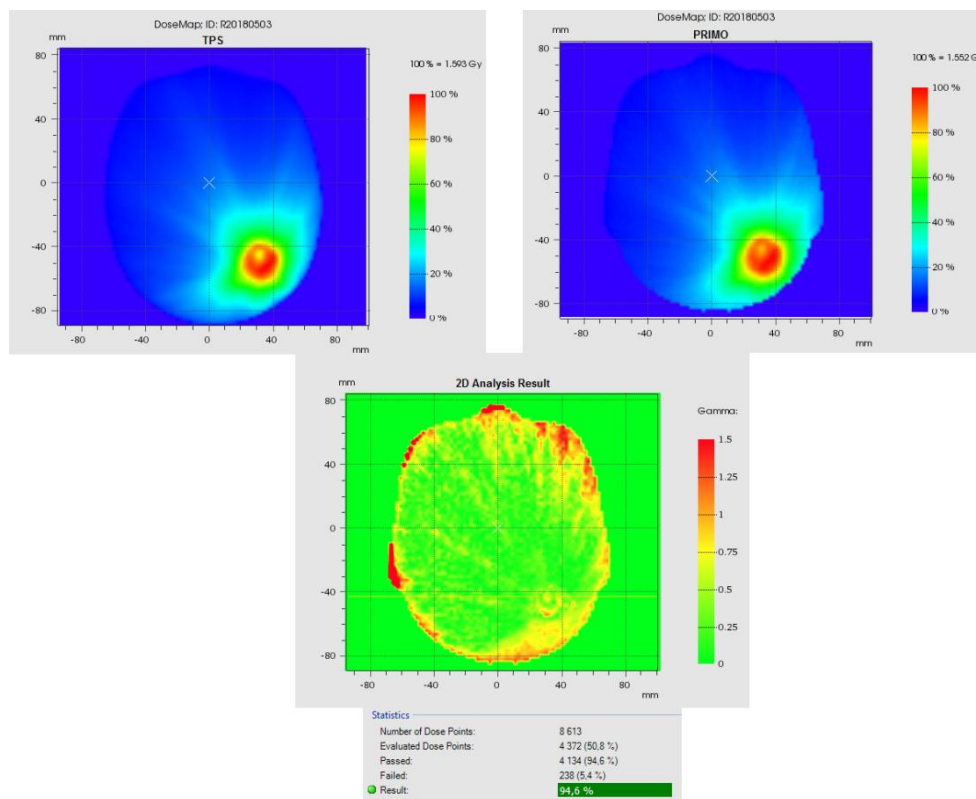
Figure 43 - 2D analysis, performed in VeriSoft®, between the TPS calculation and the PRIMO simulation after the removal of all the information outside of the body structure.

Afterwards, an additional problem appeared when the dose calculations were compared against the films. As illustrated in figure 44, the points closer to the isocenter pass the gamma criteria, however as the distance to that location increases the gamma evaluation begins to fail for the assessed points. This effect also occurs when the TPS calculation is compared with the measurement as well as for the two films analyzed.

Both calculations, i.e. TPS and PRIMO, had good agreement between them (figure 43), therefore the reason behind this significant fail of the gamma index in the regions further away from the isocenter was probably related to the film. When the dose in those regions was examined it was verified a maximum reading of 0.109Gy. This value is very close to the lower detection limit indicated for the EBT3 film (section 4.1.4.)). Consequently, it was concluded that the areas of the film more distant to the isocenter do not pass the gamma criteria because they received doses below the minimum recommended value for VMAT (0.2Gy), which were also very close, or possibly inferior, to the lowest detection capacity of the EBT3 film (0.1Gy). Nevertheless if the objective was the evaluation of the dose in those zones, this problem could have been solved by performing, for example, an irradiation corresponding to 10 fractions of 2Gy at the isocenter. As a result, in the low dose regions there would be a dose of about 1Gy, detectable by the film.

However, in this work the objective is to evaluate the dose delivered to the volumes of interest near the isocenter, therefore it was not justifiable to increase the irradiation because the upper detection limit of the film recommended for VMAT procedures is 10Gy, consequently it was desired to keep the dose below this value at that location.

The obtained results for the two dose planes evaluated, which were located at -3.5cm and -6.25cm from the isocenter marked in the phantom relatively to the z axis, are represented in tables 9 and 10 in terms of percentage of points that pass the criteria.

-3.5cm z	
Compared images	**Passing rate**
TPS + PRIMO	97.8%
Film + TPS	91.2%
Film + PRIMO	91.9%

Table 9 - Percentage of points passing the gamma criteria, considering the different dose distributions evaluated in VeriSoft® for the slice placed at -3.5cm from the isocenter marked in the phantom relatively to the z axis.
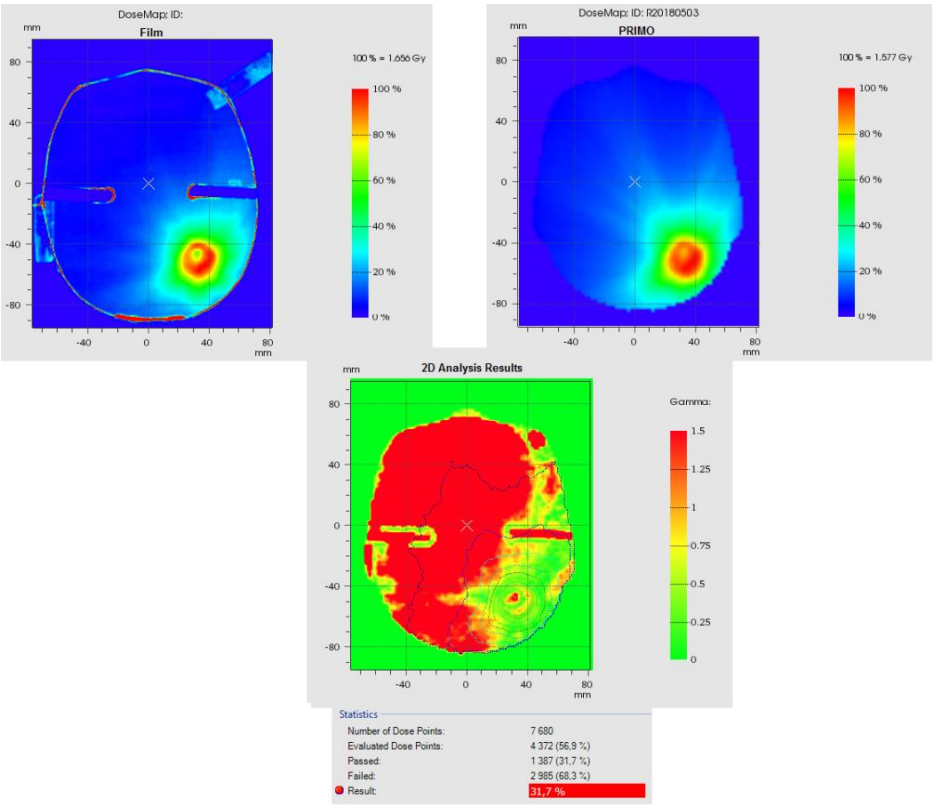
Figure 44 - Effect of the distance to the isocenter in the 2D gamma analysis results. In the bottom image the isodose lines for the PRIMO calculation are represented.
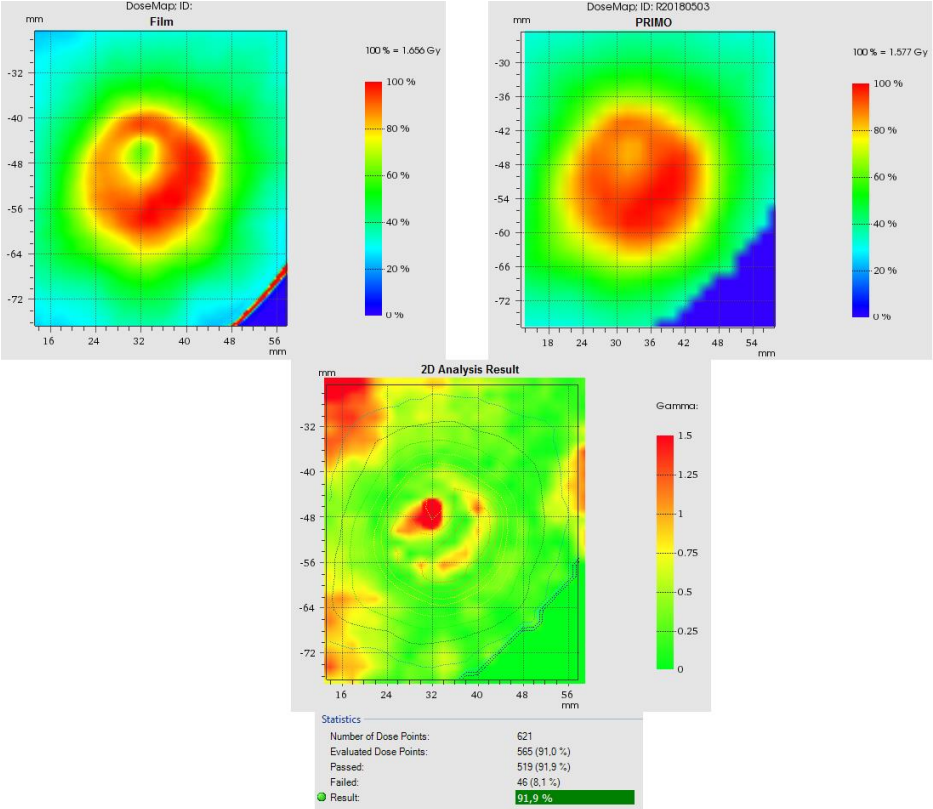
Figure 45 - Result of the gamma analysis only considering the region of the distribution closer to the isocenter.

-6.25cm z	
Compared images	**Passing rate**
TPS + PRIMO	99.6%
Film + TPS	99.6%
Film + PRIMO	99.0%

Table 10 - Percentage of points passing the gamma criteria, considering the different dose distributions evaluated in VeriSoft® for the slice placed at -6.25cm from the isocenter marked in the phantom relatively to the z axis.

In both situations, an important aspect that can affect the comparison between the measurement and the calculation (either by the TPS or PRIMO) is the fact that the boundaries of the films have an abnormal dose value. Such artifacts appear in the digitalized images because those dosimeters have to be manually cut in order to be placed between the phantom's slices. Thus, since DoseLab interprets these locations as dose received by the film in its conversion process from optical density to dose, the gamma analysis will always be influenced by this effect (figures 46 and 47).
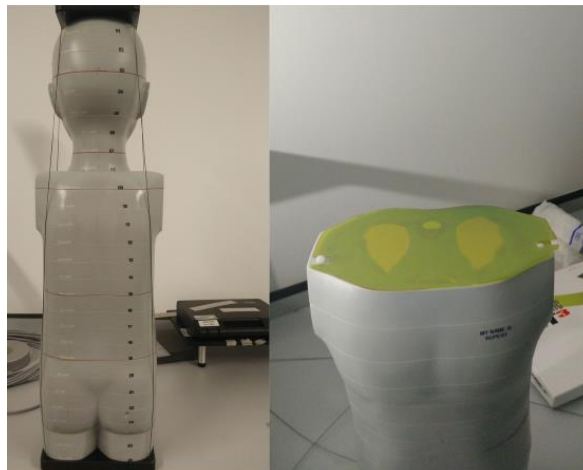
Figure 46 - Radiochromic film placing in the RUPERT phantom (adapted from Ghareeb, F. *et al*, 2017).
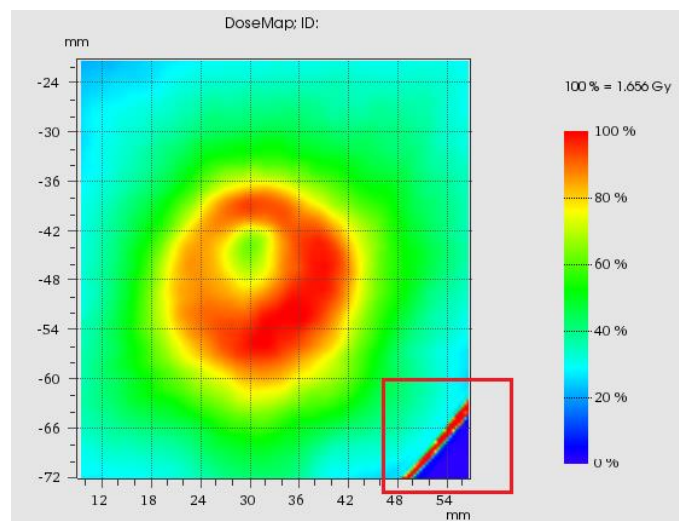
Figure 47 - Film boundary interpreted as dose in VeriSoft®.

Considering the results involving the measurement indicated in table 9, the lower gamma passing rate between the film and the TPS dose distribution can be due to various factors. One aspect possibly affecting this evaluation is that, unlike PRIMO, the TPS does not calculate the dose distribution based on the Monte Carlo method, which is considered the gold standard for the simulation of the radiation transport in matter, because the long calculation times associated with that approach still make it unsuitable for application in the clinical practice (Seco, J. *et al*, 2016). In this analysis, the dose distribution predicted by the TPS was calculated using the AAA algorithm, which is a model-based algorithm. Even though this dose calculation tool is commonly used for the clinical practice, mainly due to its fast calculation time and precision on the treatment field region, its accuracy is known to decrease on low dose regions outside the treatment field, leading to significant underestimations of the out-of-field doses; and beyond low density regions (Dunn, L. *et al*, 2015; Esch, A. V. *et al*, 2006; Kroon, P. S. *et al*, 2013; Rønde, H. S. *et al*, 2009; Shields, L. B. E. *et al*, 2015; Wang, L. *et al*, 2014). Other parameter that may be influencing the comparison is the fact that the DICOM RD file used for comparison, which represents the full TPS calculation, stores the calculated dose in a dose cube of normalized values. The DICOM header of that file includes the information required to build the dose slices of the phantom from that cube, such as number of slices, number of lines, number of columns, pixel spacing, and dose scale factor used for the normalization. This means that it is possible to extract the dose planes according to the grid defined in the header of the DICOM RD file. Consequently, if this grid does not originate sufficiently "thin" slices that correspond to the location of the measurements, an uncertainty resulting from the interpolation of the dose between various dose points of the calculation grid will occur and the gamma analysis results will be affected by this interpolation error, especially if the analysis is performed, as in this case, in steep dose gradient regions, which are very frequent in modulated techniques. The disadvantage of reducing the voxel size to produce the desired dose planes is the increase in the calculation time. On the other hand if a larger voxel size is used, the calculation is performed faster, but the spatial resolution decreases (Karen, C. S., *et al*, 2017; Siebers, J. V., 2011). Therefore a compromise between these two parameters should be made. An additional aspect that can affect this comparison is the fact that the TPS dose distribution analyzed, in this case, did not considered the effect of the couch in the dosimetric calculations performed.

In the comparison involving the film and the PRIMO calculation, two aspects that influence the gamma analysis can be considered. The first, discussed in section 5.3.), is the fact that PRIMO simulates the irradiation conditions only based on the

control points, not mimicking the continuous adjustment of the several parameters actually performed by the LINAC. The other reason is that the conversion of the dose text file exported from PRIMO to the DICOM format also depends on a grid. The characteristics of this grid (e.g., number of voxels, voxels size) are described in a dose text file exported from PRIMO. Afterwards, the MatLab® application, used for the conversion of the text file to a DICOM file, will write in the header of the newly created 3D DICOM file the information obtained from the dose file exported by PRIMO, based on the grid parameters. This file represents the dose distribution in the phantom for a discrete set of locations. Consequently the DICOM image that exactly corresponds to the measuring position in the phantom may not be available, just like in the previous case, and therefore an interpolation error occurs. As previously mentioned, this factor can be particularly relevant in the gamma analysis of steep dose gradient regions, like the one addressed in this case.

For the film placed at -6.25cm in the z axis relatively to the CT markers in the RUPERT phantom, it is possible to see that all the comparisons have a higher passing rate (table 10) than the previous case. The difference, between the results obtained for this film and for the one analyzed in table 9 is possibly due to the fact that the latter is further away from the isocenter, in a region with a steeper dose gradient (figure 48). As a result, for that film the interpolation error verified between the DICOM images and the irradiated films has a major impact in the results obtained from the gamma analysis.
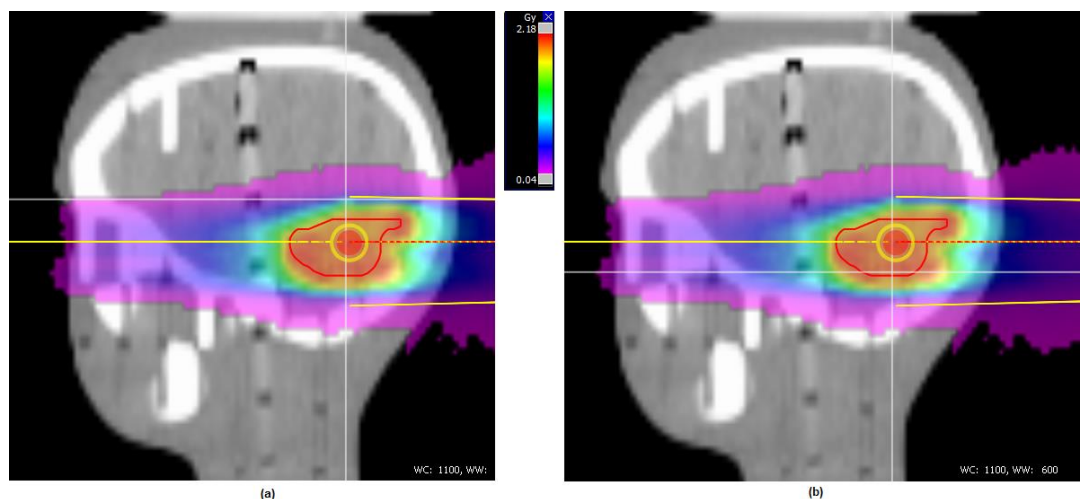
Figure 48 - Intersection of two grey axes in the sagittal view representing the localization of the films placed at **(a)** -3.5cm and at **(b)** -6.25, from the isocenter marked in the phantom relatively to the z axis. The red curve represents the PTV.

Nevertheless, all the comparisons performed have more than 90% of the points passing the gamma criteria. As a result, the PRIMO simulation of VMAT treatment plans can be considered a valid method to assess the dose distribution in clinical cases involving this technique, based on the Monte Carlo method.

5.5.) Abdominal VMAT Plan on RUPERT

After analyzing the results obtained from the brain VMAT plan, the next step consisted in assessing the dosimetric effects due to clinical setup mismatches of the RUPERT phantom, in the treatment couch of the TrueBeam^{TM} LINAC, for an abdominal VMAT plan created in Eclipse^{TM}.

5.5.1.) Influence of a RUPERT Positioning Mismatch in the Dose Distribution

5.5.1.1.) Evaluation of the Dose Delivered to the Different Volumes

Similarly to the VMAT plan for the brain, the first step in this study was the assessment of the simulated and TPS calculated (AAA and Acuros XB algorithms) dose distributions using the PRIMO gamma comparison tool for two positioning situations (section 4.3.7.)). The volumes analyzed were the ones closer to the PTV and the same criteria applied in the previous VMAT plan were used, with an identical tolerance level for the passing rate. The obtained results are presented next:

Without positioning mismatch		
	PRIMO + AAA	PRIMO + Acuros XB
Volume	Passing rate	Passing rate
CTV	91.26%	92.04%
PTV	92.03%	92.03%
Left Kidney	99.58%	99.44%
Right Kidney	99.87%	99.87%

Table 11 - Passing rates obtained in the gamma analysis for the different volumes of interest performed in PRIMO, not considering a positioning mismatch.

With positioning mismatch		
	PRIMO + AAA	PRIMO + Acuros XB
Volume	Passing rate	Passing rate
CTV	91.90%	92.02%
PTV	90.95%	91.86%
Left Kidney	97.25%	99.08%
Right Kidney	99.94%	98.42%

Table 12 - Passing rates obtained in the gamma analysis for the different volumes of interest performed in PRIMO, considering a positioning mismatch of +0.5cm in the x axis.

From both tables it is possible to verify that all the volumes considered pass the gamma evaluation in the situations analyzed. The results also show that Acuros XB generally has a slight better agreement with the PRIMO calculation than AAA, being more evident for the left kidney in the case with positioning mismatch. This can be possibly interpreted as an indicator that Acuros XB predicts the dose distribution more accurately, however a comparison involving calculations and measurements is needed in order to verify which TPS algorithm calculates the dose distribution with more precision. Consequently, in the following work four radiochromic films where placed inside the RUPERT phantom and irradiated with the same plan under identical conditions for similar setups, i.e. with and without the considered positioning mismatch.
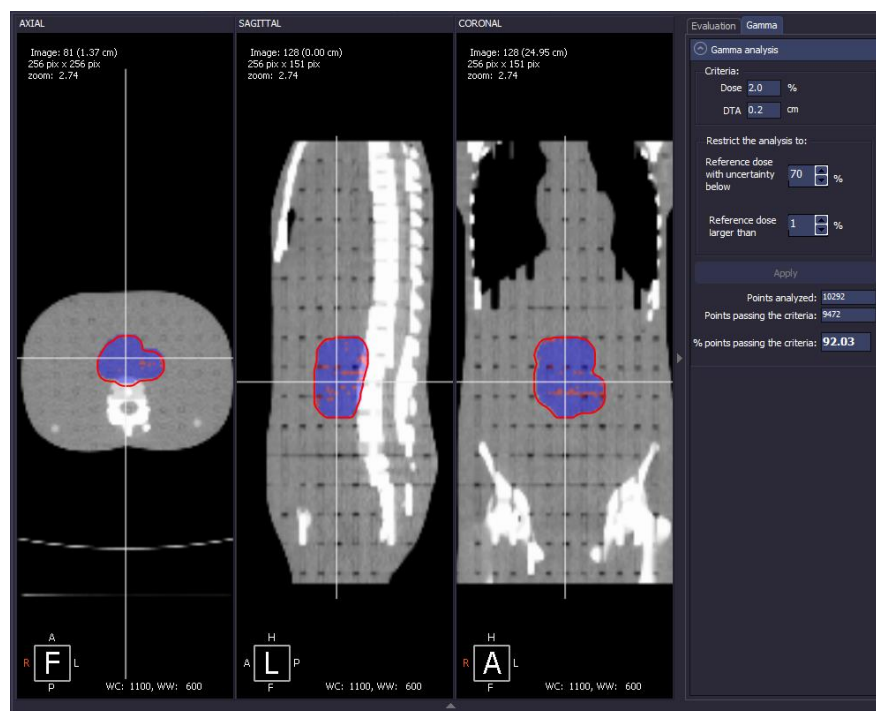
Figure 49 - Example of a gamma analysis of the PTV (red curve) performed in PRIMO for the situation without a positioning mismatch, considering the simulation and the AAA calculation. The grey axes intersection represents the isocenter.

5.5.1.2.) Evaluation of Measured and Calculated Dose Distributions

In this step, the 2D gamma analysis tool provided by VeriSoft[®] was used to perform a comparison of the dose distributions for the two positioning situations, one without any setup mismatch and the other with the phantom displaced +5mm in the x axis relatively to the isocenter of the plan. The dose distributions analyzed in this case were the PRIMO calculations, the irradiated films, and the TPS calculations (by the AAA and Acuros XB algorithms). Similarly to the analysis performed for the brain

VMAT plan, only the region of the films closer to the isocenter was considered, because an identical effect in the gamma index for areas further away from that point was verified. The obtained results of the gamma analysis, based on the same gamma criteria and tolerance level for the passing rates previously specified for VMAT procedures (section 5.4.)), are represented in tables 13 to 16:

Without positioning mismatch				
Film position	**-3.75cm**	**-1.25cm**	**+1.25cm**	**+3.75cm**
Compared images	**Passing rate**	**Passing rate**	**Passing rate**	**Passing rate**
Film + AAA	98.4%	99.0%	97.1%	88.8%
Film + PRIMO	98.9%	98.9%	96.2%	90.9%
AAA + PRIMO	100.0%	99.2%	99.0%	97.0%

Table 13 - Passing rates for the situation without any positioning mismatch, considering the AAA algorithm.

With positioning mismatch				
Film position	**-3.75cm**	**-1.25cm**	**+1.25cm**	**+3.75cm**
Compared images	**Passing rate**	**Passing rate**	**Passing rate**	**Passing rate**
Film + AAA	99.0%	99.9%	98.9%	86.5%
Film + PRIMO	99.1%	99.8%	97.5%	91.4%
AAA + PRIMO	100.0%	99.7%	99.3%	96.7%

Table 14 - Passing rates for the situation with a positioning mismatch of +0.5cm in the x axis, considering the AAA algorithm.

Without positioning mismatch				
Film position	**-3.75cm**	**-1.25cm**	**+1.25cm**	**+3.75cm**
Compared images	**Passing rate**	**Passing rate**	**Passing rate**	**Passing rate**
Film + Acuros	99.4%	99.0%	96.7%	89.3%
Film + PRIMO	98.9%	98.9%	96.2%	90.9%
Acuros + PRIMO	99.9%	99.3%	99.5%	97.9%

Table 15 - Passing rates for the situation without any positioning mismatch, considering the Acuros XB algorithm.

With positioning mismatch				
Film position	**-3.75cm**	**-1.25cm**	**+1.25cm**	**+3.75cm**
Compared images	**Passing rate**	**Passing rate**	**Passing rate**	**Passing rate**
Film + Acuros	99.2%	99.5%	97.0%	88.2%
Film + PRIMO	99.1%	99.8%	97.5%	91.4%
Acuros + PRIMO	98.8%	99.9%	99.6%	97.6%

Table 16 - Passing rates for the situation with a positioning mismatch of +0.5cm in the x axis, considering the Acuros XB algorithm.

In all the situations examined it is possible to verify that for the film placed at +3.75cm in the z axis the percentage of points that pass the gamma criteria decreases, especially in the comparison between the TPS calculations and the film. Analyzing both setups, it is verifiable that the AAA and Acuros XB calculations for the two phantom positions have a significant reduction in the gamma passing rate associated with that film. This decrease is somewhat less substantial when the PRIMO dose distribution is compared against the same film. The reason for this reduction, as can be inferred from figures 50 and 51, is probably the fact that film is placed in a region with a steep dose gradient, were the interpolation error has a major influence in the gamma analysis between measurement and calculations, just like in the brain investigation.

The results obtained also show that the gamma evaluation between PRIMO and the measurement has a higher passing rate, in some cases, than the comparison betwee the film and the TPS calculation (AAA or Acuros XB).
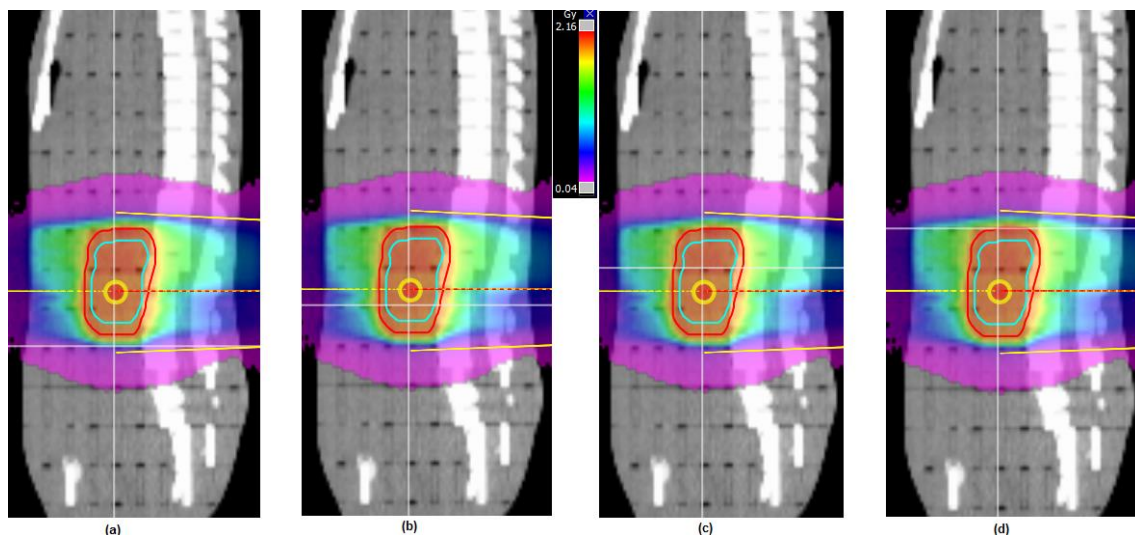
Figure 50 - Intersection of two grey axes in the sagittal view representing the localization of the films placed at **(a)** -3.75cm; **(b)** -1.25cm; **(c)** +1.25cm; **(d)** +3.75cm, from the isocenter marked in the phantom relatively to the z axis, for the case without positioning mismatch. The red curve represents the PTV and the blue curve corresponds to the CTV.
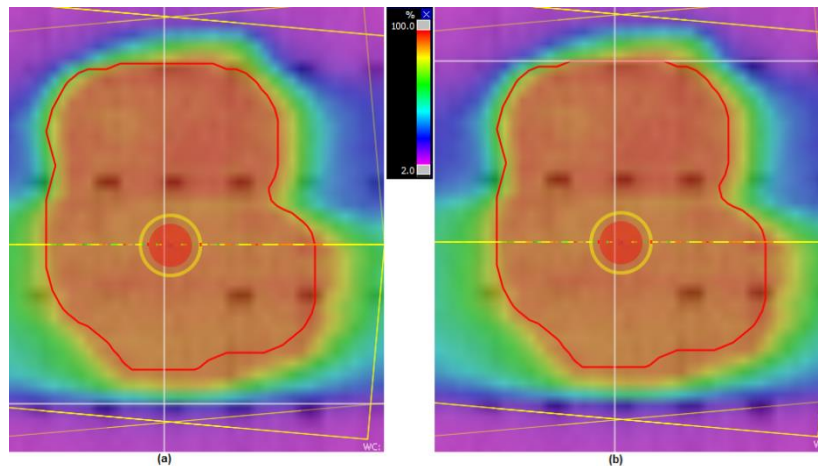
Figure 51 - Intersection of two grey axes in the coronal view representing the localization of the films placed at **(a)**
-3.75cm; **(b)** +3.75cm, from the from the isocenter marked in the phantom relatively to the z axis, for the case without
positioning mismatch. The red curve represents the PTV.

When comparing the TPS algorithms against the measurements, it is possible
to verify that in the region closer to the isocenter the AAA produced slightly better
results, however as the distance to that location increases, it is possible to verify that
Acuros XB has higher passing rates than AAA. Nevertheless, it is important to mention
that the same factors affecting the gamma analysis in the previous study of the brain
case (section 5.4.)) are present in this analysis, except for the film cutting effect due to
the region chosen for the evaluation (figure 52).
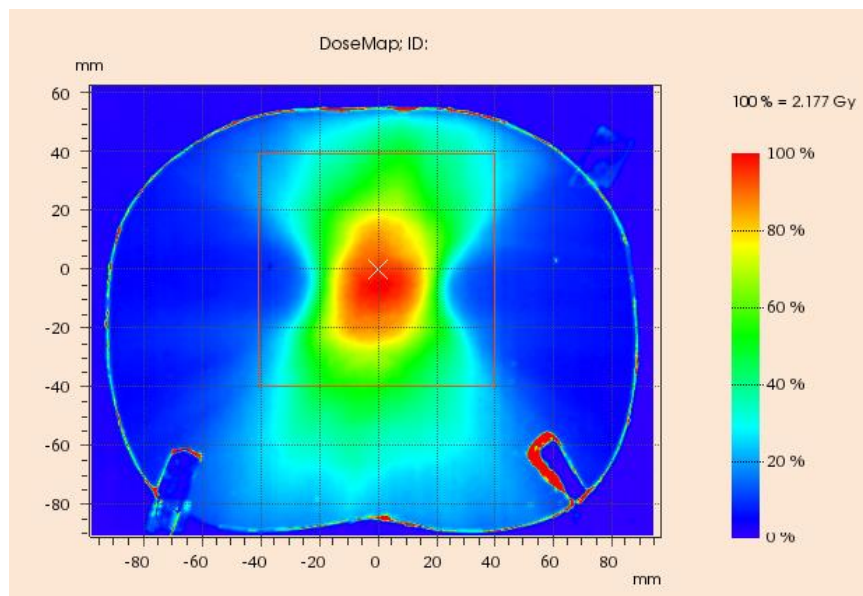
Figure 52 - Red square indicating the region of the films chosen for all the gamma analysis performed in this study.

The results obtained confirm that the dose calculated by PRIMO is comparable
to the dose distributions predicted by both TPS algorithms, particularly near the
isocenter. As Eclipse™ is considered a valid software to calculate the dose
distributions for all the treatment plans created and performed at IPOPFG, from the

results obtained it is possible to conclude that PRIMO can also be considered a valid software to simulate VMAT treatment plans with precision, since the comparison of the measured dose distributions against PRIMO frequently indicates similar, or better, agreement than the comparison between the TPS calculation and the films.

These results are clear indicators that the Monte Carlo method can be a precise dose calculation method, even with PRIMO not taking into account the continuous movement of the LINAC.

5.5.2.) Dosimetric Effects due to Clinical Setup Mismatches

The comparison between calculated and measured dose distributions, performed in the previous study, assessed the dose delivered to the various target volumes and organs-at-risk considering a single positioning mismatch. Therefore, it was of interest to evaluate the dosimetric effects for the different structures that result from additional clinical setup mismatches, in order to evaluate the dose they receive during the irradiation process and to establish the critical conditions for the patient positioning in the treatment room.

This investigation consisted in performing several simulations with various positioning mismatches in the different axis and assessing, for all the simulated cases, the dose received by the different volumes of interest through the analysis of the dose-volume histograms (DVHs), which are calculated by PRIMO (figure 53).

Based those DVHs five parameters were evaluated, namely:

➢ Dmin: the maximum dose received by 100% of the volume/organ;

➢ Dmax: the maximum dose received by the volume/organ;

➢ Dose tolerances established in QUANTEC (Marks, L. B. *et al*, 2010);

➢ V95%: percentage of the CTV and PTV that receives 95% of the prescribed dose;

➢ Percentage dose received by 98%, 50%, and 2% of the PTV.

The first two mentioned parameters where assessed for two situations: a single treatment fraction of 2Gy and a complete treatment composed by 25 individual fractions of 2Gy.

On the other hand, since QUANTEC recommendations are indicated as thresholds of total received dose for the different organs, these dosimetric references where only used in the analysis relative to full treatments, also constituted by 25 individual fractions of 2Gy.

Finally, the V95% and the dose delivered to the PTV are indicated in percentage, therefore those values can be interpreted as being for a single irradiation fraction or for a complete treatment.

In the following pages only the most relevant graphs for this analysis are represented, nevertheless the detailed results for all the considered volumes and evaluated parameters can be found on appendix B.

In graph 18, the Dmin associated to the CTV and the PTV is represented for all the positioning mismatches simulated in PRIMO, considering the 95% of the prescribed dose the dosimetric threshold. In the subsequent illustration (graph 19), the V95% parameter is represented for the same cases.

Lastly in graph 20, the dose delivered to each of the kidneys in all the clinical setup mismatches simulated is depicted considering the limit of 15Gy recommended by the QUANTEC initiative.

The CTV, the PTV, and the kidneys were the cases chosen to be illustrated below because these volumes are considered the most critical in this particular abdominal treatment plan.
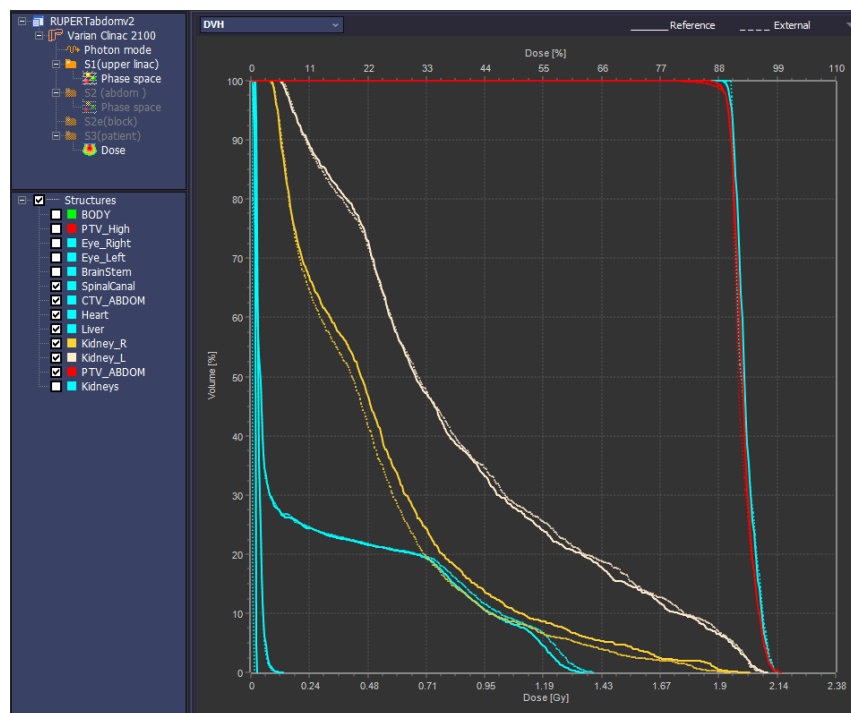
Figure 53 - DVHs comparison for the reference (PRIMO calculation) and external (AAA calculation) dose distributions, relative to the various volumes of interest for a single treatment fraction without positioning mismatch.
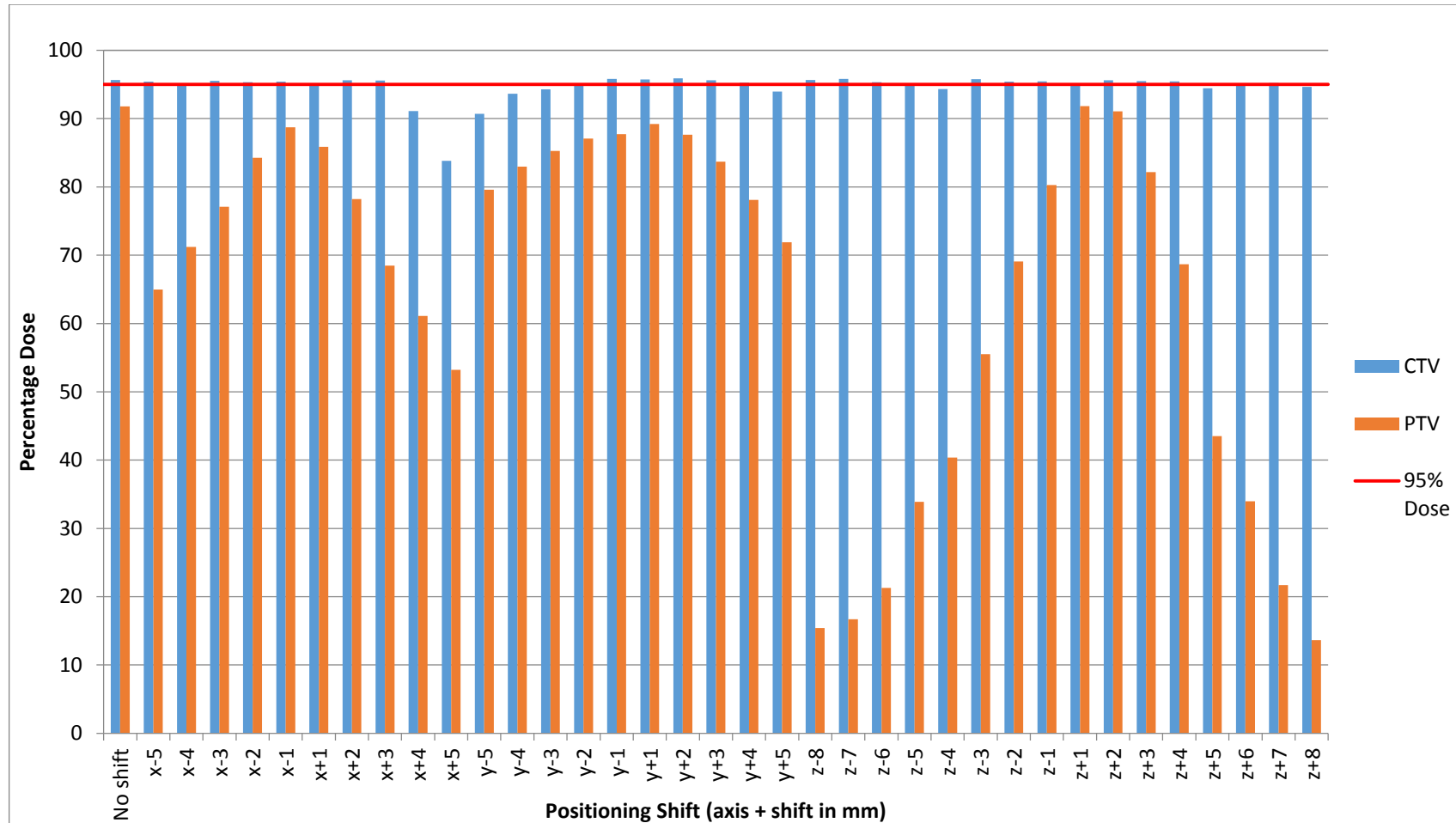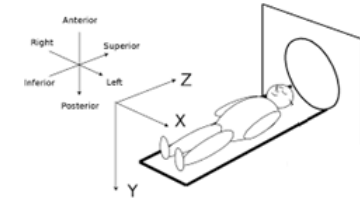
Graph 18 - Dmin parameter assessed for the CTV and for the PTV considering the various positioning mismatches simulated. The red line represents the 95% dose value.
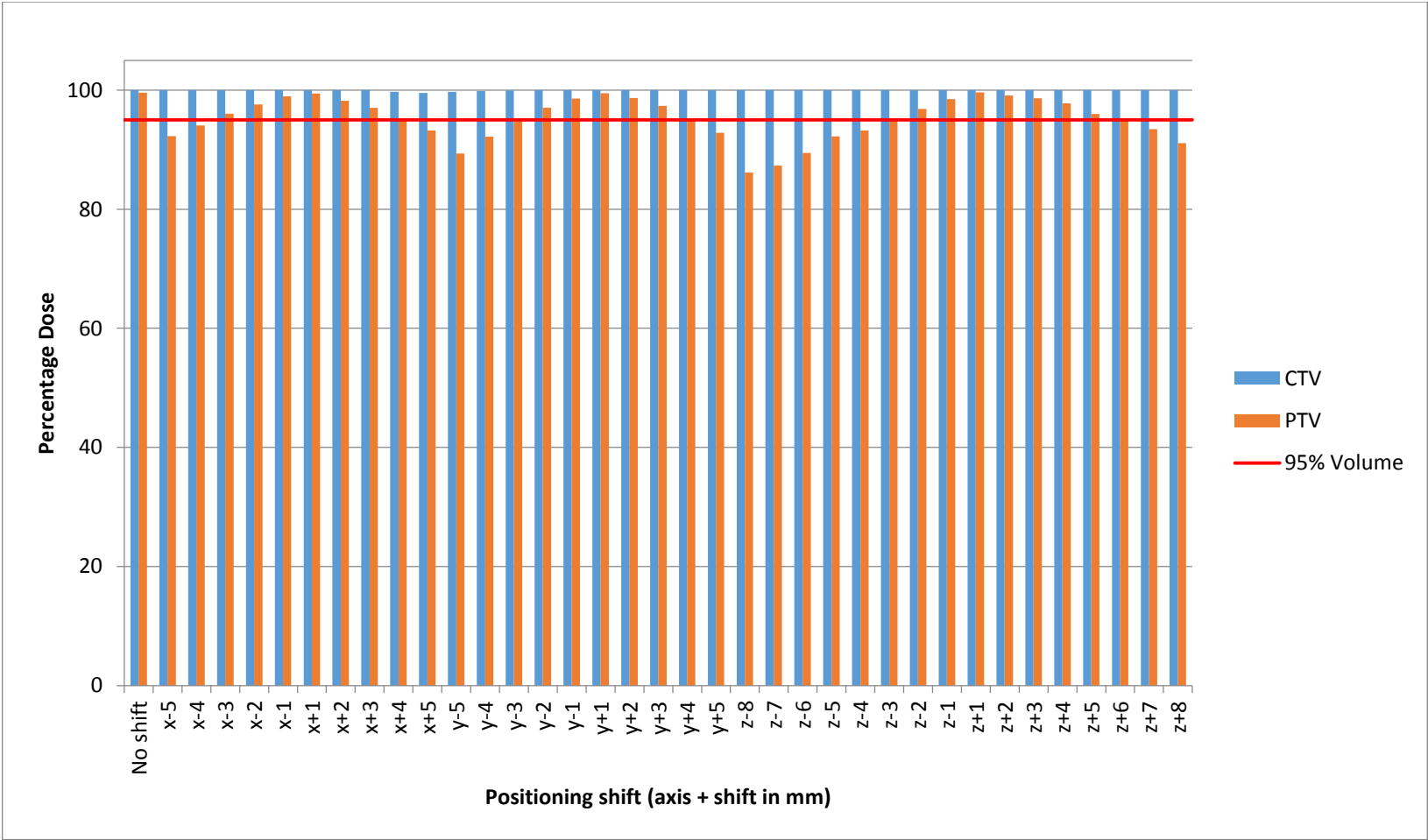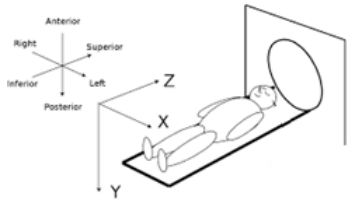
Graph 19 - V95% parameter assessed for the CTV and for the PTV considering the various positioning mismatches simulated. The red line represents the 95% dose value.
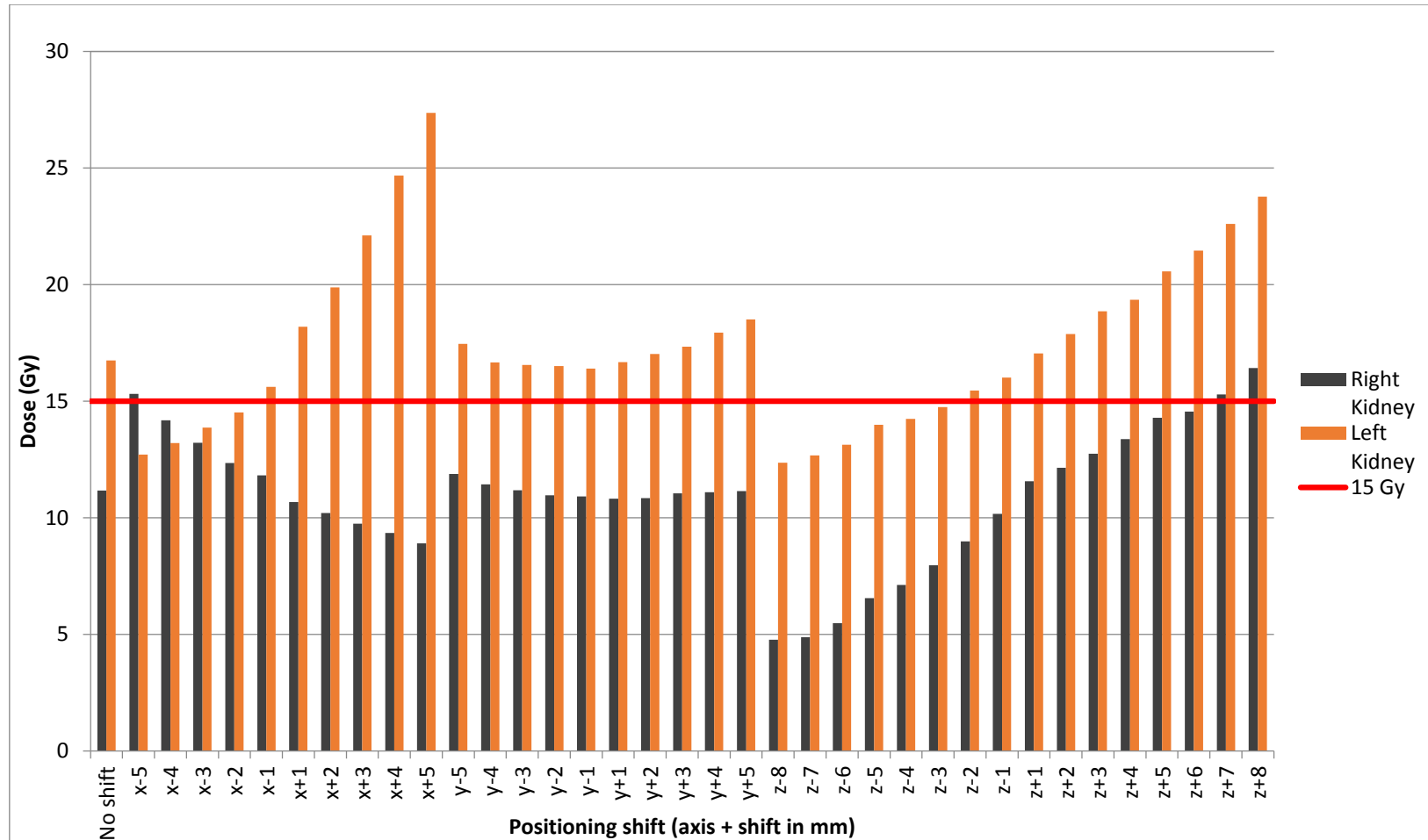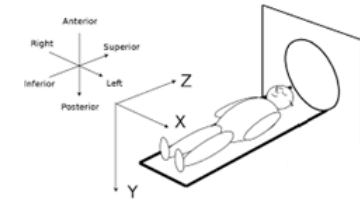
Graph 20 - Dose received by both kidneys for all the positioning shifts considered. The red line represents the 15Gy dose limit recommended by QUANTEC.

The criterion for the CTV coverage considered in this specific plan was that 100% of the volume should receive, at least, 95% of the prescribed dose in each treatment fraction. To ensure the fulfillment of such condition, the CTV was expanded to a PTV by the addition of margins that take into account uncertainties in the size, the shape, and the position of the CTV, as well as imprecisions in the patient's setup. The size of these margins will depend on various parameters, such as the CTV localization (being larger if the CTV is in a region with considerable internal mobility, like the abdomen, and smaller in region with low internal mobility, such as the brain), and inherent deviations from the positioning and treatment equipment.

For this particular plan, anterior-posterior and lateral margins of 5mm along with craniocaudal margins of 8mm were applied in the expansion of the CTV to the PTV. Therefore, the maximum positioning shifts evaluated were $\pm$5mm in the x and y axes, and $\pm$8mm in the z axis. ICRU report 83 indicates that the minimum dose delivered to the PTV depends on the pathology, the tumor localization, and the nearby organs at risk. Different dose normalizations can be used for the PTV, such as 95%, 98% or 100% of the PTV with 95% of the prescribed dose, etc. In this case, it was applied a dose normalization relative to the median dose, i.e. 50% of the PTV volume must receive 100% (2Gy) of the prescribed dose. From the histogram represented in figure 53, it is verified that, without any positioning mismatch, 97% of the PTV receives about 98% of the dose and around 106% of the prescribed dose is delivered to 2% of the PTV.

As can be seen on appendix B, for the positioning shifts in the x axis, the heart, the spinal canal, and the liver receive an approximately similar dose for all the situations. However, for the displacements on the z axis the dose to the liver slightly changes, which is due to the fact that the organ is becoming closer to the irradiation area. It was also expected that the positioning mismatches in the y axis would influence the dose delivered to the spinal canal, due to the anatomical location of that structure. From the obtained results it is possible to conclude that the dose delivered to the spinal canal is indeed affected by the clinical setup mismatch in the y axis, increasing with a mismatch in the positive direction of the axis and decreasing with a shift in the opposite direction.

From graph 18, it is verifiable that the displacements in the x and y axes considerably reduce the dose delivered to the PTV, although not significantly affecting the dose received by the CTV, for most cases. Yet, the shifts of +4mm and +5mm in the x axis and -5mm in the y axis, show a substantial reduction in the dose delivered to the CTV, besides being associated with a decrease in the dose received by the PTV.

For the z axis, even though the dose received by the CTV is always close to 95%, the dose delivered to the PTV is significantly affected by the mismatches. A parameter frequently used for the evaluation of the CTV and PTV coverage of a given plan is the V95%, represented in graph 19. Without any positioning shift it is indicated that 95% of the PTV and CTV receive about 100% of the prescribed dose. This value remains approximately constant for the CTV in all cases, however the coverage of the PTV changes more significantly with the clinical setup mismatches. The magnitude of that variation is clearly related to the size of the deviation, being verified a decrease in the V95% relative to the PTV as the shift increases. From the analysis of graph 19, it is also possible to conclude that displacements greater than 3mm may result in a coverage of the PTV below the 95% volume threshold. Appendix B.2., indicates that for both these volumes the maximum dose is very similar for all the situations analyzed, not being a very useful parameter to assess this coverage.

For the kidneys it is verified that, without any positioning shift, the dose to the left kidney is higher than the QUANTEC recommendation, meaning that the patient may develop clinical dysfunction in that structure, although with a toxicity rate lower than 5%. (in a real case, this would have been clinical decision considering the risk-benefit). A positioning shift in the +x, +y or +z directions will increase even more the dose to that specific kidney while reducing the dose to the one on the right side, this increases the probability of complications for that particular organ. On the other hand, a displacement in the opposite direction (-x, -y, or -z) is going to decrease the dose delivered to the left kidney, increasing in turn the dose received by the one on the opposite side. From graphic 20, it is possible to verify that there are some cases where the dose delivered to both kidneys is kept below the QUANTEC recommendation, however in these situations the dose delivered to the PTV, as well as its coverage, is lower, as can be seen in graphics 18 and 19. This is the reason why the TPS does not consider those patient setups the most adequate ones for the treatment.

Another conclusion from this analysis is that a certain positioning mismatch, in one given axis, produces dosimetric effects that are not necessarily compensated by shifting the patient in the opposite direction by the same distance. This result is somewhat expected because the target volumes and organs-at-risk are not always symmetrical, in relation to one or more axis. Therefore the dosimetric effects arising from clinical set-up mismatches should be compensated through the adaption of the treatment plan, taking into account the dose difference received by different volumes due to patient specific clinical set-up mismatches.

5.5.3.) Action Levels for Abdominal VMAT Plans

As it was mentioned in the introduction chapter, the complexity of the radiotherapy treatments has been increasing throughout the years, leading the enhancement of the dose delivery to malignant cells while minimizing the dose received by the normal tissues (van Dyk, J., *et al* 2014). This evolution has increased the tumor control probability and/or reduced the side effects of the treatment. However, the increase in the technological complexity associated with the treatment techniques, such as VMAT, implies an improvement in the positioning of the patient in the LINAC couch due to the reduction of the safety margins in the treatment plan (van Dyk, J. *et al*, 2014; Washington, C. M. *et al*, 2015).

Nevertheless, in radiotherapy there are often daily differences between the actual and planned position of the patient (Gupta, T. *et al*, 2012). These discrepancies are defined as setup errors and can occur due to two major types of errors (Mundt, A. J. *et al*, 2005):

> Systematic errors: occur when the patient is positioned based on wrong information. Example: incorrect alignment of the LASERs in the treatment room;

> Random errors: occur when the patient is incorrectly positioned due to daily fluctuations. Example: filling of the bladder or stomach.

The positioning mismatches can be evaluated and corrected through the image-guided radiation therapy (IGRT) positioning technique, which provides the capability to image the patient in the treatment room and subsequently compare the acquired information with a reference image that was used for the treatment planning (Gupta, T. *et al*, 2012).The goal of this process is to match the patient positioning in the treatment couch with the position established in the treatment planning, or adapt the treatment plan considering anatomical changes that occur during the course of the radiotherapy treatment (van Dyk, J. *et al*, 2014; Gupta, T. *et al*, 2012).

The setup errors can be managed and minimized, but not completely avoided because there are always uncertainties influencing the patient positioning in the treatment couch, such as stomach and bladder filling, discomfort, shift of the skin marks (tattoos) in relation to the internal tissues, alignment with the LASERs, etc (Barret, A. *et al*, 2009; Walter, *et al* ,2016).

When a setup error is identified, a correction protocol is used to define the optimal course of action. These protocols are classified as offline, online, or real-time and they have different advantages and disadvantages (section 2.6.4.1.)).

The offline correction protocols have particular interest in this study because they minimize the systematic error of the setup, not decreasing the daily setup variation

(Pawlicki, T. *et al*, 2010). In the simulations performed on PRIMO, the systematic error associated with the patient positioning was produced through different shifts in the position of the plan's isocenter, however no random error was simulated.

In this context, an action level can be interpreted as a level of permission around the planned positioning, where the target must exist in after its localization at the beginning of the treatment is determined. Therefore, this volume is said to be aligned if it is located within this action level, even though there is a difference between the measured and the planned positions (Brock, K. K., 2013; Timmerman, R. D. *et al*, 2009). Consequently, it is important to establish adequate action levels to account for all these influences in the clinical setup of the patient (Gupta, T. *et al*, 2012; Halperin, E. C. *et al*, 2013; Timmerman, R. D. *et al*, 2009).

From the analysis of graphic 19, it can be seen that the dose delivered to the PTV drops below the 95% volume threshold for some of the mismatches over 3mm. This can be interpreted, for this specific plan, as the critical positioning condition from where the treatment efficiency begins to decrease significantly. Consequently, 3mm is the action level suggested for this abdominal case.

6.) Protocol for Offline Adaptive Treatment Replanning

Taking into account the dosimetric effects resulting from all the positioning mismatches previously studied, it was of interest to create a clinically applicable protocol that could possibly improve the quality of the VMAT treatments performed in the TrueBeam^{TM} LINAC installed at IPOPFG.

The positioning LASERs located inside the treatment room are periodically checked by the medical physicists working at the hospital, therefore the protocol needed to address a different factor.

A new approach that is being implemented at IPOPFG is adaptive radiotherapy, which was already described in section 2.6.4.2.). In this context, a new protocol, based on the Monte Carlo method, for the offline replanning of the VMAT treatments performed in the TrueBeam^{TM} unit operating at the institution could be useful for the clinical practice.

This protocol is based on the all the validations performed in this work for the 6X energy of the TrueBeam^{TM}.

The steps of this protocol are:

1) Assessment of the patient's exact position in the treatment couch of the TrueBeam^{TM};
2) Realization of two simulations in PRIMO;
   a. Simulation of the treatment plan on PRIMO without any positioning mismatch;
   b. Simulation of the treatment plan on PRIMO applying the positioning shift determined in step 1;
3) Comparison of the DVHs calculated by PRIMO for the two simulations, in terms of:
   a. PTV and CTV coverage;
   b. Recommendations of the QUANTEC initiative for the involved organs-at-risk;
4) Determination of the difference between the planned and received dose for the volumes of interest;
5) Considering the dose difference for the various volumes, a new VMAT plan should be created in Eclipse^{TM}:

a. Determination of the required dose adjustment for the various volumes, in the inverse planning process, by performing the following sum for each:

$$Dose\ Adjustment = Planned\ Dose\ +\ Dose\ Difference$$

b. Determination of the new VMAT plan;

6) (For confirmation) Simulation of the newly created VMAT plan on PRIMO and execution of steps 3 and 4.

This protocol can be performed more quickly and easily using the TPS, instead of PRIMO. However, in this work it was possible to verify that PRIMO can eventually provide a more accurate dose calculation in the regions with steeper gradients, when compared to the TPS, nevertheless this precision depends mainly on the dose calculation grid. A limitation of the planning system is that its dosimetric accuracy decreases in the low dose regions outside of the treatment field, which occur mainly due to the scattering of radiation from external devices (Ghareeb, F. *et al*, 2017; Hoffman, L. *et al*, 2008). The assessment of these out-of-field doses is particularly important in pediatric patients, because the individual has a larger lifespan and, consequently, a higher probability to develop secondary cancers resulting from those radiation doses. Additionally, the Monte Carlo method can be employed to perform dose calculations in complex and dubious cases, where the dose calculation is difficult, such as those involving considerable variations of density between different media, e.g. in regions near cavities full of air.

The major disadvantage of using the Monte Carlo method to calculate the dose distributions is, naturally, the high calculation times associated with the process, which is the major setback for the application of this approach in the clinical practice.

The choice of the TPS algorithm to perform the dose calculations should take into account the specific characteristics of the target volume location. E.g., for calculations involving air medium several reports, such as Alghamdi, M. *et al*, 2015; Kroon, P. T. *et al*, 2013; and Rana, S. *et al*, 2013 concluded that the Acuros XB algorithm was more accurate than the AAA algorithm.

7.) Conclusions and Future Work

With this work it was possible to not only study the dosimetric effects resulting from clinical setup mismatches using the Monte Carlo method, but also provide to IPOPFG important information for the execution of future works.

The material provided to IPOPFG was a validated phase space, as well as the validation of the HD 120™ MLC model, for the 6X energy relative to the TrueBeam™ unit installed at the hospital; and a protocol for offline adaptive treatment replanning.

The first conclusion of this thesis is that the simulation of modulated techniques is a complex problem involving several parameters, which PRIMO tries to approach through the discretization of the continuous adjustments performed by the LINAC. Nevertheless, the results obtained demonstrate a good concordance with the measurements performed for the IMRT and VMAT techniques.

It is also possible to conclude that clinical setup deviations, in VMAT treatments, produce dosimetric effects not considered in the initial planning process. These differences increase as the mismatch gets larger, significantly decreasing the dose delivered to the target volume and therefore leading to eventual tumour recurrence and/or treatment failure. Based on those effects, an action level of 3mm was suggested for the VMAT plan analyzed.

In this work the action level established was only relative to a single abdominal plan that presented some organs at risk near the target volume, therefore a future approach on this topic could be the analysis of the dosimetric effects, and establishment of action levels, for different VMAT clinical cases. Besides addressing this topic, future works can eventually approach other questions exposed in this work, such as the development of a simulation geometry for the EPID installed in the TrueBeam™, analysis of the dosimetric effects in clinical setup mismatches involving FFF beams, correction of the abnormal dose values present in the extremities of the custom cut radiochromic films, and investigation of the effects associated with the grid size on the dose calculation accuracy.

8.) Bibliography

Abdallah, Y. M. Y., Eldien, D. E. E., and Mohamed, Z. T. E., 2011. Evaluation of Patient positioning correction approach in radiotherapy using Laser beam Positioning System. Canadian Journal on Medicine, 2(3), 49-62.

Abdelaal, A. M., Attalla, E. M., and Elshmey, W. M., 2017. Dose Estimation Outside Radiation Field Using Pinpoint and Semiflex Ionization Chamber Detectors. Radiation Physics and Chemistry, xxx(xxxx), xxx-xxx.

Adlienė, R. and Adlytė, R., 2017. Chapter 3: Dosimetry principles, dose measurements and radiation protection: Applications of ionizing radiation in materials processing – Volume 1. Institute of Nuclear Chemistry and Technology.

Ahmed, S. N., 2015. Physics and Engineering of Radiation Detection. Elsevier, 2th edition.

Akunzi, J., Leni, P., and Gschwind, R., 2016. The Monte Carlo validation of Varian 10 MV and 10 MV flattening filter free phase-spaces files for clinical quality assurance program. Physics Medica, 32.

Al-Mamgani, A., Heemsbergen, W. D., Peeters, S. T. H., and Lebesque, J. V., 2009. Role of intensity-modulated radiotherapy in reducing toxicity in dose escalation for localized prostate cancer. International Journal of Radiation Oncology • Biology • Physics, 73, 685-691.

Alghamdi, M., Olivotto, I., Khan, R. F. H., and Phan, T., 2015. Dosimetric Impact of the ACUROS Advanced Dose Calculation Algorithm on Internal Mammary Chain Nodal Coverage in Breast Cancer Patients Receiving Adjuvant Regional Nodal Irradiation. International Journal of Radiation Oncology • Biology • Physics, 93(3), Supplement.

Allen, B., Marcu, L., and Bezak, E., 2012. Biomedical Physics in Radiotherapy for Cancer. Csiro Publishing.

Amestoy, W., 2015. Review of Medical Dosimetry: A Study Guide. Springer.

Andreo, P., Burns, D. T., Nahum, A. E., Seuntjens, J., and Attix, F. H., 2017. Fundamentals of Ionizing Radiations Dosimetry. John Wiley & Sons.

Attix, F. H., 2008. Introduction to Radiological Physics and Radiation Dosimetry. John Wiley & Sons, 2008 edition.

Autran, J. and Munteanu, D., 2015. Soft Errors: From particles to Circuits. CRC Press

Barazzuol, L., Jena, R., Burnet, N. G., Jeynes, J. C. G., Merchant, M. J., Kirkby, K. J., and Kirkby N. F., 2012. *In Vitro* Evaluation of Combined Temozolomide and

Radiotherapy Using X Rays and High- Linear Energy Transfer Radiation for Glioblastoma. Radiation Research, 177(5), 651-662.

Barret, A., Dobbs, J., Morris, S., and Roques, T., 2009. Practical Radiotherapy Planning. Hodder Arnold, 4th edition.

Baskar, R., Dai, J., Wenlong, N., Yeo, R., and Yeoh, K., 2014. Biological response of cancer cells to radiation treatment. Frontiers in Molecular Biosciences, 1(24).

Beigi, M., Afarande, F., and Ghiasi, H., 2016. Safe bunker designing for the 18 MV Varian 2100 Clinac: a comparison between Monte Carlo simulation based upon data and new protocol recommendations. Reports of Practical Oncology and Radiotherapy, 21, 42-49.

Belosi, M. F., Rodriguez, M., Fogliata, A., Cozzi, L., Sempau, J., Clivio, A., Nicolini, A., Vanetti, E., Krauss, H., Khamphan, C., Fenoglietto, P., Puxeu, J., Fedele, D., Mancosu, P., and Brualla, L., 2014. Monte Carlo simulation of TrueBeam flattening-filter-free beams using varian phase-space files: comparison with experimental data. Medical Physics, 41(5),

Benedict, S. H., Schlesinger, D. J., Goetsch, S. J., and Kavanagh, B. D., 2016. Stereotactic Radiosurgery and Stereotactic Body Radiation Therapy. CRC Press.

Bentzen, S. M., Constine, L. S., Deasy, J. O., Eisbruch, A., Jackson, A., Marks, L. B., Haken, R. K. T., and Yorke, E. D., 2010. Quantitative Analyses of Normal Tissue Effects in the Clinic (QUANTEC): An Introduction to the Scientific Issues. International Journal of Radiation Oncology • Biology • Physics, 76(3).

Berbeco, R. I., 2017. Beam's Eye View Imaging in Radiation Oncology. CRC Press.

Beri, S., Tassin, P., Craggs, G., Leijtens, X., and Danckaert, J., 2010. Proceedings of the 2009 Annual Symposium of the IEEE Photonics Benelux Chapter. Asp/ Vubpress/ Upa.

Best, L., Rodrigues, G., and Velker, V., 2013. Radiation Oncology Primer and Review: Essential Concepts and Protocols. Demos Medical Publishing.

Beyzadeoglu, M., Ozyigit, G., and Ebruli, C., 2010. Basic Radiation Oncology. Springer Science & Business Media.

Beyzadeoglu, M., Ozyigit, G., and Selek, U., 2012. Radiation Oncology: A MCQ and Case Study-Based Review. Springer Science & Business Media.

Bhattacharjee, D., Tiwari, Jayaprakash, D., Mishra, R. L., Tillu, A. R., Nayak, B., Chavan, R. B., Chandan, S., Yadav, V., Ghodke, S. R., Kumar, M., Mittal, K. C.,

Chakravarthy, P., and Gantayet, L. M., 2012. Development of Electron Guns for Linacs and DC Accelerator. Journal of Physics: Conference Series, 390.

Biersack, H.-J. and Freeman, L., M., 2007. Clinical Nuclear Medicine. Springer Science & Business Media.

Bird, G. A., Gallis, M. A., Torczynski, J. R., and Rader, D. J., 2009. Accuracy and efficiency of the sophisticated direct simulation Monte Carlo algorithm for simulating noncontinuum gas flows. Physics of Fluids, 21(1).

Birgani, M. J. T., Chegeni, N., Arvandi, S., Ghalaee, S. R., Zabihzadeh, M., and Khezerloo, D., 2013. Analytical approach for determining beam profiles in water phantom of symmetric and asymmetric fields of wedged, blocked, and open photon beams. Journal of Applied Clinical Medical Physics, 14(6), 1-13.

Bissonnette, J. P. and Medlam, G., 2010. Trend analysis of radiation therapy incidents over seven years. Radiotherapy & Oncology, 96(1), 139-144.

Bortfeld, T., Schmidt-Ullrich, R., De Neve, W., and Wazer, D. E., 2006. Image-Guided IMRT. Springer Science & Business Media.

Botta, F., Mairani, A., Valente, M., Di Dia, G. A., Cremonesi, M., Ferrari, M., Paganelli, G., Pedroli, G., Ferrari, A., and Battistoni, G., 2011. Benchmark of FLUKA Monte Carlo code for dosimetry in nuclear medicine therapy through electron and isotopes dose point kernel calculation. Journal of Nuclear Medicine, 52(1), 1763.

Bottigli, U., Brunetti, A., Golosio, B., Oliva, P., Stumbo, S., Vincze, L., Randaccio, P., Bieuet, P., Simionovici, A., and Somogyi, A., 2004. Voxel-based Monte Carlo simulation of X-ray imaging and spectroscopy experiments. Spectrochimica Acta Part B: Atomic Spectroscopy, 56(10), 1747-1754.

Brahme, A., 2014 and Budinger, T. F.. Comprehensive Biomedical Physics: Volume 1. Elsevier.

Brandt, S., 2014. Data Analysis: Statistical and Computational Methods for Scientists and Engineers. Springer Science & Business Media, 4th edition.

Brock, K. K., 2013. Image Processing in Radiation Therapy. CRC Press.

Brualla, L. and Sauerwein, W., 2010. On the efficiency of azimuthal and rotational splitting for Monte Carlo simulation of clinical linear accelerators. Radiation Physics and Chemistry, 79, 929-932.

Brualla, L., Rodriguez, M., and Lallena, A. M., 2016. Monte Carlo systems used for treatment planning and dose verification. Strahlentherapie und Onkologie, 193(4), 243-259.

Brualla, L., Rodriguez, M., and Sempau, J., 2018. PRIMO User's Manual. L. Brualla, M. Rodriguez, J. Sempau©.

Burnet, N. G., Thomas, S. J., Burton, K. E., and Jefferies, S. J., 2004. Defining the tumour and target volumes for radiotherapy. Cancer Imaging, 4(2), 153-161.

Bush, K., Zavgorodni, S. F., and Beckham, W. A., 2007. Azimuthal particle redistribution for the reduction of latent phase-space variance in Monte Carlo simulations. Physics in Medicine & Biology, 52, 4345-4360.

Bushong, S. C., 2017. Radiologic Science of Technologists: Physics, Biology, and Protection. Elsevier Health Scienes, 11th edition.

Bushong, S. C., 2017. Workbook for Radiologic Science of Technologists: Physics, Biology, and Protection. Elsevier Health Scienes, 11th edition.

Cashmore, J., 2008. The characterization of unflattened photon beams from a 6MV linear accelerator. Physics in Medicine & Biology, 53(7), 1933-1946.

Castillo, M. L. R., 2015. Automation of the Monte Carlo simulation of medical linear accelerators. PhD dissertation, Institut de Tècniques Energètiques, Universitat Politècnica de Catalunya.

Chang, D., Lasley, F. D., Das, I. J., Mendonca, M. S., and Dynlacht, J. R., 2014. Basic Radiotherapy Physics and Biology. Springer.

Chao, A., 2013. Handbook of Accelerator Physics and Engineering. World Scientific, 2nd edition.

Chen, G., T. Y. and Sharp, G. C., 2009. A review of image-guided radiotherapy. Radiological Physics and Technology, 2, 1-12.

Chen, M., Lu, W., Chen, Q., Ruchala, K., and Olivera, G., 2009. Efficient gamma index calculation using fast Euclidean distance transform. Physics in Medicine & Biology, 54, 2037-2047.

Cherry, P. and Duxbury, A., 2009. Practical Radiotherapy: Physics and Equipment. Wiley-Blackwell, 2nd edition.

Chetty, I. J., Curran, B., Cygler, J. E., DeMarco, J. J., Ezzell, G., Faddegon, B. A., Kawrakow, I., Keall, P. J., Liu, H., Charlie Ma, C. M., Rogers, D. W. O., Seuntjens, J., Sheikh-Bagheri, D., and Siebers, J. V., 2007. Report of the AAPM Task Group No. 105: Issues associated with clinical implementation of Monte Carlo-based photon and electron external beam treatment planning. Medical Physics, 34(12), 4818-4853.

Chin, L. S. and Regine, W. F., 2015. Principles and Practice of Stereotactic Radiosurgey. Springer Science & Business Media, 2nd edition.

Chiu, A. G., Ramakrishnan, V. R., and Suh, J. D., 2011. Sinonasal Tumors. JP Medical Ltd.

Clark, B. G., Brown, R. J., Ploquin, J. L., Kind, A. L., and Grimard, L., 2010. The management of radiation treatment error through incident learning. Radiotherapy & Oncology, 95(3), 344-349.

Cortés-Giraldo, M. A., Quesada, J. M., Gallardo, M. I., and Capote, R., 2012. An implementation to read and write IAEA phase-space files in GEANT4-based simulations. International Journal of Radiation Biology, 88, 200-208.

Cox, J. D. and Ang, K. K., 2010. Radiation Oncology: Rationale, Technique, Results. Elsevier Health Sciences, 9th edition.

Cremer, J. T., 2012. Advances in Imaging and Electron Physics: Part 1. Academic Press.

Dalaryd, M., 2015. Dosimetric effects of removing the flattening filter in radiotherapy treatment units. Department of Medical Radiation Physics, Clinical Sciences, Lund University.

Dalaryd, M., Kragl, G., Ceberg, C., Georg, D., McClean, B., af Wetterstedt, S., Wieslander, E., and Knöös, T., 2010. A Monte Carlo study of a flattening filter-free linear accelerator verified with measurements. Physics in Medicine & Biology, 55(23), 7333-7344.

Das, I. J., Radiochromic Film: Role and Applications in Radiation Dosimetry. CRC Press.

Davidson, S. E., Cui, J., Kry, S., Deasy, J. O., Ibbott, G. S., Vicic, M., White, R. A., and Followill, D. S., 2016. Modification and validation of an analytical source model for external beam radiotherapy Monte Carlo dose calculations. Medical Physics, 43(8), 4842-4853.

Deasy, J. O., Moiseenko, V., Marks, L., Chao, K. S. C., and Eisbruch, A., 2010. Radiotherapy dose-volume effects on salivary gland function. International Journal of Radiation Oncology • Biology • Physics, 76(3), 58-63.

Deng, Z., Shen, L, Zheng, X., Zhou, Y., Yi, J., Han, C., Xie, C., and Jin, X., 2017. Dosimetric advantage of volumetric modulated arc therapy in the treatment of intraocular cancer. Radiation Oncology, 83(12).

Depuydt, T., Esch, A. V., and Huyskens, D. P., 2002. A quantitative evaluation of IMRT dose distributions: refinement and clinical assessment of the gamma evaluation. Radiohterapy and Oncology, 62, 309-319.

Dewerd, L. A. and Kissick, M., 2013. The Phantoms of Medical and Health Physics: Devices for Research and Development. Springer Science & Business Media.

Dicker, A. P., 2003. The safety and tolerability of low-dose irradiation for the management of gynaecomastia caused by antiandrogen monotherapy. The Lancer Oncology, 4, 30-36.

Dieterich, S., Ford, E., Pavord, D., and Zeng, J., 2015. Practical Radiation Oncology Physics: A Companion to Gunderson & Tepper's Clinical Radiation Oncology. Elsevier Health Sciences.

Dössel, O. and Schlegel, W. C., 2010. World Congress on Medical Physics and Biomedical Engineering September 7-12, 2009 Munich, Germany: Vol. 25/I Radiation Oncology. Springer Science & Business Media.

Dössel, O. and Schlegel, W. C., 2010. World Congress on Medical Physics and Biomedical Engineering September 7-12, 2009 Munich, Germany: Vol. 25/VIII Micro- and Nanosystems in Medicine, Active Implants, Biosensors. Springer Science & Business Media.

Dumitrache, M. and Tănase, A., 2016. Gamma Dose Distribution Evaluation of XiO Treatment Planning System for Static Field IMRT, Using AAPM TG-119.

Dunn, L., Lehmann, J., Lye, J., Kenny, J., Kron, T., Alves, A., Cole, A., Zifodya, J., and Williams, I., 2015. National dosimetric audit network finds discrepancies in AAA lung inhomogeneity corrections. Physica Medica, 31(5), 435-441.

Dvorak, P., 2018. Clinical Radiotherapy Physics with MATLAB®: A Problem-Solving Approach. CRC Press.

Elith, C. A., Dempsey, S. E., Cao, F., Farshadi, A., and Warren-Forward, H. M., 2014. The quality assurance of volumetric modulated arc therapy (VMAT) plans for early stage prostate cancer: a technical note. Journal of Medical Radiation Sciences, 61, 261-266.

Esch, A. V., Tillikainen, L., Pyykkonnen, J., Tenhunen, M., Helminen, H., Siljamäki, S., Alakuijala, J., Paiusco, M., Iori, M., and Huyskens, D. P., 2006. Testing of the analytical anisotropic algorithm for photon dose calculation. Medical Physics, 33.(11), 4130-4148.

Esposito, A., Silva, S., Cunha, L. T., Dias, A. G., Pimparel, D., Gutierrez, S., Dias, S., Lencart, J., and Santos, J. A. M., 2018. Primo software as a tool for Monte Carlo simulations of intensity modulated radiotherapy: A feasibility study. Radiation Oncology, 13(1), 91.

Esquivias, G. B. and Asteggiano, R., 2015. Cardiac Management of Oncology Patients: Clinical Handbook for Cardio-Oncology. Springer, 2015.

Faddegon, B. A., Kawrakow, I., Kubyshin, Y., Perl, J., Sempau, J., and Urban, L., 2009. Accuracy of EGSnrc, Geant4 and PENELOPE Monte Carlo systems for simulation of

electron scatter in external beam radiotherapy. Physics in Medicine & Biology, 54(20), 6151-6163.

Ezzell, G. A., Burmeister J. W., Dogan N., LoSasso T. J., Mechalakos J. G., Mihailidis D., Molineu A., Palta J. R., Ramsey C. R., Salter B. J., Shi J., Xia P., Yue N. J., and Xiao, Y., 2009. IMRT commissioning: multiple institution planning and dosimetry comparisons, a report from AAPM Task Group 119. Medical Physics, 36, 5359–5373.

Failla, G. A., Wareing, T., Archambault, Y., and Thompson, S., 2015. Acuros® XB Advanced Dose Calculation for the Eclipse™ Treatment Planning System. Varian Medical Systems.

Faught, A. M., Davidson, S. E., Popple, R., Kry, S. F., Etzel, C., Ibbott, G. S., and Followill, D. S., 2017. Development of a flattening filter free multiple source model for use as an independent, Monte Carlo, dose calculation, quality assurance tool for clinical trials. Medical Physics, 44(9), 4952-4960.

Ferreira, T. and Rasband, W., 2011. ImageJ User Guide. IJ 1.45m.

Flores, F. J. H., 2015. Measure profile in Photon beam. International Centre for Theoretical Physics.

Followill, D. S., Hanson, W. F., and Ibbott, G. S., 2003. Differences in electron beam dosimetry using two commercial ionization chambers and the TG-21 protocol: Another reason to switch to TG-51. Journal of Applied Clinical Medical Physics, 4(2), 124-131.

Foroudi, F., Haworth, A., Pangehel, A., Wong, J., Roxby, P., Duchesne, G., Williams, S., and Tai, K. H., Inter-observer variability of clinical target volume delineation for bladder cancer using CT and cone beam CT. Journal of Medical Imaging and Radiation Oncology, 53(1), 100-106.

French, S. B., Bhagroo, S., Nazareth, D. P., and Podgorsak, M. B., 2017. Adapting VMAT plans optimized for an HD120 MLC for delivery with a Millennium MLC. Radiation Oncology Physics, 18(5), 143-151.

Frøseth, T. C., Strickert, T., Solli, K., Salvesen, Ø., Frykholm, G., and Reidunsdatter, R. J., 2015. A randomized study of the effect of patient positioning on setup reproducibility and dose distribution to organs at risk in radiotherapy of rectal cancer patients. Radiation Oncology, 217(10).

Gaya, A. and Mahadevan, A., 2015. Stereotactic Body Radiotherapy: A Practical Guide. Springer.

Geant4 Collaboration, 2017. Geant4: A Simulation Toolkit. Physics Reference Manual, Release 10.4.

Ghareeb, F., Esposito, A., Lencart, J., and Santos, J., 2017. Monte Carlo simulation of "out-of-field" distributions in a pediatric phantom in external radiotherapy – Couch top impact. Physica Medica, 42, Supplement 1, 41.

Ghareeb, F., Silva, S., Lencart, J., Borges, F., and Santos, J. A. M., 2017. Comparison of Measured and Calculated Out-of-Field Doses in a Paediatric Anthropomorphic Phantom/Out of the Body Scatter Contribution Evidence. Radiation & Applications, 2(1), 20-25.

Ghilezan, M., Yan, D., and Martinez, A., 2010. Adaptive Radiation Therapy for Prostate Cancer. Seminars in Radiation Oncology, 20(2), 130-137.

Ghom, A. G., 2016. Textbook of Oral Radiology. Elsevier Health Sciences, 2nd edition.

Global Burden of Disease Cancer Collaboration, 2017. Global, Regional, and National Cancer Incidence,Mortality, Years of Life Lost, Years LivedWith Disability, and Disability- Adjusted Life-years for 32 Cancer Groups, 1990 to 2015 A Systematic Analysis for the Global Burden of Disease Study. JAMA Oncology, 3(4), 524-548.

Goh, V. and Adam, A., 2015. Diagnostic Radiology: Oncological Imaging. Elsevier Health Sciences, 6th edition.

Godley, A. and Xia, P., 2016. Physics in Radiation Oncology Self-Assessment Guide. Springer Publishing Company.

Goharian, M. and Khan, R. F. H., 2010. Measurement of time delay for a prospectively gated CT simulator. Journal of Medical Physics, 35(2), 123-127.

Goraj, A. and de Boer, S. F., 2012. Impact of the number of control points has on isodose distributions in a dynamic multileaf collimator intensity-modulated radiation therapy delivery. Medical Dosimetry, 37, 412-416.

Goyal, S. and Kataria, T., 2014. Image Guidance in Radiation Therapy: Techniques and Applications. Radiology Research and Practice, 2014.

Green, D., 2014. One Hundred Physics Visualizations Using MATLAB. World Scientific.

Gunderson, L. L. and Tepper, J. E., 2015. Clinical Radiation Oncology. Elsevier Health Sciences, 4th edition.

Gupta, T. and Narayan, C. A., 2012. Image-guided radiation therapy: Physician's perspectives. Journal of Medical Physics, 37(4), 174-182.

Haffty, B. G. and Wilson, L. D., 2009. Handbook of Radiation Oncology. Jones & Bartlett Learning.

Halperin, E. C., Perez, C. A., and Brady, L. W., 2013. Principles and Practice of Radiation Oncology. Lippincott Williams & Wilkins, 6th edition.

Hamza-Lup, F. G., Sopin, I., Lipsa, D., and Zeidan, O., 2007. X3D in Radiation Therapy Procedure Planning. Webist 2007 - 3rd International Conference on Web Information Systems and Technologies, Proceedings.

Han, B., Ding, A., Lu, M., and Xing, L., 2017. Pixel response-based EPID dosimetry for patient specific QA. Journal of Applied Clinical Medical Physics, 18(1), 9-17.

Hanna, S., 2012. RF Linear Accelerators for Medical and Industrial Applications. RF Linear Accelerators for Medical and Industrial Applications. Artech House.

Healy, B. J., van der Merwe, D., Christaki, K. E., and Meghzifene, A., 2016. Cobalt-60 Machines and Medical Linear Accelerators: Competing Technologies for External Beam Radiotherapy. Clinical Oncology, xxx, 1-6.

Haghighat, A., 2014. Monte Carlo Methods for Particle Transport. CRC Press.

Heilemann G., Poppe B., Laub W., 2013. On the sensitivity of common gamma-index evaluation methods to MLC misalignments in Rapidarc quality assurance. Medical Physics, 40.

Henley, E. M. and Garcia, A., 2007. Subatomic Physics. World Scientific Publishing Company, 3rd edition.

Herrmann, K., Nieweg, O., and Povoski, S. P., 2016. Radioguided Surgery: Current Applications and Innovative Directions in Clinical Practice. Springer.

Herman, T. F., Schnell, E., Young, J., Hildebrand, K., Algan, Ö., Syzek, E., Herman, T., and Ahmad, S., 2013. Dosimetric comparison between IMRT delivery modes: Step-and-shoot, sliding window, and volumetric modulated arc therapy - for whole pelvis radiation therapy of intermediate-to-high risk prostate adenocarcinoma. Journal of Medical Physics, 38(4), 165-172.

Hermida-López, M., Sánchez–Artuñedo, D., and Calvo–Ortega, 2018. PRIMO Monte Carlo software benchmarked against a reference dosimetry dataset for 6 MV photon beams from Varian linacs. Radiation Oncology, 144(13).

Hoffman, L. and Rønde, H. S., 2008. Validation of Varian's AAA algorithm with focus on lung treatments. Acta Oncologica, 48(2), 209-215.

Hoppe, R., Philips, T. L., and Roach, M., 2010. Leibel and Phillips Textbook of Radiation Oncology. Elsevier Health Sciences, 3rd edition.

Hoskin, P. and Coyle, C., 2011. Radiotherapy in Practice – Brachytherapy. Oxford University Press, 2nd edition.

Hornyak, G. L., Dutta, J., Tibbals, H. F., and Rao, A., 2008. Introduction to Nanoscience. CRC Press.

Hoskin, P., 2012. External Beam Therapy. Oxford University Press.

Howel, R. M., Scarboro, S. B., Taddei, P. J., Krishnan, S., Kry, S. F., and Newhauser, W. D., 2010. Methodology for determining doses to in-field, out-of-field and partially in-field organs for late effects studies in photon radiotherapy. Physics in Medicine & Biology, 55(23), 7009-7023.

Hrbacek, J., Lang, S., and Klock, S., 2011. Commissioning of photon beams of a flattening filter-free linear accelerator and the accuracy of beam modeling using an anisotropic analytical algorithm. International Journal of Radiation Oncology • Biology • Physics, 80, 1228-1237.

Huda, W., 2016. Review of Radiologic Physics. Lippincott Williams & Wilkins, 4th edition.

Hughes, J. L.., 2013. Automated Analysis of Varian Log Files for Advanced Radiotherapy Treatment Verification: A Multicenter Study. Master's Thesis, School of Physics, University of Western Australia.

Hwang, U., Jo, K., Lim, Y. K., Kwak, J. W., Choi, S. H., Jeong, C., Kim, M. Y., Jeong, C., Kim, M. Y., Jeong, J. H., Shin, D., Lee, S. B., Park, J., Park, S. Y., and Kim, S., 2016. A new method and device of aligning patient setup lasers in radiation therapy. Journal of Applied Clinical Medical Physics, 17(1), 49-61.

IAEA, 2013. IAEA Human Health Reports No.7: Record and Verify Systems for Radiation Treatment of Cancer: Acceptance Testing, Commissioning and Quality Control. IAEA Human Health Series.

International Commision on Radiation Units and Measurements (ICRU), 2010. ICRU Report No. 83: Prescribing, Recording, and Reporting Photon-Beam Intensity Modulated Radiation Therapy (IMRT). Journal of the ICRU, 10(1).

International Commision on Radiation Units and Measurements (ICRU), 2011. ICRU Report No. 85: Fundamental Quantities and Units for Ionizing Radiation. Journal of the ICRU, 11(1), revised edition.

Isa Khan, M., 2015. Dose Distribution, Calculation and Treatment Planning Accuracy in Advance Radiotherapy. PhD Dissertation, Department of Physics, Islamia University of Bahawalpur.

Izewska, J. and Rajan, G., 2012. Chapter 3: Radiation Dosimeters. Review of Radiation Oncology Physics: A Handbook for Teachers and Students. International Atomic Energy Agency.

Jabbari, K., 2011. Review of Fast Monte Carlo Codes for Dose Calculation in Radiation Therapy Treatment Planning. Journal of Medical Signals and Sensors, 1(1), 73-86.

Jaumot, M.-T., Hoornaert, M., Delval, M., Pellegri, L., Coussement, G., and Campeanu, H., 2013. Elaboration of a quality assurance programme for flattening filter free photon beams. Physica Medica, 29(1).

Jeraj, M. and Robar, V., 2004. Multileaf collimator in radiotherapy. Radiology and Oncology, 38(3), 235-240.

Jia, X. and Jiang, S. B., 2015. Graphics Processing Unit-Based High Performance Computing in Radiation Therapy. CRC Press.

Johnson, T. E., 2017. Introduction to Health Physics. McGraw Hill Professional, 5th edition.

Johnston, J. and Fauber, T. L., 2015. Essentials of Radiographic Physics and Imaging. Elsevier Health Sciences, 2nd edition.

Joiner, M. C. and van der Kogel, A., 2009. Basic Clinical Radiobiology. CRC Press, 4th edition.

Jung, K., Won, Y., Oh, C., Kong, H., Lee, D. H., and Lee, K. H., 2017. Cancer Statistics in Korea: Incidence, Mortality, Survival, and Prevalence in 2014. Cancer Research and Treatment, 49(2), 292-305.

Kainz, P., Mayrhofer-Reinhartshuber, M., and Ahammer, H., 2015. Java. IQM: An Extensible and Portable Open Source Application for Image and Signal Analysis in Java. PLoS ONE 10(1).

Kajaria, A., Sharma, N., Sharma, S., Pradhan, S., and Aggarwal, L., 2013. Review of Monte Carlo Simulation in Radio Therapy Treatment Planning System for Modelling of Radiation Transport & Dose Calculation. VAICHARIKI, 3(4), 261-268.

Karan, T., Moiseenko, V., Gill, B., Horwood, R., Kyle, A., and Minchinton, A., 2013. Radiobiological effects of altering dose rate in filter-free photon beams, 58(4), 1075-1082.

Karen, C. S., Liu, M., Zhao, B., Huang, Y., Ning, W., Chetty, I. J., and Siddiqui, M. S., 2017. Investigating the dosimetric effects of grid size on dose calculation accuracy using volumetric modulated arc therapy in spine stereotactic radiosurgery. Journal of Radiosurgery & SBRT, 4(4), 303-313.

Key, T.. Nuclear and Radiation Physics in Medicine: A Conceptual Introduction. World Scientific Publishing Company.

King, R. B., Hyland, W. B., Cole, A. J., Butterworth, K. T., McMahon, S. J., Redmond, K. M., Trainer, C., Prise, K. M., McGarry, C. K., and Hounsell, A. R., 2013. An *in vitro* study of the radiobiological effects of flattening filter free radiotherapy treatments. Physics in Medicine & Biology, 58, 83-94.

Khan, F. M., 2014. The Physics of Radiation Therapy. Wolters Kluwer, 2nd edition.

Khan, F. M. and Gibbons, J. P., 2014. Khan's The Physics of Radiation Therapy. Wolters Kluwer, 5th edition.

Kharisov, B. I., Kharissova, O. V., and Mendez, U. O., 2013. Radiation Synthesis of Materials and Compounds. CRC Press.

Kim, J., Chun, M., Wu, H-.G., Chie, E. K., Kim, H. J., Kim, J. H., and Park, J. M., 2017. Gamma analysis with a gamma criterion of 2%/1 mm for stereotactic ablative radiotherapy delivered with volumetric modulated arc therapy technique: a single institution experience. Oncotarget, 8(44), 76076-76084.

Kim, J., Han, J. S., Hsia, A. T., Li, S., Xu, Z., and Ryu, S., 2018. Relationship between dosimetric leaf gap and dose calculation errors for high definition multi-leaf collimators in radiotherapy. Physics and Imaging in Radiation Oncology, 5, 31-36.

Kim, J., Park, S.-Y., Kim, H. J., Kim, J. H., Ye, S.-J., and Park, J. M., 2014. The sensitivity of gamma-index method to the positioning errors of high-definition MLC in patient-specific VMAT QA for SBRT. Radiation Oncology, 9, 167.

Kim, J., Chun, M., Wu, H.-G., Chie, E. K., Kim, H. J., Kim, J. H., and Park, J. M., 2017. Gamma analysis with a gamma criterion of 2%/1 mm for stereotactic ablative radiotherapy delivered with volumetric modulated arc therapy technique: a single institution experience. Oncotarget, 8, 76076-76084.

Klein, E. E., Hanley, J., Bayouth, J., Yin, F.-F., Simon, W., Dresser, S., Serago, C., Aguirre, F., Ma, L., Arjomandy, B., Liu, C., Sandin, C., and Holmes, T., 2009. Task Group 192 report: quality assurance of medical accelerators. Medical Physics, 36(9), 4197-4212.

Kling, A., Barao, F. J. C., Nakagawa, M., Tavora, L., and Vaz, P., 2001. Advanced Monte Carlo for Radiation Physics, Particle Transport, Simulation and Applications: Proceedings of the Monte Carlo 2000 Conference, Lisbon, 23-26 October 2000. Springer Science & Business Media.

Klockenkämper, R. and van Bohlen, A., 2014. Total-Reflection X-Ray Fluorescence Analysis and Related Methods. John Wiley & Sons.

Klüter, S., Sroka-Perez, G., Schubert, K., and Debus, J., 2010. Impact of Beam Alignment on Leakage of the Siemens 160 MLC™. World Congress on Medical Physics and Biomedical Engineering September 7-12, 2009 Munich, Germany: Vol. 25/I Radiation Oncology. Springer Science & Business Media.

Knapp, F. F. and Dash, A., 2016. Radiopharmaceuticals for Therapy. Splinter.

Knoll, G. F., 2010. Radiation detection and measurement. Wiley, 4th edition.

Krems, R. V., 2018. Molecules in Electromagnetic Fields: From Ultracold Physics to Controlled Chemistry. John Wiley & Sons.

Kroon, P. S., Hol, S., and Essers, M., 2013. Dosimetric accuracy and clinical quality of Acuros XB and AAA dose calculation algorithm for stereotactic and conventional lung volumetric modulated arc therapy plans. Radiation Oncology, 8, 149.

Kovacs, M. J., Franco, M. H. P., and Carvalho, V. A., 2008. Temas em Psico-oncologia. Grupo Editorial Summus.

Kuppusamy, T., 2017. Basic Radiological Physics. JP Medical Ltd, 2nd edition.

Kusters, J., Louwe, R., Claessen, R., van Seters, R., and Huizenga, H., 2010. Camera-based independent couch height verification in radiation oncology. World Congress on Medical Physics and Biomedical Engineering September 7-12, 2009 Munich, Germany: 25/I Radiation Oncology. Springer Science & Business Media.

Lafond, C., Jouyaux, F., Bellec, J., Henry, O., Perdrieux, M., Le Prisé, E., de Crevoisier, R., and Manens, J. P., 2010. Which IMRT? From "step and shoot" to VMAT: physicist point of view. Cancer Radiothérapie, 14(6), 539-549.

Laub, W. and Thomas, C. R., 2013. Patient-specific quality assurance measurements for VMAT treatments: Do we really catch errors? Journal of Clinical Oncology, 31, Supplement 81.

Lecchi, M., Fossati, P., Elisei, F., Orecchia, R., and Lucignani, G., 2008. Current concepts on imaging in radiotherapy. European Journal of Nuclear Medicine and Molecular Imaging, 35, 821-837.

Lee, T. and Fang, F., 2013. Quantitative analysis of normal tissue effects in the clinic (QUANTEC) guideline validation using quality of life questionnaire datasets for parotid gland constraints to avoid causing xerostomia during head-and-neck radiotherapy. Radiotherapy and Oncology, 106, 352-358.

Lee, E. K., Yuan, F., Yu, C., Templeton, A., Yao, R., Kiel, K. D., and Chu, J. C. H., 2017. Optimizing Tumor Control Probability in Radiation Therapy Treatment Design – Application to HDR Cervical Cancer. International Journal of Radiation Oncology • Biology • Physics, 99(2).

Leroy, C., 2016. Principles of Radiation Interaction in Matter and Detection. World Scientific, 4th edition.

Levitt, S. H., Purdy, J. A., Perez, C. A, and Poortmans, P., 2012. Technical Basis of Radiation Therapy: Practical Clinical Applications. Springer Science & Business Media, 5th edition.

Li, X. A., 2011. Adaptive Radiation Therapy. CRC Press.

Li, Y. G., Mao, S. F., and Ding, Z. J., 2011. Monte Carlo Simulation of SEM and SAM Images. IntechOpen, Applications of Monte Carlo Method in Science and Engineering Shaul Mordechai, IntechOpen, 231-296.

Lim-Reinders, S., Keller, B. M., Al-Ward, S., Sahgal, A., and Kim, A., 2017. Online Adaptive Radiation Therapy. International Journal of Radiation Oncology • Biology • Physics, 99(4), 994-1003.

Lin, H., Liu, T., Su, L., Bednarz, B., Caracappa, P., and Xu, X. G., 2017. Modeling of Radiotherapy Linac Source Terms Using ARCHER Monte Carlo Code: Performance Comparison for GPU and MIC Parallel Computing Devices. EPJ Web of Conferences, 153.

Lin, M.-H., Koren, S., Veltchev, I., Li, J., Wang, L., Price, R. A., and Ma., C.-M., 2013. Measurement comparison and Monte Carlo analysis for volumetric-modulated arc therapy (VMAT) delivery verification using the ArcCHECK dosimetry system. Journal of Applied Clinical Medical Physics, 14(2), 220-233.

Liu, K., Zheng, D., Xu, G., Du, Z., and Wu, S., 2017. Local thoracic therapy improve prognosis for stage IV non-small cell lung cancer patients combined with chemotherapy: A Surveillance, Epidemiology, and End Results database analysis. PLoS ONE, 12(11).

Low, D. A., Harms, W. B., Mutic, S., and Purdy, J. A., 1998. A technique for the quantitative evaluation of dose distributions. Medical Physics, 25(5), 656-661.

Lötstedt, P.. Random Numbers and Monte Carlo Methods. Conference Proceedings, Online Publication.

Louvin, H., 2017. Development of an adaptive variance reduction technique for Monte Carlo particle transport. PhD dissertation, Computational Physics Université Paris-Saclay.

Lux, I. and Koblinger, L, 2017. Monte Carlo Partîcle Transport Methods: Neutron and Proton Calculations. CRC Press.

Lyatskaya, Y., Lu, H.-M., and Chin, L., 2006. Performance and characteristics of an IR localizing system for radiation therapy. Journal of Applied Clinical Medical Physics, 7(2), 18-37.

Manson, S., 2004. Patient positioning correction strategies in radiotherapy: A portal imaging study. Master's thesis, Department of Medical Radiation Physics, The Jubileum Institute, Lund University.

Maqbool, M., 2017. An Introduction to Medical Physics. Springer.

Marcu, L., Bezak, E., and Allen, B., 2012. Biomedical Physics in Radiotherapy for Cancer. Csiro Publishing.

Marks, L. B., Yorke, E. D., Jackson, A., Haken, R. K. T., Constine, L. S., Eisbruch, A., Bentzen, S. M., Nam, J., and Deasy, J. O., 2010. The Use of Normal Tissue Complication Probability (NTCP) Models in the Clinic. International Journal of Radiation Oncology • Biology • Physics, 76(30).

Masi, L., Casamassima, F., Doro, R., and Francescon, P., 2011. Quality assurance of volumetric modulated arc therapy: Evaluation and comparison of different dosimetric systems. Medical Physics, 38(2), 612-621.

Mayles, P., Nahum, A., and Rosenwald, J.-C., 2007. Handbook of Radiotherapy Physics: Theory and Practice. CRC Press.

McParland, B. J., 2010. Nuclear Medicine Radiation Dosimetry: Advanced Theoretical Principles. Springer Science & Business Media.

Meghzifene, A., Dance, D. R., McLean, D., and Kramer, H.-M., 2010. Dosimetry in diagnostic radiology. European Journal of Radiology, 76, 11-14.

Melman, A. and Newnham, R., 2011. After Prostate Cancer: A What-Comes-Next Guide to a Safe and Informed Recovery. Oxford University Press.

Mijnheer, B., 2017. Clinical 3D Dosimetry in Modern Radiation Therapy. CRC Press.

Miras, H. and Jimenez, R., 2017. Moving PRIMO to the Cloud. Workshop on the Monte Carlo radiotherapy system PRIMO: Book of Abstracts.

Mohammed, M., El Bardouni, T., Chakir, E., Saeed, M., Jamal, A. Z., and Mohammed, L., 2017. Validation of BEAMnrc Monte Carlo model for a 12 MV photon beam. Journal of King Saud University – Science, 30(4), 537-543.

Mohammed, M., Chakir, E., Boukhal, H., Mroan, S., and El Bardouni, T., 2017. Evaluation of the dosimetric characteristics of 6 MV flattened and unflattened photon beam. Journal of King Saud University – Science, 29(3), 371-379.

Mohammed, M., Chakir, E., Boukhal, H., Saeed, M., and El Bardouni, T., 2016. Evaluation of variance reduction techniques in BEAMnrc Monte Carlo simulation to improve the computing efficiency. Journal of Radiation Research and Applied Sciences, 9, 424-430.

Moiseenko, V., Wu, J., Hovan, A., Saleh, Z., Apte, A., Deasy, J. O., Harrow, S., Rabuka, C., Muggli, C., and Thompson, A., 2012. Treatment planning constraints to avoid xerostomia in head-and-neck radiotherapy: an independent test of QUANTEC criteria using a prospectively collected dataset. International Journal of Radiation Oncology • Biology • Physics, 82(3), 1108-1114.

Mozumder, A. and Hatano, Y., 2003. Charged Particle and Photon Interactions with Matter: Chemical, Physiochemical, and Biological Consequences with Applications. CRC Press.

Mukhopadhyay, N. D., Sampson, A. J., Deniz, D., Carlsson, G. A., Williamson, J., and Malusek, A., 2012. Estimating statistical uncertainty of Monte Carlo efficiency-gain in the context of a correlated sampling Monte Carlo code for brachytherapy treatment planning with non-normal dose distribution. Applied Radiation and Isotopes, 70(1), 315-323.

Mullins, J., DeBlois, F., and Syme, A., 2016. Experimental characterization of the dosimetric leaf gap. Biomedical Physics & Engineering Express, 2(6).

Müller, M., 2007. Electronic Structure of Ferromagnet Insulator Interfaces: Fe/MgO and Co/MgO. Forschungszentrum Jülich.

Mundt, A. J. and Roeske, J. C., 2005. Intensity Modulated Radiation Therapy: A Clinical Perspective, Volume 1. PMPH-USA.

Nakano, H., Minami, K., Yagi, M., Imaizumi, H., Otani, Y., Inoue, S., Takashina, M., Seo, Y., Takahashi, Y., Sumida, I., Ogawa, K., and Koizumi, M., 2018. Radiobiological effects of flattening filter–free photon beams on A549 non-small-cell lung cancer cells. Journal of Radiation Research, 59(4), 442-445.

Natali, M., Capomolla, C., Russo, D., Pastore, G., Cavalera, E., Leone, A., Zagari, A., and Santantonio, M., 2013. Dosimetric verification of vmat dose distribution with DELTA4® Phantom. 3rd Workshop - Plasmi, Sorgenti, Biofisica ed Applicazioni, 80-83.

National Cancer Action Team, 2012. National Radiotherapy Implementation Group Report: Image Guided Radiotherapy (IGRT) - Guidance for implementation and use. NHS.

Naseri, A. and Mesbahi, A., 2015. A review on photoneutrons characteristics in radiation therapy with high-energy photon beams. Reports of Practical Oncology and Radiotherapy, 15(5), 138-144.

Niederhuber, J. E., Armitage, J. O., Doroshow, J. H., Kastan, M. B., and Tepper, J. E., 2013. Abeloff's Clinical Oncology. Elsevier Health Sciences, 5th edition.

Nikjoo, H., Uehara, S., and Emfietzoglou, D., 2012. Interaction of Radiation with Matter. Taylor & Francis.

Nilsson, B. N., 2015. Exercises with Solutions in Radiation Physics. Walter de Gruyter GmbH & Co KG.

Ojala, J. J., Kapanen, M. K., Hyodynmaa, S. J., Wigren, T. K., and Pitkanen, M. A., 2014. Performance of dose calculation algorithms from three generations in lung

SBRT: comparison with full Monte Carlo-based dose distributions. Journal of Applied Clinical Medical Physics, 15(2), 4-18.

Ohira, S., Ueda, Y., Isono, M., Masaoka, A., Hashimoto, M., Miyazaki, M., Takashina, M., Koizumi, M., and Teshima, T., 2017. Can clinically relevant dose errors in patient anatomy be detected by gamma passing rate or modulation complexity score in volumetric-modulated arc therapy for intracranial tumors? Journal of Radiation Research, 58(5), 685-692.

Olsson, H., 2017. Utilizing the Degrees of Freedom in Radiation Therapy Optimization. School of Engineering Sciences, KTH Royal Institute of Technology.

Omer, M. O. M. E., 2014. Monte Carlo Simulation of Medical Linear Accelerator Using Primo Code. Master's thesis, Sudan Academy of Sciences.

Orlandini, L. C., Betti, M., Fulcheri, C., Coppola, M., and Cionini, L., 2015. Dosimetric impact of different multileaf collimators on prostate intensity modulated treatment planning. Reports of Practical Oncology and Radiotherapy, 20(5), 358-364.

Osorio, E. M. V., Hoogeman, M. S., Teguh, D. N., Al-Mamgani, A., Kolkman-Deurloo, I. K., Bondar, L., Levendag, P. C., and Heijmen, B. J. M., 2011. Three-Dimensional Dose Addition of External Beam Radiotherapy and Brachytherapy for Oropharyngeal Patients Using Nonrigid Registration. International Journal of Radiation Oncology • Biology • Physics, 80(4), 1268-1277.

Ozyigit, G. and Selek, U., 2017. Principles and Practice of Urooncology: Radiotherapy, Surgery and Systemic Therapy. Springer.

Paganetti, H., 2012. Proton Therapy Physics. CRC Press.

Pardee, A. B. and Stein, G. S., 2009. The Biology and Treatment of Cancer: Understanding Cancer. John Wiley & Sons.

Pathak, P., Mishra, P. K., Singh, M., and Mishra, P. K., 2015. Analytical Study of Flatness and Symmetry of Electron Beam with 2D Array Detectors. Journal of Cancer Science & Therapy, 7(10), 294-301.

Pawlicki, T., Dunscombe, P., Mundt, A. J. and Scalliet, P., 2010. Quality and Safety in Radiotherapy. CRC Press.

Pawlicki, T., Scanderberg, D. J., and Starkschall, G., 2016. Hendee's Radiation Therapy Physics. John Wiley & Sons, 4th edition.

Pehlivan, B., Pichenot, C., Castaing, M., Auperin, A., Lefkopoulos, D., Arriagada, R., and Bourthis, J., 2009. Interfractional set-up errors evaluation by daily electronic portal imaging of IMRT in head and neck cancer patients. Acta Oncologica, 48(3), 440-445.

Pianykh, O. S., 2012. Digital Imaging and Communications in Medicine (DICOM): A Practical Introduction and Survival Guide. Springer, 2nd edition.

Podesta, M., Persoon, L. C. G. G., and Verhaegen, F., 2014. A novel time dependent gamma evaluation function for dynamic 2D and 3D dose distributions. Physics in Medicine and Biology, 59, 5973-5985.

Podgorsak, E. B., 2005. Radiation Oncology Physics: A Handbook for Teachers and Students. International Atomic Energy Agency.

Podgorsak, E. B., 2005. Chapter 2: Dosimetric Principle, Quantities and Units. Radiation Oncology Physics: A Handbook for Teachers and Students, Atomic Energy Agency.

Podgorsak, E. B., 2005. Chapter 5: Treatment Machines for External Beam Radiotherapy. Radiation Oncology Physics: A Handbook for Teachers and Students, Atomic Energy Agency.

Podgorsak, E. B., 2005. Chapter 6: External Photon Beams: Physical Aspects. Radiation Oncology Physics: A Handbook for Teachers and Students, Atomic Energy Agency.

Podgorsak, E. B., 2016. Radiation Physics for Medical Physicists. Springer, 3rd edition.

Poirier, Y., 2014. An X-ray Source Model and Characterization Method for Computing kV Radiation Dose. PhD thesis, Departement of Physics and Astronomy, University of Calgary.

Prendergast, B. M., Dobelbower, M. C., Bonner, J. A., Popple, R. A., Baden, C. J., Minnich, D. J., Cerfolio, R. J., Spencer, S. A., and Fiveash, J. B., 2013. Stereotactic body radiation therapy (SBRT) for lung malignancies: preliminary toxicity results using a flattening filter-free linear accelerator operating at 2400 monitor units per minute. Radiation Oncology, 8 (1), 273.

Prezado, Y., Adam, J. F., Berkvens, P., Martinez-Rovira, I., Fois, G., Thengumpallil, S., Edouard, M., Vautrin, M., Deman, P., Bräuer-Krisch, E., Renier, M., Elleaume, H., Estève, F., and Bravin, A., 2010. Synchrotron Radiation Therapy from a Medical Physics point of view. 6th International Conference on Medical Applications of Synchrotron Radiation.

PTW, 2009. Verisoft$^®$. PTW

PTW, 2014. Ionization Chambers Type 31010, 31011, 31012 and Type 31013 (from SN 1000) (Semi-flexible Chambers). PTW.

PTW, 2016. Farmer Chamber Ionization Chamber Type 30010, 30011, 30012, 30013. PTW.

Puchalsa, M., Bilski, P., Berger, T., Hakej, M., Horwacik, T., Körner, C., Olko, P., Shurshakov, V., and Reitz, G., 2014. NUNDO: a numerical model of a human torso phantom and its application to effective dose equivalent calculations for astronauts at the ISS. Radiation and Environmental Biophysics, 53, 719-727.

Pulliam, K. B., Huang, J. Y., Howell, R. M., Followill, Bosca, R., O'Daniel, J., and Kry, S. F., 2014. Comparison of 2D and 3D gamma analyses. Medical Physics, 41(2).

Ragheb, M., 2013. Russian Roulette and Particle Splitting. M Ragheb©.

Rahbar, R., Rodriguez-Galindo, C., Meara, J. G., Smith, E. R., and Perez-Atayde, 2013. Pediatric Head and Neck Tumors: A-Z Guide to Presentation and Multimodality Management. Springer Science & Business Media.

Rana, S., Rogers, K., Pokharel, S., Lee, T., Reed, D., Biggs, C., 2013. Acuros XB Algorithm vs. Anisotropic Analytical Algorithm: A Dosimetric Study Using Heterogeneous Phantom and Computed Tomography (CT) Data Sets of Esophageal Cancer Patients. Journal of Cancer Therapy, 4, 138-144.

Rath, A. K. and Sahoo, N., 2016. Particle Radiotherapy: Emerging Technology for Treatment of Cancer. Springer.

Rodriguez, M., Sempau, J., and Brualla, L., 2012. A combined approach of variance-reduction techniques for the efficient Monte Carlo simulation of linacs. Physics in Medicine & Biology, 57, 3013-3024.

Rodriguez, M., Sempau, J., and Brualla, L., 2013. PRIMO: A graphical environment for the Monte Carlo simulation of Varian and Elekta linacs. Strahlentherapie und Onkologie, 189, 881-886.

Rodriguez, M., Sempau, J., Fogliata, A., Cozzi, L., Sauerwein, W., and Brualla, L., 2015. A geometrical model for the Monte Carlo simulation of the TrueBeam linac. Physics in Medicine & Biology, 60, 219-229.

Rodriguez, M., Zhou, H., Keall, P., and Graves, E., 2009. Commissioning of a novel micro CT/RT system for small animal conformal radiotherapy. Physics in Medicine & Biology, 54(12), 3727-3740.

Romeijn, H. E., Ahuja, R. K., Dempsey, J. F., and Kumar, A., 2005. A Column Generation Approach to Radiation Therapy Treatment Planning Using Apperture Modulation. Society for Industrial and Applied Mathematics Search: Journal on Optimization, 15(3), 838-862.

Rometsch, M., 2008. Quasi-Monte Carlo Methods in Finance with Application to Optimal Asset Allocation. Diplom.de.

Rossi, E., 2017. Dosimetric characterization of GafChromic EBT3 films in Volumetric Modulated Arc Therapy (VMAT) radiotherapy treatments. Master's thesis, School of Sciences, Department of Physics and Astronomy, University of Bologna.

Rønde, H. S. and Hoffmann, L., 2009. Validation of Varian's AAA algorithm with focus on lung treatments. Acta Oncologica, 48(2).

Rueden, C. T., Schindelin, J., Hiner, M. C., DeZonia, B. E., Walter, A. E., Arena, E. T., and Eliceiri, K. W., 2017. ImageJ2: ImageJ for the next generation of scientific image data. BMC Bioinformatics, 18, 529.

Saeed, S. B., 2015. Dynamic Log Files Analysis For Di erent Dose Rate IMRT Using DVH and Gamma Index. Master's thesis, Department of Oncology: Section of Radiation Oncology, Aga Khan University Hospital.

Saha, G. B., 2013. Physics and Radiobiology of Nuclear Medicine. Springer Science & Business Media, 4th edition.

Salles, A. A. F., Gorgulho, A., Agazaryan, N., Slotman, B., Selch, M., Burwick, A. J., and Schulz, R., 2011. Shaped Beam Radiosurgery: State of the Art. Springer Science & Business Media.

Salvat, F., 2015. PENELOPE-2014: A Code System for Monte Carlo Simulation of Electron and Photon Transport. Organization for Economic Co-operation and Development.

Salvat-Pujol, F., 2014. Simulation of radiation transport with the Monte-Carlo simulation code system Penelope. Francesc Salvat-Pujol$^{©}$.

Sarkar, B., Pradhan, A., and Ganesh, T., 2015. Derivative based sensitivity analysis of gamma index. Journal of Medical Physic, 40(4), 240-245.

Schreibmann, E., Dhabaan, A., Elder, E., and Fox, T., 2009. Patient-specific quality assurance method for VMAT treatment delivery. Medical Physics, 36(10), 4530-4535.

Schreiner, L. J., Holmes, O., and Salomons, G., 2013. Analysis and evaluation of planned and delivered dose distributions: practical concerns with γ- and χ-Evaluations. Journal of Physics: Conference Series, 444.

Seco, J. and Verhaegen, F., 2016. Monte Carlo Techniques in Radiation Therapy. CRC Press.

Seegenschmiedt, M. H., Makoski, H.-B., Trott, K.-R., and Brady, L. W., 2008. Radiotherapy for Non-Malignant Disorders. Springer Science & Business Media.

Selby, K., 2018. Three-Dimensional Radiation Treatment (3D-CRT). Asbestos.

Sharma, S., 2008. Atomic and Nuclear Physics. Pearson Education India.

Sharma, S. D., 2011. Unflattened photon beams from the standard flattening filter free accelerators for radiotherapy: Advantages, limitations and challenges. Journal of Medical Physics, 36(3), 123-125.

Shende, R. and Patel, G., 2017. Validation of Dosimetric Leaf Gap (DLG) prior to its implementation in Treatment Planning System (TPS): TrueBeamTM millennium 120 leaf MLC. Reports of Practical Oncology and Radiohterapy, 22, 485-494.

Shende, R., Gupta, G., Patel, G., and Kumar, S., 2016. Commissioning of TrueBeam^{TM} Medical Linear Accelerator: Quantitative and Qualitative Dosimetric Analysis and Comparison of Flattening Filter (FF) and Flattening Filter Free (FFF) Beam. International Journal of Medical Physics, Clinical Engineering and Radiation Oncology, 5, 51-69.

Shi, C. and Papanikolaou, N., 2007. Tracking versus Gating in the Treatment of Moving Targets. European Oncological Disease, 1(1), 83-87.

Shields, L. B. E., Bond, C., Odom, A., Sun, D. A., and Spalding, A. C., 2015. Heterogeneity correction for intensity-modulated frameless SRS in pituitary and cavernous sinus tumors: a retrospective study, 10, 193.

Sibtain, A., Morgan, A., and MacDougall, 2012. Physics for Clinical Oncology. Oxford University Press.

Siebers, J. V., 2011. Uncertainties in treatment planning dose computation. 2011 AAPM Summer School, Simon Fraser University.

Sikora, M. P., 2011. Virtual Source Modelling of Photon Beams for Monte Carlo Based Radiation Therapy Treatment Planning. PhD dissertation, University of Bergen.

Silberman, H. and Silberman, A. W., 2009. Principles and Practice of Surgical Oncology: Multidisciplinary Approach to Difficult Problems. Lippincott Williams & Wilkins.

Silver, J. J., 2006. Before and After Cancer Treatment: Heal Faster, Better, Stronger. JHU Press, 2nd edition.

Silverman, P., 2012. Oncologic Imaging: A Multidisciplinary Approach. Elsevier Health Sciences.

Singh, H., Sasane, A., and Lodha, R., 2016. Textbook of Radiology Physics. JP Medical Ltd.

Skrzyñski, W., 2004. Quality control of radiotherapy simulators. Reports of Practical Oncology and Radiotherapy, 9(6), 213-216.

Snider, J. W., and Mehta, M., 2016. Chapter 8: Principles in Radiation Therapy. Handbook of Clinical Neurology: Vol. 134 (3rd series) Gliomas. Elsevier.

Sood, S., Pokhrel, D., McClinton, C., Lominska, C., Badkul, R., Jiang, H., and Wang, F., 2017. Volumetric-modulated arc therapy (VMAT) for whole brain radiotherapy: not only for hippocampal sparing, but also for reduction of dose to organs at risk. Medical Dosimetry, 42(4), 375-383.

Sottiaux, A., Baltieri, V., Leclercq, C., Monseux, A., and Tomsej, M., 2016. Assessment of Monte Carlo calculations accuracy for VMAT treatment plans on a Novalis TrueBeam STx linac using PRIMO. Physica Medica, 32.

Splinter, R., 2016. Illustrated Encyclopedia of Applied and Engineering Physics. CRC Press.

Srinivasan, A., Mascagni, M., and Ceperley, D., 2003. Testing Parallel Random Number Generators. Parallel Computing, 29(1), 69-94.

Stathakis, S., Balbi, F., Chronopoulos, A. T., and Papanikolaou, N., 2016. Monte Carlo modeling of linear accelerator using distributed computing. Journal of BUON, 21(1), 252-260.

Stojadinovic, S., Ouyang, L., and Gu, X., 2015. Breaking bad IMRT QA practice. Journal of Applied Clinical Medical Physics, 16(3), 154-165.

Su, L., Yang, Y., Bednarz, B., Sterpin, E., Xining, D., Liu, T., Ji, W., and George Xu, X., 2014. ARCHER$_{RT}$ – A GPU-based and photon-electron coupled Monte Carlo dose computing engine for radiation therapy: Software development and application to helical tomotherapy. Medical Physics, 41(7).

Sun, Y. and Chmeilewski, A. G., 2017. Applications of Ionizing Radiation in Materials Processing: Volume 1. Institute of Nuclear Chemistry and Technology.

Sung, K., Lee, C. L., Lee, S. H., Ahn, S. H., Lee, S. H., and Choi, J., 2014. Cardiac dose reduction with breathing adapted radiotherapy using self respiration monitoring system for left-sided breast cancer. Radiation Oncology, 32(2), 84-94.

Suzuki, J., Tateoka, K., Shima, K., Yaegashi, Y., Fujimoto, K., Saitoh, Y., Nakata, A., Abe, T., Nakazawa, T., Sakata, K., and Hareyama, M., 2012. Uncertainty in patient set-up margin analysis in radiation therapy. Journal of Radiation Research, 53(4), 615-619.

Swenson, C., 2008. Modern Cryptanalysis: Techniques for Advanced Code Breaking. John Wiley & Sons, 1st edition.

Symonds, R. P., Deehan, C., Meredith, C., and Mills, J. A., 2012. Walter & Miller's Textbook of Radiotherapy: Radiation Physics, Therapy and Oncology. Elsevier Health Sciences, 7th edition.

Tang, G., Georgiev, G., Lim, S., Lovelock, D., Losasso, T., and Kirov, A. S., 2011. Dose Kernel of 6 MV FFF Beam in TrueBeam for Pencil Beam Convolution Algorithms. Medical Physics, 38(6), 3657.

Taylor, A. and Powell, M. E. B., 2004. Intensity-modulated radiotherapy—what is it?. Cancer Imaging, 4(2), 68-73.

Tavernier, S., 2010. Experimental Techniques in Nuclear and Particle Physics. Springer Science & Business Media.

Teke, T., Duzenli, C., Bergman, A., Viel, F., Atwal, P., and Gete, E., 2015. Monte Carlo validation of the TrueBeam 10XFFF phase–space files for applications in lung SABR. Medical Physics, 42(12), 6863-6874.

Teoh, M., Clark, C. H., Wood, K., Whitaker, S., and Nisbet, A., 2011. Volumetric modulated arc therapy: a review of current literature and clinical use in practice. The British Journal of Radiology, 84, 967-996.

Timmerman, R. D. and Xing, L., 2009. Image-Guided and Adaptive Radiation Therapy. Lippincott Williams & Wilkins.

The International Commission on Radiation Units and Measurements (ICRU), 2011. ICRU Report No.85: Fundamental Quantities and Units for Ionizing Radiation (Revised). Journal of the ICRU, 11(1).

MathWorks, 2006. MATLAB® The Language of Technical Computing. The MathWorks, Inc.

The Royal College of Radiologists, Institute of Physics and Engineering in Medicine and Society and College of Radiographers, 2008. Assessment of Monte Carlo calculations accuracy for VMAT treatment plans on a Novalis TrueBeam STx linac using PRIMO. The Royal College of Radiologists.

Thornton, S. T. and Rex, A., 2013. Modern Physics for Scientists and Engineers. Cengage Learning, 4th edition.

Tsunashima, Y., 2012. Verification of the clinical implementation of the respiratory gated beam delivery technique with synchrotron-based proton irradiation. PhD dissertation, UT GSBS Dissertations and Theses.

Turner, J. E., 2007. Atoms, Radiation, and Radiation Protection. John Wiley & Sons, 3rd edition.

Tweedy, J. T., 2013. Introduction to Hazard Control Management: A Vital Organizational Function. CRC Press.

Underwoord, C., 2016. The MATLAB Handbook. CreateSpace Independent Publishing Platform.

Unkelbach, J., Bortfeld, T., Craft, D., Alber, M., Bangert, M., Bokrantz, R., Chen, D., Li, R., Xing, L., Men, C., Nill, S., Papp, D., Romeijn, E., and Salari, E., 2015. Optimization approaches to volumetric modulated arc therapy planning. Medical Physics, 42(3), 1367-1377.

van de Merwe, van Dyk, J., Healy, B., Zubizarreta, E., Izewska, J., Mijnheer, B., and Meghzifene, A., 2017. Accuracy requirements and uncertainties in radiotherapy: a report of the International Atomic Energy Agency. Acta Oncologica, 56(1), 1-6.

van Dyk, J., Battista, J. J., and Bauman, G. S., 2014. Chapter 11: Accuracy and Uncertainty Considerations in Modern Radiation Oncology. The Modern Technology of Radiation Oncology: A Compendium for Medical Physicists and Radiation Oncologists, Volume 3. Medical Physics Publishing.

Vadrucci, M., Esposito, G., Rosinvalle, C., Cherubini, R., Marracino, F., Montereali, R. M., Picardi, L., Piccinini, M., Pimpinella, M., Vincenti, M. A., and De Angelis, C., 2015. Calibration of GafChromic EBT3 for absorbed dose measurements in 5 MeV proton beam and 60Co γ-rays. Medical Physics, 42(8), 4678-4684.

Varma, D. R., 2012. Managing DICOM images: Tips and tricks for the radiologist. Indian Journal of Radiology and Imaging, 22(1), 4-13.

Vassiliev, O. N., 2016. Monte Carlo Methods for Radiation Transport: Fundamentals and Advanced Topics. Springer.

Varian Medical Systems, 2010. The TrueBeam System. Centerline.

Varian Medical Systems, 2016. The TrueBeam System. Varian Medical Systems International AG.

Vidyasagar, P. B., Jagtap, S. S., and Yemul, O., 2017. Radiation in Medicine and Biology. CRC Press.

Vosper, M., Graham, D., and Cloke, P, 2011. Principles and Applications of Radiological Physics. Elsevier Health Sciences, 6th edition.

Voutilainen, A., 2016. Spatial Objectives in Radiation Therapy Treatment Planning. Master's thesis, School of Science, Aalto University.

Voyant, C., Julian, D., Roustit, R., Biffi, K., and Marcovici, C. L., 2014. Biological effects and equivalent doses in radiotherapy: a software solution. Reports of Practical Oncology & Radiotherapy, 19(1), 47-55.

Walter, F., Freislederer, P, Belka, C., Heinz, C., Söhn, M., and Roeder, F., 2016. Evaluation of daily patient positioning for radiotherapy with a commercial 3D surface-imaging system (Catalyst™). Radiation Oncology, 154(11).

Wang, L. and Ding, G. X., 2014. The accuracy of the out-of-field dose calculations using a model based algorithm in a commercial treatment planning system. Physics in Medicine & Biology, 59(13), 113-128.

Washington, C. M. and Leaver, D., 2015. Principles of Radiation Therapy. Elsevier Health Sciences, 4th edition.

Watanabe, Y., 2014. Calibration Issues of Relative Dosimeters. AAPM Chapter.

Wrennige, M., 2012. Production Volume Rendering: Design and Implementation. CRC Press.

Xhafa, B., Mulaj, T., Hodolli, G., and Nafezi, G., 2014. Dose Distribution of Photon Beam by Siemens Linear Accelerator. International Journal of Medical Physics, Clinical Engineering and Radiation Oncology, 3, 67-70.

Xiao, Y., Kry, S. F., Popple, R., Yorke, E., Papanikolaou, N., Stathakis, S., Xia, P., Huq, S., Bayouth, J., Galvin, J., and Yin, F., 2015. Flattening filter-free accelerators: a report from the AAPM Therapy Emerging Technology Assessment Work Group. Journal of Applied Clinical Medical Physics, 16(3), 12-29.

Xu, X. G., 2014. An exponential growth of computational phantom research in radiation protection, imaging, and radiotherapy: a review of the fifty-year history. Physics in Medicine & Biology, 59(18), 233-302.

Yadav, G., Yadav, R. S., and Kumar, A., 2009. Skin dose estimation for various beam modifiers and source-to-surface distance for 6MV photons. Journal of Medical Physics, 34(2), 87-92.

Yan, D., 2010. Adaptive radiotherapy: merging principle into clinical practice. Seminars in Radiation Oncology, 20(2), 79-83.

Yan, G., Mittauer, K., Huang, Y., Lu, B., Liu, C., and Li, J. G., 2013. Prevention of gross setup errors in radiotherapy with an efficient automatic patient safety system. Journal of Applied Clinical Medical Physics, 14(6), 322-337.

Yan, Y., Yaday, P., Bassetti, M., Du, K., Saenz, D., Harari, P., and Paliwal, B. R., 2016. Dosimetric differences in flattened and flattening filter-free beam treatment plans. Journal of Medical Physics, 41(2), 92-99.

Yang, C., Liu, F., Ahunbay, E., Chang, Y. W., Lawton, C., Schultz, C., Wang, D., Firat, S., Erickson, B., and Li, X., 2014. Combined online and offline adaptive radiation therapy: a dosimetric feasibility study. Practical Radiation Oncology, 4(1), 75-83.

Yang, F. and Hamilton, J. H., 2010. Modern Atomic and Nuclear Physics. World Scientific Publishing Company, revised edition.

Yao, W. and Farr, J. B., 2015. Determining the optimal dosimetric leaf gap setting for rounded leaf-end multileaf collimator systems by simple test fields. 16(4), 65-77.

Yarbro, C., Wujcik, D., and Gobel, B. H., 2010. Cancer Nursing: Principles and Practice. Jones & Bartlett Learning, 7th edition.

Yukihara, E. G. and McKeever, S. W. S., 2010. Optically Stimulated Luminescence: Fundamentals and Applications. John Wiley & Sons.

Zhang, G., Jiang, Z., Shepard, D., Earl, M., and Yu, C., 2005. Effect of beamlet step-size on IMRT plan quality. Medical Physics, 32(11), 3448-3458.

Zhang, S.-L., 2012. Raman Spectroscopy and its Application in Nanostructures. John Wiley & Sons.

Ziegenhein, P., Pirner, S., Kamerling, C. P., and Oelfke, U., 2015. Fast CPU-based Monte Carlo simulation for radiotherapy dose calculation. Physics in Medicine & Biology, 60, 6097-6111.

Ziegler, J. F., 2012. Ion Implantation Science and Technology. Elsevier, 2012 edition.

Zilles, A., 2017. Modeling of Radio Emission from Particle/Air Showers. Emission of Radio Waves in Particle Showers, Springer Theses, 15-30.

Appendix A

In this appendix the graphical representations of the measured and calculated PDDs and transverse profiles used for the validation of the phase space file mentioned in section 5.1.1.) are illustrated.

The PDDs are normalized to the dose maximum of each field size and the transversal profiles are normalized to the maximum value of the PDD, in order to establish the same normalization between the different fields.

A.1.) Measured PDDs and Transverse Profiles
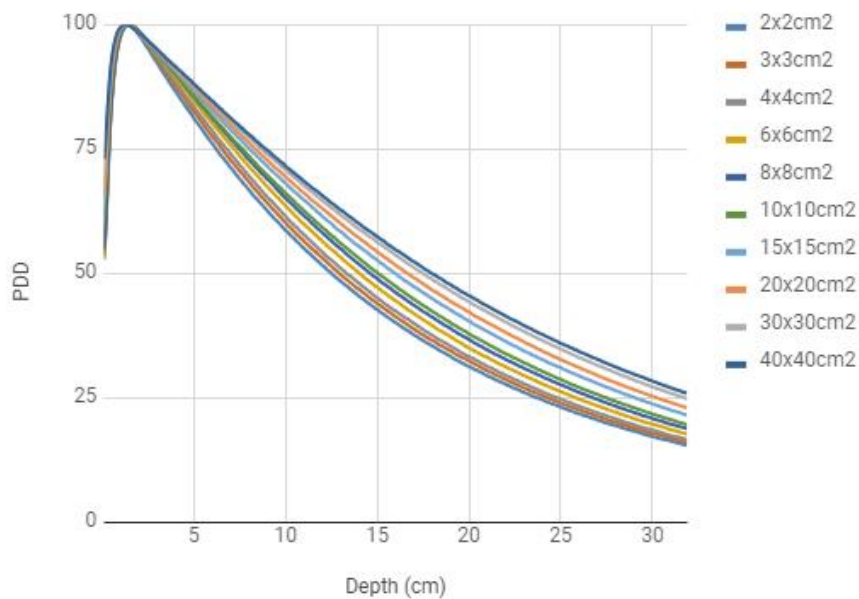
Graph A.1 - PDDs measured in the commissioning of the Varian TrueBeam unit.
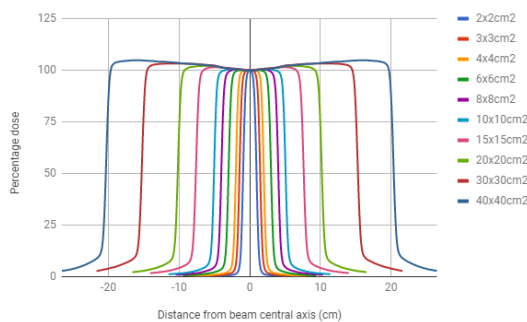
Graph A.2 - Measured transverse profiles at 1.5cm depth
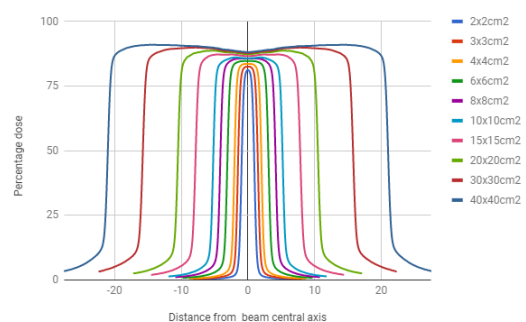
Graph A.3 - Measured transverse profiles at 5.0cm depth.
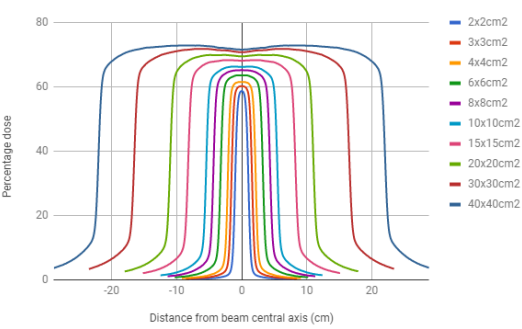
Graph A.4 - Measured transverse profiles at 10.0cm depth.
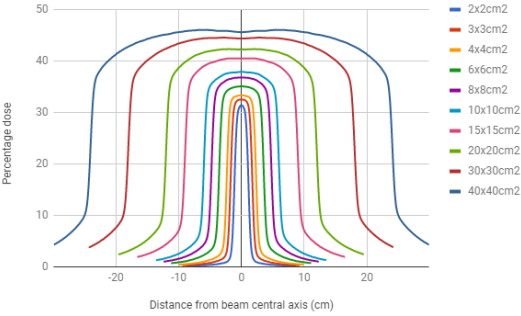
Graph A.5 - Measured transverse profiles at 20.0cm depth.
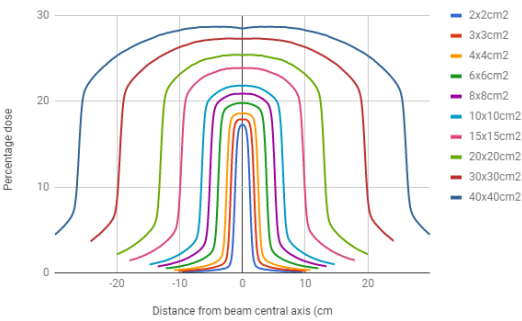
Graph A.6 - Measured transverse profiles at 30.0cm depth.
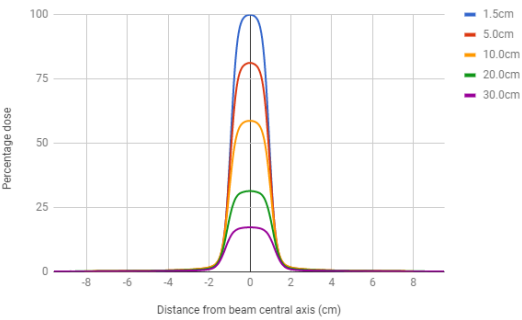
Graph A.7 – Measured transverse profiles for a 2x2cm² field size.
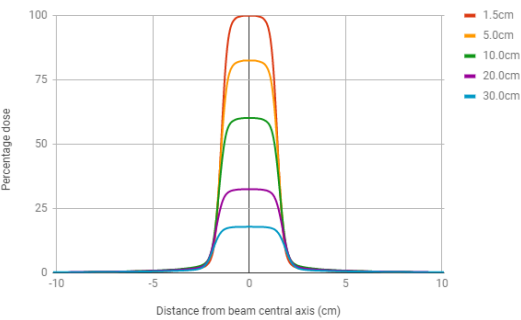
Graph A.8 - Measured transverse profiles for a 3x3cm² field size.
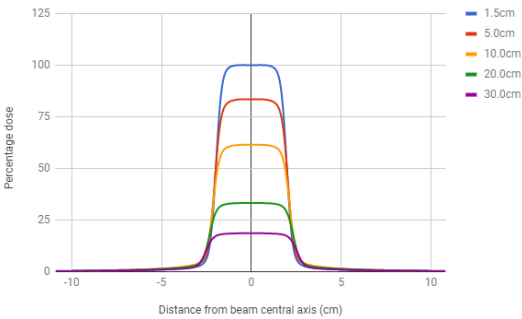
Graph A.9 - Measured transverse profiles for a 4x4cm² field size.
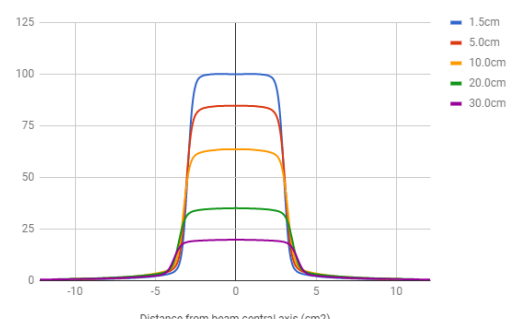
Graph A.10 - Measured transverse profiles for a 6x6cm² field size.
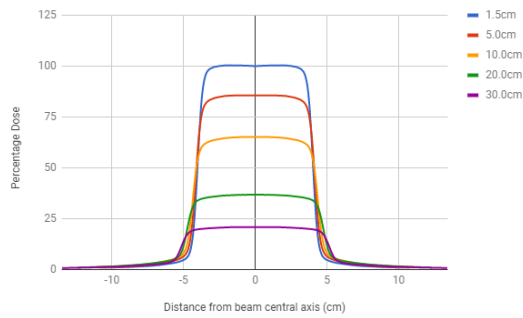
Graph A.11 - Measured transverse profiles for a 8x8cm^2
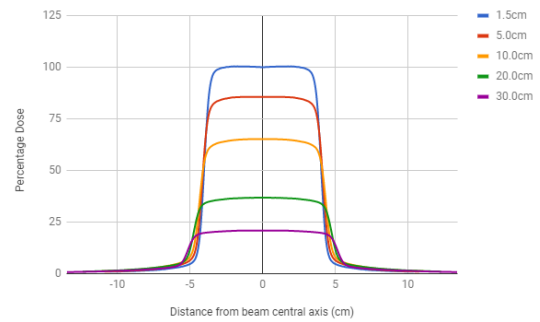
field size.

Graph A.12 - Measured transverse profiles for a 10x10cm^2
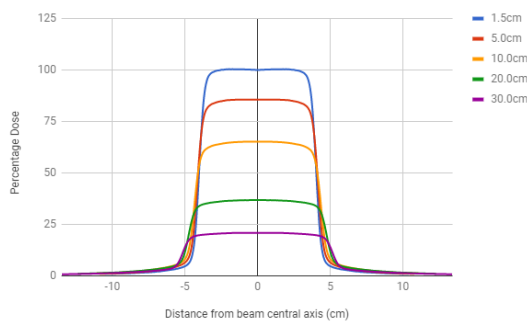
field size.

Graph A.13 - Measured transverse profiles for a 15x15cm^2
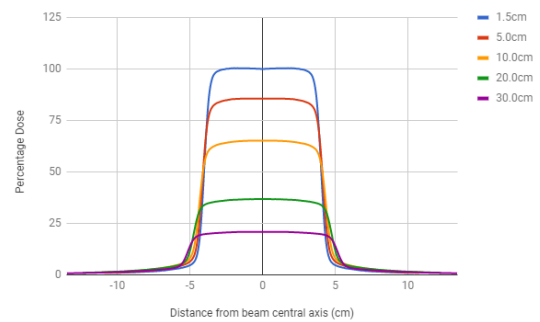
field size.

Graph A.14 - Measured transverse profiles for a 20x20cm^2
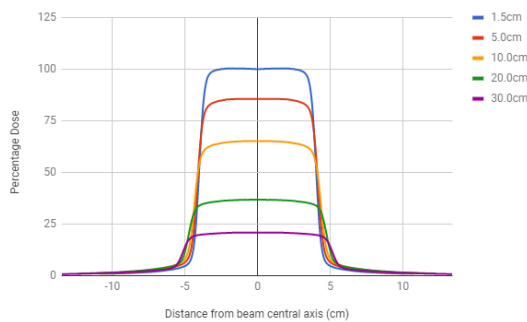
field size.

Graph A.15 - Measured transverse profiles for a 30x30cm^2
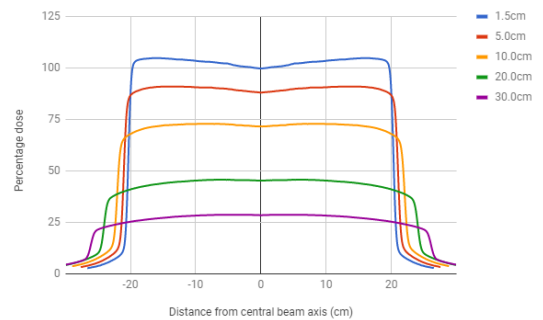
field size.

Graph A.16 - Measured transverse profiles for a 40x40cm^2

field size.

A.2.) Calculated PDDS and Transversal Profiles
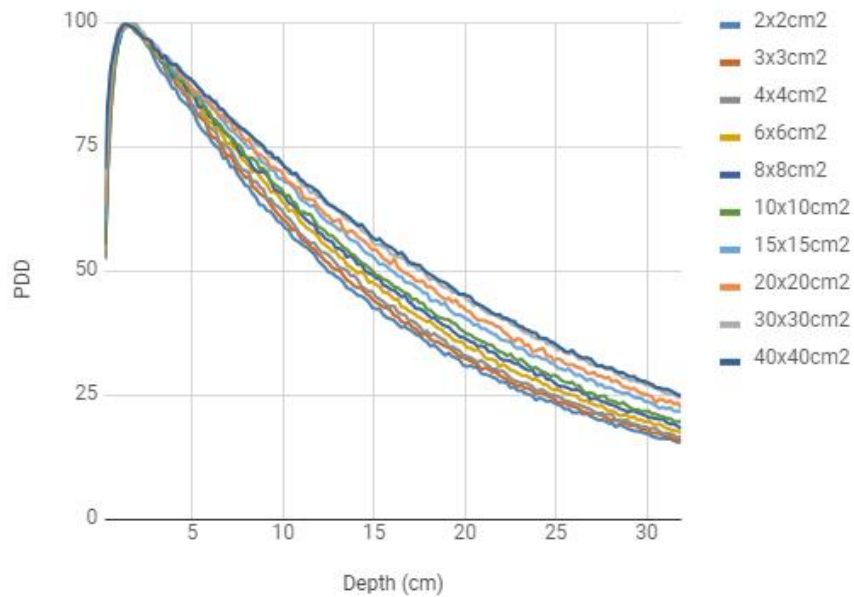
Graph A.17 - PDDs calculated with PRIMO for the Varian TrueBeam unit.
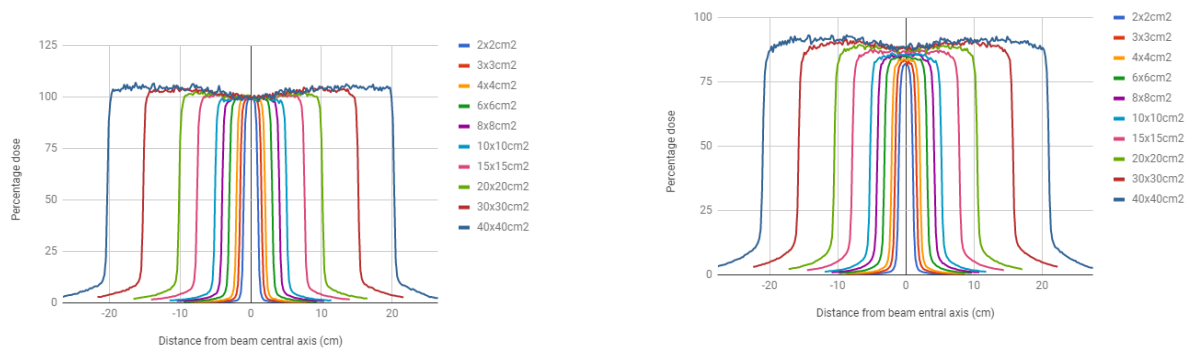
Graph A.18 - Calculated transverse profiles at 1.5cm depth.

Graph A.19 - Calculated transverse profiles at 5.0cm depth.
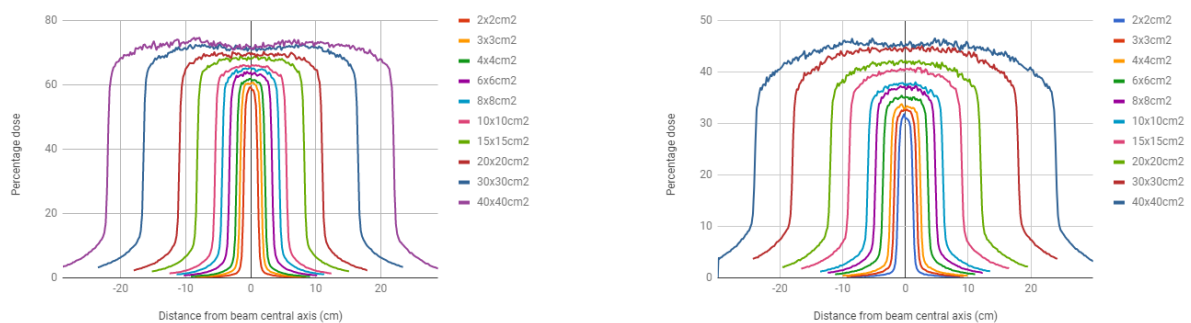
Graph A.20 - Calculated transverse profiles at 10.0cm depth.

Graph A.21 - Calculated transverse profiles at 20.0cm depth.
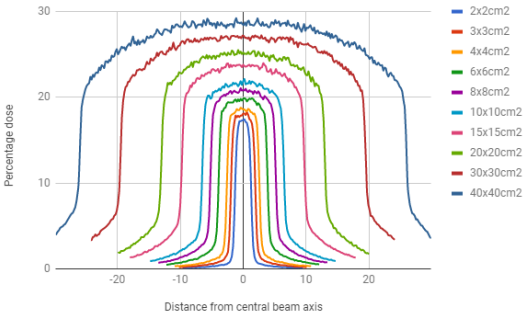
Graph A.22 - Calculated transverse profiles at 30.0cm depth.
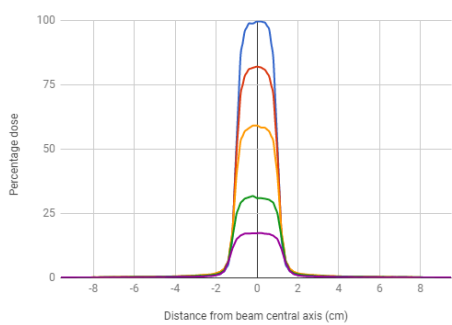
Graph A.23 - Calculated transverse profiles for a 2x2cm^2
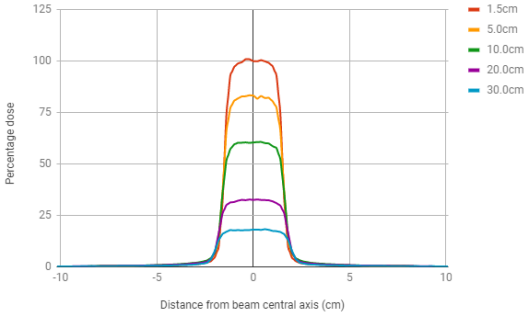
field size.

Graphi A.24 - Calculated transverse profiles for a 3x3cm^2
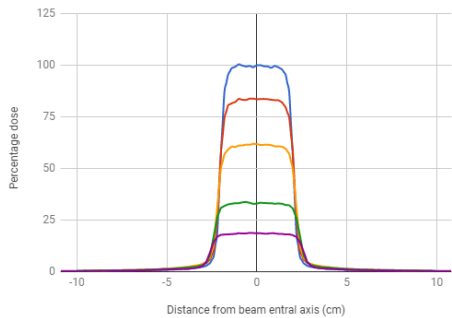
field size.

Graph A.25 - Calculated transverse profiles for a 4x4cm^2
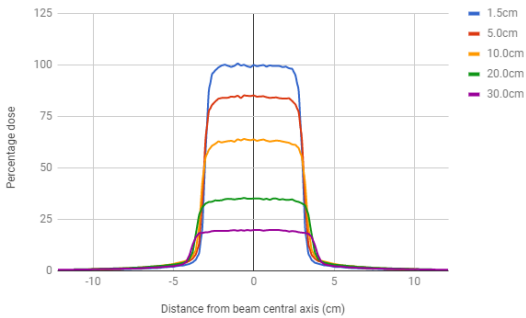
field size.

Graph A.26 - Calculated transverse profiles for a 6x6cm^2
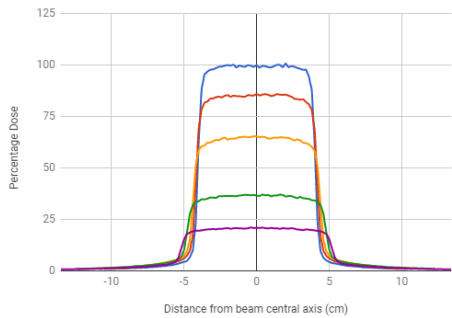
field size.

Graph A.27 - Calculated transverse profiles for a 8x8cm^2
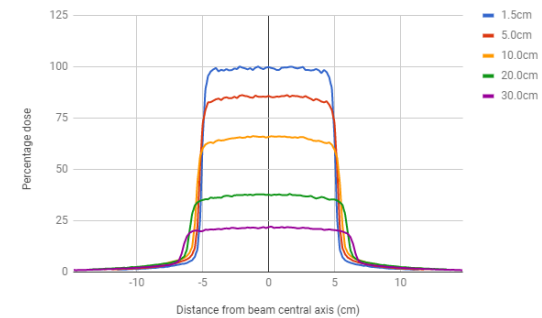
field size.

Graph A.28 - Calculated transverse profiles for a 10x10cm^2
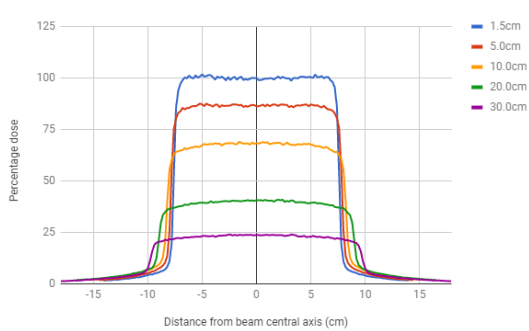
field size.

Graph A.29 - Calculated transverse profiles for a 15x15cm^2
field size.
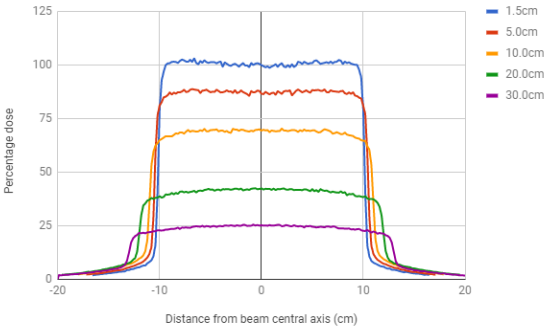
Graph A.30- Calculated transverse profiles for a 20x20cm^2
field size.
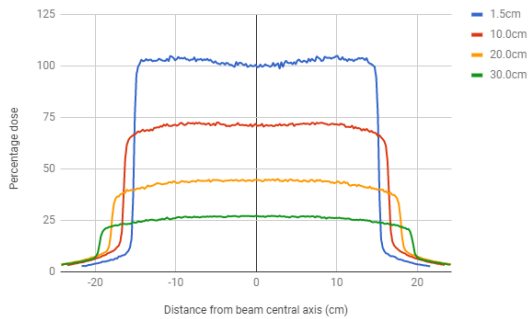
Graph A.31 - Calculated transverse profiles for a 30x30cm^2
field size.
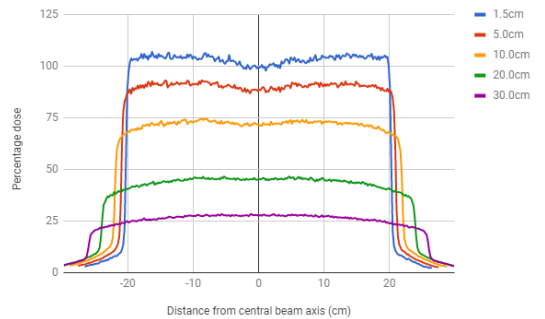
Graph A.32 - Calculated transverse profiles for a 30x30cm^2
field size.

Appendix B

This section includes the detailed results obtained from the simulations of the abdominal plan in the RUPERT phantom for all the positioning mismatches and volumes considered. As mentioned in section 5.5.2.), the data was analyzed in terms of Dmin, Dmax, dose tolerances established in QUANTEC, V95%, and percentage dose received by 98%, 50% and 2% of the PTV.

B.1.) Dmin

Shift	Dmin													
	CTV		PTV		Heart		Liver		Kidney R		Kidney L		Spinal Canal	
	Gy	%max dose	Gy	%max dose	Gy	%max dose	Gy	%max dose	Gy	%max dose	Gy	%max dose	Gy	%max dose
0mm	1.913	95.7	1.835	91.8	0.009	0.4	0.013	0.7	0.082	4.1	0.117	5.8	0.000	0.0
x+1mm	1.900	95.0	1.717	85.9	0.009	0.4	0.013	0.7	0.079	3.9	0.118	5.9	0.000	0.0
x+2mm	1.912	95.6	1.565	78.2	0.009	0.4	0.013	0.7	0.074	3.7	0.122	6.1	0.000	0.0
x+3mm	1.912	95.6	1.370	68.5	0.009	0.4	0.013	0.7	0.078	3.9	0.130	6.5	0.000	0.0
x+4mm	1.822	91.1	1.222	61.1	0.009	0.4	0.013	0.7	0.074	3.7	0.126	6.3	0.000	0.0
x+5mm	1.677	83.8	1.064	53.2	0.009	0.4	0.013	0.7	0.074	3.7	0.130	6.5	0.000	0.0
x-1mm	1.909	95.4	1.774	88.7	0.009	0.4	0.013	0.7	0.082	4.1	0.113	5.6	0.000	0.0
x-2mm	1.907	95.3	1.686	84.3	0.009	0.4	0.013	0.7	0.087	4.3	0.113	5.6	0.000	0.0
x-3mm	1.910	95.5	1.542	77.1	0.009	0.4	0.013	0.7	0.087	4.3	0.108	5.4	0.000	0.0
x-4mm	1.901	95.0	1.424	71.2	0.009	0.4	0.013	0.7	0.091	4.5	0.104	5.2	0.000	0.0
x-5mm	1.908	95.4	1.300	65.0	0.009	0.4	0.017	0.9	0.091	4.6	0.104	5.2	0.000	0.0
y+1mm	1.915	95.8	1.784	89.2	0.009	0.4	0.013	0.7	0.079	3.9	0.114	5.7	0.000	0.0
y+2mm	1.918	95.9	1.753	87.7	0.009	0.4	0.013	0.7	0.078	3.9	0.113	5.6	0.000	0.0
y+3mm	1.912	95.6	1.674	83.7	0.009	0.4	0.013	0.7	0.078	3.9	0.113	5.6	0.000	0.0

y+4mm	1.905	95.3	1.562	78.1	0.009	0.4	0.013	0.7	0.074	3.7	0.113	5.7	0.000	0.0
y+5mm	1.879	94.0	1.438	71.9	0.009	0.4	0.013	0.7	0.074	5.6	0.113	5.6	0.000	0.0
y-1mm	1.916	95.8	1.755	87.7	0.009	0.4	0.013	0.7	0.074	3.7	0.114	5.7	0.000	0.0
y-2mm	1.902	95.1	1.742	87.1	0.009	0.4	0.013	0.7	0.078	3.9	0.117	5.9	0.000	0.0
y-3mm	1.886	94.3	1.706	85.3	0.009	0.4	0.013	0.7	0.079	3.9	0.114	5.7	0.000	0.0
y-4mm	1.873	93.6	1.659	83.0	0.009	0.4	0.013	0.7	0.078	3.9	0.109	5.4	0.000	0.0
y-5mm	1.814	90.7	1.592	79.6	0.009	0.4	0.013	0.7	0.083	4.1	0.122	6.1	0.000	0.0
z+1mm	1.902	95.1	1.837	91.9	0.009	0.4	0.013	0.7	0.087	4.3	0.122	6.1	0.000	0.0
z+2mm	1.912	95.6	1.821	91.0	0.009	0.4	0.013	0.7	0.087	4.3	0.126	6.3	0.000	0.0
z+3mm	1.910	95.5	1.644	82.2	0.009	0.4	0.017	0.9	0.096	4.8	0.135	6.8	0.000	0.0
z+4mm	1.909	95.4	1.374	68.7	0.009	0.4	0.017	0.9	0.100	5.0	0.135	6.7	0.000	0.0
z+5mm	1.889	94.4	0.870	43.5	0.009	0.4	0.017	0.9	0.109	5.4	0.161	8.1	0.000	0.0
z+6mm	1.900	95.0	0.680	34.0	0.009	0.4	0.017	0.9	0.113	5.7	0.166	8.3	0.000	0.0
z+7mm	1.905	95.2	0.434	21.7	0.013	0.7	0.017	0.9	0.117	5.9	0.187	9.3	0.000	0.0
z+8mm	1.893	94.7	0.272	13.6	0.013	0.7	0.017	0.9	0.134	6.7	0.216	10.8	0.000	0.0
z-1mm	1.909	95.4	1.606	80.3	0.009	0.4	0.013	0.7	0.074	3.7	0.100	5.0	0.000	0.0
z-2mm	1.908	95.4	1.382	69.1	0.009	0.4	0.013	0.7	0.070	3.5	0.101	5.0	0.000	0.0
z-3mm	1.916	95.8	1.111	55.5	0.009	0.4	0.013	0.6	0.065	3.2	0.095	4.7	0.000	0.0
z-4mm	1.886	94.3	0.807	40.4	0.009	0.4	0.013	0.7	0.065	3.2	0.091	4.5	0.000	0.0
z-5mm	1.901	95.1	0.677	33.9	0.009	0.4	0.013	0.7	0.061	3.1	0.087	4.4	0.000	0.0
z-6mm	1.907	95.3	0.426	21.3	0.009	0.4	0.013	0.6	0.056	2.8	0.082	4.1	0.000	0.0
z-7mm	1.916	95.8	0.334	16.7	0.009	0.4	0.013	0.7	0.052	2.6	0.074	3.7	0.000	0.0
z-8mm	1.913	95.7	0.308	15.4	0.009	0.4	0.013	0.7	0.052	2.6	0.074	3.7	0.000	0.0

Table B.1 - Dmin values obtained for all the analyzed positioning mismatches and volumes in the abdominal plan for a single treatment fraction of 2 Gy.

Shift	Dmintotal													
	CTV		PTV		Heart		Liver		Kidney R		Kidney L		Spinal Canal	
	Gy	%max dose	Gy	%max dose	Gy	%max dose	Gy	%max dose	Gy	%max dose	Gy	%max dose	Gy	%max dose
0mm	47.833	95.7	45.885	91.8	0.218	0.4	0.325	0.7	2.055	4.1	2.923	5.8	0.000	0.0
x+1mm	47.510	95.0	42.935	85.9	0.218	0.4	0.328	0.7	1.963	3.9	2.943	5.9	0.000	0.0
x+2mm	47.808	95.6	39.115	78.2	0.218	0.4	0.325	0.7	1.848	3.7	3.043	6.1	0.000	0.0
x+3mm	47.788	95.6	34.243	68.5	0.218	0.4	0.325	0.7	1.950	3.9	3.250	6.5	0.000	0.0
x+4mm	45.548	91.1	30.545	61.1	0.218	0.4	0.325	0.7	1.848	3.7	3.153	6.3	0.000	0.0
x+5mm	41.913	83.8	26.603	53.2	0.218	0.4	0.325	0.7	1.845	3.7	3.258	6.5	0.000	0.0
x-1mm	47.715	95.4	44.355	88.7	0.218	0.4	0.325	0.7	2.060	4.1	2.820	5.6	0.000	0.0
x-2mm	47.663	95.3	42.138	84.3	0.218	0.4	0.325	0.7	2.168	4.3	2.818	5.6	0.000	0.0
x-3mm	47.758	95.5	38.553	77.1	0.218	0.4	0.325	0.7	2.165	4.3	2.708	5.4	0.000	0.0
x-4mm	47.518	95.0	35.610	71.2	0.218	0.4	0.325	0.7	2.273	4.5	2.598	5.2	0.000	0.0
x-5mm	47.698	95.4	32.488	65.0	0.218	0.4	0.870	0.4	2.283	4.6	2.608	5.2	0.000	0.0
y+1mm	47.878	95.8	44.598	89.2	0.218	0.4	0.328	0.7	1.968	3.9	2.843	5.7	0.000	0.0
y+2mm	47.945	95.9	43.825	87.7	0.218	0.4	0.325	0.7	1.953	3.9	2.820	5.6	0.000	0.0
y+3mm	47.800	95.6	41.840	83.7	0.218	0.4	0.325	0.7	1.950	3.9	2.818	5.6	0.000	0.0
y+4mm	47.630	95.3	39.040	78.1	0.218	0.4	0.325	0.7	1.848	3.7	2.828	5.7	0.000	0.0
y+5mm	46.983	94.0	35.940	71.9	0.218	0.4	0.325	0.7	1.840	3.7	2.815	5.6	0.000	0.0
y-1mm	47.908	95.8	43.870	87.7	0.218	0.4	0.328	0.7	1.855	3.7	2.838	5.7	0.000	0.0
y-2mm	47.558	95.1	43.540	87.1	0.218	0.4	0.325	0.7	1.955	3.9	2.933	5.9	0.000	0.0
y-3mm	47.138	94.3	42.643	85.3	0.220	0.4	0.330	0.7	1.973	3.9	2.850	5.7	0.000	0.0
y-4mm	46.815	93.6	41.480	83.0	0.218	0.4	0.328	0.7	1.960	3.9	2.723	5.4	0.000	0.0
y-5mm	45.355	90.7	39.795	79.6	0.218	0.4	0.328	0.7	2.073	4.1	3.053	6.1	0.000	0.0
z+1mm	47.718	95.4	40.143	80.3	0.218	0.4	0.325	0.7	1.840	3.7	2.488	5.0	0.000	0.0
z+2mm	47.710	95.4	34.548	69.1	0.220	0.4	0.330	0.7	1.755	3.5	2.523	5.0	0.000	0.0

z+3mm	47.888	95.8	27.763	55.5	0.215	0.4	0.323	0.6	1.615	3.2	2.368	4.7	0.000	0.0
z+4mm	47.160	94.3	20.180	40.4	0.215	0.4	0.325	0.7	1.620	3.2	2.268	4.5	0.000	0.0
z+5mm	47.528	95.1	16.935	33.9	0.218	0.4	0.328	0.7	1.530	3.1	2.185	4.4	0.000	0.0
z+6mm	47.668	95.3	10.653	21.3	0.215	0.4	0.323	0.6	1.400	2.8	2.045	4.1	0.000	0.0
z+7mm	47.905	95.8	8.345	16.7	0.218	0.4	0.325	0.7	1.300	2.6	1.843	3.7	0.000	0.0
z+8mm	47.830	95.7	7.700	15.4	0.218	0.4	0.325	0.7	1.303	2.6	1.843	3.7	0.000	0.0
z-1mm	47.553	95.1	45.925	91.9	0.218	0.4	0.325	0.7	2.173	4.3	3.040	6.1	0.000	0.0
z-2mm	47.798	95.6	45.523	91.0	0.218	0.4	0.325	0.7	2.168	4.3	3.143	6.3	0.000	0.0
z-3mm	47.740	95.5	41.093	82.2	0.218	0.4	0.435	0.9	2.398	4.8	3.380	6.8	0.000	0.0
z-4mm	47.718	95.4	34.348	68.7	0.218	0.4	0.435	0.9	2.500	5.0	3.370	6.7	0.000	0.0
z-5mm	47.215	94.4	21.758	43.5	0.218	0.4	0.435	0.9	2.720	5.4	4.025	8.1	0.000	0.0
z-6mm	47.495	95.0	16.993	34.0	0.218	0.4	0.435	0.9	2.833	5.7	4.140	8.3	0.000	0.0
z-7mm	47.613	95.2	10.845	21.7	0.325	0.7	0.435	0.9	2.928	5.9	4.663	9.3	0.000	0.0
z-8mm	47.333	94.7	6.808	13.6	0.325	0.7	0.433	0.9	3.350	6.7	5.403	10.8	0.000	0.0

Table B.2 - Dmin values obtained for all the analyzed positioning mismatches and volumes in the abdominal plan for a complete treatment composed by 25 fractions of 2 Gy each.

B.2.) Dmax

Shift	CTV			PTV			Heart			Liver			Kidney R			Kidney L			Spinal Canal		
	Gy	%max dose	Volume (%)	Gy	%max dose	Volume (%)	Gy	%max dose	Volume (%)	Gy	%max dose	Volume (%)	Gy	%max dose	Volume (%)	Gy	%max dose	Volume (%)	Gy	%max dose	Volume (%)
0mm	2.143	107.1	0.04	2.160	108.0	0.01	0.022	1.1	0.54	0.126	6.3	0.01	2.026	101.3	0.06	2.099	105.0	0.07	1.356	67.8	0.02
x+1mm	2.153	107.7	0.04	2.153	107.7	0.04	0.022	1.1	4.15	0.126	6.3	0.01	1.914	95.7	0.06	2.110	105.5	0.07	1.351	67.6	0.02
x+2mm	2.143	107.4	0.02	2.169	108.4	0.03	0.022	1.1	4.41	0.122	6.1	0.02	1.782	89.1	0.06	2.112	105.6	0.14	1.356	67.8	0.02
x+3mm	2.150	107.5	0.02	2.163	108.1	0.01	0.022	1.1	4	0.117	5.9	0.02	1.599	80.0	0.06	2.115	105.8	0.07	1.357	67.8	0.02
x+4mm	2.148	107.4	0.02	2.161	108.1	0.03	0.022	1.1	2.25	0.122	6.1	0.01	1.361	68.1	0.06	2.113	105.7	0.07	1.357	67.8	0.02
x+5mm	2.146	107.3	0.02	2.167	108.4	0.03	0.022	1.1	3.44	0.122	6.1	0.01	1.177	58.9	0.06	2.128	106.4	0.07	1.377	68.8	0.02
x-1mm	2.152	107.6	0.02	2.165	108.2	0.01	0.022	1.1	4.54	0.135	6.7	0.01	2.043	102.2	0.06	2.095	104.8	0.07	1.349	67.5	0.02
x-2mm	2.149	107.5	0.02	2.162	108.1	0.02	0.022	1.1	3.28	0.139	6.9	0.01	2.106	105.3	0.06	2.080	104.0	0.07	1.348	67.4	0.02
x-3mm	2.153	107.6	0.02	2.157	107.9	0.01	0.022	1.1	4.48	0.139	6.9	0.01	2.118	105.9	0.06	2.088	104.4	0.14	1.343	67.1	0.05
x-4mm	2.161	108.0	0.02	2.161	108.0	0.04	0.022	1.1	3.23	0.139	6.9	0.01	2.122	106.1	0.06	2.100	105.0	0.07	1.342	67.1	0.02
x-5mm	2.151	107.6	0.02	2.169	108.4	0.02	0.022	1.1	2.6	0.148	7.4	0.01	2.125	106.3	0.06	2.077	103.9	0.07	1.330	66.5	0.02
y+1mm	2.147	107.3	0.07	2.164	108.2	0.01	0.022	1.1	3.18	0.118	5.9	0.01	1.998	99.9	0.06	2.112	105.6	0.07	1.390	69.5	0.02
y+2mm	2.161	108.0	0.02	2.165	108.3	0.02	0.022	1.1	4.86	0.117	5.9	0.01	1.966	98.3	0.06	2.096	104.8	0.07	1.397	69.9	0.02
y+3mm	2.159	108.0	0.04	2.159	108.0	0.04	0.022	1.1	3.38	0.117	5.9	0.01	1.977	98.9	0.06	2.094	104.7	0.07	1.444	72.2	0.02
y+4mm	2.153	107.7	0.02	2.162	108.1	0.01	0.026	1.3	0.01	0.117	5.9	0.01	1.957	97.9	0.06	2.084	104.2	0.14	1.440	72.0	0.02
y+5mm	2.152	107.6	0.07	2.156	107.8	0.01	0.022	1.1	4.28	0.113	5.6	0.01	1.949	97.4	0.06	2.079	103.9	0.07	1.459	73.0	0.02
y-1mm	2.161	108.0	0.02	2.178	108.9	0.01	0.022	1.1	3.9	0.114	5.7	0.02	2.052	102.6	0.06	2.108	105.4	0.07	1.340	67.0	0.02
y-2mm	2.146	107.3	0.02	2.167	108.4	0.02	0.022	1.1	3.85	0.122	6.1	0.01	2.067	103.4	0.06	2.085	104.2	0.07	1.320	66.0	0.04
y-3mm	2.157	107.9	0.02	2.188	109.4	0.01	0.022	1.1	2.75	0.118	5.9	0.01	2.074	103.7	0.06	2.087	104.4	0.07	1.307	65.3	0.02

y-4mm	2.151	107.6	0.04	2.164	108.2	0.02	0.022	1.1	4.28	0.118	5.9	0.01	2.060	103.0	0.13	2.099	105.0	0.07	1.280	64.0	0.02
y-5mm	2.154	107.7	0.04	2.176	108.8	0.01	0.022	1.1	2.62	0.131	6.5	0.01	2.050	102.5	0.06	2.093	104.7	0.07	1.260	63.0	0.02
z+1mm	2.158	107.9	0.02	2.167	108.4	0.02	0.026	1.3	0.01	0.148	7.4	0.01	1.980	99.0	0.13	2.076	103.8	0.07	1.342	67.1	0.04
z+2mm	2.159	108.0	0.02	2.159	108.0	0.02	0.022	1.1	5.7	0.178	8.9	0.01	1.990	99.5	0.13	2.081	104.1	0.14	1.344	67.2	0.02
z+3mm	2.158	107.9	0.02	2.158	107.9	0.01	0.022	1.1	3.76	0.222	11.1	0.01	2.067	103.3	0.06	2.097	104.9	0.07	1.334	66.7	0.02
z+4mm	2.170	108.5	0.02	2.170	108.5	0.01	0.022	1.1	6.13	0.252	12.6	0.01	2.078	103.9	0.06	2.091	104.6	0.07	1.330	66.5	0.02
z+5mm	2.154	107.7	0.04	2.154	107.7	0.02	0.022	1.1	5.51	0.322	16.1	0.01	2.054	102.7	0.06	2.093	104.7	0.07	1.345	67.2	0.02
z+6mm	2.153	107.6	0.02	2.153	107.6	0.01	0.022	1.1	3.39	0.362	18.1	0.01	2.074	103.7	0.06	2.083	104.1	0.07	1.329	66.5	0.02
z+7mm	2.161	108.0	0.02	2.161	108.0	0.01	0.022	1.1	5.19	0.417	20.8	0.01	2.065	103.3	0.06	2.104	105.2	0.07	1.336	66.8	0.02
z+8mm	2.144	107.2	0.02	2.144	107.2	0.02	0.022	1.1	6.03	0.532	26.6	0.01	2.075	103.7	0.06	2.092	104.6	0.07	1.336	66.8	0.02
z-1mm	2.160	108.0	0.04	2.160	108.0	0.03	0.022	1.1	2.95	0.100	5.0	0.01	2.060	103.0	0.06	2.090	104.5	0.07	1.363	68.2	0.02
z-2mm	2.150	107.5	0.02	2.167	108.4	0.01	0.022	1.1	2.64	0.088	4.4	0.02	2.053	102.7	0.06	2.093	104.6	0.07	1.373	68.7	0.02
z-3mm	2.139	107.0	0.11	2.148	107.4	0.03	0.022	1.1	2.62	0.082	4.1	0.02	2.075	103.7	0.06	2.092	104.6	0.07	1.373	68.7	0.02
z-4mm	2.150	107.5	0.04	2.154	107.7	0.01	0.022	1.1	1.98	0.078	3.9	0.01	2.072	103.6	0.06	2.098	104.9	0.07	1.373	68.6	0.02
z-5mm	2.159	108.0	0.02	2.181	109.0	0.01	0.022	1.1	1.35	0.074	3.7	0.01	2.063	103.1	0.06	2.107	105.3	0.14	1.385	69.3	0.02
z-6mm	2.148	107.4	0.04	2.148	107.4	0.02	0.022	1.1	1.92	0.069	3.4	0.01	2.088	104.4	0.06	2.109	105.5	0.07	1.399	69.9	0.04
z-7mm	2.163	108.2	0.02	2.163	108.2	0.02	0.022	1.1	0.56	0.065	3.3	0.02	2.077	103.8	0.06	2.116	105.8	0.07	1.387	69.4	0.04
z-8mm	2.165	108.2	0.02	2.165	108.2	0.01	0.022	1.1	0.85	0.065	3.3	0.01	2.061	103.0	0.13	2.100	105.0	0.07	1.410	70.5	0.02

Table B.3 - Dmax values obtained for all the analyzed positioning mismatches and volumes in the abdominal plan for a single treatment fraction of 2 Gy.

Desvio	Dmax																				
	CTV			PTV			Heart			Liver			Kidney R			Kidney L			Spinal Canal		
	Gy	%max dose	Volume (%)	Gy	%max dose	Volume (%)	Gy	%max dose	Volume (%)	Gy	%max dose	Volume (%)	Gy	%max dose	Volume (%)	Gy	%max dose	Volume (%)	Gy	%max dose	Volume (%)
0mm	53.568	107.1	0.04	54.000	108.0	0.01	0.540	1.1	4.61	3.138	6.3	0.01	50.648	101.3	0.06	52.485	105.0	0.07	33.910	67.8	0.02
x+1mm	53.830	107.7	0.04	54.375	108.8	0.01	0.545	1.1	4.15	3.160	6.3	0.01	47.838	95.7	0.06	52.740	105.5	0.07	33.780	67.6	0.02
x+2mm	53.565	107.1	0.02	54.218	108.4	0.03	0.545	1.1	4.15	3.043	6.1	0.02	44.548	89.1	0.06	52.805	105.6	0.14	33.900	67.8	0.02
x+3mm	53.745	107.5	0.02	54.070	108.1	0.01	0.543	1.1	4	2.925	5.9	0.02	39.985	80.0	0.06	52.880	105.8	0.07	33.918	67.8	0.02
x+4mm	53.700	107.4	0.02	54.028	108.1	0.03	0.543	1.1	2.25	3.043	6.1	0.01	34.025	68.1	0.06	52.830	105.7	0.07	33.915	67.8	0.02
x+5mm	53.640	107.3	0.02	54.183	108.4	0.03	0.543	1.1	3.44	3.040	6.1	0.01	29.425	58.9	0.06	53.205	106.4	0.07	34.420	68.8	0.02
x-1mm	53.790	107.6	0.02	54.115	108.2	0.01	0.543	1.1	4.54	3.363	6.7	0.01	51.078	102.2	0.06	52.380	104.8	0.07	33.728	67.5	0.02
x-2mm	53.730	107.5	0.02	54.055	108.1	0.02	0.543	1.1	3.28	3.468	6.9	0.01	52.648	105.3	0.06	51.998	104.0	0.07	33.690	67.4	0.02
x-3mm	53.823	107.6	0.02	53.930	107.9	0.01	0.543	1.1	4.48	3.465	6.9	0.01	52.955	105.9	0.06	52.198	104.4	0.14	33.573	67.1	0.05
x-4mm	54.013	108.0	0.02	54.013	108.0	0.04	0.540	1.1	3.23	3.463	6.9	0.01	53.038	106.1	0.06	52.495	105.0	0.07	34.555	67.1	0.02
x-5mm	53.783	107.6	0.02	54.218	108.4	0.02	0.543	1.1	2.6	3.695	7.4	0.01	53.130	106.3	0.06	51.935	103.9	0.07	33.248	66.5	0.02
y+1mm	53.670	107.3	0.07	54.108	108.2	0.01	0.548	1.1	3.18	2.953	5.9	0.01	49.955	99.9	0.06	52.795	105.6	0.07	34.760	69.5	0.02
y+2mm	54.020	108.0	0.02	54.130	108.3	0.02	0.543	1.1	4.86	2.930	5.9	0.01	49.140	98.3	0.06	52.393	104.8	0.07	34.930	69.9	0.02
y+3mm	53.980	108.0	0.04	53.980	108.0	0.04	0.543	1.1	3.38	2.928	5.9	0.01	49.428	98.9	0.06	52.353	104.7	0.07	36.095	72.2	0.02
y+4mm	53.830	107.7	0.02	54.048	108.1	0.01	0.653	1.3	0.01	2.935	5.9	0.01	48.935	97.9	0.06	52.090	104.2	0.14	35.995	72.0	0.02
y+5mm	53.803	107.6	0.07	53.910	107.8	0.01	0.543	1.1	4.28	2.815	5.6	0.01	48.715	97.4	0.06	51.963	103.9	0.07	36.483	73.0	0.02
y-1mm	54.018	108.0	0.02	54.455	108.9	0.01	0.545	1.1	3.9	2.838	5.7	0.02	51.290	102.6	0.06	52.708	105.4	0.07	33.503	67.0	0.02
y-2mm	53.640	107.3	0.02	54.183	108.4	0.02	0.543	1.1	3.85	3.040	6.1	0.01	51.685	103.4	0.06	52.118	104.2	0.07	33.008	66.0	0.04
y-3mm	53.935	107.9	0.02	54.703	109.4	0.01	0.548	1.1	2.75	2.960	5.9	0.01	51.850	103.7	0.06	52.180	104.4	0.07	32.668	65.3	0.02
y-4mm	53.783	107.6	0.04	54.110	108.2	0.02	0.545	1.1	4.28	2.940	5.9	0.01	51.495	103.0	0.13	52.475	105.0	0.07	32.008	64.0	0.02
y-5mm	53.860	107.7	0.04	54.405	108.8	0.01	0.545	1.1	2.62	3.270	6.5	0.01	51.243	102.5	0.06	52.335	104.7	0.07	31.510	63.0	0.02
z+1mm	53.958	107.9	0.02	54.175	108.4	0.02	0.653	1.3	0.01	3.693	7.4	0.01	49.508	99.0	0.13	51.895	103.8	0.07	33.548	67.1	0.04

z+2mm	53.975	108.0	0.02	53.975	108.0	0.02	0.543	1.1	5.7	4.445	8.9	0.01	49.748	99.5	0.13	52.025	104.1	0.14	33.600	67.2	0.02
z+3mm	53.955	107.9	0.02	53.955	107.9	0.01	0.545	1.1	3.76	5.560	11.1	0.01	51.665	103.3	0.06	52.428	104.9	0.07	33.353	66.7	0.02
z+4mm	54.238	108.5	0.02	54.238	108.5	0.01	0.543	1.1	6.13	6.305	12.6	0.01	51.955	103.9	0.06	52.283	104.6	0.07	33.260	66.5	0.02
z+5mm	53.853	107.7	0.04	53.853	107.7	0.02	0.545	1.1	5.51	8.050	16.1	0.01	51.350	102.7	0.06	52.328	104.7	0.07	33.618	67.2	0.02
z+6mm	53.813	107.6	0.02	53.813	107.6	0.01	0.545	1.1	3.39	9.043	18.1	0.01	51.853	103.7	0.06	52.070	104.1	0.07	33.225	66.5	0.02
z+7mm	54.013	108.0	0.02	54.013	108.0	0.01	0.543	1.1	5.19	10.413	20.8	0.01	51.625	103.3	0.06	52.603	105.2	0.07	33.405	66.8	0.02
z+8mm	53.600	107.2	0.02	53.600	107.2	0.02	0.540	1.1	6.03	13.293	26.6	0.01	51.873	103.7	0.06	52.305	104.6	0.07	33.393	66.8	0.02
z-1mm	53.993	108.0	0.04	53.993	108.0	0.03	0.540	1.1	2.95	2.488	5.0	0.01	51.503	103.0	0.06	52.260	104.5	0.07	34.083	68.2	0.02
z-2mm	53.743	107.5	0.02	54.180	108.4	0.01	0.548	1.1	2.64	2.193	4.4	0.02	51.330	102.7	0.06	52.318	104.6	0.07	34.330	68.7	0.02
z-3mm	53.483	107.0	0.11	53.698	107.4	0.03	0.538	1.1	2.62	2.045	4.1	0.02	51.868	103.7	0.06	52.298	104.6	0.07	34.328	68.7	0.02
z-4mm	53.743	107.5	0.04	53.850	107.7	0.01	0.540	1.1	1.98	1.943	3.9	0.01	51.800	103.6	0.06	52.448	104.9	0.07	34.318	68.6	0.02
z-5mm	53.975	108.0	0.02	54.520	109.0	0.01	0.548	1.1	1.35	1.858	3.7	0.01	51.570	103.1	0.06	52.663	105.3	0.14	34.635	69.3	0.02
z-6mm	53.693	107.4	0.04	53.693	107.4	0.02	0.538	1.1	1.92	1.723	3.4	0.01	52.188	104.4	0.06	52.725	105.5	0.07	34.970	69.9	0.04
z-7mm	54.083	108.2	0.02	54.083	108.2	0.02	0.560	1.1	0.56	1.625	3.3	0.02	51.915	103.8	0.06	52.890	105.8	0.07	34.683	69.4	0.04
z-8mm	54.120	108.2	0.02	54.120	108.2	0.01	0.543	1.1	0.85	1.628	3.3	0.01	51.518	103.0	0.13	52.493	105.0	0.07	35.248	70.5	0.02

Table B.4 - Dmax values obtained for all the analyzed positioning mismatches and volumes in the abdominal plan for a complete treatment composed by 25 fractions of 2 Gy each.

B.3.) Dose Tolerances Established in QUANTEC

In this section, the values in black indicate that the dose received by the volume meets the values established by the QUANTEC initiative. On the other hand, the values in red represent dose values higher those than the QUANTEC recommendation.

Critical Structure	Volume	Dose/Volume	Max Dose	Toxicity Rate	Toxicity Endpoint	No shift	x+1 mm	x+2 mm	x+3 mm	x+4 mm	x+5 mm	x-1 mm	x-2 mm	x-3 mm	x-4 mm	x-5 mm
Spinal cord			50 Gy	0.20%	Myelopathy	33.910 Gy	33.780 Gy	33.900 Gy	33.918 Gy	33.915 Gy	34.420 Gy	33.728 Gy	33.690 Gy	33.573 Gy	34.555 Gy	33.248 Gy
Spinal cord			60 Gy	6%	Myelopathy	33.910 Gy	33.780 Gy	33.900 Gy	33.918 Gy	33.915 Gy	34.420 Gy	33.728 Gy	33.690 Gy	33.573 Gy	34.555 Gy	33.248 Gy
Spinal cord			69 Gy	50%	Myelopathy	33.910 Gy	33.780 Gy	33.900 Gy	33.918 Gy	33.915 Gy	34.420 Gy	33.728 Gy	33.690 Gy	33.573 Gy	34.555 Gy	33.248 Gy
Heart (Pericardium)	Mean	<26 Gy		<15%	Pericarditis	0.455 Gy	0.455 Gy	0.459 Gy	0.455 Gy	0.453 Gy	0.458 Gy	0.454 Gy	0.451 Gy	0.452 Gy	0.444 Gy	0.451 Gy
Heart (Pericardium)	V30	<46 %		<15%	Pericarditis	0.0%	0.0%	0.0%	0.0%	0.0%	0.0%	0.0%	0.0%	0.0%	0.0%	0.0%
Heart	V25	<10 %		<1%	Long term cardiac mortality	0.0%	0.0%	0.0%	0.0%	0.0%	0.0%	0.0%	0.0%	0.0%	0.0%	0.0%
Liver	Mean	<30-32 Gy		<5%	RILD (in normal liver function)	0.778 Gy	0.870 Gy	0.760 Gy	0.723 Gy	0.748 Gy	0.739 Gy	0.779 Gy	0.786 Gy	0.792 Gy	0.800 Gy	0.806 Gy
Liver	Mean	<42 Gy		<50%	RILD (in normal liver function)	0.778 Gy	0.870 Gy	0.760 Gy	0.723 Gy	0.748 Gy	0.739 Gy	0.779 Gy	0.786 Gy	0.792 Gy	0.800 Gy	0.806 Gy

Liver	Mean	<28 Gy		<5%	RILD (in Child-Pugh A or HCC)	0.778 Gy	0.870 Gy	0.760 Gy	0.723 Gy	0.748 Gy	0.739 Gy	0.779 Gy	0.786 Gy	0.792 Gy	0.800 Gy	0.806 Gy
Liver	Mean	<36 Gy		<50%	RILD (in Child-Pugh A or HCC)	0.778 Gy	0.870 Gy	0.760 Gy	0.723 Gy	0.748 Gy	0.739 Gy	0.779 Gy	0.786 Gy	0.792 Gy	0.800 Gy	0.806 Gy
Kidney, bilateral	Mean	<15-18 Gy		<5%	Clinical dysfunction	R - 11.175 Gy ; L - 16.754 Gy	R - 10.680 Gy ; L - 18.198 Gy	R - 10.212 Gy ; L - 19.882 Gy	R - 9.753 Gy ; L - 22.105 Gy	R - 9.348 Gy ; L - 24.675 Gy	R - 8.905 Gy ; L - 27.363 Gy	R - 11.820 Gy ; L - 15.615 Gy	R - 12.350 Gy ; L - 14.515 Gy	R - 13.213 Gy ; L - 13.863 Gy	R - 14.180 Gy ; L - 13.205 Gy	R - 15.320 Gy ; L - 12.715 Gy
Kidney, bilateral	Mean	<28 Gy		<50%	Clinical dysfunction	R - 11.175 Gy ; L - 16.754 Gy	R - 10.680 Gy ; L - 18.198 Gy	R - 10.212 Gy ; L - 19.883 Gy	R - 9.753 Gy ; L - 22.105 Gy	R - 9.348 Gy ; L - 24.675 Gy	R - 8.905 Gy ; L - 27.363 Gy	R - 11.820 Gy ; L - 15.615 Gy	R - 12.350 Gy ; L - 14.515 Gy	R - 13.213 Gy ; L - 13.863 Gy	R - 14.180 Gy ; L - 13.205 Gy	R - 15.320 Gy ; L - 12.715 Gy
Kidney, bilateral	V12	<55%		<5%	Clinical dysfunction	R - 46.6% ; L -72.2%	R - 42.7% ; L - 75.1%	R - 40.4 % ; L - 77.1%	R - 37.1% ; L - 80.0%	R - 35.1% ; L - 84.2%	R - 31.9% ; L - 83.7%	R - 49.1% ; L - 68.5%	R - 52.0% ; L - 65.6%	R - 54.8% ; L - 62.4%	R - 57.3% ; L - 58.7%	R - 59.9% ; L - 56.0%
Kidney, bilateral	V20	<32%		<5%	Clinical dysfunction	R - 19.2% ; L - 40.7%	R - 15.7% ; L - 46.3%	R - 11.9% ; L - 49.4%	R - 9.3% ; L - 55.5%	R - 6.7% ; L - 58.8%	R - 4.6% ; L - 64.6%	R - 23.0% ; L - 37.4%	R - 27.00% ; L - 31.4%	R - 31.6% ; L - 28.3%	R - 35.4% ; L - 23.0%	R - 39.5% ; L - 20.6%
Kidney, bilateral	V23	<30%		<5%	Clinical dysfunction	R - 14.7% ; L - 35.0%	R - 11.2% ; L - 38.6%	R - 8.4% ; L - 44.2%	R - 5.8% ; L - 47.8%	R - 3.7% ; L - 53.8%	R - 2.1% ; L - 57.3%	R - 18.6% ; L - 29.5%	R - 23.0% ; L - 26.2%	R - 26.5% ; L - 21.1%	R - 31.0% ; L - 18.2%	R - 34.6% ; L - 14.6%
Kidney, bilateral	V28	<20%		<5%	Clinical dysfunction	R - 9.6% ; L - 26.2%	R - 7.0% ; L - 30.0%	R - 4.5 % ; L - 35.3%	R - 2.7% ; L - 39.3%	R - 1.3% ; L - 44.5%	R - 0.3% ; L - 48.4%	R - 13.0% ; L -21.9%	R - 16.4% ; L - 18.5%	R - 23.0% ; L -15.0%	R - 21.0% ; L - 12.5%	R - 28.4% ; L - 10.9%

Table B.5 – Dose received by the various organs in the abdominal plan for the simulated positioning shifts in the x axis, considering the QUANTEC initiative.

Critical Structure	Volume	Dose/Volume	Max Dose	Toxicity Rate	Toxicity Endpoint	No shift	y+1mm	y+2mm	y+3mm	y+4mm	y+5mm	y-1mm	y-2mm	y-3mm	y-4mm	y-5mm
Spinal cord			50 Gy	0.20%	Myelopathy	33.910 Gy	34.760 Gy	34.930 Gy	36.095 Gy	35.995 Gy	36.483 Gy	33.503 Gy	33.008 Gy	32.668 Gy	32.008 Gy	31.510 Gy
Spinal cord			60 Gy	6%	Myelopathy	33.910 Gy	34.760 Gy	34.930 Gy	36.095 Gy	35.995 Gy	36.483 Gy	33.503 Gy	33.008 Gy	32.668 Gy	32.008 Gy	31.510 Gy
Spinal cord			69 Gy	50%	Myelopathy	33.910 Gy	34.760 Gy	34.930 Gy	36.095 Gy	35.995 Gy	36.483 Gy	33.503 Gy	33.008 Gy	32.668 Gy	32.008 Gy	31.510 Gy
Heart (Pericardium)	Mean	<26 Gy		<15%	Pericarditis	0.455 Gy	0.452 Gy	0.449 Gy	0.448 Gy	0.455 Gy	0.449 Gy	0.449 Gy	0.451 Gy	0.448 Gy	0.452 Gy	0.451 Gy
Heart (Pericardium)	V30	<46%		<15%	Pericarditis	0.0%	0.0%	0.0%	0.0%	0.0%	0.0%	0.0%	0.0%	0.0%	0.0%	0.0%
Heart	V25	<10%		<1%	Long term cardiac mortality	0.0%	0.0%	0.0%	0.0%	0.0%	0.0%	0.0%	0.0%	0.0%	0.0%	0.0%
Liver	Mean	<30-32 Gy		<5%	RILD (in normal liver function)	0.778 Gy	0.760 Gy	0.760 Gy	0.757 Gy	0.757 Gy	0.757 Gy	0.760 Gy	0.760 Gy	0.760 Gy	0.761 Gy	0.768 Gy
Liver	Mean	<42 Gy		<50%	RILD (in normal liver function)	0.778 Gy	0.760 Gy	0.760 Gy	0.757 Gy	0.757 Gy	0.757 Gy	0.760 Gy	0.760 Gy	0.760 Gy	0.761 Gy	0.768 Gy
Liver	Mean	<28 Gy		<5%	RILD (in Child-Pugh A or HCC)	0.778 Gy	0.760 Gy	0.760 Gy	0.757 Gy	0.757 Gy	0.757 Gy	0.760 Gy	0.760 Gy	0.760 Gy	0.761 Gy	0.768 Gy
Liver	Mean	<36 Gy		<50%	RILD (in Child-Pugh	0.778 Gy	0.760 Gy	0.760 Gy	0.757 Gy	0.757 Gy	0.757 Gy	0.760 Gy	0.760 Gy	0.760 Gy	0.761 Gy	0.768 Gy

					A or HCC)										
Kidney, bilateral	Mean	<15-18 Gy		<5%	Clinical dysfunction	R - 11.175 Gy ; L - 16.754 Gy	R - 10.823 Gy ; L - 16.678 Gy	R - 10.848 Gy ; L - 17.030 Gy	R - 11.055 Gy ; L - 17.343 Gy	R - 11.093 Gy ; L - 17.943 Gy	R - 11.150 Gy ; L - 18.513 Gy	R - 10.913 Gy ; L - 16.400 Gy	R - 10.968 Gy ; L - 16.505 Gy	R - 11.183 Gy ; L - 16.553 Gy	R - 11.433 Gy ; L - 16.666 Gy	R - 11.885 Gy ; L - 17.455 Gy
Kidney, bilateral	Mean	<28 Gy		<50%	Clinical dysfunction	R - 11.175 Gy ; L - 16.754 Gy	R - 10.823 Gy ; L - 16.678 Gy	R - 10.848 Gy ; L - 17.030 Gy	R - 11.055 Gy ; L - 17.343 Gy	R - 11.093 Gy ; L - 17.943 Gy	R - 11.150 Gy ; L - 18.513 Gy	R - 10.913 Gy ; L - 16.400 Gy	R - 10.968 Gy ; L - 16.505 Gy	R - 11.183 Gy ; L - 16.553 Gy	R - 11.433 Gy ; L - 16.666 Gy	R - 11.885 Gy ; L - 17.455 Gy
Kidney, bilateral	V12	<55%		<5%	Clinical dysfunction	R - 46.6% ; L -72.2%	R - 44.3% ; L - 71.3%	R - 44.5% ; L - 71.8%	R - 44.9% ; L - 73.2%	R - 45.7% ; L - 74.3%	R - 45.8% ; L - 75.1%	R - 45.1% ; L - 70.3%	R - 45.4% ; L - 70.1%	R - 46.2% ; L - 70.5%	R - 47.4% ; L - 71.3%	R - 49.6% ; L - 73.1%
Kidney, bilateral	V20	<32%		<5%	Clinical dysfunction	R - 19.2% ; L - 40.7%	R - 18.4% ; L - 40.5%	R - 18.6% ; L - 41.6%	R - 19.1% ; L - 42.5%	R - 19.6% ; L - 44.1%	R - 20.3% ; L - 45.5%	R - 18.8% ; L - 39.1%	R - 19.0% ; L - 39.2%	R - 20.0% ; L - 39.5%	R - 20.5% ; L - 39.8%	R - 22.9% ; L - 41.7%
Kidney, bilateral	V23	<30%		<5%	Clinical dysfunction	R - 14.7% ; L - 35.0%	R - 14.0% ; L -35.0%	R - 14.1% ; L - 35.7%	R - 14.6% ; L - 37.1%	R - 14.8% ; L - 38.3%	R - 15.3% ; L - 40.0%	R - 14.1% ; L - 33.7%	R - 14.4% ; L - 33.7%	R - 15.0% ; L - 33.3%	R - 15.8% ; L - 34.3%	R - 17.5% ; L - 35.0%
Kidney, bilateral	V28	<20%		<5%	Clinical dysfunction	R - 9.6% ; L - 26.2%	R - 9.1% Gy ; L -26.4%	R - 9.3% ; L - 27.5%	R - 9.4% ; L - 28.5%	R - 9.7% ; L - 29.7%	R - 9.5% ; L - 30.7%	R - 9.4% ; L - 25.2%	R - 9.8% ; L - 25.0%	R - 10.4% ; L - 24.6%	R - 10.9% ; L - 24.7%	R - 11.4% ; L - 24.8%

Table B.6 - Dose received by the various organs in the abdominal plan for the simulated positioning shifts in the y axis, considering the QUANTEC initiative.

Critical Structure	Volume	Dose/Volume	MaxDose	Toxicity Rate	Toxicity Endpoint	No shift	z+1mm	z+2mm	z+3mm	z+4mm	z+5mm	z+6mm	z+7mm	z+8 mm	z-1mm	z-2mm	z-3mm	z-4mm	z-5mm	z-6mm	z-7mm	z-8 mm
Spinal cord			50 Gy	0.20%	Myelopathy	33.910 Gy	33.548 Gy	33.600 Gy	33.353 Gy	33.260 Gy	33.618 Gy	33.225 Gy	33.405 Gy	33.393 Gy	34.083 Gy	34.330 Gy	34.328 Gy	34.318 Gy	34.635 Gy	34.970 Gy	34.683 Gy	35.248 Gy
Spinal cord			60 Gy	6%	Myelopathy	33.910 Gy	33.548 Gy	33.600 Gy	33.353 Gy	33.260 Gy	33.618 Gy	33.225 Gy	33.405 Gy	33.393 Gy	34.083 Gy	34.330 Gy	34.328 Gy	34.318 Gy	34.635 Gy	34.970 Gy	34.683 Gy	35.248 Gy
Spinal cord			69 Gy	50%	Myelopathy	33.910 Gy	33.548 Gy	33.600 Gy	33.353 Gy	33.260 Gy	33.618 Gy	33.225 Gy	33.405 Gy	33.393 Gy	34.083 Gy	34.330 Gy	34.328 Gy	34.318 Gy	34.635 Gy	34.970 Gy	34.683 Gy	35.248 Gy
Heart (Pericardium)	Mean	<26 Gy		<15%	Pericarditis	0.455 Gy	0.453 Gy	0.463 Gy	0.463 Gy	0.465 Gy	0.469 Gy	0.469 Gy	0.471 Gy	0.470 Gy	0.449 Gy	0.437 Gy	0.436 Gy	0.433 Gy	0.431 Gy	0.430 Gy	0.421 Gy	0.417 Gy
Heart (Pericardium)	V30	<46%		<15%	Pericarditis	0.0%	0.0%	0.0%	0.0%	0.0%	0.0%	0.0%	0.0%	0.0%	0.0%	0.0%	0.0%	0.0%	0.0%	0.0%	0.0%	0.0%
Heart	V25	<10%		<1%	Long term cardiac mortality	0.0%	0.0%	0.0%	0.0%	0.0%	0.0%	0.0%	0.0%	0.0%	0.0%	0.0%	0.0%	0.0%	0.0%	0.0%	0.0%	0.0%
Liver	Mean	<30-32 Gy		<5%	RILD (in normal liver function)	0.778 Gy	0.784 Gy	0.806 Gy	0.830 Gy	0.856 Gy	0.895 Gy	0.910 Gy	0.937 Gy	0.985 Gy	0.739 Gy	0.721 Gy	0.707 Gy	0.685 Gy	0.679 Gy	0.650 Gy	0.636 Gy	0.630 Gy
Liver	Mean	<42 Gy		<50%	RILD (in normal liver function)	0.778 Gy	0.784 Gy	0.806 Gy	0.830 Gy	0.856 Gy	0.895 Gy	0.910 Gy	0.937 Gy	0.985 Gy	0.739 Gy	0.721 Gy	0.707 Gy	0.685 Gy	0.679 Gy	0.650 Gy	0.636 Gy	0.630 Gy
Liver	Mean	<28 Gy		<5%	RILD (in Child-Pugh A or HCC)	0.778 Gy	0.784 Gy	0.806 Gy	0.830 Gy	0.856 Gy	0.895 Gy	0.910 Gy	0.937 Gy	0.985 Gy	0.739 Gy	0.721 Gy	0.707 Gy	0.685 Gy	0.679 Gy	0.650 Gy	0.636 Gy	0.630 Gy
Liver	Mean	<36 Gy		<50%	RILD (in Child-Pugh A or HCC)	0.778 Gy	0.784 Gy	0.806 Gy	0.830 Gy	0.856 Gy	0.895 Gy	0.910 Gy	0.937 Gy	0.985 Gy	0.739 Gy	0.721 Gy	0.707 Gy	0.685 Gy	0.679 Gy	0.650 Gy	0.636 Gy	0.630 Gy

Organ	Metric	Constraint		<5%	Endpoint																	
Kidney, bilateral	Mean	<15-18 Gy		<5%	Clinical dysfunction	R - 11.175 Gy ; L - 16.754 Gy	R - 11.563 Gy ; L - 17.045 Gy	R - 12.140 Gy ; L - 17.883 Gy	R - 12.753 Gy ; L - 18.858 Gy	R - 13.370 Gy ; L - 19.348 Gy	R - 14.294 Gy ; L - 20.563 Gy	R - 14.560 Gy ; L - 21.460 Gy	R - 15.293 Gy ; L - 22.600 Gy	R - 16.425 Gy ; L - 23.775 Gy	R - 10.170 Gy ; L - 16.013 Gy	R - 8.993 Gy ; L - 15.465 Gy	R - 7.963 Gy ; L - 14.743 Gy	R - 7.123 Gy ; L - 14.245 Gy	R - 6.555 Gy ; L - 13.985 Gy	R - 5.488 Gy ; L - 13.128 Gy	R - 4.878 Gy ; L - 12.680 Gy	R - 4.773 Gy ; L - 12.365 Gy
Kidney, bilateral	Mean	<28 Gy		<50%	Clinical dysfunction	R - 11.175 Gy ; L - 16.754 Gy	R - 11.563 Gy ; L - 17.045 Gy	R - 12.140 Gy ; L - 17.883 Gy	R - 12.753 Gy ; L - 18.858 Gy	R - 13.370 Gy ; L - 19.348 Gy	R - 14.294 Gy ; L - 20.563 Gy	R - 14.560 Gy ; L - 21.460 Gy	R - 15.293 Gy ; L - 22.600 Gy	R - 16.425 Gy ; L - 23.775 Gy	R - 10.170 Gy ; L - 16.754 Gy	R - 8.993 Gy ; L - 15.465 Gy	R - 7.963 Gy ; L - 14.743 Gy	R - 7.123 Gy ; L - 14.245 Gy	R - 6.555 Gy ; L - 13.985 Gy	R - 5.488 Gy ; L - 13.128 Gy	R - 4.878 Gy ; L - 12.680 Gy	R - 4.773 Gy ; L - 12.365 Gy
Kidney, bilateral	V12	<55%		<5%	Clinical dysfunction	R - 46.6% ; L - 72.2%	R - 47.4% ; L - 73.3%	R - 50.7% ; L - 73.4%	R - 53.7% ; L - 78.4%	R - 57.1% ; L - 81.6%	R - 61.1% ; L - 85.0%	R - 62.8% ; L - 86.1%	R - 65.5% ; L - 87.4%	R - 70.4% ; L - 90.1%	R - 42.3% ; L - 68.9%	R - 39.8% ; L - 66.2%	R - 37.0% ; L - 63.1%	R - 35.1% ; L - 60.3%	R - 34.2% ; L - 59.0%	R - 30.8% ; L - 55.0%	R - 28.7% ; L - 52.5%	R - 27.8% ; L - 51.3%
Kidney, bilateral	V20	<32%		<5%	Clinical dysfunction	R - 19.2% ; L - 40.7%	R - 19.9% ; L - 41.9%	R - 22.3% ; L - 43.5%	R - 24.7% ; L - 45.8%	R - 26.9% ; L - 48.0%	R - 31.0% ; L - 51.4%	R - 31.9% ; L - 53.4%	R - 35.1% ; L - 55.2%	R - 39.1% ; L - 58.1%	R - 16.9% ; L - 37.5%	R - 15.9% ; L -35.8%	R - 14.8% ; L -34.0%	R - 13.9% ; L - 32.7%	R - 13.5% ; L - 31.4%	R - 12.7% ; L - 30.4%	R - 12.1% ; L - 29.1%	R - 11.8% ; L - 28.8%
Kidney, bilateral	V23	<30%		<5%	Clinical dysfunction	R - 14.7% ; L - 35.0%	R - 15.3% ; L - 35.3%	R - 17.5% ; L - 38.0%	R - 19.4% ; L - 39.8%	R - 21.9% ; L - 41.8%	R - 25.7% ; L - 45.7%	R - 26.1% ; L - 46.8%	R - 29.2% ; L - 49.1%	R -33.2% ; L - 51.9%	R - 12.9% ; L - 31.8%	R - 12.2% ; L - 30.7%	R - 11.7% ; L - 28.5%	R - 11.0% ; L - 27.6%	R - 10.8% ; L - 27.1%	R - 10.5% ; L - 25.7%	R - 10.2% ; L - 25.7%	R -9.9% ; L - 25.1%
Kidney, bilateral	V28	<20%		<5%	Clinical dysfunction	R - 9.6% ; L - 26.2%	R - 10.1% ; L - 26.9%	R - 11.2% ; L - 29.3%	R - 13.1% ; L - 31.2%	R - 14.7% ; L - 33.1%	R - 18.0% ; L - 36.3%	R - 18.5% ; L - 37.4%	R - 21.2% ; L - 39.6%	R - 24.7% ; L - 42.9%	R - 8.6% ; L - 24.2%	R - 8.5% ; L - 22.8%	R - 8.0% ; L - 21.6%	R - 8.0% ; L - 20.7%	R - 7.8% ; L - 20.7%	R - 7.6% ; L - 20.3%	R - 7.5% ; L - 19.8%	R - 7.5% ; L - 19.6%

Table B.7 - Dose received by the various organs in the abdominal plan for the simulated positioning shifts in the z axis, considering the QUANTEC initiative.

B.4.) V95%

Positioning	CTV	PTV
No shift	100.00	99.57
x-5	100.00	92.26
x-4	100.00	94.08
x-3	100.00	96.06
x-2	100.00	97.61
x-1	100.00	98.98
x+1	100.00	99.44
x+2	100.00	98.23
x+3	100.00	97.03
x+4	99.70	95.23
x+5	99.54	93.21
y-5	99.70	89.36
y-4	99.87	92.19
y-3	99.94	94.77
y-2	100.00	97.04
y-1	100.00	98.58
y+1	100.00	99.47
y+2	100.00	98.70
y+3	100.00	97.38
y+4	100.00	95.13
y+5	99.98	92.83
z-8	100.00	86.15
z-7	100.00	87.32
z-6	100.00	89.45
z-5	100.00	92.23
z-4	99.98	93.21
z-3	100.00	95.12
z-2	100.00	96.82
z-1	100.00	98.47
z+1	100.00	99.64
z+2	100.00	99.09
z+3	100.00	98.61
z+4	100.00	97.78
z+5	99.98	95.99
z+6	100.00	95.24
z+7	100.00	93.44
z+8	99.98	91.08

Table B.8 – V95% values for the CTV and the PTV.

B.5.) Dose received by the PTV

Table B.9 represents the percentage dose received by 98% (D98%), 50% (D50%) and 2% (D2%) of the PTV volume, for each positioning mismatch simulated in PRIMO.

PTV	D98%	D50%	D2%
No shift	96.4%	100.0%	105.3%
x+1mm	96.3%	100.0%	105.5%
x+2mm	95.3%	99.9%	105.4%
x+3mm	93.6%	99.9%	105.3%
x+4mm	90.0%	99.8%	105.4%
x+5mm	84.4%	99.7%	105.4%
x-1mm	95.9%	99.9%	105.4%
x-2mm	94.6%	99.9%	105.4%
x-3mm	91.7%	99.9%	105.4%
x-4mm	87.5%	99.7%	105.5%
x-5mm	83.9%	99.7%	105.4%
y+1mm	96.4%	99.9%	108.1%
y+2mm	95.9%	99.9%	108.3%
y+3mm	94.3%	99.8%	108.1%
y+4mm	91.6%	99.7%	107.9%
y+5mm	88.3%	99.6%	108.1%
y-1mm	95.6%	100.0%	108.4%
y-2mm	94.3%	100.0%	108.4%
y-3mm	92.3%	99.9%	108.7%
y-4mm	89.7%	99.9%	108.2%
y-5mm	87.0%	99.7%	108.6%
z+1mm	95.4%	100.0%	108.0%
z+2mm	93.2%	99.9%	108.0%
z+3mm	88.2%	99.9%	107.4%
z+4mm	80.5%	99.8%	107.6%
z+5mm	76.5%	99.8%	108.8%
z+6mm	61.1%	99.8%	107.4%
z+7mm	51.2%	99.7%	108.1%
z+8mm	46.9%	99.7%	107.8%
z-1mm	96.3%	100.0%	108.4%
z-2mm	96.0%	100.0%	108.0%
z-3mm	95.7%	99.9%	107.8%
z-4mm	94.7%	99.8%	107.8%
z-5mm	90.3%	99.8%	107.7%
z-6mm	86.3%	99.8%	107.3%
z-7mm	74.8%	99.7%	107.8%
z-8mm	60.1%	99.6%	107.2%

Table B.9 - Percentage dose received by different percentages of the PTV.